
THE UNIVERSITY OF QUEENSLAND

AUSTRALIA

# Designed synthesis of mono-dispersed silica-based nanostructures and their applications in drug/gene delivery

Meihua Yu

Doctor of Philosophy

*A thesis submitted for the degree of Doctor of Philosophy at*

*The University of Queensland in 2014*

Australian Institute for Bioengineering & Nanotechnology

**Abstract**

Over the last two decades, silica based nanoparticles (SiNPs) have been extensively investigated as promising nano-carriers to deliver various therapeutic/diagnostic agents into living systems, due to their unique properties of tunable pore structure and particle size, easy surface modification and low cost. In particular, SiNPs with small sizes (< 100 nm) and high monodispersity, SiNPs possess great advantages in cell endocytosis process, which is vital to achieve high efficiency in biomedical applications. Although there have been tremendous studies in the synthesis of monodisperse nanometer-sized SiNPs, more efforts are still needed to develop facile, economic and environmentally friendly synthesis approaches for fabricating novel monodisperse SiNPs with desired particle size, nano-structure and functionality. The as-designed novel SiNPs are expected to expand their capacity in various biomedical applications, such as enhanced bio-imaging performance in three dimensional spheroid models, improved cellular drug/gene delivery efficiency.

The aim of this project is to develop novel and facile approaches to prepare highly mono-dispersed SiNPs with finely controlled structures for drug/gene delivery and gain insight into the roles of particle size, surface functionality on cell penetration performance and drug/gene delivery efficiency. The main achievements obtained in this thesis are listed below.

In the first part, a new and facile approach has been developed to prepare monodisperse mesoporous silica nanospheres (MMSNs) with controlled particle sizes (50-100 nm) and pore diameters (2.8-4.0 nm). In this approach, MMSNs were synthesized simply in a sodium acetate solution without adding any other alkali or alcohol additives. By further investigations on formation process, we proposed a spherical micelle templating mechanism to explain the formation of MMSNs in our system, which is different from that of traditional highly ordered mesoporous silica nanoparticles (MCM-41). MMSNs developed in this part are expected to have potential applications in drug/gene delivery and cell imaging.

In the second part, even smaller mono-dispersed SiNPs (ultra-small hybrid silica spheres, UHSS) with a diameter of only ~ 10 nm were developed by a facile strategy under phosphate-citrate buffer solution (pH = 4.6) at room temperature without addition of toxic additives. Compared to traditional MCM-41 nanomaterials, the designed novel UHSS showed enhanced penetration ability in three dimensional glioma spheroids.

Following the second part, epoxysilane functionalized UHSS (Epoxy-UHSS) with a diameter of ~10 nm were designed under similar synthesis conditions, which can be easily covalently conjugated with cationic polyethyleneimine (PEI) (PEI-UHSS). This designed positively charged PEI-UHSS demonstrated excellent delivery efficiency of a functional siRNA against polo-like kinase 1 (PLK1-siRNA) in osteosarcoma cancer cells (KHOS) and survivin-siRNA in human colon cancer cells (HCT-116) inducing a significant cell inhibition, which is comparable to commercial

agents. These results indicated that suitable functionality of SiNPs is significant to achieve efficient gene delivery.

In the fourth part, we further investigated the influence of surface functionality of SiNPs on drug delivery efficiency. Hyaluronic acid (HA) modified mesoporous silica nanoparticles (MSNs) were developed, which possess specific affinity to CD44 over expressed on the surface of a specific cancer cell line, HCT-116 (human colon cancer cells). Compared with bare MSNs, HA-MSNs exhibited a higher cellular uptake via HA receptor mediated endocytosis. An anticancer drug, doxorubicin hydrochloride (Dox), were loaded into MSNs and HA-MSNs. Dox loaded HA-MSNs showed greater cytotoxicity to HCT-116 cells than free Dox and Dox-MSNs due to the enhanced cell internalization behavior of HA-MSNs. This work indicated that the desired surface functionality is also crucial to improve drug delivery efficiency.

Apart from surface functionality, the particle size of SiNPs is expected to have significant effect on gene delivery efficiency. In the last part, amine modified monodisperse Stöber spheres ($NH_2$-SS) with various diameters of 125, 230, 330, 440 and 570 nm were synthesized. The *in vitro* transfection efficiencies of $NH_2$-SS were studied in HEK293T cells by delivering plasmid DNA encoding green fluorescent protein (GFP) (pcDNA3-EGFP, abbreviated as pcDNA, 6.1kbp). It was found that an optimized particle size of 330 nm exhibited the highest expression of GFP. Our mechanistic study showed that the binding affinity of pcDNA/$NH_2$-SS complexes decreased while the cellular uptake ability increased with $NH_2$-SS size increasing from 125 to 570 nm. The opposite effects lead to an optimal $NH_2$-SS size of 330 nm that provides the maximum gene delivery efficiency. A similar size-dependent gene delivery relationship was further demonstrated in another plasmid DNA with a bigger size of 8.9 kbp. This work for the first time demonstrates the significant role of particle size of cationic silica nano-carriers on gene delivery efficiency. The knowledge obtained from this work is crucial for the rational design of synthetic gene delivery systems with improved efficiency for gene therapy.

**Declaration by author**

This thesis is composed of my original work, and contains no material previously published or written by another person except where due reference has been made in the text. I have clearly stated the contribution by others to jointly-authored works that I have included in my thesis.

I have clearly stated the contribution of others to my thesis as a whole, including statistical assistance, survey design, data analysis, significant technical procedures, professional editorial advice, and any other original research work used or reported in my thesis. The content of my thesis is the result of work I have carried out since the commencement of my research higher degree candidature and does not include a substantial part of work that has been submitted to qualify for the award of any other degree or diploma in any university or other tertiary institution. I have clearly stated which parts of my thesis, if any, have been submitted to qualify for another award.

I acknowledge that an electronic copy of my thesis must be lodged with the University Library and, subject to the General Award Rules of The University of Queensland, immediately made available for research and study in accordance with the *Copyright Act 1968*.

I acknowledge that copyright of all material contained in my thesis resides with the copyright holder(s) of that material. Where appropriate I have obtained copyright permission from the copyright holder to reproduce material in this thesis.

**Publications during candidature**

***Peer-reviewed papers***

1. **Yu, Meihua**; Zhou, Liang; Zhang, Jun; Yuan, Pei; Thorn, Peter; Gu, Wenyi; Yu, Chengzhong, A simple approach to prepare monodisperse mesoporous silica nanospheres with adjustable sizes, *Journal of Colloid and Interface Science* **2012**, 376, 67-75.
2. **Yu, Meihua**; Jambhrunkar, Siddharth; Thorn, Peter; Chen, Jiezhong; Gu, Wenyi; Yu, Chengzhong, Hyaluronic acid modified mesoporous silica nanoparticles for targeted drug delivery to CD44-overexpressing cancer cells, *Nanoscale* **2013**, 5, 178-183. (This work has been highlighted as the inside cover paper)
3. **Yu, Meihua**; Karmakar, Surajit; Yang, Jie; Zhang, Hongwei; Yang, Yannan; Thorn, Peter; Yu, Chengzhong, Facile synthesis of ultra-small hybrid silica spheres for enhanced penetration in 3D glioma spheroids, *Chemical Communications* **2014**, 50, 1527-1529. (This work has been highlighted as the back cover paper)
4. **Yu, Meihua**; Niu, Yuting; Yang, Yannan; Hartono, Sandy B; Yang, Jie; Huang, Xiaodan; Thorn, Peter; Yu, Chengzhong, An approach to prepare polyethyleneimine functionalized silica-based spheres with small size for siRNA delivery, *ACS Applied Materials & Interfaces*, **2014**, 6, 15626-15631.
5. **Yu, Meihua**; Niu, Yuting; Zhang, Jun; Zhang, Hongwei; Yang, Yannan; Taran, Elena; Jambhrunkarar, Siddharth; Gu, Wenyi; Thorn, Peter; Yu, Chengzhong, An unusual size-dependent gene delivery relationship of monodispersed silica nanoparticles, *ACS Nano* (nn-2014-011842, under revision).
6. Jambhrunkar, Siddharth; **Yu, Meihua**; Yang, Jie; Zhang, Jun; Shrotri, Abhijit; Endo-Munoz, Liliana; Moreau, Joël; Lu, Gaoqing; Yu, Chengzhong, Stepwise Pore Size Reduction of Ordered Nanoporous Silica Materials at Angstrom Precision, *Journal of the American Chemical Society* **2013**, 135, 8444-8447.
7. Niu, Yuting; **Yu, Meihua**; Hartono, Sandy B.; Yang, Jie; Xu, Hongyi; Zhang, Hongwei; Zhang, Jun; Zou, Jin; Dexter, Annette; Gu, Wenyi; Yu, Chengzhong, Nanoparticles Mimicking Viral Surface Topography for Enhanced Cellular Delivery, *Advanced Materials* **2013**, 25, 6233-6237.
8. Hartono, Sandy B; **Yu, Meihua**; Gu, Wenyi; Yang, Jie; Strounina, Ekaterina; Wang, Xiaolin; Qiao, Shizhang; Yu, Chengzhong, Synthesis of multi-functional large pore mesoporous silica nanoparticles as gene carriers, *Nanotechnology* **2014**, 25, 055701.

9. Zhang, Jun; **Yu, Meihua**; Yuan, Pei; Lu, Gaoqing; Yu, Chengzhong, Controlled release of volatile (−)-menthol in nanoporous silica materials, *Journal of Inclusion Phenomena and Macrocyclic Chemistry* **2011**, 71, 593-602.
10. Yan, Yannan.; Karmakar, Surajit.; Zhang, Jun.; **Yu, Meihua**; Mitter, Neena.; Yu, Chengzhong, Synthesis of SBA-15 Rods with Small Sizes for Enhanced Cellular Uptake. *Journal of Materials Chemistry B* **2014**, 2, 4929-4934
11. Zhang, Jun.; Karmakar, Surajit.; **Yu, Meihua**; Mitter, Neena.; Zou, Jin.; Yu, Chengzhong, Synthesis of Silica Vesicles with Controlled Entrance Size for High Loading, Sustained Release, and Cellular Delivery of Therapeutical Proteins. *Small* **2014**. (DOI: 10.1002/smll.201401538)
12. Yang, Jie; Zhang, Hongwei; **Yu, Meihua**; Emmanuelawati, Irene; Zou, Jin; Yuan, Zhiguo; Yu, Chengzhong, High-Content, Well-Dispersed γ-Fe2O3 Nanoparticles Encapsulated in Macroporous Silica with Superior Arsenic Removal Performance, *Advanced Functional Materials* **2014**, 24, 1354–1363.
13. Budi Hartono, Sandy; Truong, Nghia Phuoc; **Yu, Meihua**; Jia, Zhongfan; Monteiro, Michael; Qiao, Shizhang; Yu, Chengzhong, Functionalized Large Pore Mesoporous Silica Nanoparticles for Gene Delivery featuring Time-dependent Release and Co-delivery, *Journal of Materials Chemistry B* **2014**, 2, 718 - 726.
14. Niu, Yuting; Popat, Amirali; **Yu, Meihua**; Karmakar, Surajit; Gu, Wenyi; Yu, Chengzhong, Recent advances in the rational design of silica-based nanoparticles for gene therapy, *Therapeutic Delivery* **2012**, 3, 1217-1237.
15. Yang, Yannan; Karmakar, Surajit; **Yu, Meihua**; Popat, Amirali; Yu, Chengzhong, Synthesis of Silica Vesicles with Small Sizes and Reduced Aggregation for Photodynamic Therapy, *Chemistry Letters* **2014**, 43, 316–318.
16. Jambhrunkar, Siddharth; Karmakar, Surajit; Popat, Amirali; **Yu, Meihua**; Yu, Chengzhong, Mesoporous silica nanoparticles enhance the cytotoxicity of curcumin, *RSC Advances* **2014**, 4, 709-712.
17. Qian, Kun; Zhou, Liang; Liu, Jian; Yang, Jie; Xu, Hongyi; **Yu, Meihua**; Nouwens, Amanda; Zou, Jin; Monteiro, Michael J.; Yu, Chengzhong, Laser Engineered Graphene Paper for Mass Spectrometry Imaging, *Scientific Reports* **2013**, 3, 1415 (DOI:10.1038/srep01415).
18. Shen, Shaodian; Gu, Tao; Mao, Dongsen; Xiao, Xiuzhen; Yuan, Pei; **Yu, Meihua**; Xia, Liyang; Ji, Qiong; Meng, Liang; Song, Wei; Yu, Chengzhong; Lu, Guanzhong, Synthesis of Nonspherical Mesoporous Silica Ellipsoids with Tunable Aspect Ratios for Magnetic Assisted Assembly and Gene Delivery, *Chemistry of Materials* **2011**, 24, 230-235.

19. Zhu, Jie; Wang, Huixiang; Liao, Lei; Zhao, Lingzhi; Zhou, Liang; **Yu, Meihua**; Wang, Yunhua; Liu, Baohong; Yu, Chengzhong, Small Mesoporous Silica Nanoparticles as Carriers for Enhanced Photodynamic Therapy, *Chemistry–An Asian Journal* **2011**, 6, 2332-2338.

***Conference proceedings***

1. **Yu, Meihua**; Gu, Wenyi; Jambhrunkar, Siddharth; Thorn, Peter; Chen, Jiezhong; Yu, Chengzhong, Hyaluronic Acid Modified Mesoporous Silica Nanoparticles for Targeted Delivery of Doxorubicin to CD44-overexpressing Cancer Cells

   **1st International Conference on BioNano Innovation (ICBNI)**, 18-20 July 2012, Brisbane Convention & Exhibition Centre, Australia (Oral presentation)

**Publications included in this thesis**

**Yu, Meihua**; Zhou, Liang; Zhang, Jun; Yuan, Pei; Thorn, Peter; Gu, Wenyi; Yu, Chengzhong, A simple approach to prepare monodisperse mesoporous silica nanospheres with adjustable sizes, *Journal of Colloid and Interface Science* **2012**, 376, 67-75. – incorporated as Chapter 4.

| Contributor | Statement of contribution |
|---|---|
| Author Yu, Meihua (Candidate) | Experimental design and performance (80 %)<br>Analysis and interpretation of data (75 %)<br>Drafting and writing (75 %) |
| Author Zhou, Liang | Analysis and interpretation of data (10 %) |
| Author Zhang, Jun | Experimental performance (5%) |
| Author Yuan, Pei | Experimental performance (5%) |
| Author Thorn, Peter | Drafting and writing (5 %) |
| Author Gu, Wenyi | Drafting and writing (5 %) |
| Author Yu, Chengzhong | Experimental design and performance (10 %)<br>Analysis and interpretation of data (15 %)<br>Drafting and writing (15 %) |

**Yu, Meihua**; Karmakar, Surajit; Yang, Jie; Zhang, Hongwei; Yang, Yannan; Thorn, Peter; Yu, Chengzhong, Facile synthesis of ultra-small hybrid silica spheres for enhanced penetration in 3D glioma spheroids, *Chemical Communications* **2014**, 50, 1527-1529. – incorporated as Chapter 5.

| Contributor | Statement of contribution |
|---|---|
| Author Yu, Meihua (Candidate) | Experimental design and performance (40 %)<br>Analysis and interpretation of data (70 %)<br>Drafting and writing (70 %) |
| Author Karmakar, Surajit | Experimental design and performance (40 %)<br>Analysis and interpretation of data (20 %)<br>Drafting and writing (15 %) |
| Author Yang, Jie | Experimental performance (5%) |
| Author Zhang, Hongwei | Experimental performance (5%) |
| Author Yang, Yannan | Experimental performance (5%) |
| Author Thorn, Peter | Drafting and writing (5 %) |
| Author Yu, Chengzhong | Experimental design and performance (5 %)<br>Analysis and interpretation of data (10 %)<br>Drafting and writing (10 %) |

**Yu, Meihua**; Niu, Yuting; Yang, Yannan; Hartono, Sandy B; Yang, Jie; Huang, Xiaodan; Thorn, Peter; Yu, Chengzhong, A novel approach to prepare polyethyleneimine functionalized silica-based spheres with small size for siRNA delivery, *ACS Applied Materials & Interfaces*, **2014**, 6, 15626-15631.– Incorporated as Chapter 6.

| Contributor | Statement of contribution |
|---|---|
| Author Yu, Meihua (Candidate) | Experimental design and performance (75%)<br>Analysis and interpretation of data (75 %)<br>Drafting and writing (85 %) |
| Author Niu, Yuting | Experimental performance (4 %)<br>Analysis and interpretation of data (5%) |
| Author Yang, Yannan | Experimental performance (4%)<br>Analysis and interpretation of data (5%) |
| Author Hartono, Sandy B | Experimental performance (4%)<br>Analysis and interpretation of data (5%) |
| Author Yang, Jie | Experimental performance (4%) |
| Author Huang, Xiaodan | Experimental performance (4%) |
| Author Thorn, Peter | Drafting and writing (5 %) |
| Author Yu, Chengzhong | Experimental design and performance (5 %)<br>Analysis and interpretation of data (10 %) |

| | |
|---|---|
| | Drafting and writing (10 %) |

**Yu, Meihua**; Jambhrunkar, Siddharth; Thorn, Peter; Chen, Jiezhong; Gu, Wenyi; Yu, Chengzhong, Hyaluronic acid modified mesoporous silica nanoparticles for targeted drug delivery to CD44-overexpressing cancer cells, *Nanoscale* **2013**, 5, 178-183. – incorporated as Chapter 7.

| Contributor | Statement of contribution |
|---|---|
| Author Yu, Meihua (Candidate) | Experimental design and performance (80 %)<br>Analysis and interpretation of data (75 %)<br>Drafting and writing (75 %) |
| Author Jambhrunkar, Siddharth | Experimental performance (5 %)<br>Analysis and interpretation of data (5%) |
| Author Chen, Jiezhong | Experimental performance (5%) |
| Author Thorn, Peter | Drafting and writing (5 %) |
| Author Gu, Wenyi | Experimental design and performance (5 %)<br>Analysis and interpretation of data (10 %)<br>Drafting and writing (10 %) |
| Author Yu, Chengzhong | Experimental design and performance (5 %)<br>Analysis and interpretation of data (10 %)<br>Drafting and writing (15 %) |

**Yu, Meihua**; Niu, Yuting; Zhang, Jun; Zhang, Hongwei; Yang, Yannan; Taran, Elena; Jambhrunkarar, Siddharth; Gu, Wenyi; Thorn, Peter; Yu, Chengzhong, An unusual size-dependent gene delivery relationship of monodispersed silica nanoparticles, *ACS Nano*, (nn-2014-011842, under revision). – incorporated as Chapter 8.

| Contributor | Statement of contribution |
|---|---|
| Author Yu, Meihua (Candidate) | Experimental design and performance (60%)<br>Analysis and interpretation of data (75 %)<br>Drafting and writing (85 %) |
| Author Niu, Yuting | Experimental performance (25 %)<br>Analysis and interpretation of data (5%) |
| Author Zhang, Jun | Experimental performance (3%) |
| Author Zhang, Hongwei | Experimental performance (3%) |
| Author Yang, Yannan | Experimental performance (3%) |
| Author Taran, Elena | Experimental performance (3%) |

| | |
|---|---|
| Author Jambhrunkarar, Siddharth | Analysis and interpretation of data (3 %) |
| Author Gu, Wenyi | Experimental design and performance (2%) |
| Author Thorn, Peter | Drafting and writing (5 %) |
| Author Yu, Chengzhong | Analysis and interpretation of data (15 %)<br>Drafting and writing (10 %) |

**Contributions by others to the thesis**

The solid state $^{13}C$ NMR was conducted by Dr. Ekaterina Strounina (Chapter 5, 6 and 7). ICP-OES analysis was performed by Dr. David Appleton (Chapter 8). The plasmid DNA (H1) (Chapter 8) and B16F0 cells (Chapter 5) were provided by Dr. Barbara Rolfe. U87MG cells were kindly provided by Prof. Marie-Odile Parat (Chapter 5).

**Statement of parts of the thesis submitted to qualify for the award of another degree**

None

**Acknowledgements**

Most importantly, I would like to express my gratitude and great appreciation to my supervisor Prof. Chengzhong (Michael) Yu for his advice, outstanding guidance, support and friendship during my PhD study. Also, I would like to thank my co-supervisors Dr. Wenyi Gu and Prof. Peter Thorn, for their advice, guidance, kind help and continuous encouragement in my PhD research work.

I am greatly indebted to my colleagues, Ms Celestien Warnaar-Notschaele, Ms Cheryl Berquist, and Mr Chaoqing Lu, for their kind help in office and lab daily work, Mr Siddharth Jambhrunkar for helping me to improve my English as well as his excellent suggestions and friendship, Dr. Liang Zhou, Dr. Surajit Karmakar for their helpful discussions, Dr. Jie Yang, Mr Yuting Niu, Dr. Yian Zhu, Ms Jun Zhang, Ms Haiyang Dong, Mr Kun Qian, Mr Chun Xu, Ms Chang Lei for their wonderful suggestions on my project and for their friendship.

Many thanks to the staff in the Australian National Fabrication Facility and the Australian Microscopy and Microanalysis Research Facility at the Center for Microscopy and Microanalysis, The University of Queensland, for providing the training and technical analysis help. I would like to thank Dr Ekaterina Strounina for the $^{13}C$ NMR technical help from Center for Advanced Imaging, the University of Queensland, and Mr. David Appleton for his help in ICP-OES analysis from the School of Agriculture and Food Sciences, the University of Queensland.

The financial support in terms of International Postgraduate Research Scholarship (IPRS), University of Queensland Centennial Scholarship (UQCent), University of Queensland Advantage Top-Up Scholarship (UQAdv) is greatly appreciated.

Finally, I would like to thank my parents and my husband Dr. Bin Hu for their forever support, love and encouragement through my PhD study.

**Keywords**

Monodisperse silica nanoparticles, surface modification, drug delivery, gene delivery, plasmid DNA, siRNA, cellular uptake,

**Australian and New Zealand Standard Research Classifications (ANZSRC)**

ANZSRC code: 100708, Nanomaterials, 40%

ANZSRC code: 090302, Biomedical Engineering, 40%

ANZSRC code: 100712, Nanoscale Characterisation, 20%

**Fields of Research (FoR) Classification**

FoR code: 0903, Biomedical Engineering, 40%

FoR code: 1007, Nanotechnology, 60%

**Table of Contents**

List of Figures & Tables

**Figure 7.4** (a) Fluorescence activated cell sorter (FACS)analysis of the FITCintensity of the cells treatedwith an FITC labeled CD44 antibody, MSNs, and HA-MSNs in the absence or in the presence of free HA (10 mg $mL^{-1}$); (b) bar chart of FITC mean intensity of the gated positive cells (M1 indicated in Fig. 4a) treated with FITC modified silica particles.

**Figure 7.5** Cytotoxicity of free Dox, Dox-HA-MSNs, Dox-MSNs, HA-MSNs and MSNs against HCT-116 cells at different concentrationsC1, C2 and C3(for details, see Table1).

**Scheme 8.1** A schematic illustration of the bind affinity between $NH_2$-SS and pcDNA and cellular uptake performance of their complexes as a function of particle size. The GFP transfection efficiency is the highest when the binding affinity and cellular uptake of pcDNA/$NH_2$-SS complexes is balanced.

**Figure 8.1** TEM images of $NH_2$-SS125 (a), $NH_2$-SS230 (b), $NH_2$-SS330 (c), $NH_2$-SS440 (d), $NH_2$-SS570 (e), $NH_2$-SS125/pcDNA (f), $NH_2$-SS230/pcDNA(g), $NH_2$-SS330/pcDNA(h), $NH_2$-SS440/pcDNA(i) and $NH_2$-SS570/pcDNA(j).

**Figure 8.2** GFP expression levels in HEK 293T cells by flow cytometry, after treated with naked pcDNA, $NH_2$-SS125/pcDNA, $NH_2$-SS230/pcDNA, $NH_2$-SS330/pcDNA, $NH_2$-SS440/pcDNA and $NH_2$-SS570/pcDNA at different weight ratios of $NH_2$-SS to pcDNA. The Y value of fluorescence intensity of GFP = GFP positive cell percentage × GFP mean intensity per GFP positive cell.

**Figure 8.3** AFM images of pcDNA deposited onto mica.

**Figure 8.4** pcDNA binding capacities of $NH_2$-SS125, $NH_2$-SS230, $NH_2$-SS330, $NH_2$-SS440 and $NH_2$-SS570 measured by Nanodrop.

**Figure 8.5** Agarose gel electrophoresis of $NH_2$-SS/pcDNA demonstrating plasmid DNA/nanoparticle complexation with increasing amounts of $NH_2$-SS (μg). The amount of pcDNA was constant (0.5 μg).

**Figure 8.6** Internalization performances of complexes $NH_2$-SS125/pcDNA, $NH_2$-SS230/pcDNA, $NH_2$-SS330/pcDNA, $NH_2$-SS440/pcDNA and $NH_2$-SS570/pcDNA into HEK 293T cells by measuring the silicon amount per cell.

**Figure 8.7** GFP expression levels in HEK 293T cells by flow cytometry after treated with naked H1, $NH_2$-SS125/H1, $NH_2$-SS230/H1, $NH_2$-SS330/H1, $NH_2$-SS440/H1 and $NH_2$-SS570/H1 at different weight ratios of $NH_2$-SS to H1. The Y value of fluorescence intensity of GFP = GFP positive cell percentage × GFP mean intensity per GFP positive cell.

**Figure 8.8** a) H1 adsorption capacities of $NH_2$-SS125, $NH_2$-SS230, $NH_2$-SS330, $NH_2$-SS440 and $NH_2$-SS570 measured by Nanodrop; b) agarose gel electrophoresis of $NH_2$-SS/H1demonstrating plasmid DNA/nanoparticle complexation with increasing amounts of $NH_2$-SS (μg). The amount of H1 was constant (0.5 μg).

**Figure 8.9** Internalization performances of complexes $NH_2$-SS125/H1, $NH_2$-SS230/H1, $NH_2$-SS330/H1, $NH_2$-SS440/H1and $NH_2$-SS570/H1 at w/w = 160 into HEK 293T cells by measuring the silicon amount per cell.

**Table 8.S2** Elemental analysis results of $NH_2$-SS and the calculated N/P ratios of $NH_2$-SS/DNA complexes with different w/w ratios.

**Table 8.S3** The comparison of $NH_2$-SS binding affinity toward pcDNA measured by Nanodrop and gel retardation assay.

**List of Abbreviations used in the thesis**

SiNPs: silica based nanoparticles

pDNA: plasmid DNA

MMSNs: monodisperse mesoporous silica nanospheres

UHSS: ultra-small hybrid silica spheres

Epoxy-UHSS: epoxysilane functionalized UHSS

PEI: polyethyleneimine

HA: hyaluronic acid

Dox: doxorubicin hydrochloride

MSNs: mesoporous silica nanoparticles

$NH_2$-SS: amine modified monodisperse Stöber spheres

FDA: Food and Drug Administration

GRAS: Generally Recognized As Safe

CTAB: cetyltrimethylammonium bromide

TEOS: tetraethyl orthosilicate

LCT: Liquid crystal templating

CMS: colloidal mesoporous silica

TEA: triethanolamine

THF: tetrahydrofuran

PDMA: poly(2-(dimethylamino)ethyl methacrylate)

PDPA: poly(2-(diisopropylamino)ethyl methacrylate)

TMB: trimethylbenzene

CPT: camptothecin

PSs: photosensitizers

PDT: photodynamic therapy

ROS: reactive oxygen species

EPR: enhanced permeation and retention effect

ORMOSIL: organically modified silica

VEGF: vascular endothelial growth factor

ABTS: 2,2’-azino-bis(3-ethylbenzthiazoline-6-sulfonate)

n-ODMS: n-octadecyltrimethoxysilane

HMSCs: hollow mesoporous silica capsules

BSA: bovine serum albumin

PCV2: porcine circovirus type-2

OVA: antigen ovalbumin

cAMP: cyclic adenosine monophosphate

PAMAM: amine-terminated polyamidoamine

MDR: multiple drug resistance

HMS: hollow mesoporous silica

PEG: poly(ethylene glycol)

cRGD: cyclic argininеglycine-aspartic acid

MCSs: multicellular spheroids

ECM: cell-to-extracellular matrix

FRET: fluorescence resonance energy transfer

PET: positron emission tomography

MRI: magnetic resonance imaging

LA: lactobionic acid

TAMRA: tetramethylrhodamine

FITC: fluorescein-5-isothiocyanate

CTAC: cetyltrimethylammonium chloride

TMOS: tetramethyl orthosilane

DMDMS: dimethoxydimethylsilane

DGMS: diethoxy(3-glycidyloxypropyl)methylsilane

APTES: (3-aminopropyl)triethoxysilane

NHS: N-hydroxysuccinimide

EDC: N-(3-dimethylaminopropyl)-N-ethylcarbodiimide  hydrochloride

RBTC: Rhodamine B isothiocyanate

APTMS: (3-aminopropyl)trimethoxysilane

XRD: X-ray Diffraction

TEM: transmission Electron Microscopy

SEM: scanning Electron Microscopy

BJH: Barrett–Joyner–Halanda

BET: Brunauer–Emmett–Teller

ATR-FTIR: attenuated total reflectance -Fourier transform infrared spectroscopy

EA: elemental Analysis

DLS: dynamic light scattering

ICP-OES: Inductively Coupled Plasma-Optical Emission Spectroscopy

MTT: 3-[4,5-dimethylthiazol-2-yl]-2,5-diphenyl tetrazolium bromide

CLSM: confocal laser scanning microscopy

# Chapter 1

# Introduction

## 1.1 Significance of the project

In recent decades, the application of nanotechnology in medicine (so called nanomedicine) has been revolutionized due to the rapid developments in nanotechnology.[1] Various kinds of nanomaterials have been used in nanomedicine, because they can penetrate into cells and efficiently deliver therapeutic or diagnostic agents into living systems by taking advantage of their small sizes.[2-4] Compared with traditional organic lipid or polymer based nanomaterials, the inorganic counterparts possess unique properties including inertness, stability and ease of functionalization. In particular, silica based nanoparticles (SiNPs) with excellent biocompatibility, tunable pore/ particle size and controllable surface chemistry have attracted enormous research interest in various bio-applications, including cell imaging, diagnosis and bioanalysis, and drug/gene delivery.[5-7] SiNPs with a small size (< 100 nm) and high monodispersity possess advantages in cell endocytosis process, which is vital to achieve high efficiency in biomedical applications. Although there have been tremendous studies in the synthesis of mono-dispersed nanometer-sized SiNPs, still more efforts are needed to develop facile, economic and environmentally friendly synthesis approaches for fabricating novel mono-dispersed SiNPs with desired particle sizes, nano-structures and functionalities. The designed novel SiNPs are expected to expand their capacity in various biomedical applications, such as enhanced bio-imaging performance in three dimensional (3D) spheroid models, and improved cellular drug/gene delivery efficiency.

## 1.2 Research objective and scope

This project aims to develop novel and facile approaches to prepare highly mono-dispersed SiNPs with finely controlled pore structures, particle sizes (10-100 nm), surface functionality for highly efficient drug/gene delivery and gain insight into the roles of particle size, surface functionality on cell penetration performance and drug/gene delivery efficiency. This thesis does not only focus on the development of facile synthesis of highly mono-dispersed SiNPs with novel structure properties,

but also provide some guidelines for the design of highly efficient delivery systems for various biomedical applications. The objectives of this project are specified as follows:

1) To develop facile approaches to synthesize various types of highly mono-dispersed SiNPs with finely controlled pore structure (dense, porous and hybrid), particle size (10-100 nm) and surface functionality and then to fully characterize their structure properties.

2) To evaluate the influence of particle size and mono-dispersity of SiNPs on cell penetration ability in both monolayer and 3D spheroid models of various types of cells.

3) To comprehensively study the influence of surface functionality of SiNPs on small anticancer drug and siRNA delivery efficiency;

4) To gain insight of the role of particle size of highly mono-dispersed SiNPs on large plasmid DNA (pDNA) transfection efficiency by deeply investigating the interaction between SiNPs and pDNA and the cellular uptake performance.

SiNPs with various nano-structures can be fabricated by controlling the nucleation and growth in the sol-gel process of silica precursors and/or its assembly process with structure directing agents (surfactants). During the sol-gel process, a strong acid or alkali usually is utilized as a catalyst to initiate the hydrolysis and condensation of silicon alkoxides. It would be of great interest if the harsh conditions could be avoided to generate mono-dispersed SiNPs with small sizes for bio-medical applications. In this thesis, it is hypothesized that a salt of a weak acid and a strong base (e.g. NaAc), biological buffer with a pH near neutral condition could slow down the hydrolysis and condensation of silica sources, which is beneficial for the generation of mono-dispersed SiNPs with small sizes within 100 nm (Objective 1, Chapter 4, 5 and 6). For mono-dispersed SiNPs with ultra-small sizes, it is hypothesized its cell penetration ability is much higher in mono-layer and 3D spheroid models, compared with conventional SiNPs (Objective 2, Chapter 5). Besides particle sizes, surface functionality is also crucial on cell penetration performance and subsequent anticancer drug/siRNA delivery efficiency. Polyethylenimine (PEI) has been regarded as an efficient cationic group, which has a higher endosomal escape capability, favoring a high gene silencing efficacy. It is hypothesized that successful surface modification of PEI on the ultra-small SiNPs could highly improve the siRNA delivery efficiency by taking advantages of small particle sizes and proper surface functionality (Objective 3, Chapter 6). For anticancer drugs, it is hypothesized that surface modification of biodegradable and biocompatible hyaluronic acid (HA) could increase anticancer accumulation carried by HA attached SiNPs in CD44 over-expressing cancer cells (Objective 3, Chapter 7). Different from small cargoes, plasmid DNA (pDNA) is much

bigger. It is hypothesized that pDNA would affect the sizes of SiNPs and subsequent cellular uptake after forming complexes, and there is an optimized particle size of highly mono-dispersed SiNPs for a high transfection efficiency of pDNA (Objective 4, Chapter 8).

## 1.3 Thesis outline

This thesis is written according to the guidelines of the University of Queensland. The outcomes of this PhD thesis are presented in the form of journal publications. The chapters in this thesis are presented in the following sequence:

**Chapter 1. Introduction**

This chapter introduces the background of this project and outlines the research objectives

**Chapter 2. Literature review**

This chapter presents an overview on current synthesis mechanism, functionalization strategies for SiNPs and their biological applications in drug/gene/protein delivery and cell imaging/sensing.

**Chapter 3. Methodology**

This chapter summarizes the strategies utilized in the whole PhD project, including material synthetic methods for SiNPs, and the techniques for material characterizations and biological evaluations.

**Chapter 4. A Simple Approach to Prepare Monodisperse Mesoporous Silica Nanospheres with Adjustable Sizes**

This chapter reports a new and facile approach to prepare monodisperse mesoporous silica nanospheres (MMSNs) with controlled particle sizes (50-100 nm) and pore diameters (2.8-4.0 nm). MMSNs developed in this part are expected to have potential applications in drug/gene delivery and cell imaging.

**Chapter 5. Facile synthesis of ultra-small hybrid silica spheres for enhanced penetration of 3D glioma spheroids**

In this chapter, even smaller mono-dispersed SiNPs (ultra-small hybrid silica spheres, UHSS) with a diameter of only ~ 10 nm were developed by a new and facile strategy under phosphate-citrate buffer solution (pH = 4.6) at room temperature without addition of toxic additives. Compared with

traditional MCM-41 nanomaterials, the designed novel UHSS showed enhanced penetration ability in 3D glioma spheroids.

**Chapter 6. An approach to prepare polyethylenimine functionalized silica-based spheres with small size for siRNA delivery**

Following Chapter 5, epoxysilane functionalized UHSS (Epoxy-UHSS) with a same diameter of ~10 nm were designed under similar synthesis condition, which can be easily covalently conjugated with cationic PEI (PEI-UHSS). This designed positively charged PEI-UHSS demonstrated excellent delivery efficiency of functional siRNA against polo-like kinase 1 (PLK1-siRNA) in osteosarcoma cancer cells (KHOS) and survivin-siRNA in human colon cancer cells (HCT-116) by inducing a significant cell inhibition, which is comparable to commercial agents. These results indicated that suitable functionality of SiNPs is significant to achieve efficient gene delivery.

**Chapter 7. Hyaluronic Acid Modified Mesoporous Silica Nanoparticles for Targeted Drug Delivery to CD44-overexpressing Cancer Cells**

In this chapter, the influence of surface functionality of SiNPs was further evaluated on small anticancer drug delivery efficiency. HA modified SiNPs were designed, which possess specific affinity to CD44 over expressed on the surface of a specific cancer cell line, HCT-116 (human colon cancer cells). An anticancer drug (doxorubicin hydrochloride, Dox) loaded HA-SiNPs showed greater cytotoxicity to HCT-116 cells than free Dox and Dox-SiNPs due to the enhanced cell internalization behavior of HA-SiNPs. This work indicated that the desired surface functionality is also crucial to improve drug delivery efficiency.

**Chapter 8. An unusual size-dependent gene delivery relationship of monodispersed silica nanoparticles**

Apart from surface functionality, the particle size of SiNPs is expected to have significant effect on gene delivery efficiency. In Chapter 8, positively charged solid mono-dispersed SiNPs with various diameters (125-570 nm) were designed to exclude the influence of internal porosity of nanoparticles. It was found that an optimized particle size of 330 nm exhibited the highest expression of GFP by delivering the large pDNA (6.1 and 8.9 kbp) into cells. This unusual observation is different from the well-accepted understanding that small particle sizes (< 100 nm) are preferred for efficient cellular delivery. It was identified that both factors of binding affinity and cellular uptake were crucial to the performance of gene therapy. These findings provide design modes to optimize gene transfection efficiency of synthetic gene delivery systems.

**Chapter 9. General discussion and outlook**

This chapter presents a general discussion of the work in this thesis and outlook for the future work.

## 1.4 References


1. Kim, B.Y.S., J.T. Rutka, and W.C.W. Chan, Current Concepts: Nanomedicine. *New England Journal of Medicine*, 2010, **363**(25), 2434-2443.
2. Liong, M., et al., Multifunctional inorganic nanoparticles for imaging, targeting, and drug delivery. *Acs Nano*, 2008, **2**(5), 889-896.
3. Torchilin, V.P., Recent advances with liposomes as pharmaceutical carriers. *Nature Reviews Drug Discovery*, 2005, **4**(2), 145-160.
4. Doane, T.L. and C. Burda, The unique role of nanoparticles in nanomedicine: imaging, drug delivery and therapy. *Chemical Society Reviews*, 2012, **41**(7), 2885-2911.
5. Mai, W.X. and H. Meng, Mesoporous silica nanoparticles: A multifunctional nano therapeutic system. *Integrative Biology*, 2013, **5**(1), 19-28.
6. Mamaeva, V., C. Sahlgren, and M. Linden, Mesoporous silica nanoparticles in medicine-Recent advances. *Advanced Drug Delivery Reviews*, 2013, **65**(5), 689-702.
7. Tang, F.Q., L.L. Li, and D. Chen, Mesoporous Silica Nanoparticles: Synthesis, Biocompatibility and Drug Delivery. *Advanced Materials*, 2012, **24**(12), 1504-1534.

# *Chapter 2*

# Literature review

This chapter reviews the existing studies on silica based nanoparticles (SiNPs) for biomedical applications. It begins with a brief introduction to current nanomaterials that have been widely used in medicine in 2.1. SiNPs are then proposed to be promising candidates to deliver therapeutic or diagnostic agents into living systems. The background of SiNPs in synthesis mechanism, functionalization strategies is overviewed in section 2.2. The biological applications of SiNPs in drug/gene/protein delivery and cell imaging/sensing are reviewed in section 2.3. Finally the conclusion is given in section 2.4 and the critical issues and potential challenges are discussed on synthesis design and biological applications of SiNPs.

## 2.1 Nanoparticles for applications in medicine

Nanomedicine in clinical diagnosis and treatment has been revolutionized due to the rapid developments in nanotechnology.[1] The application of nanoparticles in medicine is an emerging field of nanomedicine. Because of their small sizes, nanoparticles can penetrate into cells and efficiently deliver therapeutic or diagnostic agents into living systems.[2-4] Numerous kinds of nanoparticles (Figure 2.1) have been extensively tested on biosystems, which can be generally divided into organic and inorganic nanoparticle systems. Many of the conventional organic drug delivery systems (such as liposomes, micelles and polymers) have reached the later stages towards clinical applications (Figure 2.1) and a few of them have even received U.S. Food and Drug Administration (FDA) approval (Table 2.1). From a scientific point of view, there are several major barriers hindering the clinical translation of laboratory-developed nanocarriers:[5,6] (1) insufficient loading capacity of therapeutic agents with controlled release profiles, (2) limited targeting ability towards desired sites in the context of multiple *in vivo* physiological barriers, (3) inherent toxicity properties and (4) cost and scalable fabrication. Because of the limitations of conventional nanocarriers, a variety of inorganic delivery systems are emerging, which have special structures and chemophysical properties (such as robust framework, ease of preparation and functionalization).[2,7] Compared with conventional drug delivery nanocarriers, most of inorganic nanocarriers (e.g. quantum dots, iron oxide, mesoporous silica nanoparticles (MSNs) are still in their pre-clinical stages of development (Figure 2.1), with a few exceptions (such as Gold nanoparticles listed in Table 2.1). However, successful demonstrations of some inorganic nanocarriers' efficacy, excellent

biocompatibility and safety profile at the cellular and intact animal level are extremely encouraging from the perspective of moving these platforms into clinical trials. For example, silica-based nanoparticles (SiNPs) have tunable pore structures and particle sizes, high specific surface area, large pore volume and easy surface modification. These unique properties endow them with advantages to load and deliver various therapeutic agents to the targeted sites.[6-8] Additionally the fabrication of SiNPs is simple, scalable and cost-effective. More importantly, silica has excellent compatibility and is accepted as "Generally Recognized As Safe" (GRAS) by the FDA and has been widely used as additives in cosmetics and food.[9,10] Recently, the first silica based diagnostic nanoparticles called "C-dots" (Cornell dots)[11,12] have received the FDA approval for stage I human clinical trial in melanoma patients. This represents an important step towards clinical applications of SiNPs.

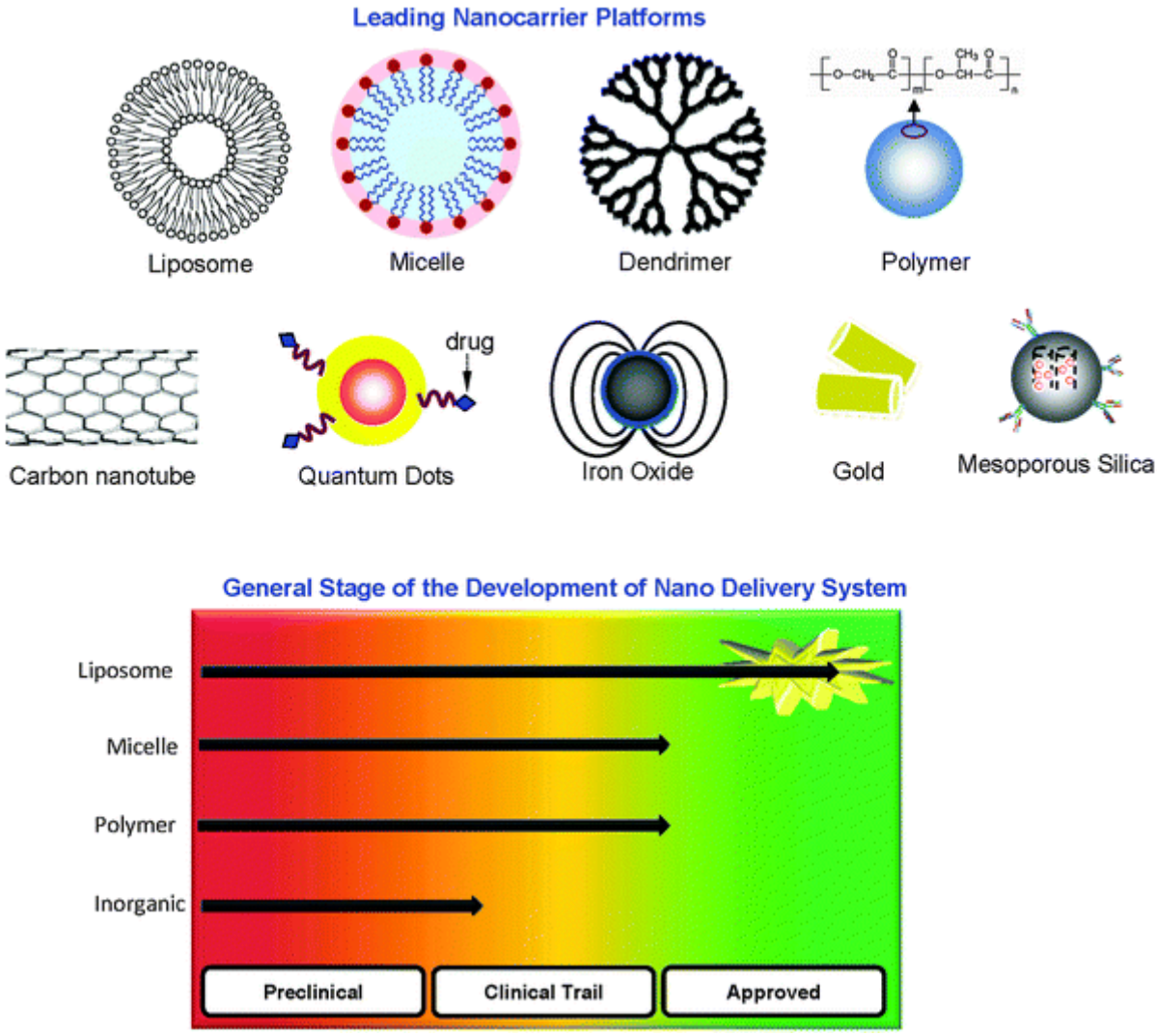


**Figure 2.1** The scheme shows the leading nanocarriers for drug delivery and their general stages of development. The top row shows the representative conventional nanocarriers such as liposomes,

micelles, dendrimers, and polymers. The bottom row shows novel inorganic nanocarriers such as carbon nanotubes, quantum dots, iron oxide, gold, and mesoporous silica nanoparticles.[7]

**Table 2.1** Representative drug delivery carriers on the market or in clinical trial.[7]

| Nanocarrier platform | Delivered therapeutic agent | Stage (Date) in development | Drug name | Indications |
|---|---|---|---|---|
| Liposome | Doxorubicin | Approved ((November 17, 1995) | Doxil | Kaposi's sarcoma, recurrent breast cancer, and ovarian cancer[13] |
| | Vincristine | Approved (May 21, 2004) | OncoTCS | Non-Hodgkin's lymphoma[14] |
| | Daunoxome | Approved (May, 1996) | Daunoxome | Kaposi's sarcoma[15] |
| Polymeric micelle | Paclitaxel | Phase II clinical trial | Genexol-PM | Non-small-cell lung cancer (NSCLC)[16] |
| Albumin (protein–drug conjugate) | Paclitaxel | Approved (January 7th, 2005) | Abraxane | Metastic breast cancer[17] |
| Gold | Recombinant human tumor necrosis factor (rhTNF) | Phase II clinical trial | AurImmune™ | Pancreatic cancer, melanoma, soft tissue sarcoma, ovarian, and breast cancer[18] |
| Silica | cyclic argininegly cine-aspartic acid (cRGD) peptide, and 124I | Phase I clinical trial | C dots | Human melanoma[12] |

## 2.2. Synthesis and functionalization of SiNPs

A wide variety of SiNPs have developed for biomedical applications such as therapeutic drug/gene/protein delivery, cell imaging and intracellular sensing, which include solid, mesoporous, hollow and hybrid silica particles.

### 2.2.1 Synthetic routes of SiNPs

Sol-gel technique is the most common method for SiNPs fabrications. Knowledge of nucleation and growth mechanisms in sol-gel process of silica precursors is an important prerequisite for controllable synthesis of SiNPs with desired nanostructures.

In 1968, Stöber et al.[19] described a pioneering method for the synthesis of mono-dispersed solid SiNPs by the hydrolysis and condensation of silicon alkoxides in a mixture of alcohol and water using ammonia as a catalyst. The silica particle diameter can be adjusted from 50 nm to 2 μm, simply by varying the catalyst and/or precursor concentrations. It has been demonstrated that solid SiNPs synthesized by Stöber method can be used in gene delivery utilizing the surface space and

surface charge properties, which will be introduced in details in section "2.3.1.2 Gene delivery". By a modified Stöber method, C dots (a class of highly fluorescent and photostable core-shell solid SiNP with diameters of 7-30 nm) have been synthesized for diagnostic applications and have reached stage I human clinical trial.[11,12]

MSNs are the most common used type of SiNPs for nanomedicine applications. MCM-41 type of MSNs with uniform mesopore sizes and a long-range ordered pore structure were first reported in the early 1990s by soft-templating method.[20,21] Since then, different types of MSNs with various pore sizes/nanostrucutres and morphology have been developed and widely used in many applications such as catalysis, separation, sensors and drug delivery. The following section is going to focus on the controlled synthesis of several major types of MSNs that have been utilized for bio-applications, including MCM-41, MCM-48 and SBA-15 types of MSNs.

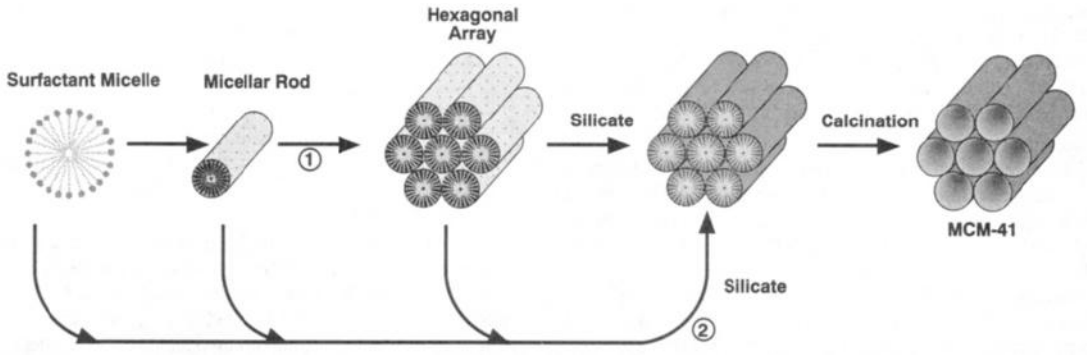


**Figure 2.2** Possible mechanistic pathways for the formation of MCM-41: ( 1 ) liquid crystal phase initiated and (2) silicate anion initiated.[20]

MCM-41 is the most extensively studied type of MSNs for biomedical applications. MCM-41 with two-dimensional (2D) hexagonal *p6m* mesopore structure and a pore size of 2-3 nm was synthesized by utilizing cetyltrimethylammonium bromide (CTAB) as the templating surfactant, tetraethyl orthosilicate (TEOS) or sodium silicate ($Na_2SiO_3$) as the silica sources, and alkali as catalyst.[21] Liquid crystal templating (LCT) mechanism was proposed for the formation of MCM-41 with two possible pathways (Figure 2.2). (1) The surfactant self-aggregates into micelles in aqueous solution, followed by the formation of micellar rods. After stacking of the cylindrical micelles into a regular array of micelle liquid crystals, the anionic silicate will deposit on the positively charged micelle liquid crystals. Removing surfactant leads to mesoporous silica materials. (2) The cooperative assembly of surfactant and silicate leads to the generation of organic-inorganic composite of liquid crystals. The mesopores of silica materials will be generated after removing surfactants. With deep understanding on the formation mechanisms of MSNs and availability of various types of surfactants, the particle sizes, morphology, pore sizes/structures of MSNs can be

rationally controlled.[22,23] Particle size has been regarded as one of the most important structure parameters of MSNs for biomedical applications, because MSNs with small sizes possess advantage in cell endocytosis process, which is crucial to achieve high efficiency in bio-applications.[24,25]

Biomedical applications require MCM-41 type MSNs with an ideal diameter less than 100 nm, and these have been prepared by different methods. For example, Imai and co-workers have successfully synthesized MCM-41 type MSNs with diameters of 20-50 nm using a binary surfactant templating approach,[26] however, aggregation and polydispersity of MSNs are limitations for their biological application. To resolve the aggregation issue, uniform and highly ordered MSNs were prepared utilizing highly diluted surfactant solutions,[27-30] however this method leads to low yields and difficulty in product collection. Bein et al. reported a high-yield approach to synthesize colloidal mesoporous silica (CMS) particles with controlled sizes and various functional groups,[31-33] where triethanolamine (TEA) was used as the base and also the complexing agent for silicate species to limit the growth and aggregation of particles. Huo and his co-workers further investigated the formation of CMS, and proposed a new mechanism to understand the growth mechanism of CMS.[34] It is proposed that the rate of hydrolysis and condensation of silicon alkoxide at different pH controls the sizes of CMS, and the addition of additive agents with certain acid-base buffer capacity is necessary to obtain homogeneous CMS.[34] Tatsumi and his co-workers have reported a new method to obtain discrete mesoporous silica nanospheres, which was based on the emulsion system containing silica source, surfactant, water and basic amino acid.[35] Until now, the availability of various MCM-41 type MSNs with small sizes (< 100 nm) and high monodispersity provides the possibility of improving the efficiency of MSNs in bio-applications.

MCM-48 as another important type of MSNs has also attracted much attention in biomedical applications, which has three-dimensional (3D) bicontinuous mesopores with cubic Ia3d structure.[36,37] The bicontinuous pore channels are considered to be helpful for fast molecular transport and easy molecular accessibility. In 1990s, the synthesis of MCM-48 was rather complicated where cationic-anionic co-surfactants were utilized as templates and high temperature and long reaction time was involved. Moreover, the particle sizes of MCM-48 were large (> 1 μm), which were not suitable for biomedical applications. In 2010, Kim et al. reported a facile approach to synthesize mono-dispersed spherical MCM-48 based on modified Stöber method utilizing triblock copolymer Pluronic F127 as a particle size designer. The particle sizes can be controlled within the range of 70-500 nm by adjusting the amount of F127. Moreover, the pore diameter can also be precisely controlled from 2.3 to 3.3 nm by using different alkyl chain surfactants. The ability of tailoring the particle sizes and monodispersity of MCM-48 type MSNs is important to achieve their applications in biomedical fields.[38,39]

Another type of MSNs for bioapplications is SBA-15 silica materials. SBA-15 was firstly synthesized in strong acidic condition using amphiphilic triblock copolymer $EO_{20}PO_{70}EO_{20}$ [Pluronic P123, EO refers to poly(ethylene oxide), PO refers to poly(propylene oxide)] as template in 1998.[40] SBA-15 also has a 2D hexagonal *p6mm* mesostructure, but has a much thicker wall and bigger pore sizes (5-30 nm) than MCM-41. Generally the particle sizes of SBA-15 are in several micrometers. In recent years, several methods have been developed to generate SBA-15 type MSNs in sphere, rod and ellipsoid shapes with reduced sizes in sub-micrometer range.[41-43] However, there are still few successful examples of SBA-15 type MSNs utilized in biomedical applications.[43] Most of the SBA-15 type MSNs is still far away from ideal candidates for biomedical applications with a particle size less than 200 nm and excellent monodispersity.

In the past decade, mono-dispersed silica-based spheres with diameters of several to a few tens of nanometres, an emerging type of SiNPs, have attracted increasing attention in fluorescence and magnetic resonance imaging, and diagnosis applications.[44-48] Several synthesis methods have been developed to generate mono-dispersed silica-based spheres with small sizes. For example, Huo et al. reported the use of FDA approved Pluronic F127 micelles to template silica deposition in the hydrophilic PEO shell region in acidic solution, to form robust silica cross-linked micellar core-shell nanoparticles with an ultrafine and uniform size of ~ 12 nm.[44] To terminate the silicate condensation and prevent interparticle aggregation and growth, dimethyl-silane was introduced in the reaction solution after a certain time of adding TEOS. Tan et al. reported a facile synthesis of similar hybrid micelles with a diameter of ~ 14 nm by interfacial templating condensation method in the mixture of water and tetrahydrofuran (THF).[45] Yuan et al. reported the use of commercially unavailable diblock copolymer micelles comprising cationic poly(2-(dimethylamino)ethyl methacrylate) (PDMA) coronas and hydrophobic poly(2-(diisopropylamino)ethyl methacrylate) (PDPA) cores as nanosized templates for the deposition of silica under neutral aqueous solution at 20°C, to form silica hybrid spheres with a diameter of ~ 35 nm.[49] In a previously reported work, ultra-small silica hollow spheres with a diameter of ~ 24.7 nm were synthesized in strong acidic condition after removing surfactant where trimethylbenzene (TMB) is utilized as a swelling agent.[25] Recently, Ma et al. reported one-pot synthesis of PEGylated MSNs with controllable diameters from 6 to 9 nm where cationic CTAB was used as the template and the extraction process to remove the toxic surfactant.[50] Such small silica-based spheres with uniform nanometer-size and excellent monodispersity and stability in aqueous media have shown enhanced cellular uptake in their bio-applications.[25] It is crucial for further bio-medical applications towards clinical use.

In addition, hollow/rattle type of SiNPs also shows great potentials in bio-medical applications.[6,51] As this type of SiNPs is not the focus in this thesis, detailed information about their synthesis and bio-application will not be introduced here.

### 2.2.2 Surface functionalization strategies of SiNPs

Besides particle size, surface property is another key factor affecting the efficacy of SiNPs in biomedical applications. SiNPs modified with desired functional groups have shown improved adsorption capacities to bioactive molecules/drugs, increased targeting ability to desired sites, enhanced biocompatibility, demanded release of cargos, etc.

The surface of SiNPs can be modified by two commonly used methods: co-condensation (one-post synthesis) or grafting (post-synthesis modification).[52] The surface functional groups can be selectively either on the external or internal surfaces of SiNPs.

In co-condensation (one-pot) synthetic method, organoalkoxysilanes with functional groups and tetraalkoxysilane silica sources are added into the reaction solution together to produce organic-functionalized SiNPs in one step. The advantages of this method are: (1) suitable for various organoalkoxysilanes; (2) applicable to different reaction conditions; (3) homogeneous coverage of functional groups. However, the addition of organoalkoxysilanes into the tetraalkoxysilane/surfactant solution could affect the self-assembly process and the structure/morphology of the final materials. Thus, in this method, the concentration and type of organoalkoxysilanes should be carefully chosen during the synthesis functionalized SiNPs. Moreover, this method results in non-selective modification of functional groups on both internal and external surfaces of MSNs type SiNPs. Additionally, solvent extraction method is the only way to remove the surfactant to preserve the organic functional groups introduced to the mesostructured SiNPs.

In the case of grafting (post-synthesis method), the functional organoalkoxysilanes are introduced on the surface of SiNPs by silylation on free (≡Si-OH) and germinal (= $Si(OH)_2$ ) silanol groups. For MSNs type of SiNPs, the surfactant is usually removed by calcination or extraction method. Calcination (normally at 400-650°C) process leads to the condensation of silanol groups, limiting the grafting amount of functional groups, while the extraction process (acid/alcohol mixtures for cationic surfactants, alcohols for non-ionic surfactant) will maintain most of surface silanol groups. This method has some advantages: (1) retaining the mesostructure of MSNs type of SiNPs after grafting functional groups; (2) having a wide range of functional groups by utilizing different organoalkoxysilanes; (3) selectively functionalizing the internal or external surface of MSNs type of

SiNPs. As shown in Figure 2.3, the as-synthesized MSNs with surfactant inside the mesopores will be obtained by self-assembly process (Figure 2.3A-B), then could be first grafted with one organoalkoxysilane on the external surface (Figure 2.3C). After removal of the surfactant by extraction method (Figure 2.3D), the inner surface can be grafted with another functional group before loading cargo inside inner pores (Figure 2.3E). However, the functional groups introduced by grafting method have an inhomogeneous distribution on the surface of MSNs type of SiNPs with a higher density around the pore entrance and the external surface of final materials.

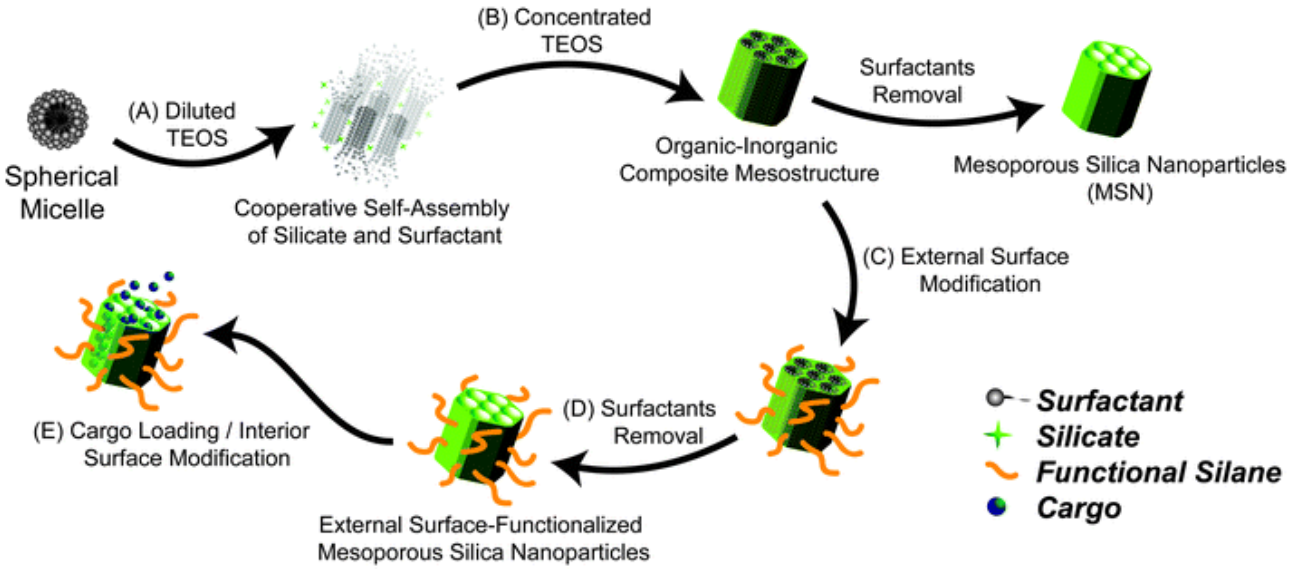


**Figure 2.3** Schematic illustration for the synthesis and selective functionalization of MSNs.[53]

The selective modification of the external surface is important with specific ligands for tumor targeting,[54] pore gating molecules for controlled release[55] or cationic groups/polymer for carrying negative cargos on the outer surface.[56] Desired surface modification can be easily achieved in SiNPs due to the unique chemist properties, but serious aggregation of SiNPs tends to happen. Thus, researchers should pay special attention to maintain the dispersity of SiNPs during the fabrication of multifunctional SiNPs.

### 2.3 Cellular uptake mechanisms of SiNPs

Efficient cellular uptake of SiNPs is of great significance during their biological applications, which is dependent on particle sizes,[24,25] surface charges,[57-59] shapes[60-62] and structures, and has also been reported to be cell type-specific.[57,58,62] Xing et al. demonstrated that the uptake of silica-coated nanoparticles by human cervical cancer cells (HeLa) was a concentration-, time-, and energy-dependent endocytic process.[63] The uptake of silica-coated nanoparticle was found to take place through adsorptive endocytosis and fluid-phase endocytosis. Slowing et al. investigated the influence of the external surface functionalities of MCM-41-type on the uptake efficiency of MCM-

41 as well as their ability to escape endosomal compartments.[59] By controlling the surface charge (zeta potential) of MCM-41, the authors demonstrated that ionic MCM-41 with high surface charges can easily escape endosomal entrapment, which could be attributed to the osmotic pressure caused by the high density of ions of highly charged MCM-41. The endosomal escape ability is a key factor taken into account in designing effective intracellular delivery vehicles for drugs and genetic molecules. In addition, the uptake efficiency by cancer cells significantly increased by grafting folic acid on the surface of MCM-41, which was associated with the participation of folic acid receptors in the surface of the cells. Clathrin pits were identified as the main pathway of non-functionalized MCM-41 while folic acid receptor-mediated endocytosis of folic acid modified MCM-41. Amine and guanidinium functionalized MCM-41 entered into cells by a clathrin and caveolae independent mechanism.[59] Huang et al. designed three different shaped mono-dispersed MSNs with similar particle size and surface charge but different aspect ratios (ARs, 1, 2, 4).[61] It was found that these different shaped MSNs were internalized into A375 human melanoma cells by nonspecific cellular uptake. Rod-shaped MSNs with a larger AR showed increased and faster cellular uptake and consequently a greater effect on apoptosis, migration and disturbed organization of the cytoskeleton.

These studies have shown that MSNs themselves can also play an active role in mediating biological systems. Therefore, the knowledge on cellular uptake mechanisms of SiNPs provides useful information for the design of efficient drug/gene delivery systems.

## 2.4 Biological applications of SiNPs

In 2001, MCM-41 type of SiNPs was firstly reported as a drug nanocarrier, which exhibited high drug loading and sustained drug release in simulated body fluid.[64] Since then, the influence of structure parameters were extensively studied on *ex vivo* drug release performance.[65] It was not until 2003 that drug delivery into cells using MSNs as a vehicle was reported.[55] The bio-applications of MSNs type of SiNPs have become one of the most attractive areas in nanomedicine. MSNs have been successfully developed as a multi-functional nanocarrier to deliver therapeutic/diagnostic agents (such as chemical drugs, genetic molecules, and imaging probes) into various cells or animal models. [6,8,51]

### 2.4.1 Therapeutic agent delivery

SiNPs with various structures have demonstrated the capacity of delivering different types of guest molecules, including pharmaceutical drugs, therapeutic genes and proteins (Figure 2.4).

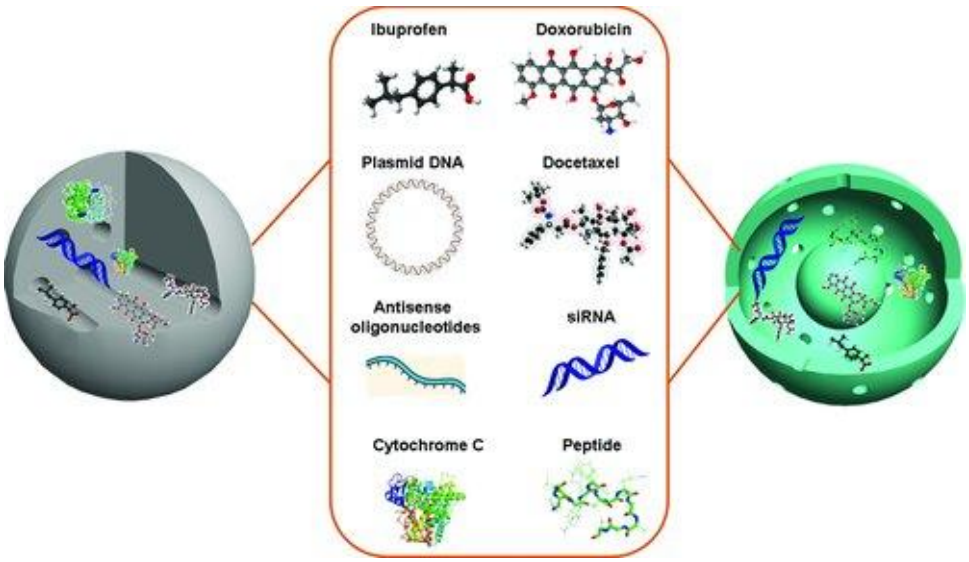


**Figure 2.4** SiNPs as versatile drug delivery systems for a variety of therapeutic agents including pharmaceutical drugs (ibuprofen, doxorubicin, and docetaxel), therapeutic genes (plasmid DNA, antisense oligonucleotides, and siRNA), and therapeutic proteins and peptides (cytochrome C and peptide).[6]

#### 2.4.1.1 Drug delivery

SiNPs have been used as nanocarriers for various types of pharmaceutical drugs such as anti-inflammatory drug ibuprofen,[64] hydrophilic anticancer drug doxorubicin,[66] hydrophobic camptothecin[67] and curcumin.[68] Take hydrophobic drugs for example, low aqueous solubility hampers the ability of drugs to be administered through the intravenous and oral routes. The intestinal permeability classification is based on a comparison to the intravenous injection. Both solubility and permeability are highly important for orally administered drugs. According to the Biopharmaceutics Classification System (BCS), drugs can be divided into four classes: class I-high soluble and high permeable, class II-low soluble and high permeable, class III-high soluble and low permeable and class IV-low soluble and low permeable. The poor solubility and low dissolution rate of hydrophobic drugs in the aqueous gastrointestinal fluids often cause very low oral bioavailability. Especially for class II drugs, the bioavailability may be enhanced by increasing the solubility and dissolution rate of the drug in aqueous media. As for BCS class II drugs, bioavailability limiting is caused by low drug release rate from the dosage form and low solubility in the gastric fluids, not the insufficient absorption, thus solubility increase in turn enhances the bioavailability for BCS class II drugs. MSNs have been developed as efficient delivery systems for solubility enhancement. Lu et al. reported the first use of MCM-41 with pore diameter of 2 nm to deliver hydrophobic camptothecin (CPT, a class II drug) into various cell lines, which shown enhanced the cellular uptake of CPT compared to pure CPT in aqueous medium.[67] However, the

solubility and oral bioavailability of CPT after confining in MCM-41 were not evaluated in this work. Mellaerts et al. utilized MSNs with a pore size of 7.3 nm as a carrier for poorly water-soluble drug itraconazole, a class II drug.[69] After loading into MSNs, the oral bioavailability of itraconazole was significantly increased in rabbits and dogs, compared with the marketed product Sporanox® and pure itraconazole, due to the enhanced solubility and dissolution rate in aqueous environment. However, the pore size influence is not clear on the solubility enhancement of poorly water-soluble drugs. In a recent published report,[68] by confining the hydrophobic anticancer drug curcumin, a class IV drug, into a serial of MCM-41 materials with adjustable pore sizes from 1.0 to 2.2 nm, its solubility increased with decreasing the pore size, reaching a maximum of 1.40 μg/ml (4.5 times of pure curcumin) at the optimal pore size of 1.70 nm. However, the curcumin solubility significantly deceased when the pore size of MCM-41 was further decreased from 1.7 to 1.0 nm, due to the failure of encapsulating curcumin into MCM-41 with small pore sizes. The further application of MCM-41 with finely controlled pore sizes is on the way to optimize the oral bioavailability of curcumin in rats.

SiNPs have also been widely used to deliver another hydrophobic drug, photosensitizers (PSs), to improve the efficiency of photodynamic therapy (PDT). As an emerging new medical treatment, PDT has been used for both internal cancers (lung, stomach or bladder cancers)[70-72] and surface skin diseases.[73] It involves the use of low toxicity PSs and harmless visible light in combination with oxygen to produce cytotoxic reactive oxygen species (ROS) such as singlet oxygen ($^1O_2$), which oxidize cellular molecules and kill malignant cells.[74] PSs described so far in literature have presented several disadvantages. Mainly, most existing PSs are hydrophobic and may aggregate in a physiological environment, which leads to the decrease of $^1O_2$ quantum and limit their potential clinical applications.[75] Moreover, ROS are also usually involved in the initiation, progression and metastasis of cancers, thus are considered oncogenic when applied in healthy cells.[76] Therefore, PSs are required to selectively accumulate in tumor cells. Even though much efforts are focused on developing the third generation of PSs with a covalently link to target receptors over-expressed in cancer cells, very few have been evaluated for their clinical applications mainly because the *in vivo* selectivity is not high enough.[77] In order to address this issue, many groups are trying to incorporate PSs into various biocompatible nanocarriers, such as liposomes,[78] oligopeptide,[79] polymeric micelles[80] and SiNPs.[81-84] Indeed, encapsulation had led to the administration of the PSs in monomeric form without loss of activity.[81] Moreover, nano-scaled carriers tend to be entrapped within solid tumors due to leaky vasculature of the fast-growing tumor, which is called “enhanced permeation and retention effect” (EPR) or “passive” targeting.[85] Among various nanoparticles, SiNPs have recently emerged as a promising vehicle for PDT applications. This is because the

porosity of porous silica nano-materials is not susceptible to swell or decompose with pH change. More importantly, the feasibility of surface modification of silica nanoparticles offers an opportunity to achieve "active" targeting to tumor cells, via conjugating with cell membrane receptor antibodies, peptides or other small cell surface ligands. Generally, PSs can be immobilized into the pores/surface of silica nanoparticles through covalent or non-covalent interactions, and both methods appear to be efficient in PDT.[81] SiNPs functionalized with specific biomolecules for PDT applications have been reported (a monoclonal antibody,[86] mannose,[87] cRGDyK peptides,[88] or folic acid[89]), in order to target various human cancer cells (breast cancer cells and human glioblastoma cells).

#### 2.4.1.2 Gene delivery

Gene therapy is a promising treatment where foreign genetic molecules (nucleic acids) are introduced into living cells to supplement or alter genes to treat various diseases.[90,91] Therapeutic genes generally include small-interfering RNA (siRNA), plasmid DNA (pDNA) and antisense RNA during gene therapy. However, naked nucleic acids themselves cannot enter into cells and are easily degraded by nucleases in the blood,[92] therefore, current research efforts are focused on the design of efficient carriers, which could compact and protect nucleic acids (DNA or RNA). Generally, gene delivery systems are divided into viral[93] or non-viral vectors.[94] Initial studies mainly focused on using viral carries, due to their high efficiency at delivering genetic agents. However, there are some issues associated with viral vectors, including toxicity, immunogenicity, inflammatory response, and carcinogenicity.[95-97] Compared with viral vectors, synthetic gene delivery systems (Figure 2.5) including polymeric[98] and liposomal[99] agents, peptides[100] and inorganic nanoparticles (such as gold, quantum dots, layer double hydroxides, calcium phosphate, carbon nanotubes, and silica) exhibit moderate gene delivery efficiency, but offer many advantages, such as ease of preparation/functionalization, and reduced risk of immunogenicity. Over the years silica based nanocarriers have attracted increasing attention for gene delivery because of their unique properties, such as tunable particle/pore sizes, stable and rigid framework, feasibility of surface modification and low cost.[56,101-103]

In 2000, Chen et al. firstly reported the application of solid SiNPs in gene delivery.[105] The aminosilane modified solid silica nanoparticles were prepared with diameters of 10-100 nm, which demonstrated strong binding capacity toward pDNA and efficient protection against enzymatic degradation.[105] Successful *in vitro* gene transfection induced by such nanoparticles was observed, especially in the presence of serum and chloroquine.[106] At the same time, Luo et al. found that the unmodified solid silica nanoparticles can serve as mediators to enhance gene transfection efficiency.

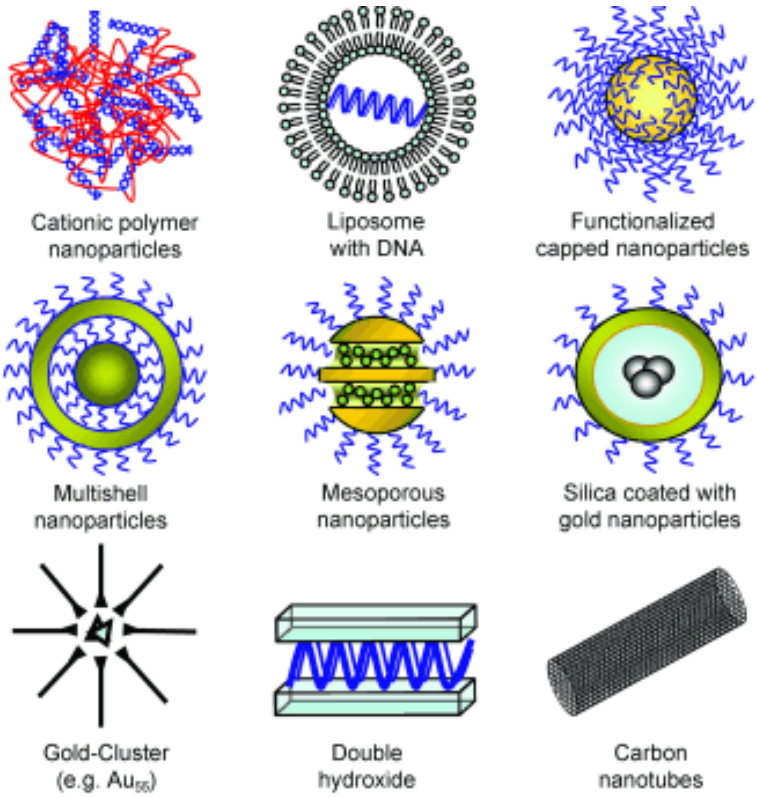


**Figure 2.5** Different types of nanoparticles which can be used for the transfer of nucleic acids into living cells.[104]

In a three-component transfection system (i.e. unmodified solid silica nanoparticles-pDNA-commercial transfection agent), the unmodified dense silica nanoparticles could enhance β-galactosidase protein expression by up to 750% over the commercial transfection reagents.[107] The increment was attributed to increased accumulation of pDNA-transfection agent complexes at the cell surface. Moreover, the enhancement of gene transfection was dependent on the diameter of silica nanoparticles; the larger silica nanoparticles with a diameter of 225 nm increased the gene transfection more significantly than the smaller ones (25 and 50 nm in diameters), which was attributed to the faster settling of larger silica particles on cell surface.[108] In 2004, MSNs with a diameter of about 180 nm were first used for pDNA delivery, in which a polyamidoamine dendrimer was covalently bound to the surface of MSNs to complex with the negatively charged pDNA while the mesopores carried a fluorescent dye as a drug model.[56] This cationic MSNs exhibited higher transfection efficiency compared with several commercial cationic polymers. The particle sedimentation effect[108] was introduced to explain the transfection enhancement. In 2005, Bharali et al. reported the application of organically modified silica (ORMOSIL) nanoparticles as vectors for efficient *in vivo* gene delivery.[109] After stereotaxic injections of ORMOSIL nanoparticles complexed with pDNA encoding for EGFP, into the mouse brain, the results showed that the transfection efficiency of ORMOSIL equalled or exceeded that by using viral vector. This

success is a significant landmark in nonviral gene carries because of a comparable *in vivo* transfection efficiency compared with viral vectors. In 2011, Kim et al. demonstrated that aminated mono-dispersed mesoporous silica nanoparticles (MMSN) (250 nm in diameters) with large pores (~ 23 nm) showed a higher loading capacity for pDNA, significantly efficient protection from nuclease-mediated degradation and much higher transfection efficiency, compared to those with small pores (~ 2 nm).[102] This work emphasizes the significance of pore size of silica nanoparticles in gene transfection efficiency.

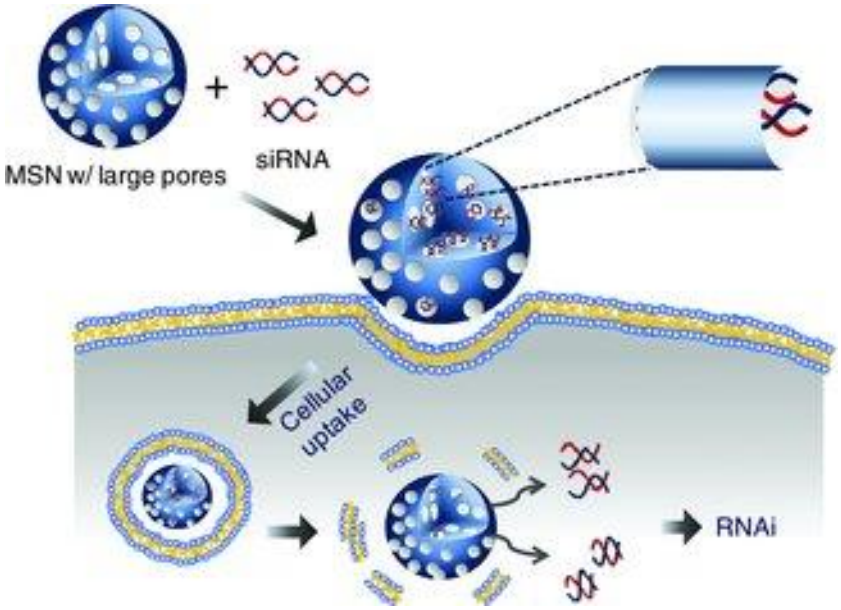


**Figure 2.6** The siRNA delivery system using a silica nanoparticle with a large pore diameter of about 23 nm.[110]

Gene silencing via siRNA in particular has great potential in the treatment of various diseases due to its outstanding efficiency and target specificity.[112] siRNAs are duplexes of 21-23 nucleotides with a size of approximately 7.5×2 nm,[113] which can be synthesized and introduced into cells directly. The introduced siRNAs form complex with RNA-Induced Silencing Complex (RISC) in the cytoplasm and then unwind into single stranded RNAs which guide the RISCs to complementary RNA molecules, where the new synthetic double-stranded RNAs are cleaved by the Argonaute protein (AGO), and then the targeted mRNA is silenced.[114] The negative charge and big molecular size of siRNA impair its accessibility to the cells. To achieve the gene silencing efficiency of siRNA, effective intracellular delivery systems are desired to exploit the therapeutic potential of siRNA. In 2009, polyethylenimine (PEI) functionalized MCM-41 was used for siRNA delivery, showing efficient knockdown of green fluorescent protein (GFP) and low cytotoxicity.[115]

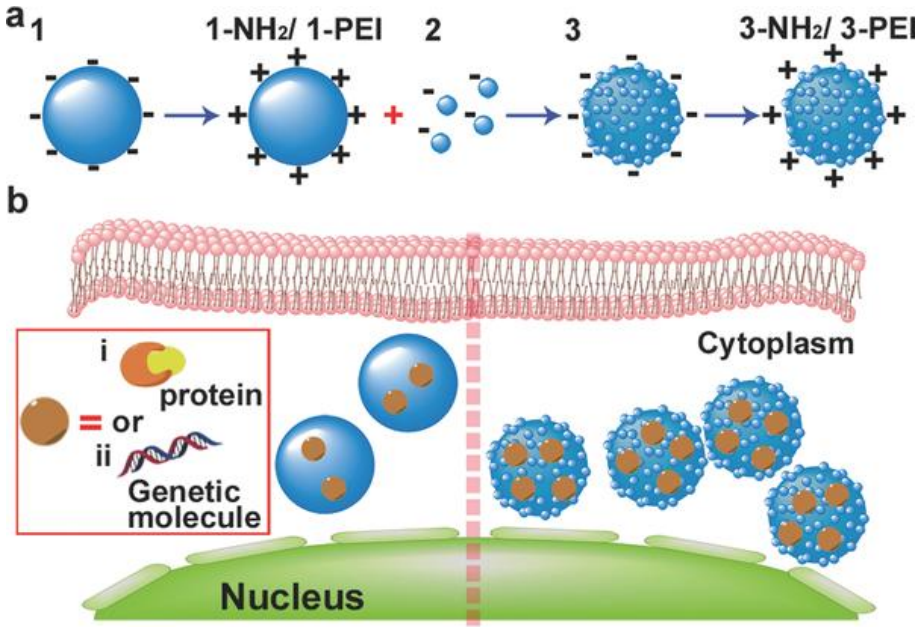


**Figure 2.7** Illustration of: a) the synthesis procedure, and, b) the comparison of cellular delivery performance between two nanocarriers. a) Sample 1 represents silica nanoparticles, which can be further modified with positively charged amine groups or polyethylenimine (PEI). Sample 2 comprises the negatively charged silica nanoparticles with small diameters. Sample 3 was prepared by using amino-modified 1 as the core and 2 as the shell particles after calcination, which is modified with amine groups or PEI. b) Compared to smooth nanocarriers, rough ones exhibit both higher binding ability towards biomolecules (e.g., proteins and genetic molecules) and increased cellular uptake efficiency, independent of surface functionality.[111]

In 2012, Na et al. reported the use of amine-functionalized MSNs with a large pore diameter of 23 nm to deliver siRNA in *in vitro* and *in vivo*, which showed highly efficient knockdown efficiency of target proteins (vascular endothelial growth factor (VEGF) and GFP).[110] Compared with commercial gene transfection agent, Lipofectamine 2000, this delivery vehicle demonstrated higher gene silencing efficiency and much lower cytotoxicity. As shown in Figure 2.6, this siRNA delivery vehicle was able to load siRNA molecules into the pores with high loading capacity and protection from nuclease, which could explain its high gene transfection efficiency. Hartono et al. also successfully prepared a poly-L-lysine functionalized large pore MSNs but with a cubic mesostructure for siRNA delivery, where the particle size was about 100-200 nm and the pore diameter was ~ 28 nm.[116] The authors chose PLK1 (polo-like kinase 1)-siRNA to investigate the gene delivery efficiency of the large pore MSNs. It has been well reported that PLK1 gene is highly expressed in osteosarcoma cells and knockdown of PLK1 proteins induces apoptosis.[117] After adsorption of PLK1-siRNA into the inner pores, significant inhibition of osteosarcoma cancer cell viability was observed due to the efficient silence of PLK1 proteins. Apart from pore sizes, the

topology of SiNPs also plays a significant role in siRNA delivery efficiency. Recently, solid rough SiNPs mimicking viral surface topography showed enhanced siRNA delivery efficiency compared with smooth solid SiNPs.[111] The rough surface enhanced the siRNA adsorption and cellular uptake performance, resulting in efficient gene silence. Furthermore, rough SiNPs exhibited both higher binding ability towards other biomolecules (e.g., proteins and DNA) and increased cellular uptake efficiency, independent of surface functionality, compared with smooth ones (Figure 2.7). Additionally, Li et al. developed a multifunctional MSNs-based siRNA delivery functionalized with magnetic nanoparticles, PEI and fusogenic peptide, which was highly effective for initiating targeted gene silencing both in *in vitro* and *in vivo*.[118]

#### 2.4.1.3 Peptide and protein delivery

Furthermore, SiNPs held a promise as carriers for therapeutic peptides and proteins in many medical applications, including cancer treatment, vaccination and regenerative medicine.[119,120] Compared with gene therapy, protein-based treatments may be safer because permanent genetic changes are not involved, only transient alterations of proteins.

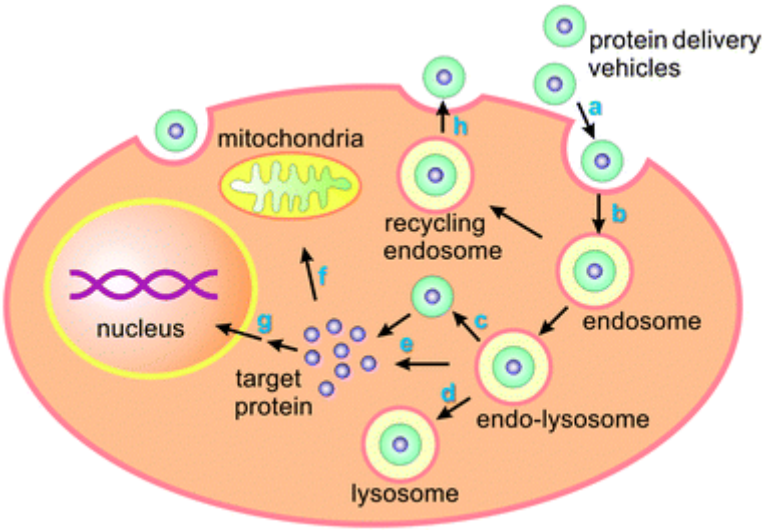


**Figure 2.8** Schematic process of a typical endocytic pathway for delivery vehicles with protein cargoes. (a) Cell-surface attachment of protein delivery vehicles; (b) internalization of delivery vehicles via endocytosis; (c) endosomal escape of delivery vehicles or (d) lysosomal degradation; (e) target protein diffuses into cytoplasm; (f) transport of target proteins to specific organelle; (g) participation in cellular functions such as signal transduction; (h) exocytosis of delivery vehicles.[120]

Intracellular protein delivery is the main hurdle of protein-based approaches due to the large sizes, varying surface charges and fragility of most native and active proteins.[121] The native proteins are unstable and rapidly degraded or inactivated in serum. Moreover, native proteins are membrane impermeable because of the electrostatic repulsions. Therefore, efficient delivery carriers for

protein cargoes are highly demanded. Additionally, the carriers are required to help the proteins to achieve endosomal escape (Figure 2.8), like the case in siRNA delivery. To successfully reach the desired subcellular compartments, the carriers/proteins must be able to escape from the endosome to avoid the clearance and degradation under harsh lysosomal conditions.[122] In the past decade, various nanocarriers have been generated to deliver proteins into cells and have demonstrated promising efficacy in protein-based treatments, including liposomes, polymers, inorganic nanoparticles and protein-based carriers.[120] The recently reported examples of nanocarriers for protein delivery are listed in Table 2.2. It can be seen that nanosized SiNPs have proven the potential of immobilization and intracellular delivery of various types of proteins.[123,124] Slowing et al. first reported the utilization of MSNs with a large pore diameter of 5.4 nm for intracellular delivery of cytochrome C.[123] The authors quantitatively analysed enzymatic activity of the released protein in physiological buffer solutions and found that the enzymes released from the MSNs were still functional and highly active in catalyzing the oxidation of 2, 2'-azino-bis(3-ethylbenzthiazoline-6-sulfonate) (ABTS) in the presence of hydrogen peroxide, which was identical compared to native cytochrome C. Moreover, it showed that MSNs with large pores was an efficient transmembrane delivery vehicle and achieved controlled release of the membrane-impermeable protein of cytochrome C in human cervical cancer cells (HeLa). Bale et al. utilized the hydrophobic solid SiNPs functionalized with n-octadecyltrimethoxysilane (n-ODMS) (15±5 nm in diameter) to immobilize and effectively deliver proteins into a human breast cancer cell line (MCF-7) and rat neural stem cells (NSCs) while retaining the biological activity of the delivered proteins.[124] The authors demonstrated that delivery of ribonuclease A (RNase A) and the antibody to phospho-Akt (pAkt) resulted in the initiation of cell death. In contrast, delivery of control protein conjugates (e.g., those containing green fluorescent protein or goat antirabbit IgG) resulted in minimal cell death. Lim et al. reported the use of hollow mesoporous silica capsules (HMSCs) with large surface holes (25-50 nm) to effectively transport large functional proteins such as antibodies into HeLa cells.[125]

**Table 2.2** Summary of recently reported nanocarriers for the protein intracellular delivery. [120]

| | Types of nanocarriers | Physical properties | Delivered protein | Cell lines used |
|---|---|---|---|---|
| Lipid-mediated | Cationic lipid TFA-DODAPL:DOPE[126] | Positively charged | Phycoerythrin α-chain, β-chain; BSA; β-galactosidase; caspase-3; caspase 8; granzyme B; cytochrome c | NIH-3T3; HeLa-S3; BHK-21; CHO-K1; B16-F0; 293; MDCK; P19; Jurkat; Ki-Ras 267β1 |
| | DOGS (dioctadecylglycylspermine)[127] | Size: 500–900 nm; | BSA; β-galactosidase; IgG(anti-actin); IgG(anti- | CHO; BHK; Jurkat |

| | Types of nanocarriers | Physical properties | Delivered protein | Cell lines used |
|---|---|---|---|---|
| | | positively charged | tubulin); phycoerythrin | |
| | FuGENE6™; BioPORTER™[128] | Positively charged | β-Galactosidase; caspase-3 | C6 glioma cells; rBCEC4 |
| | Amphiphile (CholCSper)/DOPE[129] | Size: 200 nm; positively charged | Phycoerythrin | BHK-21 |
| Polymeric-based | PEI-based attachment[130-135] | Positively charged | RNase; eGFP; IgG; anti-S100C; p53; simian virus 40 large T-antigen | NIH-3T3; KMS-6; OUMS-36; HEK293; HeLa; K562; HFL-1; Saos-2 |
| | PPAAc-$NH_2$/streptavidin[136] | | Biotinylated anti-CD3 antibody | Jurkat |
| | Glucose-coated beads[137] | Size: 150 nm | EGFP | mES; Hela |
| | pH-responsive core–shell nanoparticles[138] | Size: 200 nm at pH 7.4, 580 nm below pH 6.8 | Ovalbumin (OVA) | BMDCs; dendritic DC2.4 |
| | Self-assembled cationic nanogels[139,140] | Size: 20–40 nm; positively charged | BSA; β-galactosidase; Tat-NLS-GFP; BoHc/A | CHO-K1; cos-7; NIH-3T3; HeLa; nasal mucosal dendritic cells |
| | Acid-degradable particles by inverse emulsion polymerization[141] | Size: 200–500 nm | OVA | RAW309.1 CR macrophage |
| | Acid-degradable particles by double emulsion evaporation[142,143] | Size: 250 nm | OVA | RAW309.1 CR macrophage |
| | Single-protein nanocapsules[144-146] | Size: 8–20 nm; positively charged | GFP; BSA; HRP; SOD; caspase-3; Klf4 | HeLa; MCF-7; CHO; MEF |
| | Charge-conversional polyion complex (PIC) micelles[147] | Size: 50 nm; positively charged | Cytochrome c; anti-NPC mouse IgG | HuH-7 |
| | Amphiphilic poly(amino acid) derivatives[148] | Size: 250–300 nm; negatively charged | OVA | Immature DCs |
| Inorganic-based | Single-walled carbon nanotubes (SWNT)[149-151] | Size: 1–5 nm in diameter for SWNT | BSA; streptavidin; cytochrome c | HL60; Jurkat; CHO; NIH-3T3 |
| | Quantum dots [152] | Core diameter: 20 nm | YFP; b-phycoerythrin | HEK 293T/17; COS-1 |

| | Types of nanocarriers | Physical properties | Delivered protein | Cell lines used |
|---|---|---|---|---|
| | Gold nanoparticles [153] | Core diameter: 2.5 nm; positively charged | β-Galactosidase | HeLa; COS-1; MCF-7; C2C12 |
| | Mesoporous silica nanoparticles (MSNs)[123] | Size: 200 nm; pore diameter: 5.4 nm | Cytochrome c | HeLa |
| | Hydrophobically functionalized silica nanoparticles[124] | Size: 15 nm | Anti-pAkt | MCF-7; NSCs |
| | Magnetic nanoparticles[154] | Size: 300–400 nm; negatively charged; magnetic moment at saturation: 14.3 emu $g^{-1}$ | SOD; catalase | BAEC |
| Protein-mediated | Polyomavirus-like nanoparticles[155] | Size: 35 nm | GFP | Swiss 3T3 |
| | Superpositively charged GFP variants[156] | Positively charged | Cre recombinase | HeLa; BSR; NIH-3T3; IMCD PC12 |
| | Engineered protein G system[157] | | Goat anti-mouse IgG | HeLa |

The authors found that the efficiency of protein delivery by HMSC was 3-22 folds higher than that of conventional MSNs.

There are limited reports on the use of SiNPs as antigen carriers for vaccine delivery.[119] The potential of MSNs as a vaccine delivery system was firstly reported by Mercuri et al. in 2006 where SBA-15 type MSNs was utilized as a carrier to carry, protect and deliver antigens, bacterial recombinant protein *In1β*.[158] The author demonstrated improved antibody responsiveness in mice.

The ability of SBA-15 as an antigen carrier to elicit an immune response was further confirmed by Carvalho et al. in 2010.[159] The authors evaluated the ability of SBA-15 to modulate the immune responsiveness of mice immunized with bovine serum albumin (BSA) encapsulated SBA-15 through the intramuscular or oral route and compared with the responsiveness induced by BSA encapsulated aluminum hydroxide salts or emulsified Incomplete Freund adjuvant. The results shown that SBA-15 type MSNs improved the immunogenicity and repaired the responsiveness of the constitutively low responder individuals inducing both the IgG2a and the IgG1 isotypes. In 2012, Wang et al. investigated the vaccine delivery capacity of three different types of MSNs (S2, S1 and SBA-15) with different particle sizes (130, 430 nm and 1-2 μm), pore sizes and shapes by oral route

to find out the relationship between the silica architecture and immunological properties.[160] Model antigen BSA was chosen to load into these MSNs. S2 shown highest level of IgG and IgA titers induced by loading BSA (S1>S2>SBA-15) due to its large honeycombed pores and the optimal particle diameter of 430 nm. The hollow structured MSNs (HMSN) were also studied as vaccine carriers by Guo et al.[161] Porcine circovirus type-2 (PCV2) GST-ORF2-E protein was loaded into HMSNs and then injected into mice. HMSNs were found to have better binding capacity and delivery profile of protein. Importantly, the immune response induced by HMSN/PCV2 GST-ORF2-E complex was maintained for a relatively long period of time. Recently, Mahony et al. investigated the immunization of model protein antigen ovalbumin (OVA) on MCM-41 for vaccine delivery vehicle in mice.[162] The authors found that amino-functionalized MCM-41 (AM-41) showed enhanced binding capacity towards OVA, 1.5 times higher (72 mg OVA/g AM-41) than nonfunctionalized MCM-41 (29 mg OVA/g MCM-41). OVA adsorbed AM-41 induced both antibody and cell-mediated immune responses after subcutaneous injections. It is concluded that exciting progress has been achieved in the field of vaccine delivery using SiNPs in the last decade.

#### 2.4.1.4 Combination therapy

Recently, combination therapy with complementary or synergistic effect has attracted increasing attention for various diseases treatment. It is highly desired to develop efficient delivery systems which could simultaneously carry two or more therapeutic agents in a coordinated manner. With advantages of tunable pore/particle sizes and large pore volume, MSNs have been proven to be promising co-delivery systems. [101,163-168] MSNs offer both internal and external surface for loading different cargoes to achieve co-delivery. In 2009, Zhao et al. designed boronic acid-functionalized MSNs (BA-MSN) to achieve glucose-responsive controlled release of both insulin immobilized on the exterior surface and cyclic adenosine monophosphate (cAMP) loaded in the interior mesopores. [163] Chen et al. utilized MSNs to co-deliver anticancer drug doxorubicin (Dox) and a siRNA (as a suppressor of cellular antiapoptotic defense) simultaneously into multidrug-resistant cancer cells for efficient cancer therapy.[101] Specifically, Dox was encapsulated into the interior meopores of MSNs. Then the Dox loaded MSNs were modified with generation 2 (G2) amine-terminated polyamidoamine (PAMAM) dendrimers to efficiently complex with siRNAs targeted against mRNA encoding nonpump resistance Bcl-2 protein. The authors found that the complex can enter into multidrug-resistant A2780/AD human ovarian cancer cells to induce cell death. The anticancer efficacy of Dox increased 132 times compared to free Dox, because the simultaneously delivered siRNA efficiently overcome the nonpump resistance. Meng et al. further proved that co-delivery strategy is highly efficient to overcome multiple drug resistance (MDR) to improve cancer treatment.[167,168] The authors used functionalized MSNs to effectively deliver anticancer drug Dox as

well as P-glycoprotein (Pgp) siRNA to a drug-resistant cancer cell line (KB-V1 cells) to accomplish cell killing in a synergistic manner.[167] Recently, the authors further demonstrated that the dual delivery system resulted in synergistic inhibition of MDR breast cancer cells (MCF-7/MDR cells) *in vitro* as well as tumor growth *in vivo*.[168] Zhu et al. for the first time designed an enzyme-triggered drug and gene co-delivery system by utilizing hollow mesoporous silica (HMS) modified with enzyme degradable PLL polymer as nanocarriers.[169] Ashley et al. reported report MSNs-supported lipid bilayers (called protocells) to synergistically combine the advantages of liposomes and MSNs.[164] After modification with a targeting peptide, protocells exhibited a 10,000-fold greater affinity for targeted human hepatocellular carcinoma than for hepatocytes, endothelial cells or immune cells. Furthermore, protocells can be loaded with therapeutic (drug cocktail, siRNA and toxins) and diagnostic (quantum dots) agents. The designed multi-functional protocells can efficiently cause a kill of drug-resistant human hepatocellular carcinoma cell, with a $10^6$-fold improvement over comparable liposomes.

### 2.4.2 Targeted delivery

It has been well documented that targeted delivery is vital for efficient cancer therapy because most anticancer drugs distribute throughout the body and can be harmful to healthy cells.[170] To minimize side effects, it would be desirable to specifically increase therapeutic agents' concentration at the target sites. Much efforts has been devoted to develop SiNPs modified with active targeting moieties, including specific ligands (such as folic acid,[171,172] mannose[87] and arginine-glycine-aspartate (RGD)[173]), peptides,[88] and antibodies.[54] The abundant silanol groups (Si–OH) facilitate the modification of the above active moieties, thereby achieving active targeting of SiNPs to specific cancer cells. Active targeting action will enhance the cellular uptake of SiNPs in defective cells, leading to significant improvement in cancer therapy.

Hyaluronic acid (HA) is a biodegradable, biocompatible and non-immunogenic glycosaminoglycan. As a major component of extracellular matrix, HA is essential for proper cell growth, organ structural stability and tissue organization,[174,175] and has been extensively investigated for biomedical and pharmaceutical applications. In particular, researchers focused on the use of HA as a targeting moiety for cancer therapy, because many types of tumor cells over-express HA receptors like CD44.[170] Since HA has multiple functional groups available for chemical conjugation with anticancer drugs[170,176] or nanocarriers of drugs/gene,[177,178] HA-attached drugs/nanocarriers have been developed to increase therapeutic agent accumulation specifically in CD44 over-expressing cancer cells. In addition to the targeting function, HA modified delivery systems can enter cells more efficiently via the HA receptor-medicated endocytosis pathway. Utilizing CD44-HA specific affinity is therefore an attractive strategy for cancer targeting treatment.

Ma et al. firstly reported the design synthesis of MSNs-HA conjugate.[179] After loading with CPT, HA-MSNs showed enhanced cytotoxicity to HeLa cells. However, the improvement in cell toxicity is not significant compared to free CPT. Although it was claimed in this report that CD44 positive HeLa cells were used, there is no evidence or literature support that the HeLa cells used in this work are CD-44 positive. Moreover, because HA coated at the outer surface of MSNs is very hydrophilic; the nature of drug may also have influence on the cytotoxicity. Therefore, more efforts are still needed to rationally design targeting moieties modified SiNPs to improve drug delivery efficiency at targeted cells/sites.

### 2.4.3 2D and 3D *in vitro* models of tumors

Most cancer and tumor biological studies of SiNPs are based on two-dimensional (2D) cell models (monolayers). However, the flat and hard plastic or glass substrates commonly used for monolayer cell cultures are not representative of multi-layer cellular environment in the real tissues. Such simplified conditions limit the potential of 2D cell culture model to predict the cellular responses of real organisms. In contrast, three-dimensional (3D) culture models more closely mimic the cell-to-cell and cell-to-extracellular matrix (ECM) interactions as well as the topography found in *in vivo* tumor environment.[180]

Many studies have demonstrated significant differences between 2D and 3D culture models in terms of gene expression, [181] cell physiology,[182] chemosensitivity, [183] and survival advantages.[184] To model solid tumors more effectively, various 3D culture systems have been established including cellular multilayers, matrix embedding cultures, hollow fiber bioreactor, *ex vivo* cultures and multicellular spheroids (MCSs).

Cellular multilayer model is the simplest approach to generate 3D culture where the cells are cultured on porous membranes coated with collagen up to 20 layers. This model has been used for drug discovery and transport studies,[185,186] which is convenient for the measurement of the mass transport depth. It is particularly useful for cancer cell lines which do not form spherical clusters. However, it fails to take into account of the blood vessel barrier during the transport studies.

In the hollow fiber bioreactor approach, cells form solid model in capillaries made of polyvinylidine fluoride (PVDF). This model has been utilized to investigate the metabolism and cancer cell resistance generated in solid tumors. The major drawback of this 3D model is the fiber wall influence on tumor growth.

The *ex vivo* culture system is to culture tissue explants *in vitro*, which are closest to *in vivo* tumors. However, the availability and reproducibility of this approach is limited.

Table 2.3 Advantages of the techniques for self-assembly of MCSs.[187]

| | Pellet Culture | Spinner Culture | Hanging Drop | Liquid Overlay | Rotating Wall Vessel | External Force | Cell Sheets | Micro-fluidics | Micro-molded Hydrogels |
|---|---|---|---|---|---|---|---|---|---|
| Good Size Control | + | | + | | | | + | + | + |
| Low Shear Stresses | | | + | + | | + | + | + | + |
| High Yield | | + | | | + | | | + | + |
| Good Control of Heterotypic Cell to Cell Ratio | + | | + | | | | + | + | + |
| Good control of the microenvironment over time | + | | + | | + | | | + | + |
| Minimal Labor | + | + | | | + | | | | + |
| Easy to Handle Micro-tissues | + | + | | | + | | | + | + |
| Possibility of Complex Shapes | | | | | | | | | + |
| Observe by Microscopy | | | + | + | | | + | + | + |
| Cell Type Independent | | | + | + | | + | | + | + |

MCSs are the most widely used 3D tumor models. In the absence of attachment substrates or scaffolds, cells aggregate and compact to form tightly bounded cellular spheres through the self-assembly process. The spheroid creates the *in vivo* like microenvironment by forming molecular gradients, complex cell-to-cell interactions and cell-to-(ECM) interactions.[187] Various methods have been developed to form spheroids, including pellet culture, spinner culture, handing drop, liquid overlay, rotating wall vessel, external force, cell sheets, microfluidics and micro-molded hydrogels.[187] The advantages of these spheroid forming techniques are summarized in Table 2.3. It is important to note that not all cell lines readily form well-defined spheroids, and some cells have been demonstrated to form only loose aggregates. The sizes of spheroid tumors can be varied from 20 μm to larger than 1mm in diameter.[188] The cells in the outer layer are exposed to nutrients, leading to a rapid proliferation. The enclosed layer consist of quiescent cells followed by a necrotic core. Compared to monolayer cancer cells, such 3D tumor structures have demonstrated significantly increased resistance to chemotherapeutic drugs, such as cisplatin and paclitaxel,[189,190] because the drugs have limited access to the necrotic core. Cellular adhesion in the 3D systems has also been found as another reason for increased resistance to therapeutics.[191,192] Therefore, traditional 2D cell culture models have limitations for studying *in vivo* cell biology and cell physiology. Cells grown in a three-dimensional (3D) environment more closely represent cellular function of natural organs and tissues.

There are increasing reports on the penetration ability evaluation of nanoparticles in 3D culture models.[193,194] However, the behavior of SiNPs in 3D culture models has rarely been studied. More efforts are desired to investigate the penetration ability of SiNPs and subsequent delivery efficiency of therapeutic agents.

### 2.4.4 Cell imaging and sensing

Molecular imaging is the visualization, characterization, and measurement of biological processes at the molecular and cellular levels in humans and other living systems,[195] which is very important to gain better understanding on mystery of life. Due to the diversity, temporal-spatial variation of biological activities in cells and the whole body, the precise monitor and visualization of biological processes in highly changing. Therefore, the analysis techniques are required to be fast-response, high stable, *in situ* and in-real time. The functionalized fluorescent nanoparticles based cell imaging and sensing techniques are of great interest because they have great potential to meet such requirements.[196-199] Taking advantage of their small sizes, nanoparticles-based imaging agents can offer unprecedented interactions with biomolecules on surface of/inside cells. More importantly, multi-functionality is the main advantage of fluorescent nanoparticles over traditional approaches. Nanoparticles can integrate targeting ligands, imaging labels, and other agents for targeted molecular imaging. Several types of nanoparticles have been employed for cell imaging and sensing applications, including quantum dots,[197] Gold nanoparticles,[198] carbon dots,[200], dye-doped SiNPs[199,201] etc. Of these agents, functionalized dye-doped SiNPs have widely used for intracellular sensing, tracking, cell surface reporter recognition and fluorescence imaging both in *in vitro* and *in vivo* (Figure 2.9), due to their stable fluorescent brightness, high chemical stability, excellent biocompability and flexible modification properties.[199]

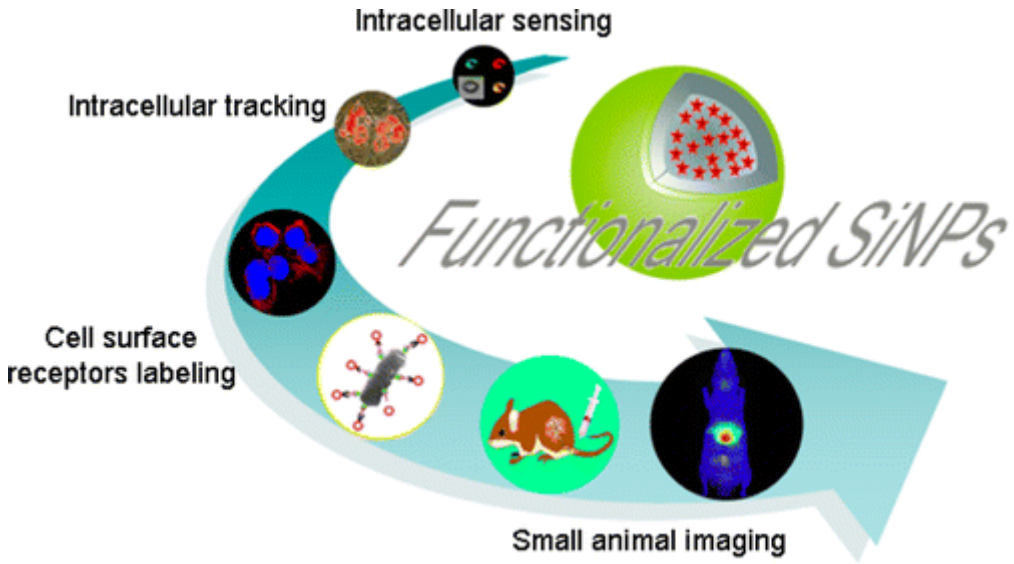


**Figure 2.9** Functionalized fluorescent SiNPs in the applications of intracellular sensing and tracking, cell surface reporter recognition and fluorescence imaging in small animals.[199]

Generally, various luminescent organic or inorganic dye molecules can be encapsulated inside of silica matrix to form dye-doped SiNPs, which can produce a highly amplified signal and improve the imaging sensitivity, compared with a single dye molecule. In addition, functionalized fluorescent SiNPs can protect the biological environment from potentially toxic interaction between

cells and doped-dye SiNPs, also greatly reduce photobleaching and photodegradation of free dye molecules.

#### 2.4.4.1 Synthesis of fluorescent SiNPs

There are two principal approaches to synthesize dye-doped SiNPs: the Stöber method and reverse microemulsion method.

As introduced in Section 2.2.1, Stöber method is simple and efficient approach to produce mono-dispersed solid SiNPs with a broad range of diameters from 50 nm to 2μm. Van Blaaderen and co-workers for the first time reported the covalent incorporation of organic fluorescent dye into Stöber silica spheres.[202] In 2005, Wiesner and co-workers at Cornell University further extended this approach to develop water-soluble, non-toxic fluorescent core-shell silica nanoparticles (C dots) in a size range of 20-30 nm.[11] The C dots as biological probes shown enhanced dye quantum efficiencies, brightness and stability and reduced energy transfer effects, because of the restricted rotational mobility of organic dyes entrapped in the core of the C dots and the protection from molecular quenchers and solvent effects.[203] In 2009, the authors developed even smaller C-dots (~7 nm) and further modified with poly(ethylene glycol) (PEG), which showed efficient renal clearance in mice compared with unmodified C dots.[204] Moreover, the C dots modified with the cyclic argininеglycine-aspartic acid (cRGD) peptide and radiolabeled with 124I showed its selective tumor targeting and real-time multimodal imaging in both small and large animal models.[12] This work has led to C dots receiving the FDA investigational new drug approval for a first-in-human clinical trial in 2011. The researchers are about to launch their first-in-human clinical trial in melanoma patients using this silica based inorganic nanoparticle to be approved as a diagnostic agent.

The second method to prepare dye-doped SiNPs is a water-in-oil reverse microemulsion protocol,[205] which involves water, surfactant and oil. The hydrolysis and condensation of silica precursors and the formation of nanoparticles with dye trapped inside occur at the interface of surfactant stabilized water droplet inside the oil phase, to form fluorescent SiNPs. By changing the charge and packing properties of the surfactant in the micelles, water to surfactant ratio or the amount of free water and ammonium hydroxide concentration, the diameter of spherical and mono-dispersed SiNPs can be adjusted from 20 to 500 nm.[206,207] The monnodispersity of SiNPs with diameters of 30-60 nm obtained by reverse microemulsion method is superior compared to Stöber approach. However, the use of large amount of surfactants requires an extensive washing time, which limits the potential of microemulsion method for industrial/mass production.

At the beginning, the reverse microemulsion method can only be used to incorporate inorganic dyes, but the resultant inorganic-dye-doped SiNPs have limited fluorescence intensity, because inorganic dyes have lower quantum yields compared with organic fluorophores.[208,209] Organic dye-doped SiNPs are difficult to prepare using this method due to hydrophobic properties of the organic dyes compared with the hydrophilic surface of the SiNPs. In 2004, Tan and co-workers reported a modified microemulsion method to successfully incorporate the organic dye into SiNPs.[210] Since then, various single-dye doped SiNPs and multiple-dye incorporated SiNPs can be generated using this method for ratiometric fluorescence probes or fluorescence resonance energy transfer (FRET) mediated large Stokes shifting fluorescence probes.[199] In addition, hybrid SiNPs doped with quantum dots have also been reported for cell imaging using the microemulsion method.[211] The coating of silica shell can reduce quantum dots' toxicity and improve its water-solubility.

In addition, Huo et al. developed an hybrid fluorescent SiNPs by micelle templating approach, where F127 micelles to template silica deposition in the hydrophilic PEO shell region in acidic solution, to form a robust silica cross-linked micellar core-shell nanoparticles with a ultrafine and uniform size of ~ 12 nm.[44] Recently, Wang et al. utilized this approach to obtain an ultra-small, high stable and sensitive dual nanosensor for imaging intracellular oxygen and pH in cytosol.[47] Furthermore, the fluorescent pH-sensitive small SiNPs doped in an agarose matrix demonstrated their potential in monitoring bacterial growth and metabolism.[48]

Furthermore, hollow mesoporous silica nanoparticles (HMSNs) with a large cavity inside and mesopores in the silica walls have also been reported for optical imaging, positron emission tomography (PET), magnetic resonance imaging (MRI) and ultrasound imaging in both *in vitro* and *in vivo* models.[212]

#### 2.4.4.2 Fluorescent SiNPs for cell imaging

Sensitive and selective labelling and tracking of cell surface receptors is significant for diagnosis of early stage diseases and monitoring biological processes. Antigen-antibody and ligand-receptor recognition processes offer specific affinity, thus dye-doped SiNPs as cell imaging agents were modified with different antibodies or targeting ligands to selectively and efficiently label antigens or receptors over-expressed in targeted cells. For example, Peng et al. utilized lactobionic acid (LA)-conjugated RuBpy-doped SiNPs to successfully identify live liver cancer cells in a mixed cell system and precisely label a few liver cancer cells in blood.[213] Double labelling target cells have also been achieved by conjugating two different antibodies with fluorescent SiNPs.[214] Because both anti-CEA antibody and anti-CK19 antibody can efficiently bond to MGC-803 gastric cancer cells, anti-CEA antibody-conjugated FITC doped SiNPs and anti-CK19 antibody-conjugated RuBPY

doped SiNPs were designed and applied in both *in vitro* cultured MGC-803 cells and *ex-vivo* primary MGC-803 cells from the tumor tissues of mice bearing MGC-803 gastric cancer tumor xenografts. The MGC-803 gastric cancer cells were successfully double-labelled in both models. In addition, intracellular labelling and tracking have also been reported using functional fluorescent SiNPs.[215] Shi et al. developed a long-lived lysosome labelling and tracking probes based on tetramethylrhodamine (TAMRA)-doped SiNPs.[215] It showed that TAMRA-doped SiNPs selectively accumulated in lysosomes of HeLa cells and its photostability was about 30 times as long as that of LysoTracker Green. Compared to LysoTracker Green and Alexa 488-dextran, the fluorescence of TAMRA-doped SiNPs could be detected over a 5-day postrecultivation period and was quite stable and sensitive even in fixed cells. The lysosome labelling ability of TAMRA-doped SiNPs was further demonstrated in other cell lines.

SiNPs are also a useful model to investigate biodistribution and the fate of SiNPs utilizing *in vivo* fluorescence imaging. For example, He et al. investigated the biodistribution and urinary excretion of SiNPs (~ 45nm) with surface modification of OH, COOH and PEG functional groups in mice using doped RuBpy dye for an *in vivo* optical imaging probe.[216] After intravenous injection of these SiNPs, the *in vivo* imaging results indicated that three types of SiNPs were all cleared from blood circulation, but the clearance time and subsequent biological organ deposition were dependent on the surface chemical modification of the SiNPs. The PEG-SiNPs exhibited relatively longer blood circulation times and lower uptake by liver than OH-SiNPs and COOH-SiNPs.

#### 2.4.4.3 Fluorescent SiNPs for cell sensing

Fluorescent SiNPs have also been explored in the applications of intracellular sensing of oxygen, pH, temperature, carbon dioxide, and others.[201] The real-time quantification of the intercellular analyte concentration using fluorescent probes is very important to provide insights into chemical microenvironment of sub-cellular compartments. In the following section, some examples are going to be introduced using fluorescent SiNPs to monitor typical analyte concentrations.

*Oxygen sensing* Kopelman and co-workers first reported SiNPs based nanosensors to achieve reliable, real-time measurements of intracellular oxygen in 2001.[217] The SiNPs sensors were prepared by incorporating an oxygen-sensitive fluorescent dye, Ru(II)−tris(4,7-diphenyl-1,10-phenanthroline) chloride ($[Ru(dpp)_3]^{2+}$), and a reference dye, Oregon Green 488-dextran for the purpose of ratiometric intensity measurements. The developed sensors were applied in rat C6 glioma cells for real-time intracellular oxygen analysis with minimal physical and chemical perturbations to their biological functions. The results demonstrated that SiNPs protected the fluorescent dyes from interference by proteins in cells, achieving reliable *in vivo* chemical analysis,

compared with using free dyes for intracellular measurements. In 2004, the same group developed a new type of oxygen-sensitive nanosensors for dissolved oxygen based on ORMOSIL nanoparticles. The ORMOSIL nanoparticles included core particles formed by phenyltrimethoxysilane precursor and a coating layer formed by methyltrimethoxysilane precursor. The sensors incorporated the oxygen-sensitive platinum porphyrin dye as an indicator and an oxygen-insensitive dye as a reference for ratiometric intensity measurement. The sensors demonstrated an excellent sensitivity with an overall quenching response of 97%, and excellent linearity of the Stern−Volmer plot ($r^2$ = 0.999) over the tested dissolved oxygen concentrations. After injecting the nanosensors into rat C6 glioma cells, intracellular changes of dissolved oxygen due to cell respiration were monitored.[218]

*pH sensing* Wiesner group first reported pH-sensitive SiNPs by incorporating the reference dye tetramethylrhodamine and the pH-sensitive FITC in the core and shell of SiNPs, respectively for the ratiometric detection of pH.[203,219] The authors investigated the intracellular pH sensing capability of the fluorescent SiNPs in rat basophilic leukemia mast cells (RBL-2H3).[219] The confocal images showed a variation of pH values from 6.5 to 5.5, indicating the intracellular locations of SiNPs in early endosme and late endosome/lysosome, respectively. The C dots[11] developed by the same group was also utilized to monitor the pH in microbial biofilms[220] and electrospun cellulose acetate fibers.[221] Fluorescent MSNs was also utilized to monitor intracellular pH values by Chen et al.[222] The MSNs-based ratiometric pH-sensor demonstrated the capacity of mapping the location of the MSNs by monitoring the pH in HeLa cells. Positively charged MSNs was found to locate in higher pH region cytosol mostly while negatively charged MSNs in acidic endosomes. In addition, the hybrid ultra-small SiNPs synthesized by micelle templating method was also reported as pH sensors in normal rat kidney cells[47] and bacteria.[48]

*Sensing of ionic species* As the most abundant inorganic anion in living organisms, the chloride transport across both the plasma membrane and intracellular membranes is involved in several important physiological processes, such as cell volume regulation, organellar acidification, and neurotransmission.[223] Dysfunctional chloride transport causes a number of diseases, including cystic fibrosis,[224] myotonia congenita,[225] and kidney stone diseases.[226] Therefore, monitoring the intracellular chloride levels is of primary importance. Baù et al. reported a SiNPs based fluorescent probe (NanoChlor) for chloride.[227] The chloride-sensitive dye 6-methoxyquinolinium and the reference dye fluorescein were covalently grafted on commercially available 20 nm SiNPs (Ludox AS-30), which was further modified with PEG group to improve water solubility and prevent nonspecific interactions with biomolecules. The capacity of NanoChlor to monitor the variations of chloride levels inside live cells was tested in hippocampal cells. NanoChlor displayed ratiometric response when different chemical stimuli were added into cells. There are many other ionic species

playing important roles in living organisms. Fluorescent SiNPs could incorporate with a specific ion sensitive dye for other ion detection (such as $Ca^{2+}$, $Zn^{2+}$, $Cu^{2+}$ and $Pb^{2+}$) in living cells.[201]

The unique characteristics of SiNPs including adjustable sizes, high loading capacity, and suitability for various modifications have enabled them to be efficient and sensitive agents for cell imaging and intracellular sensing at the cell and small animal levels. Ongoing and future efforts will be on the clinical applications of functional fluorescent SiNPs for molecular imaging, disease diagnose and treatment. There are still a number of challenges and opportunities in this area, such as facile and reproducible synthesis of functionalized SiNPs with desired structure parameters and functional groups, further understanding on the interaction between SiNPs and large animals.

## 2.5 Conclusion

The development of nanomaterials has profoundly affected nanomedicine in the fields of diseases diagnosis and treatment. SiNPs in biomedical nanotechnology have been regarded as promising candidates for drug/gene/protein delivery and cell imaging/sensoring, because of their versatile pore structure, particle size, morphology and functionality. However, more efforts are needed to enable a transition to clinical trials of this promising delivery platform. Although there have been tremendous efforts in the synthesis of mono-dispersed SiNPs for various applications, more efforts are still needed to develop facile, economic and environmentally friendly synthesis approaches for fabricating novel mono-dispersed SiNPs with desired particle size, nano-structure and functionality (Objective 1 in this thesis). The novel designed SiNPs are expected to expand their capacity in various biomedical applications. For example, SiNPs with ultra-small particle sizes and excellent monodispersity is expected to have much higher cell penetration ability in 3D spheroid models compared to conventional SiNPs (Objective 2). Besides small particle sizes, desired surface functionality is also crucial on cell penetration performance and subsequent anticancer drug/siRNA delivery efficiency. For example, surface modification of targeting moieties on SiNPs is an efficient approach to improve drug delivery at targeted cells (Objective 2). Furthermore, better understanding on the toxicity of SiNPs with various surface functionalities not only allows a better estimation of the potential risk, but also helps to find a balanced point between efficacy and safety. For example, PEI has been regarded as efficient cationic group, which has a higher endosomal escape capability, favoring a high gene silencing efficacy. However, the cytotoxicity of PEI is relatively high. A suitable dosage of PEI modified SiNPs should be chosen for siRNA delivery with maximal therapeutic efficiency and minimal toxic side-effects (Objective 3). Although plasmid DNA (pDNA) has also been extensively studied in SiNPs-based gene therapy, however, the influence of particle size of silica nanoparticles on pDNA transfection efficiency has not been reported (Objective

4).Thorough understanding on the interactions between SiNPs and pDNA is desired to fully utilize SiNPs for efficient gene therapy (Objective 4).

More efforts are required to understand the relationship between sub-cellular organelle escape/target and structure and functionality of designed SiNPs. Efficient imaging cell activity by utilizing various SiNPs based sensors is very helpful for understanding the intracellular activities of designed SiNPs (Proposed study in the future).

The research on SiNPs for biomedical applications is taking off and has demonstrated tremendously positive results. It is an encouraging advance in biomedicine applications of SiNPs that the C-dots developed by Wiesner group have reached the first-in-human clinical trial stage. Nevertheless, it is still a long way to translate SiNPs-based drug delivery systems or diagnostic agents into clinical market because more evidence needs to prove their efficacy and safety. Finally, the development of multifunctional SiNPs combing diagnostic and therapeutic capabilities is worthy of special efforts, which provides the great potential and opportunities for improving various disease diagnose and treatment. The opportunities could be ravelled out by combining interdisciplinary knowledge in chemistry, biology, material science and clinical medicine.

## 2.6 References


1. Kim, B.Y.S., J.T. Rutka, and W.C.W. Chan, Current Concepts: Nanomedicine. *New England Journal of Medicine*, 2010, **363**(25), 2434-2443.
2. Liong, M., et al., Multifunctional inorganic nanoparticles for imaging, targeting, and drug delivery. *Acs Nano*, 2008, **2**(5), 889-896.
3. Torchilin, V.P., Recent advances with liposomes as pharmaceutical carriers. *Nature Reviews Drug Discovery*, 2005, **4**(2), 145-160.
4. Doane, T.L. and C. Burda, The unique role of nanoparticles in nanomedicine: imaging, drug delivery and therapy. *Chemical Society Reviews*, 2012, **41**(7), 2885-2911.
5. Jain, R.K. and T. Stylianopoulos, Delivering nanomedicine to solid tumors. *Nature Reviews Clinical Oncology*, 2010, **7**(11), 653-664.
6. Tang, F.Q., L.L. Li, and D. Chen, Mesoporous Silica Nanoparticles: Synthesis, Biocompatibility and Drug Delivery. *Advanced Materials*, 2012, **24**(12), 1504-1534.
7. Mai, W.X. and H. Meng, Mesoporous silica nanoparticles: A multifunctional nano therapeutic system. *Integrative Biology*, 2013, **5**(1), 19-28.
8. Mamaeva, V., C. Sahlgren, and M. Linden, Mesoporous silica nanoparticles in medicine-Recent advances. *Advanced Drug Delivery Reviews*, 2013, **65**(5), 689-702.

9. Garcia-Bennett, A.E., Synthesis, toxicology and potential of ordered mesoporous materials in nanomedicine. *Nanomedicine*, 2011, **6**(5), 867-877.
10. Halas, N.J., Nanoscience under glass: The versatile chemistry of silica nanostructures. *Acs Nano*, 2008, **2**(2), 179-183.
11. Ow, H., et al., Bright and stable core-shell fluorescent silica nanoparticles. *Nano Letters*, 2005, **5**(1), 113-117.
12. Benezra, M., et al., Multimodal silica nanoparticles are effective cancer-targeted probes in a model of human melanoma. *Journal of Clinical Investigation*, 2011, **121**(7), 2768-2780.
13. Barenholz, Y., Doxil (R) - The first FDA-approved nano-drug: Lessons learned. *Journal of Controlled Release*, 2012, **160**(2), 117-134.
14. Sarris, A.H., et al., Liposomal vincristine in relapsed non-Hodgkin's lymphomas: Early results of an ongoing phase II trial. *Annals of Oncology*, 2000, **11**(1), 69-72.
15. Petre, C.E. and D.P. Dittmer, Liposomal daunorubicin as treatment for Kaposi's sarcoma. *International Journal of Nanomedicine*, 2007, **2**(3), 277-288.
16. Werner, M.E., et al., Preclinical Evaluation of Genexol-PM, a Nanoparticle Formulation of Paclitaxel, as a Novel Radiosensitizer for the Treatment of Non-Small Cell Lung Cancer. *International Journal of Radiation Oncology Biology Physics*, 2013, **86**(3), 463-468.
17. Ciruelos, E. and C. Jackisch, Evaluating the role of nab-paclitaxel (Abraxane) in women with aggressive metastatic breast cancer. *Expert Review of Anticancer Therapy*, 2014, **14**(5), 511-521.
18. Libutti, S.K., et al., Phase I and Pharmacokinetic Studies of CYT-6091, a Novel PEGylated Colloidal Gold-rhTNF Nanomedicine. *Clinical Cancer Research*, 2010, **16**(24), 6139-6149.
19. Stober, W., A. Fink, and E. Bohn, CONTROLLED GROWTH OF MONODISPERSE SILICA SPHERES IN MICRON SIZE RANGE. *Journal of Colloid and Interface Science*, 1968, **26**(1), 62-&.
20. Beck, J.S., et al., A New Family of Mesoporous Molecular-Sieves Prepared with Liquid-Crystal Templates. *Journal of the American Chemical Society*, 1992, **114**(27), 10834-10843.
21. Kresge, C.T., et al., Ordered Mesoporous Molecular-Sieves Synthesized by a Liquid-Crystal Template Mechanism. *Nature*, 1992, **359**(6397), 710-712.
22. Hoffmann, F., et al., Silica-based mesoporous organic-inorganic hybrid materials. *Angewandte Chemie-International Edition*, 2006, **45**(20), 3216-3251.
23. Wan, Y. and D.Y. Zhao, On the controllable soft-templating approach to mesoporous silicates. *Chemical Reviews*, 2007, **107**(7), 2821-2860.
24. Lu, F., et al., Size Effect on Cell Uptake in Well-Suspended, Uniform Mesoporous Silica Nanoparticles. *Small*, 2009, **5**(12), 1408-1413.

25. Zhu, J., et al., Ultrasmall, Well-Dispersed, Hollow Siliceous Spheres with Enhanced Endocytosis Properties. *Small*, 2010, **6**(2), 276-282.
26. Suzuki, K., K. Ikari, and H. Imai, Synthesis of silica nanoparticles having a well-ordered mesostructure using a double surfactant system. *Journal of the American Chemical Society*, 2004, **126**(2), 462-463.
27. Cai, Q., et al., Dilute solution routes to various controllable morphologies of MCM-41 silica with a basic medium. *Chemistry of Materials*, 2001, **13**(2), 258-263.
28. Fowler, C.E., et al., Nanoscale materials with mesostructured interiors. *Advanced Materials*, 2001, **13**(9), 649-652.
29. Nooney, R.I., et al., Synthesis of nanoscale mesoporous silica spheres with controlled particle size. *Chemistry of Materials*, 2002, **14**(11), 4721-4728.
30. Rathousky, J., et al., Synthesis and characterization of colloidal MCM-41. *Colloids and Surfaces a-Physicochemical and Engineering Aspects*, 2004, **241**(1-3), 81-86.
31. Moller, K., J. Kobler, and T. Bein, Colloidal suspensions of mercapto-functionalized nanosized mesoporous silica. *Journal of Materials Chemistry*, 2007, **17**(7), 624-631.
32. Moller, K., J. Kobler, and T. Bein, Colloidal suspensions of nanometer-sized mesoporous silica. *Advanced Functional Materials*, 2007, **17**(4), 605-612.
33. Kobler, J., K. Moller, and T. Bein, Colloidal suspensions of functionalized mesoporous silica nanoparticles. *Acs Nano*, 2008, **2**(4), 791-799.
34. Qiao, Z.A., et al., Synthesis of Mesoporous Silica Nanoparticles via Controlled Hydrolysis and Condensation of Silicon Alkoxide. *Chemistry of Materials*, 2009, **21**(16), 3823-3829.
35. Yokoi, T., et al., Synthesis of Mesoporous Silica Nanospheres Promoted by Basic Amino Acids and their Catalytic Application. *Chemistry of Materials*, 2010, **22**(13), 3900-3908.
36. Alfredsson, V. and M.W. Anderson, Structure of MCM-48 revealed by transmission electron microscopy. *Chemistry of Materials*, 1996, **8**(5), 1141-1146.
37. Chen, F.X., L.M. Huang, and Q.Z. Li, Synthesis of MCM-48 using mixed cationic-anionic surfactants as templates. *Chemistry of Materials*, 1997, **9**(12), 2685-+.
38. Popat, A., et al., Enzyme-Responsive Controlled Release of Covalently Bound Prodrug from Functional Mesoporous Silica Nanospheres. *Angewandte Chemie-International Edition*, 2012, **51**(50), 12486-12489.
39. Guillet-Nicolas, R., et al., pH-Responsive NutraceuticalMesoporous Silica Nanoconjugates with Enhanced Colloidal Stability. *Angewandte Chemie-International Edition*, 2013, **52**(8), 2318-2322.
40. Zhao, D.Y., et al., Triblock copolymer syntheses of mesoporous silica with periodic 50 to 300 angstrom pores. *Science*, 1998, **279**(5350), 548-552.

41. Ji, X.L., et al., Strategic synthesis of SBA-15 nanorods. *Chemical Communications*, 2008, (36), 4288-4290.
42. He, Q.J., et al., Bottom-up tailoring of nonionic surfactant-templated mesoporous silica nanomaterials by a novel composite liquid crystal templating mechanism. *Journal of Materials Chemistry*, 2009, **19**(36), 6498-6503.
43. Shen, S.D., et al., Synthesis of Nonspherical Mesoporous Silica Ellipsoids with Tunable Aspect Ratios for Magnetic Assisted Assembly and Gene Delivery. *Chemistry of Materials*, 2012, **24**(1), 230-235.
44. Huo, Q.S., et al., A new class of silica cross-linked micellar core-shell nanoparticles. *Journal of the American Chemical Society*, 2006, **128**(19), 6447-6453.
45. Tan, H., et al., Facile synthesis of hybrid silica nanocapsules by interfacial templating condensation and their application in fluorescence imaging. *Chemical Communications*, 2009, (41), 6240-6242.
46. Tan, H., et al., Synthesis of PEOlated Fe3O4@SiO2 Nanoparticles via Bioinspired Silification for Magnetic Resonance Imaging. *Advanced Functional Materials*, 2010, **20**(5), 722-731.
47. Wang, X.D., et al., Ultra-Small, Highly Stable, and Sensitive Dual Nanosensors for Imaging Intracellular Oxygen and pH in Cytosol. *Journal of the American Chemical Society*, 2012, **134**(41), 17011-17014.
48. Wang, X.D., R.J. Meier, and O.S. Wolfbeis, Fluorescent pH-Sensitive Nanoparticles in an Agarose Matrix for Imaging of Bacterial Growth and Metabolism. *Angewandte Chemie-International Edition*, 2013, **52**(1), 406-409.
49. Yuan, J.J., et al., Cross-linking of cationic block copolymer micelles by silica deposition. *Journal of the American Chemical Society*, 2007, **129**(6), 1717-1723.
50. Ma, K., H. Sai, and U. Wiesner, Ultrasmall Sub-10 nm Near-Infrared Fluorescent Mesoporous Silica Nanoparticles. *Journal of the American Chemical Society*, 2012, **134**(32), 13180-13183.
51. Chen, Y., H.-R. Chen, and J.-L. Shi, Construction of Homogenous/Heterogeneous Hollow Mesoporous Silica Nanostructures by Silica-Etching Chemistry: Principles, Synthesis, and Applications. *Accounts of Chemical Research*, 2013, DOI: 10.1021/ar400091e.
52. Slowing, II, et al., Mesoporous silica nanoparticles as controlled release drug delivery and gene transfection carriers. *Advanced Drug Delivery Reviews*, 2008, **60**(11), 1278-1288.
53. Wu, S.H., Y. Hung, and C.Y. Mou, Mesoporous silica nanoparticles as nanocarriers. *Chemical Communications*, 2011, **47**(36), 9972-9985.
54. Tsai, C.P., et al., Monoclonal antibody-functionalized mesoporous silica nanoparticles (MSN) for selective targeting breast cancer cells. *Journal of Materials Chemistry*, 2009, **19**(32), 5737-5743.

55. Lai, C.Y., et al., A mesoporous silica nanosphere-based carrier system with chemically removable CdS nanoparticle caps for stimuli-responsive controlled release of neurotransmitters and drug molecules. *Journal of the American Chemical Society*, 2003, **125**(15), 4451-4459.
56. Radu, D.R., et al., A polyamidoamine dendrimer-capped mesoporous silica nanosphere-based gene transfection reagent. *Journal of the American Chemical Society*, 2004, **126**(41), 13216-13217.
57. Tao, Z.M., et al., Mesoporosity and Functional Group Dependent Endocytosis and Cytotoxicity of Silica Nanomaterials. *Chemical Research in Toxicology*, 2009, **22**(11), 1869-1880.
58. Chung, T.H., et al., The effect of surface charge on the uptake and biological function of mesoporous silica nanoparticles 3T3-L1 cells and human mesenchymal stem cells. *Biomaterials*, 2007, **28**(19), 2959-2966.
59. Slowing, I., B.G. Trewyn, and V.S.Y. Lin, Effect of surface functionalization of MCM-41-type mesoporous silica nanoparticleson the endocytosis by human cancer cells. *Journal of the American Chemical Society*, 2006, **128**(46), 14792-14793.
60. Meng, H., et al., Aspect Ratio Determines the Quantity of Mesoporous Silica Nanoparticle Uptake by a Small GTPase-Dependent Macropinocytosis Mechanism. *Acs Nano*, 2011, **5**(6), 4434-4447.
61. Huang, X.L., et al., The effect of the shape of mesoporous silica nanoparticles on cellular uptake and cell function. *Biomaterials*, 2010, **31**(3), 438-448.
62. Trewyn, B.G., et al., Biocompatible mesoporous silica nanoparticles with different morphologies for animal cell membrane, penetration. *Chemical Engineering Journal*, 2008, **137**(1), 23-29.
63. Xing, X.L., et al., Uptake of silica-coated nanoparticles by HeLa cells. *Journal of Nanoscience and Nanotechnology*, 2005, **5**(10), 1688-1693.
64. Vallet-Regi, M., et al., A new property of MCM-41: Drug delivery system. *Chemistry of Materials*, 2001, **13**(2), 308-311.
65. Vallet-Regi, M., F. Balas, and D. Arcos, Mesoporous materials for drug delivery. *Angewandte Chemie-International Edition*, 2007, **46**(40), 7548-7558.
66. Yu, M.H., et al., Hyaluronic acid modified mesoporous silica nanoparticles for targeted drug delivery to CD44-overexpressing cancer cells. *Nanoscale*, 2013, **5**(1), 178-183.
67. Lu, J., et al., Mesoporous silica nanoparticles as a delivery system for hydrophobic anticancer drugs. *Small*, 2007, **3**(8), 1341-1346.

68. Jarnbhrunkar, S., et al., Stepwise Pore Size Reduction of Ordered Nanoporous Silica Materials at Angstrom Precision. *Journal of the American Chemical Society*, 2013, **135**(23), 8444-8447.
69. Mellaerts, R., et al., Increasing the oral bioavailability of the poorly water soluble drug itraconazole with ordered mesoporous silica. *European Journal of Pharmaceutics and Biopharmaceutics*, 2008, **69**(1), 223-230.
70. Pass, H.I., Photodynamic Therapy in Oncology - Mechanisms and Clinical Use. *Journal of the National Cancer Institute*, 1993, **85**(6), 443-456.
71. Pope, A.J., J.R.W. Masters, and A.J. Macrobert, The Photodynamic Effect of a Pulsed Dye-Laser on Human Bladder-Carcinoma Cells-Invitro. *Urological Research*, 1990, **18**(4), 267-270.
72. Perry, R.R., et al., Sensitivity of Different Human Lung-Cancer Histologies to Photodynamic Therapy. *Cancer Research*, 1990, **50**(14), 4272-4276.
73. Choudhary, S., K. Nouri, and M.L. Elsaie, Photodynamic therapy in dermatology: a review. *Lasers in Medical Science*, 2009, **24**(6), 971-980.
74. Castano, A.P., P. Mroz, and M.R. Hamblin, Photodynamic therapy and anti-tumour immunity. *Nature Reviews Cancer*, 2006, **6**(7), 535-545.
75. Konan, Y.N., R. Gurny, and E. Allemann, State of the art in the delivery of photosensitizers for photodynamic therapy. *Journal of Photochemistry and Photobiology B-Biology*, 2002, **66**(2), 89-106.
76. Wang, J. and J. Yi, Cancer cell killing via ROS To increase or decrease, that is the question. *Cancer Biology & Therapy*, 2008, **7**(12), 1875-1884.
77. Taquet, J.P., et al., Phthalocyanines covalently bound to biomolecules for a targeted photodynamic therapy. *Current Medicinal Chemistry*, 2007, **14**(15), 1673-1687.
78. Derycke, A.S.L. and P.A.M. de Witte, Liposomes for photodynamic therapy. *Advanced Drug Delivery Reviews*, 2004, **56**(1), 17-30.
79. Choi, Y., et al., Conjugation of a photosensitizer to an oligoarginine-based cell-penetrating peptide increases the efficacy of photodynamic therapy. *Chemmedchem*, 2006, **1**(4), 458-463.
80. van Nostrum, C.F., Delivery of photosensitizers in photodynamic therapy. *Advanced Drug Delivery Reviews*, 2004, **56**(1), 5-6.
81. Couleaud, P., et al., Silica-based nanoparticles for photodynamic therapy applications. *Nanoscale*, 2010, **2**(7), 1083-1095.
82. Wang, S.Z., et al., Nanomaterials and singlet oxygen photosensitizers: potential applications in photodynamic therapy. *Journal of Materials Chemistry*, 2004, **14**(4), 487-493.
83. Taillefer, J., et al., Preparation and characterization of pH-responsive polymeric micelles for the delivery of photosensitizing anticancer drugs. *Journal of Pharmaceutical Sciences*, 2000, **89**(1), 52-62.

84. Zhu, J., et al., Small Mesoporous Silica Nanoparticles as Carriers for Enhanced Photodynamic Therapy. *Chemistry-an Asian Journal*, 2011, **6**(9), 2332-2338.
85. Hoffman, A.S., The origins and evolution of "controlled" drug delivery systems. *Journal of Controlled Release*, 2008, **132**(3), 153-163.
86. Zhang, P., et al., Versatile photosensitizers for photodynamic therapy at infrared excitation. *Journal of the American Chemical Society*, 2007, **129**(15), 4526-+.
87. Brevet, D., et al., Mannose-targeted mesoporous silica nanoparticles for photodynamic therapy. *Chemical Communications*, 2009, (12), 1475-1477.
88. Cheng, S.H., et al., Tri-functionalization of mesoporous silica nanoparticles for comprehensive cancer theranostics-the trio of imaging, targeting and therapy. *Journal of Materials Chemistry*, 2010, **20**(29), 6149-6157.
89. Wang, F., et al., Synthesis of magnetic, fluorescent and mesoporous core-shell-structured nanoparticles for imaging, targeting and photodynamic therapy. *Journal of Materials Chemistry*, 2011, **21**(30), 11244-11252.
90. Roy, K., et al., Oral gene delivery with chitosan-DNA nanoparticles generates immunologic protection in a murine model of peanut allergy. *Nature Medicine*, 1999, **5**(4), 387-391.
91. Luo, D. and W.M. Saltzman, Synthetic DNA delivery systems. *Nature Biotechnology*, 2000, **18**(1), 33-37.
92. Lew, D., et al., CANCER GENE-THERAPY USING PLASMID DNA - PHARMACOKINETIC STUDY OF DNA FOLLOWING INJECTION IN MICE. *Human Gene Therapy*, 1995, **6**(5), 553-564.
93. Giacca, M. and S. Zacchigna, Virus-mediated gene delivery for human gene therapy. *Journal of Controlled Release*, 2012, **161**(2), 377-388.
94. Mintzer, M.A. and E.E. Simanek, Nonviral Vectors for Gene Delivery. *Chemical Reviews*, 2009, **109**(2), 259-302.
95. Crystal, R.G., TRANSFER OF GENES TO HUMANS - EARLY LESSONS AND OBSTACLES TO SUCCESS. *Science*, 1995, **270**(5235), 404-410.
96. Tripathy, S.K., et al., Immune responses to transgene-encoded proteins limit the stability of gene expression after injection of replication-defective adenovirus vectors. *Nature Medicine*, 1996, **2**(5), 545-550.
97. Bessis, N., F.J. GarciaCozar, and M.C. Boissier, Immune responses to gene therapy vectors: influence on vector function and effector mechanisms. *Gene Therapy*, 2004, **11**, S10-S17.
98. Boussif, O., et al., A VERSATILE VECTOR FOR GENE AND OLIGONUCLEOTIDE TRANSFER INTO CELLS IN CULTURE AND IN-VIVO - POLYETHYLENIMINE.

*Proceedings of the National Academy of Sciences of the United States of America*, 1995, **92**(16), 7297-7301.

99. Zhang, S.B., D.F. Zhi, and L. Huang, Lipid-based vectors for siRNA delivery. *Journal of Drug Targeting*, 2012, **20**(9), 724-735.
100. Hoyer, J. and I. Neundorf, Peptide Vectors for the Nonviral Delivery of Nucleic Acids. *Accounts of Chemical Research*, 2012, **45**(7), 1048-1056.
101. Chen, A.M., et al., Co-delivery of Doxorubicin and Bcl-2 siRNA by Mesoporous Silica Nanoparticles Enhances the Efficacy of Chemotherapy in Multidrug-Resistant Cancer Cells. *Small*, 2009, **5**(23), 2673-2677.
102. Kim, M.H., et al., Facile Synthesis of Monodispersed Mesoporous Silica Nanoparticles with Ultralarge Pores and Their Application in Gene Delivery. *Acs Nano*, 2011, **5**(5), 3568-3576.
103. Niu, Y., et al., Recent advances in the rational design of silica-based nanoparticles for gene therapy. *Therapeutic Delivery*, 2012, **3**(10), 1217-1237.
104. Sokolova, V. and M. Epple, Inorganic nanoparticles as carriers of nucleic acids into cells. *Angewandte Chemie-International Edition*, 2008, **47**(8), 1382-1395.
105. Kneuer, C., et al., Silica nanoparticles modified with aminosilanes as carriers for plasmid DNA. *International Journal of Pharmaceutics*, 2000, **196**(2), 257-261.
106. Kneuer, C., et al., A nonviral DNA delivery system based on surface modified silica-nanoparticles can efficiently transfect cells in vitro. *Bioconjugate Chemistry*, 2000, **11**(6), 926-932.
107. Luo, D. and W.M. Saltzman, Enhancement of transfection by physical concentration of DNA at the cell surface. *Nature Biotechnology*, 2000, **18**(8), 893-895.
108. Luo, D., et al., A self-assembled, modular DNA delivery system mediated by silica nanoparticles. *Journal of Controlled Release*, 2004, **95**(2), 333-341.
109. Bharali, D.J., et al., Organically modified silica nanoparticles: A nonviral vector for in vivo gene delivery and expression in the brain. *Proceedings of the National Academy of Sciences of the United States of America*, 2005, **102**(32), 11539-11544.
110. Na, H.K., et al., Efficient Functional Delivery of siRNA using Mesoporous Silica Nanoparticles with Ultralarge Pores. *Small*, 2012, **8**(11), 1752-1761.
111. Niu, Y., et al., Nanoparticles Mimicking Viral Surface Topography for Enhanced Cellular Delivery. *Advanced Materials*, 2013, **25**(43), 6233-6237.
112. Tan, S.J., et al., Engineering Nanocarriers for siRNA Delivery. *Small*, 2011, **7**(7), 841-856.
113. Kesharwani, P., V. Gajbhiye, and N.K. Jain, A review of nanocarriers for the delivery of small interfering RNA. *Biomaterials*, 2012, **33**(29), 7138-7150.

114. Ameres, S.L., J. Martinez, and R. Schroeder, Molecular Basis for Target RNA Recognition and Cleavage by Human RISC. *Cell*, **130**(1), 101-112.
115. Xia, T.A., et al., Polyethyleneimine Coating Enhances the Cellular Uptake of Mesoporous Silica Nanoparticles and Allows Safe Delivery of siRNA and DNA Constructs. *Acs Nano*, 2009, **3**(10), 3273-3286.
116. Hartono, S.B., et al., Poly-L-lysine Functionalized Large Pore Cubic Mesostructured Silica Nanoparticles as Biocompatible Carriers for Gene Delivery. *Acs Nano*, 2012, **6**(3), 2104-2117.
117. Yamaguchi, U., et al., Functional genome screen for therapeutic targets of osteosarcoma. *Cancer Science*, 2009, **100**(12), 2268-2274.
118. Li, X., et al., A mesoporous silica nanoparticle - PEI - Fusogenic peptide system for siRNA delivery in cancer therapy. *Biomaterials*, 2013, **34**(4), 1391-1401.
119. Mody, K.T., et al., Mesoporous silica nanoparticles as antigen carriers and adjuvants for vaccine delivery. *Nanoscale*, 2013, **5**(12), 5167-5179.
120. Gu, Z., et al., Tailoring nanocarriers for intracellular protein delivery. *Chemical Society Reviews*, 2011, **40**(7), 3638-3655.
121. Leader, B., Q.J. Baca, and D.E. Golan, Protein therapeutics: A summary and pharmacological classification. *Nature Reviews Drug Discovery*, 2008, **7**(1), 21-39.
122. Bareford, L.A. and P.W. Swaan, Endocytic mechanisms for targeted drug delivery. *Advanced Drug Delivery Reviews*, 2007, **59**(8), 748-758.
123. Slowing, II, B.G. Trewyn, and V.S.Y. Lin, Mesoporous silica nanoparticles for intracellular delivery of membrane-impermeable proteins. *Journal of the American Chemical Society*, 2007, **129**(28), 8845-8849.
124. Bale, S.S., et al., Nanoparticle-Mediated Cytoplasmic Delivery of Proteins To Target Cellular Machinery. *Acs Nano*, 2010, **4**(3), 1493-1500.
125. Lim, J.S., et al., Intracellular protein delivery by hollow mesoporous silica capsules with a large surface hole. *Nanotechnology*, 2012, **23**(8), 11.
126. Zelphati, O., et al., Intracellular Delivery of Proteins with a New Lipid-mediated Delivery System. *Journal of Biological Chemistry*, 2001, **276**(37), 35103-35110.
127. Dalkara, D., G. Zuber, and J.-P. Behr, Intracytoplasmic Delivery of Anionic Proteins[ast]. *Mol Ther*, 2004, **9**(6), 964-969.
128. Zassler, B., I. Blasig, and C. Humpel, Protein delivery of caspase-3 induces cell death in malignant C6 glioma, primary astrocytes and immortalized and primary brain capillary endothelial cells. *Journal of Neuro-Oncology*, 2005, **71**(2), 127-134.

129. Dalkara, D., C. Chandrashekhar, and G. Zuber, Intracellular protein delivery with a dimerizable amphiphile for improved complex stability and prolonged protein release in the cytoplasm of adherent cell lines. *Journal of Controlled Release*, 2006, **116**(3), 353-359.
130. Futami, J., et al., Intracellular delivery of proteins into mammalian living cells by polyethylenimine-cationization. *Journal of Bioscience and Bioengineering*, 2005, **99**(2), 95-103.
131. Murata, H., et al., Intracellular Delivery of Glutathione S-transferase-fused Proteins into Mammalian Cells by Polyethylenimine–Glutathione Conjugates. *Journal of Biochemistry*, 2008, **144**(4), 447-455.
132. Futami, J. and H. Yamada, Design of cytotoxic ribonucleases by cationization to enhance intracellular protein delivery. *Curr Pharm Biotechnol*, 2008, **9**(3), 180-4.
133. Murata, H., et al., Denatured and reversibly cationized p53 readily enters cells and simultaneously folds to the functional protein in the cells. *Biochemistry*, 2006, **45**(19), 6124-32.
134. Kitazoe, M., et al., Protein transduction assisted by polyethylenimine-cationized carrier proteins. *J Biochem*, 2005, **137**(6), 693-701.
135. Murata, H., et al., Transient cell proliferation with polyethylenimine-cationized N-terminal domain of simian virus 40 large T-antigen. *J Biosci Bioeng*, 2008, **105**(1), 34-8.
136. Lackey, C.A., et al., A biomimetic pH-responsive polymer directs endosomal release and intracellular delivery of an endocytosed antibody complex. *Bioconjug Chem*, 2002, **13**(5), 996-1001.
137. Jung, S., et al., Intracellular protein delivery by glucose-coated polymeric beads. *Chemical Communications*, 2009, (33), 5003-5005.
138. Hu, Y., et al., Cytosolic delivery of membrane-impermeable molecules in dendritic cells using pH-responsive core-shell nanoparticles. *Nano Lett*, 2007, **7**(10), 3056-64.
139. Ayame, H., N. Morimoto, and K. Akiyoshi, Self-assembled cationic nanogels for intracellular protein delivery. *Bioconjug Chem*, 2008, **19**(4), 882-90.
140. Nochi, T., et al., Nanogel antigenic protein-delivery system for adjuvant-free intranasal vaccines. *Nat Mater*, 2010, **9**(7), 572-8.
141. Murthy, N., et al., A macromolecular delivery vehicle for protein-based vaccines: acid-degradable protein-loaded microgels. *Proc Natl Acad Sci U S A*, 2003, **100**(9), 4995-5000.
142. Bachelder, E.M., et al., Acetal-derivatized dextran: an acid-responsive biodegradable material for therapeutic applications. *J Am Chem Soc*, 2008, **130**(32), 10494-5.
143. Bachelder, E.M., et al., Acid-degradable polyurethane particles for protein-based vaccines: biological evaluation and in vitro analysis of particle degradation products. *Mol Pharm*, 2008, **5**(5), 876-84.

144. Yan, M., et al., A novel intracellular protein delivery platform based on single-protein nanocapsules. *Nat Nanotechnol*, 2010, **5**(1), 48-53.
145. Gu, Z., et al., Protein nanocapsule weaved with enzymatically degradable polymeric network. *Nano Lett*, 2009, **9**(12), 4533-8.
146. Biswas, A., et al., Endoprotease-mediated intracellular protein delivery using nanocapsules. *ACS Nano*, 2011, **5**(2), 1385-94.
147. Lee, Y., et al., Charge-conversional polyionic complex micelles-efficient nanocarriers for protein delivery into cytoplasm. *Angew Chem Int Ed Engl*, 2009, **48**(29), 5309-12.
148. Akagi, T., et al., Protein direct delivery to dendritic cells using nanoparticles based on amphiphilic poly(amino acid) derivatives. *Biomaterials*, 2007, **28**(23), 3427-36.
149. Shi Kam, N.W., et al., Nanotube molecular transporters: internalization of carbon nanotube-protein conjugates into Mammalian cells. *J Am Chem Soc*, 2004, **126**(22), 6850-1.
150. Kam, N.W., Z. Liu, and H. Dai, Carbon nanotubes as intracellular transporters for proteins and DNA: an investigation of the uptake mechanism and pathway. *Angew Chem Int Ed Engl*, 2006, **45**(4), 577-81.
151. Kam, N.W. and H. Dai, Carbon nanotubes as intracellular protein transporters: generality and biological functionality. *J Am Chem Soc*, 2005, **127**(16), 6021-6.
152. Medintz, I.L., et al., Intracellular delivery of quantum dot-protein cargos mediated by cell penetrating peptides. *Bioconjug Chem*, 2008, **19**(9), 1785-95.
153. Ghosh, P., et al., Intracellular delivery of a membrane-impermeable enzyme in active form using functionalized gold nanoparticles. *J Am Chem Soc*, 2010, **132**(8), 2642-5.
154. Chorny, M., et al., Endothelial delivery of antioxidant enzymes loaded into non-polymeric magnetic nanoparticles. *J Control Release*, 2010, **146**(1), 144-51.
155. Abbing, A., et al., Efficient intracellular delivery of a protein and a low molecular weight substance via recombinant polyomavirus-like particles. *J Biol Chem*, 2004, **279**(26), 27410-21.
156. Cronican, J.J., et al., Potent delivery of functional proteins into Mammalian cells in vitro and in vivo using a supercharged protein. *ACS Chem Biol*, 2010, **5**(8), 747-52.
157. Lim, Y.T., et al., Simultaneous intracellular delivery of targeting antibodies and functional nanoparticles with engineered protein G system. *Biomaterials*, 2009, **30**(6), 1197-204.
158. Mercuri, L.P., et al., Ordered mesoporous silica SBA-15: a new effective adjuvant to induce antibody response. *Small*, 2006, **2**(2), 254-6.
159. Carvalho, L.V., et al., Immunological parameters related to the adjuvant effect of the ordered mesoporous silica SBA-15. *Vaccine*, 2010, **28**(50), 7829-36.

160. Wang, T., et al., Enhanced mucosal and systemic immune responses obtained by porous silica nanoparticles used as an oral vaccine adjuvant: effect of silica architecture on immunological properties. *Int J Pharm*, 2012, **436**(1-2), 351-8.
161. Guo, H.C., et al., Immunization of mice by hollow mesoporous silica nanoparticles as carriers of porcine circovirus type 2 ORF2 protein. *Virol J*, 2012, **9**, 108.
162. Mahony, D., et al., Mesoporous Silica Nanoparticles Act as a Self-Adjuvant for Ovalbumin Model Antigen in Mice. *Small*, 2013, **9**(18), 3138-3146.
163. Zhao, Y., et al., Mesoporous silica nanoparticle-based double drug delivery system for glucose-responsive controlled release of insulin and cyclic AMP. *J Am Chem Soc*, 2009, **131**(24), 8398-400.
164. Ashley, C.E., et al., The targeted delivery of multicomponent cargos to cancer cells by nanoporous particle-supported lipid bilayers. *Nat Mater*, 2011, **10**(5), 389-397.
165. Bhattarai, S.R., et al., Enhanced Gene and siRNA Delivery by Polycation-Modified Mesoporous Silica Nanoparticles Loaded with Chloroquine. *Pharmaceutical Research*, 2010, **27**(12), 2556-2568.
166. Zhu, Y.F., et al., Rattle-Type Fe3O4@SiO2 Hollow Mesoporous Spheres as Carriers for Drug Delivery. *Small*, 2010, **6**(3), 471-478.
167. Meng, H., et al., Engineered design of mesoporous silica nanoparticles to deliver doxorubicin and P-glycoprotein siRNA to overcome drug resistance in a cancer cell line. *ACS Nano*, 2010, **4**(8), 4539-50.
168. Meng, H., et al., Codelivery of an optimal drug/siRNA combination using mesoporous silica nanoparticles to overcome drug resistance in breast cancer in vitro and in vivo. *ACS Nano*, 2013, **7**(2), 994-1005.
169. Zhu, Y.F., et al., Hollow Mesoporous Silica/Poly(L-lysine) Particles for Codelivery of Drug and Gene with Enzyme-Triggered Release Property. *Journal of Physical Chemistry C*, 2011, **115**(28), 13630-13636.
170. Platt, V.M. and F.C. Szoka, Anticancer therapeutics: Targeting macromolecules and nanocarriers to hyaluronan or CD44, a hyaluronan receptor. *Molecular Pharmaceutics*, 2008, **5**(4), 474-486.
171. Zhu, Y.F., Y. Fang, and S. Kaskel, Folate-Conjugated Fe(3)O(4)@SiO(2) Hollow Mesoporous Spheres for Targeted Anticancer Drug Delivery. *Journal of Physical Chemistry C*, 2010, **114**(39), 16382-16388.
172. Lu, J., et al., Biocompatibility, Biodistribution, and Drug-Delivery Efficiency of Mesoporous Silica Nanoparticles for Cancer Therapy in Animals. *Small*, 2010, **6**(16), 1794-1805.

173. Fang, I.J., et al., Ligand Conformation Dictates Membrane and Endosomal Trafficking of Arginine-Glycine-Aspartate (RGD)-Functionalized Mesoporous Silica Nanoparticles. *Chemistry-a European Journal*, 2012, **18**(25), 7787-7792.
174. Knudson, C.B. and W. Knudson, HYALURONAN-BINDING PROTEINS IN DEVELOPMENT, TISSUE HOMEOSTASIS, AND DISEASE. *Faseb Journal*, 1993, **7**(13), 1233-1241.
175. Hua, Q., C.B. Knudson, and W. Knudson, INTERNALIZATION OF HYALURONAN BY CHONDROCYTES OCCURS VIA RECEPTOR-MEDIATED ENDOCYTOSIS. *Journal of Cell Science*, 1993, **106**, 365-375.
176. Rivkin, I., et al., Paclitaxel-clusters coated with hyaluronan as selective tumor-targeted nanovectors. *Biomaterials*, 2010, **31**(27), 7106-7114.
177. Lee, M.Y., et al., Target-Specific Gene Silencing of Layer-by-Layer Assembled Gold-Cysteamine/siRNA/PEI/HA Nanocomplex. *Acs Nano*, 2011, **5**(8), 6138-6147.
178. Lee, H., C.H. Ahn, and T.G. Park, Poly[lactic-co-(glycolic acid)]-Grafted Hyaluronic Acid Copolymer Micelle Nanoparticles for Target-Specific Delivery of Doxorubicin. *Macromolecular Bioscience*, 2009, **9**(4), 336-342.
179. Ma, M., et al., Hyaluronic acid-conjugated mesoporous silica nanoparticles: excellent colloidal dispersity in physiological fluids and targeting efficacy. *Journal of Materials Chemistry*, 2012, **22**(12), 5615-5621.
180. Pampaloni, F., E.G. Reynaud, and E.H.K. Stelzer, The third dimension bridges the gap between cell culture and live tissue. *Nature Reviews Molecular Cell Biology*, 2007, **8**(10), 839-845.
181. Boxberger, H.-J. and T.F. Meyer, A new method for the 3-D in vitro growth of human RT112bladder carcinoma cells using the alginate culture technique. *Biology of the Cell*, 1994, **82**(2-3), 109-119.
182. Pampaloni, F., et al., Madin–Darby canine kidney cells are increased in aerobic glycolysis when cultured on flat and stiff collagen-coated surfaces rather than in physiological 3-D cultures. *PROTEOMICS*, 2010, **10**(19), 3394-3413.
183. Loessner, D., et al., Bioengineered 3D platform to explore cell–ECM interactions and drug resistance of epithelial ovarian cancer cells. *Biomaterials*, 2010, **31**(32), 8494-8506.
184. Li, C.L., et al., Survival advantages of multicellular spheroids vs. monolayers of HepG2 cells in vitro. *Oncol Rep*, 2008, **20**(6), 1465-71.
185. Elliott, N.T. and F. Yuan, A Review of Three-Dimensional In Vitro Tissue Models for Drug Discovery and Transport Studies. *Journal of Pharmaceutical Sciences*, 2011, **100**(1), 59-74.

186. Kunz-Schughart, L.A., et al., The use of 3-D cultures for high-throughput screening: The multicellular spheroid model. *Journal of Biomolecular Screening*, 2004, **9**(4), 273-285.
187. Achilli, T.M., J. Meyer, and J.R. Morgan, Advances in the formation, use and understanding of multi-cellular spheroids. *Expert Opinion on Biological Therapy*, 2012, **12**(10), 1347-1360.
188. Wang, C.Y., et al., Three-dimensional in vitro cancer models: a short review. *Biofabrication*, 2014, **6**(2).
189. Hoffman, R.M., THE 3-DIMENSIONAL QUESTION - CAN CLINICALLY RELEVANT TUMOR DRUG-RESISTANCE BE MEASURED IN-VITRO. *Cancer and Metastasis Reviews*, 1994, **13**(2), 169-173.
190. Miller, B.E., F.R. Miller, and G.H. Heppner, ASSESSING TUMOR DRUG SENSITIVITY BY A NEW INVITRO ASSAY WHICH PRESERVES TUMOR HETEROGENEITY AND SUBPOPULATION INTERACTIONS. *Journal of Cellular Physiology*, 1984, 105-116.
191. McMillin, D.W., J.M. Negri, and C.S. Mitsiades, The role of tumour-stromal interactions in modifying drug response: challenges and opportunities. *Nature Reviews Drug Discovery*, 2013, **12**(3), 217-228.
192. Hida, K., et al., Tumour endothelial cells acquire drug resistance in a tumour microenvironment. *Journal of Biochemistry*, 2013, **153**(3), 243-249.
193. Jiang, X.Y., et al., Integrin-facilitated transcytosis for enhanced penetration of advanced gliomas by poly(trimethylene carbonate)-based nanoparticles encapsulating paclitaxel. *Biomaterials*, 2013, **34**(12), 2969-2979.
194. Basuki, J.S., et al., Using Fluorescence Lifetime Imaging Microscopy to Monitor Theranostic Nanoparticle Uptake and Intracellular Doxorubicin Release. *Acs Nano*, 2013, **7**(11), 10175-10189.
195. Mankoff, D.A., A definition of molecular imaging. *Journal of Nuclear Medicine*, 2007, **48**(6), 18N-+.
196. Ng, K.K., J.F. Lovell, and G. Zheng, Lipoprotein-inspired nanoparticles for cancer theranostics. *Acc Chem Res*, 2011, **44**(10), 1105-13.
197. Gao, X., et al., In vivo cancer targeting and imaging with semiconductor quantum dots. *Nat Biotechnol*, 2004, **22**(8), 969-76.
198. Sperling, R.A., et al., Biological applications of gold nanoparticles. *Chem Soc Rev*, 2008, **37**(9), 1896-908.
199. Wang, K., et al., Functionalized Silica Nanoparticles: A Platform for Fluorescence Imaging at the Cell and Small Animal Levels. *Accounts of Chemical Research*, 2013, **46**(7), 1367-1376.
200. Wang, F., et al., Highly Luminescent Organosilane-Functionalized Carbon Dots. *Advanced Functional Materials*, 2011, **21**(6), 1027-1031.

201. Korzeniowska, B., et al., Silica nanoparticles for cell imaging and intracellular sensing. *Nanotechnology*, 2013, **24**(44), 20.
202. Van Blaaderen, A. and A. Vrij, Synthesis and characterization of colloidal dispersions of fluorescent, monodisperse silica spheres. *Langmuir*, 1992, **8**(12), 2921-2931.
203. Burns, A., H. Ow, and U. Wiesner, Fluorescent core-shell silica nanoparticles: towards "Lab on a Particle" architectures for nanobiotechnology. *Chemical Society Reviews*, 2006, **35**(11), 1028-1042.
204. Burns, A.A., et al., Fluorescent Silica Nanoparticles with Efficient Urinary Excretion for Nanomedicine. *Nano Letters*, 2009, **9**(1), 442-448.
205. Osseo-Asare, K. and F.J. Arriagada, Preparation of SiO2 nanoparticles in a non-ionic reverse micellar system. *Colloids and Surfaces*, 1990, **50**(0), 321-339.
206. Arriagada, F.J. and K. Osseo-Asare, Synthesis of Nanosize Silica in a Nonionic Water-in-Oil Microemulsion: Effects of the Water/Surfactant Molar Ratio and Ammonia Concentration. *Journal of Colloid and Interface Science*, 1999, **211**(2), 210-220.
207. Arriagada, F.J. and K. Osseo-Asare, Controlled hydrolysis of tetraethoxysilane in a nonionic water-in-oil microemulsion: a statistical model of silica nucleation. *Colloids and Surfaces A: Physicochemical and Engineering Aspects*, 1999, **154**(3), 311-326.
208. Santra, S., et al., Conjugation of biomolecules with luminophore-doped silica nanoparticles for photostable biomarkers. *Anal Chem*, 2001, **73**(20), 4988-93.
209. Santra, S., et al., Development of novel dye-doped silica nanoparticles for biomarker application. *Journal of Biomedical Optics*, 2001, **6**(2), 160-166.
210. Zhao, X., R.P. Bagwe, and W. Tan, Development of Organic-Dye-Doped Silica Nanoparticles in a Reverse Microemulsion. *Advanced Materials*, 2004, **16**(2), 173-176.
211. Tan, T.T., et al., Size Control, Shape Evolution, and Silica Coating of Near-Infrared-Emitting PbSe Quantum Dots. *Chemistry of Materials*, 2007, **19**(13), 3112-3117.
212. Shi, S.X., F. Chen, and W.B. Cai, Biomedical applications of functionalized hollow mesoporous silica nanoparticles: focusing on molecular imaging. *Nanomedicine*, 2013, **8**(12), 2027-2039.
213. Peng, J., et al., Identification of live liver cancer cells in a mixed cell system using galactose-conjugated fluorescent nanoparticles. *Talanta*, 2007, **71**(2), 833-840.
214. He, X., et al., FSiNPs mediated improved double immunofluorescence staining for gastric cancer cells imaging. *Talanta*, 2008, **76**(5), 1199-206.
215. Shi, H., et al., Nanoparticle-based biocompatible and long-life marker for lysosome labeling and tracking. *Anal Chem*, 2010, **82**(6), 2213-20.

216. He, X., et al., In vivo study of biodistribution and urinary excretion of surface-modified silica nanoparticles. *Anal Chem*, 2008, **80**(24), 9597-603.
217. Xu, H., et al., A Real-Time Ratiometric Method for the Determination of Molecular Oxygen Inside Living Cells Using Sol−Gel-Based Spherical Optical Nanosensors with Applications to Rat C6 Glioma. *Analytical Chemistry*, 2001, **73**(17), 4124-4133.
218. Koo, Y.-E.L., et al., Real-Time Measurements of Dissolved Oxygen Inside Live Cells by Organically Modified Silicate Fluorescent Nanosensors. *Analytical Chemistry*, 2004, **76**(9), 2498-2505.
219. Burns, A., et al., Core/Shell Fluorescent Silica Nanoparticles for Chemical Sensing: Towards Single-Particle Laboratories. *Small*, 2006, **2**(6), 723-726.
220. Hidalgo, G., et al., Functional Tomographic Fluorescence Imaging of pH Microenvironments in Microbial Biofilms by Use of Silica Nanoparticle Sensors. *Applied and Environmental Microbiology*, 2009, **75**(23), 7426-7435.
221. Hendrick, E., et al., Cellulose Acetate Fibers with Fluorescing Nanoparticles for Anti-counterfeiting and pH-sensing Applications. *Journal of Engineered Fibers and Fabrics*, 2010, **5**(1), 21-30.
222. Chen, Y.-P., et al., Surface charge effect in intracellular localization of mesoporous silica nanoparticles as probed by fluorescent ratiometric pH imaging. *RSC Advances*, 2012, **2**(3), 968-973.
223. Edwards, J.C. and C.R. Kahl, Chloride channels of intracellular membranes. *FEBS Letters*, 2010, **584**(10), 2102-2111.
224. Cheng, S.H., et al., Defective intracellular transport and processing of CFTR is the molecular basis of most cystic fibrosis. *Cell*, 1990, **63**(4), 827-34.
225. Koch, M.C., et al., The skeletal muscle chloride channel in dominant and recessive human myotonia. *Science*, 1992, **257**(5071), 797-800.
226. Lloyd, S.E., et al., A common molecular basis for three inherited kidney stone diseases. *Nature*, 1996, **379**(6564), 445-9.
227. Baù, L., et al., A Cell-Penetrating Ratiometric Nanoprobe for Intracellular Chloride. *Organic Letters*, 2012, **14**(12), 2984-2987.

# *Chapter 3*

# Methodology

This chapter summarizes the strategies utilized in the whole PhD project, including synthetic methods for silica based nanoparticles and the techniques for material characterizations and biological evaluations.

## 3.1 Material synthesis

Three types of silica based nanoparticles (SiNPs) have been fabricated by controlling the nucleation and growth in the sol-gel process of silica precursors and its assembly process with structure directing agents (surfactants).[1] (1) Mesoporous silica nanoparticles are obtained by utilizing cationic cetyltrimethylammonium bromide (CTAB) or cetyltrimethylammonium chloride (CTAC) as the templating surfactant, tetraethyl orthosilicate (TEOS) as the silica source and alkali or sodium acetate (NaAc) as a catalyst. During the sol-gel process, the silicate oligomers react with surfactants to form mesostructured silica nanoparticles. The complete condensation or pore diameter adjustment can be achieved by further hydrothermal treatment in an autoclave. After removing the surfactants by calcination process, the mesoporous silica nanoparticles are obtained. (2) Mono-dispersed hybrid SiNPs with desired functional groups are synthesized using the tri-block copolymer $EO_{106}PO_{70}EO_{106}$ [Pluronic F127, EO refers to poly(ethylene oxide), PO refers to poly(propylene oxide)] as the template, mixture of tetramethyl orthosilane (TMOS) and dimethoxydimethylsilane (DMDMS) [or diethoxy(3-glycidyloxypropyl)methylsilane (DGMS)] as silica sources, phosphate-citrate buffer solution as a catalyst. (3) Mono-dispersed solid SiNPs are synthesized by the hydrolysis and condensation of silicon alkoxides in a mixture of alcohol and water using ammonia as a catalyst. The silica particle diameter can be adjusted from 125 nm to 570 nm, simply by varying the catalyst and precursor concentrations.

### 3.1.1 Synthesis of monodisperse mesoporous silica nanospheres (MMSNs)

In a typical synthesis, 53.4 g of water, 6.24 g of CTAC (25wt% solution), and 0.3 g of $NaAc{\cdot}3H_2O$ were mixed and stirred in a silicon oil bath at different temperatures (T = 40, 50, 60, 80 °C) for 2 h. Then 4.35 mL of TEOS was added into the above mixture dropwise within 3 min under steady stirring at about 400RPM. The solution was stirred for 24 h before cooling to room temperature in silicon oil bath, then centrifuged at 20,000 RPM for 10 min to isolate the products from the

suspension. After washing with water for 3 times, the final products were obtained by calcination at 650 °C for 5 h, and denoted as MMSNs-T. For example, MMSNs-40 stands for the material prepared at a synthesis temperature of 40 °C.

In the preparation of MMSNs-60, the pH of mother solutions in three independent batches after 24 h reaction since the addition of TEOS was adjusted to 10.0, 11.5, and 12.0, respectively, by adding 2M NaOH solution. The mixture was then hydrothermally treated at 130 °C in an autoclave for 3 days. After that, MMSNs were collected by centrifugation at 20,000 RPM, and washed by water for three times. The final products were obtained by the same calcination process as described above, denoted MMSNs-60-B10.0, MMSNs-60-B11.5, MMSNs-60-B12.0, respectively (B refers to hydrothermal treatment under basic conditions).

The as-synthesized product MMSNs-60 after washing was put into an autoclave containing 0.01 M HCl (pH~2), and then hydrothermally treated at different temperatures (100, 130, 160 °C) for 24 h. After hydrothermal treatment, the samples were centrifuged and washed with water for 2 times. The final products were obtained by calcination at 650 °C for 5 h, and denoted MMSNs-60-A100, MMSNs-60-A130 and MMSNs-60-A160 (the latter number refers to the hydrothermal treatment temperature and A denotes hydrothermal treatment under acidic conditions).

### 3.1.2 Synthesis and functionization of MCM-41

MCM-41 was synthesized according to an approach reported in our previous work[2] with slight modifications. In a typical synthesis, 1.0 g of CTAB was dissolved in 480 g of deionized water under stirring at room temperature followed by the addition of 3.5 mL of NaOH (2 M). The temperature of the solution was raised and kept at 80 ℃. To this solution, 6.7 mL of TEOS was added. The mixture was continuously stirred for additional 2 h. The resultant products were collected by filtration and dried at room temperature. The templates were removed by calcination at 550 ℃ for 5 h.

Synthesis of hyaluronic acid (HA) conjugated MCM-41 (HA-MCM-41): First, 1.5 g of calcined MCM-41 was added to 60 mL of toluene and stirred for 6h before adding 1.0 mL of (3-aminopropyl)triethoxysilane (APTES). After stirring at room temperature for 24 h, the particles were extensively washed with toluene and dried in fume-hood at room temperature (denoted $NH_2$-MCM-41). Next, in order to graft HA, the carboxyl group of HA was activated with N-hydroxysuccinimide (NHS), using N-(3-dimethylaminopropyl)-N-ethylcarbodiimide hydrochloride (EDC) as coupling agents. The activated carboxyl group of HA then combined with the amine end of $NH_2$-MCM-41. Specifically, 1 g of the prepared $NH_2$-MCM-41 powder was dispersed in 100mL

of deionized water. In another reaction vessel, 20mL of aqueous solution containing NHS (0.37g) and EDC (0.2g) were mixed with 60mL of HA (113 mg) deionized water solution. Finally the two solutions were mixed and the pH was adjusted to 9.0 using triethylamine as a catalyst. The mixture was stirred at 38 °C overnight. The HA modified MCM-41 (HA-MCM-41) were obtained by centrifugation, washing three times by deionized water, and freeze-drying using Christ Alpha 2-4LDplus (John Morris Scientific).

FITC modification of MCM-41 and HA-MCM-41: Not all amino groups in $NH_2$-MCM-41 reacted with HA, thus the remaining free $NH_2$ moieties were utilized for labeling with FITC. The functional group of FITC, thiocyanate, is highly aminoreactive, therefore the prepared $NH_2$-MCM-41 and HA-MCM-41 can be conjugated with FITC. Specifically, 20mg of HA-MCM-41s or $NH_2$-MCM-41 powders were put in 3mL of deionized water, and mixed with 5mL of FITC ethanol solution (0.3mg/ml). After stirring in dark for 6 h, the nanoparticles were centrifuged and washed with ethanol for three times until the supernatants were colorless.

### 3.1.3 Synthesis and functionization of ultra-small hybrid silica spheres (UHSS)

Synthesis of UHSS and Epoxy-UHSS: For the synthesis of mono-dispersed ultra-small hybrid silica spheres (UHSS), 0.5g of F127 was dissolved in 30 ml of phosphate-citrate buffer solution (pH=4.6, 46.6 μM $Na_2HPO_4$, 26.7 μM HAc) under stirring at room temperature. Then mixed silica sources of TMOS (0.6 ml) and DMDMS (0.59 ml) was added into the surfactant homogeneous solution under stirring. The reaction was continued at room temperature for 3 days. Afterwards, the clear solution was transferred into a dialysis membrane tube (Sigma-Aldrich, molecular weight cut off 14,000) and dialyzed in 1L of D.I. water for 3 days, to completely remove the salts, methanol and ethanol (resulted from the hydrolysis of TMOS and DMDMS). The D.I. water was refreshed twice per day. Finally the UHSS particles were stored in D.I. water for further use.

For the synthesis of Epoxy-UHSS, the mixture of 0.8ml TMOS and 0.75ml DGMS was utilized as the silica source and the other synthesis procedures are the same as described above.

Synthesis of RBTC-UHSS: For the synthesis Rhodamine B isothiocyanate (RBTC) modified UHSS (RBTC-UHSS), 4 mg of RBTC and 44 μl of (3-aminopropyl)trimethoxysilane (APTMS) was dissolved in 1ml of ethanol and stirred at room temperature overnight in dark. Afterwards, the mixture was added into 30 ml of phosphate-citrate buffer solution (pH=4.6, 46.6 μM $Na_2HPO_4$, 26.7 μM HAc) containing 0.5g of F127 under stirring at room temperature. After stirring for 2 minutes, the mixed silica sources of TMOS (0.6 ml) and DMDMS (0.59 ml) was added into above solution and stirred for 3 days. Afterwards, the clear red colour solution was transferred into a dialysis membrane tube and dialyzed in 50% (v/v) ethanol D.I. water solution for 2 days in dark, to

completely remove the remaining RBTC, then dialyzed in D.I. water for another 3 days. The 50% ethanol solution or D.I. water was refreshed twice per day. Finally the RBTC-UHSS sample was stored in D.I. water for further use.

Synthesis of PEI-UHSS: The conjugation process of polyethylenimine (PEI, M.W. 1800) on Epoxy-UHSS was performed using a modified approach reported in a previously reported study.[3] Typically, 4 ml of Epoxy-UHSS solution prepared in the last step was added in to 8 ml of 2.5mg/ml PEI solution in carbonate buffer ($NaHCO_3$-$Na_2CO_3$, Ct [$CO_3^{2-}$] = 50 mM, pH= 9.5) at room temperature, and the mixture stirred for 8 hours. After that, the final product was dialyzed in 1L of deionized water for 3 days using dialysis membrane tube, to complete remove the salts and free PEI molecules. The sample was denoted as PEI-UHSS.

### 3.1.4 Synthesis of amine modified monodisperse silica Stöber spheres ($NH_2$-SS)

Mono-dispersed silica spheres were prepared by the modified Stöber method.[4] In a typical experiment, two solutions were rapidly mixed together. The first solution was the mixture of TEOS and ethanol (EtOH), and the second solution was the mixture of 28 wt% ammonia, deionized water, and EtOH. The first solution was added to the second solution under stirring. The resulting mixture was further stirred for certain time. Finally, silica spheres were separated from the suspension by centrifugation and washed with ethanol twice, and further washed with water twice. The detailed chemical amount and synthesis condition are listed in Table 3.1. After drying in a 50°C oven overnight, 0.1g of silica spheres were suspended in 40 ml of toluene. Then the mixture was refluxed in a three-neck flask under stirring at 110 °C for 2h, followed by adding 93.6μl of APTES. After stirring for further 20h, the suspension was centrifuged and washed with ethanol and water. The final products were collected by drying process at 50°C overnight, and denoted as $NH_2$-SSx, where 'x' stands for the particle diameters of amine modified Stöber spheres ($NH_2$-SS) estimated by TEM analysis. For example, $NH_2$-SS125 represents amine modified Stöber spheres with a diameter of 125 nm.

**Table 3.1** Experimental conditions for the synthesis of silica Stöber spheres with different diameters

| Sample | The first solution | | The second solution | | | T (°C) | *t* (h) |
|---|---|---|---|---|---|---|---|
| | EtOH (ml) | TEOS (ml) | $H_2O$ (ml) | EtOH (ml) | $NH_4OH$ (ml) | | |
| **$NH_2$-SS125** | 22.2 | 2.8 | 6.8 | 17.6 | 0.700 | 25 | 13 |
| **$NH_2$-SS230** | 22.2 | 4.5 | 6.8 | 17.6 | 0.700 | 25 | 4.5 |
| **$NH_2$-SS330** | 45.5 | 5.0 | 16.25 | 24.75 | 9.0 | 25 | 2 |
| **$NH_2$-SS440** | 45.5 | 5.0 | 16.25 | 24.75 | 9.0 | 22 | 2 |
| **$NH_2$-SS570** | 45.5 | 5.0 | 16.25 | 24.75 | 9.0 | 15 | 2 |

*T*: reaction temperature; *t*: reaction time

## 3.2 Characterization

### 3.2.1 X-ray Diffraction (XRD)

Small-angle XRD patterns of MMSNs and MCM-41 were recorded on a German Bruker D4 X-ray Diffractometer (40 kV, 30 mA) with Ni-filtered Cu Kα ($\lambda$ = 0.15418 nm) Radiation at a scanning rate of 0.2˚ $min^{-1}$ from 0.5˚ to 5.0˚.

The interplanar spacing is calculated based on the following Bragg equation:

$2d_{hkl} \sin\theta = n\lambda$

where $d_{hkl}$ is the interplanar distance between a set of parallel planes described by the Miller indices (*hkl*) (nm), λ is the wavelength of Cu Kα ray (nm), θ is the angle of incident beam (˚), and n is integer determined by a given order.[5]

### 3.2.2 Transmission Electron Microscopy (TEM)

Transmission electron microscopy (TEM) images of the samples synthesized in this thesis were obtained with a JEOL 1010 operated at 100 kV, JEOL 2100 at 200 kV or FEI Tecnai F30 operated at 300 kV. The samples for TEM measurements were prepared by dispersing the powder samples in ethanol, after which they were dispersed and dried on carbon film on a Cu grid.

### 3.2.3 Scanning Electron Microscopy (SEM)

The morphologies of the samples MMNSs were observed using a JEOL6610 scanning electron microscope (SEM) operated at 5 kV. Samples were dispersed on a carbon tape with Pt/carbon coating.

### 3.2.4 Nitrogen sorption

Nitrogen adsorption/desorption isotherms were measured at 77 K by using a Micromeritics ASAP Tristar II 3020 system. The samples were degassed at 473 K overnight on a vacuum line. The pore size distribution curve was derived from the adsorption branch of the isotherm using the Barrett–Joyner–Halanda (BJH) method. The Brunauer–Emmett–Teller (BET) method was utilized to calculate the specific surface areas. The total pore volume was calculated from the amount adsorbed at a maximum relative pressure ($P/P_0$) of 0.99.

### 3.2.5 Attenuated Total Reflectance (ATR)-Fourier transform infrared (FTIR) spectroscopy

Attenuated total reflectance (ATR) is a sampling technique used in conjunction with infrared spectroscopy which enables samples to be analyzed directly in solid or liquid state without further treatement. An attenuated total reflection accessory is to measure the changes occurring in a totally internally reflected infrared beam when the beam contacts with loaded sample (indicated in Figure 3.1).[6] An infrared beam passes through an optically dense crystal with a high refractive index at a certain angle. This internal reflectance generates an evanescent wave which extends into the sample on the surface of crystal. The penetration depth of this evanescent wave beyond crystal surface is only 0.5-5 μm. Consequently, this technology requires a good contact between the sample and the crystal surface. The evanescent wave will be attenuated or altered in the regions of the infrared spectrum where the sample absorbs specific energy. The attenuated energy from each evanescent wave is passed back to the IR beam, then to the detector in the IR spectrometer. Finally, an infrared spectrum is generated by this system.

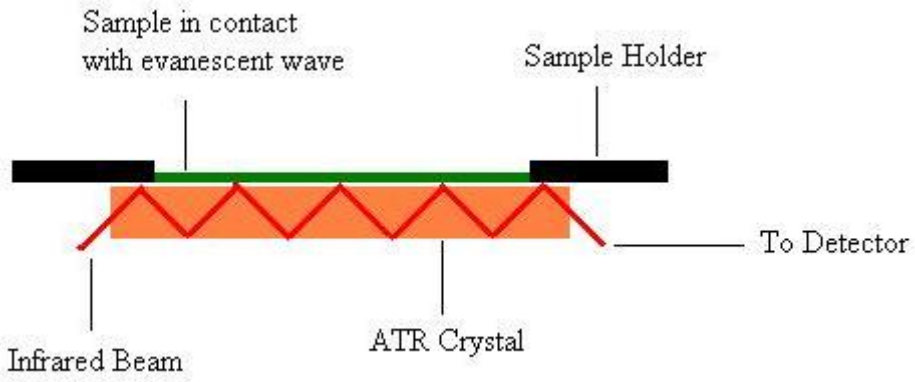


**Figure 3.1** Schematic diagram of a multiple refection ATR system.[6]

In this thesis, the ATR-FTIR was utilized to monitor the silica species in situ as the function of reaction time during the MMSNs synthesis process. The liquid samples were simply dropped onto the crystal to obtain optimal contact. The surface functional groups of MSNs, $NH_2$-MSNs and HA-MSNs in Chapter 7 were also investigated by ATR-FTIR. The silica nanoparticles were pressed down on the crystal to obtain good contact between samples and crystal. The ATR-FTIR spectra were collected with ThermoNicolet Nexus 6700 FTIR spectrometer equipped with Diamond ATR Crystal. For each spectrum, 32 scans were collected at a resolution of 4 $cm^{-1}$ over the range 400–3400 $cm^{-1}$.

### 3.2.6 Elemental Analysis (EA)

In this project, elemental analysis was conducted on a CHNS-O Analyzer (Flash EA1112 Series, Thermo Electron Corporation) to determine the percentages of carbon (C), hydrogen (H) and nitrogen (N) in the samples of F127, Epoxy-UHSS and PEI-UHSS. In this analysis, several

milligrams of the sample is loaded in a tin capsule, and then dropped into a quartz tube at 1020 ℃ with constant helium flow (carrier gas). Before the sample drops into the combustion tube, the stream is enriched with a measured amount of high purity oxygen to achieve a strong oxidizing environment which guarantees almost complete oxidation even of thermally resistant substances. The combustion gas mixture is driven through an oxidation catalyst ($WO_3$) zone, then through a subsequent copper zone which reduces nitrogen oxides and sulphuric anhydride ($SO_3$). The resulting four components of the combustion mixture are detected by a Thermal Conductivity detector in the sequence $N_2$, $CO_2$, $H_2O$ and $SO_2$. In case of oxygen which is analyzed separately, the sample undergoes immediate pyrolysis in a Helium stream which ensures quantitative conversion of organic oxygen into carbon monoxide separated on a GC column packed with molecular sieves.

### 3.2.7 Dynamic light scattering (DLS)

Dynamic light scattering (DLS) is a non-invasive, well-established technique for particle size characterization of proteins, polymers and colloidal dispersions.[7] The Brownian motion of particles or molecules in suspension causes laser light to be scattered at different intensities. Analysis of these intensity fluctuations yields the velocity of the Brownian motion and hence the particle size using the Stokes-Einstein relationship. The hydrodynamic sizes of particle samples in this PhD project were measured using DLS measurements on a Malvern NanoZS zetasizer at 25 °C in ethanol or water solutions. The DLS data in this thesis were presented as number based data, because the number based distribution is biased to small particles synthesized in this thesis.

### 3.2.8 Zeta potential analysis

Zeta potential analysis is a technique for measuring of the surface charge of nanoparticles in solution (colloids). Nanoparticles with a surface charge attract a thin layer of ions with opposite charge to the nanoparticle surface. This double layer of ions travels with the nanoparticle as it diffuses throughout the solution. The electric potential at the boundary of the double layer is defined as the Zeta potential of the nanoparticles. In this thesis, zeta potential measurements were carried out on a Malvern NanoZS zetasizer at 25°C in distilled water or PBS solution.

### 3.2.9 Inductively Coupled Plasma-Optical Emission Spectroscopy (ICP-OES)

Inductively coupled plasma-optical emission spectrometry (ICP-OES) is an analytical technique used for the detection of trace metals.[8] It uses the inductively coupled plasma to produce excited atoms and ions that emit electromagnetic radiation at wavelengths characteristic of a particular element.[9] The intensity of this emission is indicative of the concentration of the element within the sample. In this PhD project, ICP-OES technology was utilized to quantify the silicon concentrations

in cells after following treatment of cells. The HEK-293T cells were incubated with the $NH_2$-SS/plasmid DNA complexes for 4 hours, then washed with PBS and harvested with trypsin. After washing with PBS and centrifugation, cell lysis buffer was added to allow dissolution of cells under sonication process. The supernatants (containing cell components) were discarded after centrifugation, and the precipitates were washed with PBS, followed by drying at 50°C overnight. Aqueous NaOH solution was then added to dissolve the silica nanoparticles. The silicon concentrations in the final solutions were measured by ICP-OES with a Vista-PRO instrument (Varian Inc, Australia). The mass of silicon in per cell was calculated based on the ICP-OES results and cell numbers by counting.

### 3.2.10 $^{13}$C nuclear magnetic resonance (NMR) spectroscopy

$^{13}$C NMR spectroscopy was utilized to determine the organic groups in functional SiNPs (Chapter 5-7 in this thesis). $^{13}$C NMR spectra of SiNPs were measured by solid state Bruker Avance III spectrometer with 7T (300MHz for 1H) magnet, Zirconia rotor, 4mm, rotated at 7 kHz.

## 3.3 Biological techniques

### 3.3.1 CellTiter-Blue assay

The CellTiter-Blue® Cell Viability Assay is a simple and inexpensive approach that uses an optimized reagent containing resazurin.[10] The reagent is added directly to the cultured cells at a recommended ratio of 20 µl of reagent to 100 µl of culture medium. The plates are then incubated at 37 ℃ for 1-4 hours to allow viable cells to convert resazurin to the fluorescent resorufin product. The conversion of resazurin to fluorescent resorufin is proportional to the number of metabolically active, viable cells. The signal is recorded using a standard plate reader. Because different cell types have different abilities to reduce resazurin, optimizing the length of incubation with the CellTiter-Blue® Reagent can improve assay sensitivity. In this PhD project, the optimized incubation time after adding the regent was found to be 4 hours for the cytotoxicity of human colon cancer HCT-116 cells in Chapter 7). HCT-116 cells were maintained in Dulbecco's Modified Eagle Medium (DMEM) supplemented with fetal calf serum (10%, Sigma, MO), L-glutamine (2%), penicillin (1%), streptomycin (1%) in 5% $CO_2$ at 37 ℃. The medium was routinely changed every 2 days and the cells were separated by trypsinization before reaching confluency. In CellTiter-Blue assay, HCT-116 cells were seeded in a 96-well plate at a density of $2\times10^4$ cells/well and cultured in 5% $CO_2$ at 37 ℃ for 24 h. Then, free Dox, Dox-HA-MSNs, Dox-MSNs were added to the cells in DMEM medium at a different Dox concentration of 0.25, 0.125, 0.05µg/mL respectively, and the cells were further incubated in 5% $CO_2$ at 37 ℃ for 24 h. Subsequently, 15 µL of CellTiter-Blue

Reagent was added to each well, shaked for 10 seconds and then incubated at 37 °C for 4 h. Then fluorescence readings were measured with excitation wavelength at 560 nm and emission wavelength of 590 nm using a microplate reader (SpectraMax M5, Bio-Strategy, Ltd). The cells incubated in the absence of particles were used as the control.

### 3.3.2 CellTiter-Glo assay

The CellTiter-Glo® Luminescent Cell Viability Assay is a homogeneous method to determine the number of viable cells. This method utilizes the luciferase reaction to measure the amount of ATP of viable cells. The amount of ATP in cells correlates with cell viability. The CellTiter-Glo® Reagent does three things after addition into cells. It lyses cell membranes to release ATP, inhibits endogenous ATPases, and provides luciferin, luciferase and other reagents necessary to measure ATP. The unique properties of a proprietary stable luciferase mutant enabled a robust, single-addition reagent. The signal can be recorded with a luminometer, and generally has a half-life of five hours. The CellTiter-Glo® Assay is very sensitive and can detect as few as 10 cells. The luminescent signal can be detected as soon as 10 minutes after adding reagent, or several hours later, providing flexibility for batch processing of plates. In Chapter 6, this agent was utilized to evaluate the cell viability of osteosarcoma cell line (KHOS cells) after treated with functional siRNA. KHOS cells were maintained in DMEM supplemented with fetal calf serum (10%), L-glutamine (2%), penicillin (1%), streptomycin (1%) in 5% $CO_2$ at 37 ℃. The medium was routinely changed every 2 days and the cells were separated by trypsinization before reaching confluency. To test the functional siRNA delivery, KHOS cells were seeded in a 96-well cell culture plate with a density of $5\times10^3$ cells/well in 100 μL of complete DMEM medium, and grew for 24h before treatment. The complexes of PLK1-siRNA/PEI-UHSS, and PLK1-siRNA/PEI were formed after mixing and incubating in PBS solution at 4°C overnight, then were added to cells. After further incubation at 37°C for 48h, the silencing effect or cell viability was determined by Cell-Titer Glo method according to the protocol provided by the manufacturer. The cells incubated in the equal amount of PBS solution were used as the control.

### 3.3.3 3-[4,5-dimethylthiazol-2-yl]-2,5-diphenyl tetrazolium bromide (MTT) assay

MTT assay is a simple, accurate and reproducible method to determine the activity of viable cultured cells.[11] The MTT chemical is dissolved in a physiological buffer solution, then added to cells in culture, usually at a final concentration of 0.2-0.5mg/ml. The plates are incubated for 1 to 4 hours. Viable cells with active metabolism can convert MTT into a purple colored formazan with an absorbance maximum near 570 nm. The quantity of formazan (presumably directly proportional to the number of viable cells) is measured by recording changes in absorbance at 570 nm using a plate

reader. In this thesis, MTT assay was used to evaluate the cell viability of human embryonic kidney 293T (HEK 293T) cells treated with $NH_2$-SS samples and human malignant brain tumour U87MG cells treated with UHSS. HEK 293T and U87MG cells were maintained in DMEM supplemented with fetal bovine serum, L-glutamine (2%), penicillin (1%), and streptomycin (1%) in a 5% $CO_2$ incubator at 37 ℃. The medium was routinely changed every 2 days and the cells were separated by trypsinization before reaching confluency. The cytotoxicity of $NH_2$-SS with different sizes in HEK 293T cells and UHSS in U87MG cells was evaluated as follows. HEK 293T or U87MG cells were seeded in a 96-well cell culture plate with a density of $5\times10^3$ cells/well. After incubation for 24 h, the cells were added with different concentrations of $NH_2$-SS or UHSS PBS solution. After 48 h, the media was removed, and 100 μl of fresh DMEM medium was added each well, followed by addition of 10 μL of MTT solution (5mg/ml). Plate was then incubated in the culture oven for 4 h before adding 100 μl of DMSO to each well for 0.5h. Then absorbance readings were measured at wavelength of 540 nm using a Synergy HT microplate reader, and background absorbance of media was subtracted. The cells incubated in the absence of particles were used as the control.

### 3.3.4 Confocal Laser Scanning Microscopy (CLSM)

Laser scanning confocal microscopy (CLSM) has become an invaluable tool for a wide range of investigations in the biological and medical sciences for imaging thin optical sections in living and fixed specimens ranging in thickness up to 100 micrometers. It is a technique to obtain high-resolution optical images with selected depth.[12] CLSM is normally equipped with 3-5 laser systems with a precise control in wavelength and excitation intensity. These microscopes coupled with photomultipliers are capable of detecting fluorescence emission ranging from 400 to 750 nm. In this thesis, all the confocal images of fixed cells were observed under a confocal microscope (LSM Zeiss 710).

### 3.3.5 Flow Cytometry

Flow cytometry is a laser-based, biophysical technology for cell counting, cell sorting, biomarker detection and protein engineering, by suspending cells in a stream of fluid and passing them by an electronic detection apparatus.[13] It allows simultaneous multiparametric analysis of the physical and chemical characteristics of up to thousands of particles per second. Modern instruments usually have multiple lasers and fluorescence detectors, which can precisely identify and quantify target population by their fluorescent markers inside/on the surface of cells. In this thesis, the intracellular uptake of fluorescent silica nanoparticles and GFP transfected cells was quantified using a FACSAria Cell Sorter (Becton Dickinson BD).

### 3.3.6 Nanodrop 1000

The Thermo Scientific NanoDrop 1000 is a full-spectrum UV-Vis spectrophotometer used to quantify nucleic acids, proteins, fluorescent dyes and other compounds.[14] This instrument enables highly accurate analyses of 1-2 μl samples with remarkable reproducibility. The concentration of plasmid DNA amplified in *E. coil* was determined by the Nanodrop 1000 based on the absence at 260 nm. Also the quantification of adsorption amount of plasmid DNA was determined by the concentrations before and after incubation with $NH_2$-SS samples measured on Nanodrop 1000. In Chapter 6, Nanodrop 1000 was utilized to evaluate the RNase A protection ability of PEI-UHSS. 10μg of PEI-UHSS and 50 pmol of PLK1-siRNA were mixed in RNase free water and incubated at room temperature for 30 minutes. Afterwards, 1μg of RNase A was added into the complex solution with a total volume of 10μl, then the absorbance at 260 nm ($Abs_{260}$) was measured by a Nanodrop 1000 with an incubation time of 0 and 30 minutes at room temperature. For the free PLK1-siRNA control, 50pmol of PLK1-siRNA and 1μg of RNase A were mixed in RNase free water with a total volume of 10μl, then the value of $Abs_{260}$ was measured by Nanodrop after incubation at room temperature for 0 and 30 minutes. The increase percentage of $Abs_{260}$ = [$Abs_{260}$ (30 minutes) - $Abs_{260}$ (0 minute)]/$Abs_{260}$ (0 minute).

### 3.3.7 Agarose gel electrophoresis

Agarose gel electrophoresis is a technique used to separate and purify macromolecules (proteins and nucleic acids) with a different size, charge or conformation. It is one of most widely-used techniques in biochemistry and molecular biology.[15] When charged molecules are placed in an electric field, they migrate toward the positive or negative pole opposite to their charge. For example, nucleic acids have a consistent negative charge imparted by their phosphate backbone; they migrate toward the anode when the electric field is applied to a nucleic acid loaded agarose gel in running buffer. In this PhD project, this technology was utilized to test the binding capacity of $NH_2$-SS samples toward plasmid DNA in Chapter 8. The $NH_2$-SS/pDNA complex was prepared by the following process. Briefly, 0.5 μg of pDNA was incubated with varying amounts of $NH_2$-SS at 4 °C in 10 μl of PBS overnight. 2 μl of 6×DNA loading buffer was added into each mixture, and then the mixtures were loaded on a 1% agarose gel containing 1× SYBR Safe. The electrophoresis was carried out at 80V for 1h in TAE buffer, and the bands were visualized on a UV trans-illuminator (Bio-Rad reader).

### 3.3.8 Western-blot analysis

Western blot is an important method to separate and identify proteins.[16] A mixture of proteins extracted from cells is separated based on molecular weight by gel electrophoresis. These results are transferred to a membrane producing a band for each protein. The membrane is then incubated with

antibodies specific to the protein of interest. The unbound antibody is washed off leaving only the bound antibody to the protein of interest, which are detected by developing the film. The antibodies only bind to the specific protein, thus only one band can be visible. The thickness of the band represents the amount of present protein. Specific protein knock down efficiency induced siRNA delivered by PEI-UHSS was evaluated by western blot analysis in Chapter 6. KHOS or HCT-116 cells were seeded in 6-well plates at a seeding density of $1\times10^5$ cells/well. After 24 h incubation, the complexes of siRNA/PEI-UHSS, control siRNA/PEI-UHSS, siRNA/PEI, siRNA/Oligofectamine, and control siRNA/Oligofectamine along with siRNA only were added into the cells. After further incubation at 37°C for 48h, cells were washed with PBS, collected and lysed in cold RIPA buffer (50 mM Tris, pH 8.0, 150 mM NaCl, 1 mM EGTA, and 0.25% sodium deoxycholate). The lysates were incubated for 15 min at 4°C and removed by centrifugation at 12,000 rpm for 15 min. Supernatants were analysed for protein concentrations using the Bradford assay (Bio-Rad, Hercules, USA). Equal amount (10 mg) of protein was subjected to electrophoresis on a polyacrylamide gel containing SDS and then transferred to nitrocellulose membranes. Afterwards, the membranes were blocked with tris-buffered saline (TBS) containing 5% (w/v) skimmed milk. After being washed with TBS, the membranes were incubated 4°C overnight at with the first antibody (PLK1 Rabbit mAb, survivin Rabbit mAb and β-Tubulin Rabbit mAb) diluted in TBS. After washing, the membranes were incubated at room temperature for 1 h with the second antibody (Anti-rabbit IgG, HRP-linked Antibody). Bands were detected by were visualized on a Bio-Rad reader.

### 3.3.9 U87MG spheroids culture

Compared to traditional two-dimensional (2D) cell models (monolayers), three-dimensional (3D) culture models more closely mimic the cell-to-cell and cell-to-extracellular matrix (ECM) interactions as well as the topography found in an *in vivo* tumour environment. Spheroids are the most widely used 3D tumour models. In the absence of attachment substrates or scaffold, cells aggregate and compact to form tightly bounded cellular spheres with a size from 50 μm to 1mm. The penetration ability of UHSS was evaluated in glioblastoma U87MG spheroids in Chapter 5. The glioblastoma spheroids were developed using the modified liquid overlay technique.[17] In brief, exponentially growing monolayer cells were trypsinized and $3\times10^5$ cells were seeded in 1% agar-coated 6-well plates containing Dulbecco modified Eagle medium (GIBCO) supplemented with FCS (10%), L-glutamine (2%), nonessential amino acids (4%) and penicillin/streptomycin (2%). The plates were incubated in a tissue culture incubator at 37 ℃ (95% humidity, 95% air, and 5% $CO_2$) and cultured for 3-5 days, until spheroids were formed. Half of the culture medium was replaced with fresh medium twice a week. After round spheroids were formed and those with 200

μm diameter were collected, transferred and culture in agarose-coated (0.1%) glass cover slip in 6-well plates with same culture medium.

### 3.4 References


1. Wu, S.H., Y. Hung, and C.Y. Mou, Mesoporous silica nanoparticles as nanocarriers. *Chemical Communications*, 2011, **47**(36), 9972-9985.
2. Yang, S., et al., On the origin of helical mesostructures. *Journal of the American Chemical Society*, 2006, **128**(32), 10460-10466.
3. Hartono, S.B., et al., Poly-L-lysine Functionalized Large Pore Cubic Mesostructured Silica Nanoparticles as Biocompatible Carriers for Gene Delivery. *Acs Nano*, 2012, **6**(3), 2104-2117.
4. Stober, W., A. Fink, and E. Bohn, CONTROLLED GROWTH OF MONODISPERSE SILICA SPHERES IN MICRON SIZE RANGE. *Journal of Colloid and Interface Science*, 1968, **26**(1), 62-&.
5. Weidenthaler, C., Pitfalls in the characterization of nanoporous and nanosized materials. *Nanoscale*, 2011, **3**(3), 792-810.
6. FT-IR Spectroscopy-Attenuated Total Reflectance (ATR), Perkin Elmer Life and Analytical Sciences, 2005, http://web.archive.org/web/20070216065646/http://las.perkinelmer.com/content/TechnicalInfo/TCH_FTIRATR.pdf.
7. Pecora, R., Dynamic light scattering measurement of nanometer particles in liquids. *Journal of Nanoparticle Research*, 2000, **2**(2), 123-131.
8. Scott, R.H., et al., INDUCTIVELY COUPLED PLASMA-OPTICAL EMISSION ANALYTICAL SPECTROMETRY - COMPACT FACILITY FOR TRACE ANALYSIS OF SOLUTIONS. *Analytical Chemistry*, 1974, **46**(1), 75-81.
9. Stef ánsson, A., I. Gunnarsson, and N. Giroud, New methods for the direct determination of dissolved inorganic, organic and total carbon in natural waters by Reagent-Free™ Ion Chromatography and inductively coupled plasma atomic emission spectrometry. *Analytica Chimica Acta*, 2007, **582**(1), 69-74.
10. Bigl, K., et al., Comparison of results of the CellTiter Blue, the tetrazolium (3- 4,5-dimethylthioazol-2-y1 -2,5-diphenyl tetrazolium bromide), and the lactate dehydrogenase assay applied in brain cells after exposure to advanced glycation endproducts. *Toxicology in Vitro*, 2007, **21**(5), 962-971.
11. Mosmann, T., RAPID COLORIMETRIC ASSAY FOR CELLULAR GROWTH AND SURVIVAL - APPLICATION TO PROLIFERATION AND CYTO-TOXICITY ASSAYS. *Journal of Immunological Methods*, 1983, **65**(1-2), 55-63.

12. Minsky, M., MEMOIR ON INVENTING THE CONFOCAL SCANNING MICROSCOPE. *Scanning*, 1988, **10**(4), 128-138.
13. Gray, J.W., FLOW CYTOMETRY AND CELL-CYCLE ANALYSIS. *Radiation Research*, 1978, **74**(3), 460-460.
14. Radpour, R., et al., Simultaneous Isolation of DNA, RNA, and Proteins for Genetic, Epigenetic, Transcriptomic, and Proteomic Analysis. *Journal of Proteome Research*, 2009, **8**(11), 5264-5274.
15. Johansso.Bg, AGAROSE-GEL ELECTROPHORESIS. *Scandinavian Journal of Clinical & Laboratory Investigation*, 1972, **29**, 7-19.
16. Mahmood, T. and P.C. Yang, Western blot: technique, theory, and trouble shooting. *N Am J Med Sci*, 2012, **4**(9), 429-34.
17. Carlsson, J. and J.M. Yuhas, LIQUID-OVERLAY CULTURE OF CELLULAR SPHEROIDS. *Recent Results in Cancer Research*, 1984, **95**, 1-23.

# Chapter 4

# A Simple Approach to Prepare Monodisperse Mesoporous Silica Nanospheres with Adjustable Sizes

This chapter reported a new and facile approach to prepare monodisperse mesoporous silica nanospheres (MMSNs) with controlled particle sizes (50-100 nm) and pore diameters (2.8-4.0 nm). In this approach, MMSNs were synthesized simply in a sodium acetate solution without adding any other alkali or alcohol additives. After further investigations, a spherical micelle templating mechanism was proposed to explain the formation of MMSNs in this work, which is different from that of traditional highly ordered mesoporous silica nanoparticles (MCM-41). MMSNs developed in this part are expected to have potential applications in drug/gene delivery and cell imaging.

Journal of Colloid and Interface Science 376 (2012) 67–75

Contents lists available at SciVerse ScienceDirect

Journal of Colloid and Interface Science

www.elsevier.com/locate/jcis

# A simple approach to prepare monodisperse mesoporous silica nanospheres with adjustable sizes

Meihua Yu [a], Liang Zhou [a], Jun Zhang [a], Pei Yuan [a], Peter Thorn [b], Wenyi Gu [a], Chengzhong Yu [a,*]

[a] ARC Centre of Excellence for Functional Nanomaterials and Australian Institute for Bioengineering and Nanotechnology, The University of Queensland, Brisbane, QLD 4072, Australia
[b] School of Biomedical Sciences, The University of Queensland, Brisbane, QLD 4072, Australia

ARTICLE INFO

*Article history:*
Received 8 November 2011
Accepted 3 March 2012
Available online 12 March 2012

*Keywords:*
Mesoporous silica
Monodisperse spheres
Self-assembly
Hydrothermal treatment
Formation mechanism

ABSTRACT

A new and facile approach has been developed to prepare monodisperse mesoporous silica nanospheres (MMSNs) with controlled particle sizes and pore structures. In our approach, MMSNs were synthesized simply in a sodium acetate solution without adding any other alkali or alcohol additives. MMSNs have a spherical shape and uniform particle sizes, which can be adjusted from 50 to 110 nm by increasing the reaction temperature from 40 to 80 °C. By performing a subsequent hydrothermal treatment (HT) under basic condition (pH = ~11.5) at 130 °C, the mesoporous pore volume and surface area can be enhanced, while keeping the mono-dispersion characteristics and the mesopore size almost unchanged. The pore sizes of MMSNs can be adjusted from 2.8 to 4.0 nm under acidic solutions by changing the HT temperature from 100 to 130 °C. The formation process of MMSNs has been investigated by transmission electron microscopy (TEM) and attenuated total reflection Fourier transform infrared (ATR-FTIR) techniques. A spherical micelle templating mechanism is proposed to explain the formation of MMSNs in our system, which is different from that of traditional highly ordered mesoporous silica nanoparticles (MCM-41).



## 1. Introduction

Since the discovery of mesoporous silica M41S in the early 1990s [1,2], mesoporous materials prepared by the organic–inorganic self-assembly approach have been widely studied [3–5]. Due to their high surface area, tunable pore sizes and easy surface modification, functional mesoporous materials have attracted enormous interest in various applications, such as catalysis, adsorption, separation, chromatography, and bioscience [6–10]. Recently, the synthesis of mesoporous silica nanoparticles (MSNs) with controllable particle size has received much attention with emerging applications in biomedicine including cell imaging [11,12], diagnosis and bioanalysis [13], and drug/gene/protein delivery [14–17]. Compared with conventional mesoporous silica materials with relatively large sizes, nanometer-sized MSNs (<100 nm) with high dispersity possess advantage in cell endocytosis process [18,19], which is vital to achieve high efficiency in bio-applications.

Several approaches have been developed to prepare MSNs with particle sizes in the range of hundreds of nanometers to tens of micrometers [20–24]. Biomedical applications require MSNs with diameters less than 100 nm, and these have been prepared by different methods. For example, Imai and co-workers have successfully synthesized well-ordered MSNs with diameters of 20–50 nm using a binary surfactant templating approach [22], however, aggregation and polydispersity of MSNs are limitations for their biological application. To resolve the aggregation issue, uniform and highly ordered MSNs were prepared utilizing highly diluted surfactant solutions [25–28], however this method leads to low yields and difficulty in product collection. Bein et al. reported a high-yield approach to synthesize colloidal mesoporous silica (CMS) particles with controlled size and various functional groups [29–31], where triethanolamine (TEA) was used as a base and also a complexing agent for silicate species to limit the growth and aggregation of particles.

Huo and his coworkers further investigated the formation of CMS, and proposed a new mechanism to understand the growth mechanism of CMS [32]. It is proposed that the rate of hydrolysis and condensation of silicon alkoxide at different pH controls the size of CMS, and the addition of additive agents with certain acid–base buffer capacity is necessary to obtain homogeneous CMS [32]. Recently, Tatsumi and his co-workers have reported a new method to obtain discrete mesoporous silica nanospheres, which is based on the emulsion system containing silica source, surfactant, water and basic amino acid [33]. This approach is organic solvent free, but specific basic amino acids are needed, which are expensive and may limit the application of MSNs prepared by this method.

* Corresponding author. Fax: +61 7 334 63973.
*E-mail address:* c.yu@uq.edu.au (C. Yu).

0021-9797/$ - see front matter © 2012 Elsevier Inc. All rights reserved.
http://dx.doi.org/10.1016/j.jcis.2012.03.014

More recently, a new family of high surface area silica nanospheres KCC-1 has been discovered [34], which has an unprecedented fibrous morphology, different from the conventional mesoporous silica materials. Well-defined and ordered fibers expand from the center of KCC-1 particles and distribute uniformly in all directions. This new type of nano-sized dispersed silica spheres shows promising applications in silica-supported catalysts and bio-applications, because the accessibility of active sites can be increased significantly. However, the synthesis method is rather complicated, and requires organic solvents and microwave reactors.

Here we present a new and economic approach to prepare monodisperse mesoporous silica nanospheres (MMSNs). The synthesis involves only three chemicals, a surfactant template, a silica source, and a sodium acetate solution, avoiding the use of any other organic solvents, organic or inorganic alkali as additives. The diameters of MMSNs can be adjusted from 50 to 110 nm by increasing reaction temperature. By investigating the reaction process, we propose a spherical micelle templating mechanism to explain the formation of MMSNs, which is different from that of traditional MCM-41 type mesoporous materials [35], and the new type porous silica material of KCC-1 [34].

## 2. Experimental section

### 2.1. Chemicals

Tetraethoxysilane (TEOS, 98%), an aqueous solution of cetyltrimethylammonium chloride (CTAC, $C_{16}H_{33}N$-$(CH_3)_3Cl$, 25 wt.% in water), and sodium acetate trihydrate ($NaAc{\cdot}3H_2O$) were purchased from Sigma–Aldrich. Sodium hydroxide (NaOH) and hydrochloric acid (HCl, 32%) were received from ChemSupply and Ajax Finochem Pty Ltd., respectively. Distilled water was used in the experiments.

### 2.2. Synthesis of MMSNs with controllable particle sizes

In a typical synthesis, 53.4 g of water, 6.24 g of CTAC (25 wt.% solution), and 0.3 g of $NaAc{\cdot}3H_2O$ were mixed and stirred in a silicon oil bath at different temperature ($T$ = 40, 50, 60, 80 °C) for 2 h. Then 4.35 mL of TEOS was added into the above mixture dropwise within 3 min under steadily stirring at about 400 RPM. The solution was stirred for 24 h before cooling to room temperature in silicon oil bath, then centrifuged at 20,000 RPM for 10 min to isolate the products from the suspension. After washing with water for 3 times, the final products were obtained by calcination at 650 °C for 5 h, and denoted MMSNs-T. For example, MMSNs-40 stands for the material prepared at a synthesis temperature of 40 °C.

### 2.3. Hydrothermal treatment

#### 2.3.1. Under basic solution

In the preparation of MMSNs-60, the pH of mother solutions in three independent batches after 24 h reaction since the addition of TEOS was adjusted to 10.0, 11.5, and 12.0, respectively, by adding 2 M NaOH solution. The mixture was then hydrothermally treated at 130 °C in an autoclave for 3 days. After that, MMSNs were collected by centrifugation at 20,000 RPM, and washed by water for three times. The final products were obtained by the same calcination process as described above, denoted MMSNs-60-B10.0, MMSNs-60-B11.5, MMSNs-60-B12.0, respectively (B refers to hydrothermal treatment under basic conditions).

#### 2.3.2. Under acidic solution

The as-synthesized product MMSNs-60 after washing was put into an autoclave containing 0.01 M HCl (pH ~ 2), and then hydrothermally treated at different temperatures (100, 130, 160 °C) for 24 h. After hydrothermal treatment, the samples were centrifuged and washed with water for 2 times. The final products were obtained by calcination at 650 °C for 5 h, and denoted MMSNs-60-A100, MMSNs-60-A130 and MMSNs-60-A160 (the latter number refers to the hydrothermal treatment temperature and A denotes hydrothermal treatment under acidic conditions).

### 2.4. ATR-FTIR study

Attenuated total reflection Fourier transform infrared (ATR-FTIR) spectra were collected to monitor the hydrolysis and condensation of TEOS in our reaction system. A series of ATR-FTIR spectra were collected at different reaction times (10, 20, 30 min, 1, 2, 3, 4, 24 h). The time was recorded from the addition of TEOS into the solution. Each spectrum was obtained against a background measured under diamond crystal.

### 2.5. Characterization

X-ray diffraction (XRD) patterns were recorded on a German Bruker D4 X-ray diffractometer with Ni-filtered Cu Kα Radiation. The morphologies of the samples were observed using a JEOL6610 scanning electron microscope (SEM) operated at 5 kV. Transmission electron microscopy (TEM) images were obtained with a JEOL 1010 operated at 100 kV, or JEOL 2100 at 200 kV. For TEM measurements, the samples were prepared by dispersing the powder samples in ethanol, after which they were dispersed and dried on carbon film on a Cu grid. Nitrogen adsorption/desorption isotherms were measured at 77 K by using a Micromeritics ASAP Tristar II 3020 system. The samples were degassed at 453 K overnight on a vacuum line. The Brunauer–Emmett–Teller (BET) method was utilized to calculate the specific surface areas. The pore volume and pore size distribution curves were derived from the adsorption branches of the isotherms using the Barrett–Joyner–Halanda (BJH) method. The total pore volume was calculated from the amount adsorbed at a maximum relative pressure ($P/P_0$). Dynamic light scattering (DLS) studies were carried out on a Malvern NanoZS zetasizer at 25 °C in ethanol solution. The in situ ATR-FTIR spectra were collected with ThermoNicolet Nexus 6700 FTIR spectrometer equipped with Diamond ATR Crystal. For each spectrum, 32 scans were collected at a resolution of 4 $cm^{-1}$ over the range 400–3400 $cm^{-1}$. The pH value of the reaction mixture was measured with a labCHEM-pH meter.

## 3. Results and discussion

### 3.1. Synthesis of MMSNs with controllable particle sizes

MMSNs with controlled sizes were prepared by adjusting reaction temperature from 40 to 80 °C while keeping the other parameters unchanged. TEM images indicate that all calcined MMSNs synthesized by our method are well-dispersed (Fig. 1). Irregularly patterned mesopores with diameters of ~2–3 nm within the spherical particles can be observed in all TEM images in Fig. 1. The average particle size of MMSNs calculated by measuring ~100 silica spheres is 53, 65, 77 and 110 nm for samples prepared at 40, 50, 60 and 80 °C (Fig. 1a–d), respectively, indicating that the particle size increases with the increase of reaction temperature. It is noted that for MMSNs obtained at relatively lower temperatures of 40 and 50 °C, few irregularly shaped particles are observed (indicated by arrows in Fig. 1a–b), in which disordered mesopores (~2–3 nm in diameter) are also observed. However, the sample prepared at 60 °C shows nearly perfect spherical morphology with a uniform size (Fig. 1c). When the reaction temperature is further

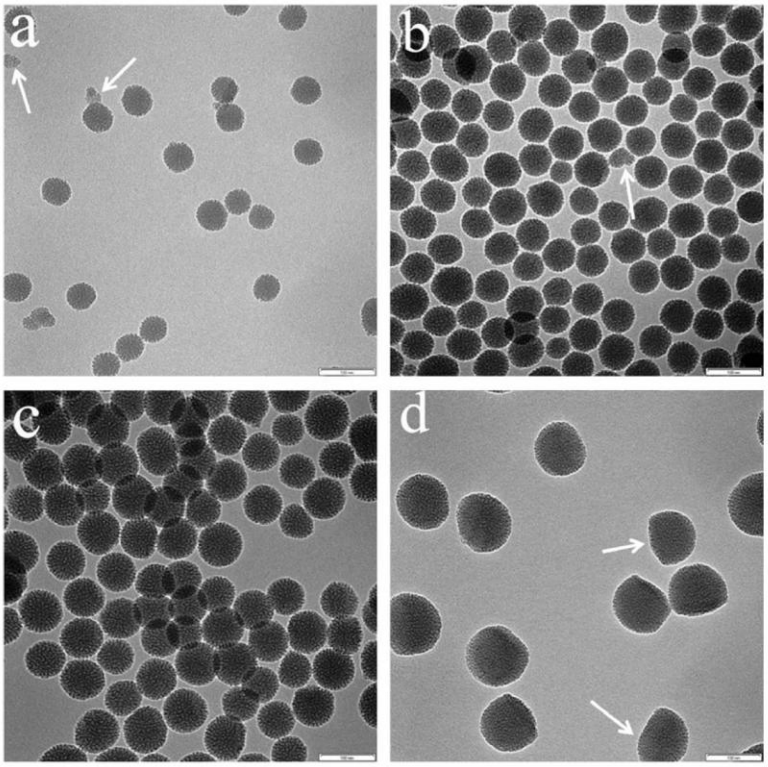


**Fig. 1.** TEM images of (a) MMSNs-40; (b) MMSNs-50; (c) MMSNs-60 and (d) MMSNs-80. All scale bars are 100 nm.

increased to 80 °C, some particles appear in a truncated spherical shape (indicated by arrows in Fig. 1d). It is noted that in some previous reports, the TEM images of as-prepared MSNs before calcination were provided [29,32], and it is also reported that MSNs with small particle sizes have tendency to aggregate to form larger particles during the template removal processes [22,26,35,36]. It is noted that the MMSNs prepared by our simple approach are not aggregated, even after calcination, this is crucial for the future biomedical applications.

The DLS method is utilized to further determine the size and dispersity of calcined materials MMSNs-T prepared at different temperatures. The DLS data in Fig. 2 shows that the diameters of MMSNs-40, MMSNs-50, MMSNs-60 and MMSNs-80 are about 46.3, 65.7, 78.0 and 99.8 nm, respectively. The DLS results further

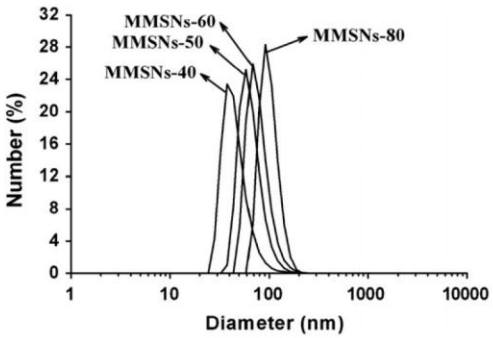


**Fig. 2.** DLS measurements of the samples MMSNs-40, MMSNs-50, MMSNs-60 and MMSNs-80.

demonstrate that the sizes of MMSNs increase by increasing the reaction temperature, which is consistent with what has been observed in TEM images (Fig. 1). Moreover, the particles in all samples show a narrow particle size distribution and the sizes measured by DLS and TEM techniques are similar (see Table 1), suggesting that the MMSNs prepared by our method are highly monodisperse without significant aggregation.

Fig. 3A shows the SEM image of MMSNs-60 synthesized by our approach, where spheres with a uniform size smaller than 100 nm are observed. The XRD pattern of MMSNs-60 exhibits a broad shoulder peak centered at $2\theta = 1.4°$ (Fig. 3B), indicating that the mesostructure in MMSNs-60 is disordered, consistent with the TEM result (Fig. 1c). This observation is different from the typical XRD patterns of ordered MCM-41 type materials prepared using the same surfactant template, which generally have more than three reflections with the first (100) reflection at $2\theta$ of 2.2–2.5° [2]. The single broad diffraction peak gives a $d$-spacing around 6.3 nm, corresponding to closest neighboring pore-to-pore distance while the packing pores are not ordered [37,38]. The nitrogen adsorption–desorption plot of MMSNs-60 gives the typical type IV isotherm (Fig. 3C). The capillary condensation step occurred at high relative pressure of ~0.94 should be attributed to the textural porosity formed by the aggregation of nanospheres, which is quite normal for MMSNs with small particle sizes [22,32]. The BET surface area and pore volume of calcined MMSNs-60 are 136 $m^2/g$ and 0.49 $cm^3/g$ respectively (listed in Table 1). Because the internal pore volume of MMSNs is more important in their biomedical applications as nano-carriers, the pore volume calculated at $P/P_0 = 0.90$ is also listed in Table 1. It can be seen that the internal pore volume of MMSNs-60 is relatively low (0.13 $cm^3/g$). The pore size distribution curve of MMSNs-60 (inset of Fig. 3C) shows two peaks with one centered at 3.1 nm contributed by the internal

**Table 1**
Physicochemical properties of samples synthesized at different conditions.

| Sample | $T_1$ (°C) | $T_2$ (°C) | Average size (nm) | | $D_p$ (nm) | $S_{BET}$ ($m^2$/g) | $V_p$ ($cm^3$/g) | $V_{int}$ ($cm^3$/g) |
|---|---|---|---|---|---|---|---|---|
| | | | TEM | DLS | | | | |
| MMSNs-40 | 40 | / | 53 | 46.3 | / | 266.8 | 0.55 | 0.22 |
| MMSNs-50 | 50 | | 65 | 65.7 | 3.0 | 191.2 | 0.46 | 0.19 |
| MMSNs-60 | 60 | | 77 | 78.0 | 3.1 | 136.0 | 0.49 | 0.13 |
| MMSNs-80 | 80 | | 110 | 99.8 | 3.0 | 67.6 | 0.22 | 0.10 |
| MMSNs-60-B10.0 | 60 | 130 | 70 | 68.4 | 3.1 | 199.4 | 0.63 | 0.21 |
| MMSNs-60-B11.5 | 60 | 130 | 87 | 80.8 | 2.9 | 409.2 | 0.70 | 0.39 |
| MMSNs-60-B12.0 | 60 | 130 | 85 | 91.2 | 2.8 | 543.7 | 0.77 | 0.50 |
| MMSNs-60-A100 | 60 | 100 | 72 | 73.3 | 2.8 | 539.1 | 0.51 | 0.44 |
| MMSNs-60-A130 | 60 | 130 | 68 | 69.3 | 4.0 | 305.3 | 0.41 | 0.29 |
| MMSNs-60-A160 | 60 | 160 | 67 | 69.3 | / | 125.8 | 0.26 | 0.16 |

$T_1$: reaction temperature; $T_2$: hydrothermal treatment temperature; $D_p$: pore diameter from the BJH pore size distribution curves; $S_{BET}$: BET surface area; $V_p$: total pore volume; $V_{int}$: internal pore volume calculated at $P/P_0 = 0.90$.

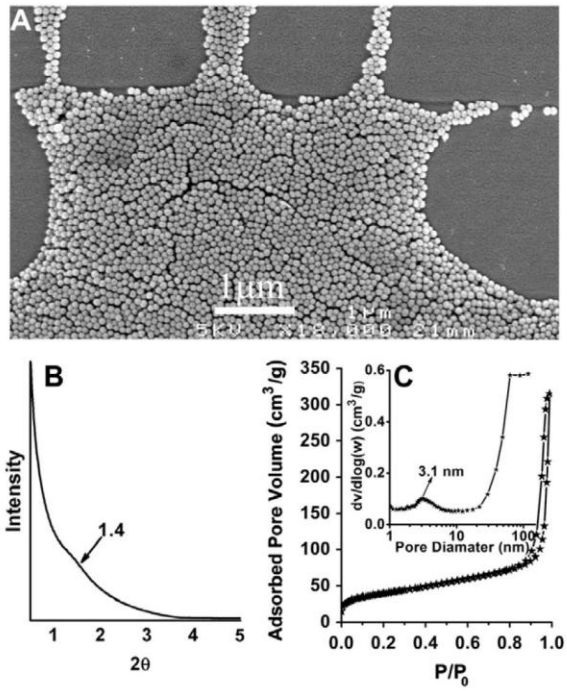


**Fig. 3.** (A) SEM image; (B) XRD pattern and (C) $N_2$ adsorption–desorption isotherms and corresponding pore size distribution (inset of C) of MMSNs-60.

mesopores, and the other at around 85 nm attributed to the interparticle voids.

As shown in the pore size distribution curve in Fig. 3C, the intensity of the first peak is very weak, which implies that the mesopore volume of 3.1 nm pores is low, in order to increase the mesoporosity, we further investigate the influence of hydrothermal treatment on the mesoporous volume of MMSNs-60.

### 3.2. Hydrothermal treatment in basic conditions

The XRD patterns of calcined MMSNs-60-B10.0, MMSNs-60-B11.5 and MMSNs-60-B12.0 are shown in Fig. S1. All XRD patterns display a broad peak centered at 1.4°, similar to that of MMSNs-60 (Fig. 3B), indicating that the disordered pore structures are retained after the hydrothermal treatment under basic conditions. Moreover, the intensity of the reflection gradually increases with the increase of pH value, indicating the increase in mesoporosity because the peak intensity increases with the contrast between silica and air (pore). Fig. 4a–c presents the TEM images of calcined MMSNs-60-B10.0, MMSNs-60-B11.5 and MMSNs-60-B12.0, respectively. Fig. 4a shows that nanospheres in MMSNs-60-B10.0 are uniform with an average size of ~70 nm, which is about 7 nm smaller than that of MMSNs-60. The DLS measurements also show similar results, the average particle size determined by DLS is 78.0 and 68.4 nm for MMSNs-60 and MMSNs-60-B10.0, respectively (Fig. 4d and Table 1). The decreased particle size should be explained by the hydrothermal treatment at basic conditions. The solubility of silica becomes higher with the increase of temperature and pH, leading to slight migration of silica species from the surface of MMSNs-60 into solution. The disordered mesopores can be also clearly observed, and the particles are still dispersed without obvious aggregation, which is similar to that of MMSNs-60. When the pH increases to 11.5, the mean particle size of MMSNs-130-B11.5 is measured to be 87 (TEM) and 80.8 nm (DLS), respectively. Interestingly, it is observed that two particles are connected together by forming a "neck" as indicated by arrows shown in Fig. 4b. When the pH is further increased to 12, more aggregated particles connected by necks are found in MMSNs-60-B12.0 (Fig. 4c), thus the particle size measured by TEM (85 nm) and DLS (91 nm) are both larger than that of MMSNs-60 (Table 1).

The formation of aggregated particles connected by necks is caused by a dissolution–reprecipitation process driven by differences in solubility between surfaces with different curvatures [39]. The silica dissolves at high pH and temperature as shown in the case of MMSNs-60-B10.0, and the dissolved silica species can reprecipitate onto silica particles. However, the solubility of a spherical particle surface with a positive curvature is higher than that of a neck region with a negative curvature, leading to a net migration of silica to necks that connect particles together [39].

The nitrogen sorption analysis results of MMSNs-60-B10.0, MMSNs-60-B11.5 and MMSNs-60-B12.0 are displayed in Fig. 4e. All the adsorption–desorption plots are typical type IV isotherms with two obvious capillary condensation steps, the first step at $P/P_0 = \sim 0.4$ and the second at higher $P/P_0 > 0.90$. The first step is characteristic of mesoporous materials with relatively small pores, and the second is assigned to the textural interparticle macroporosity. Compared to the isotherm of MMSNs-60 (Fig. 3c), all the hydrothermally treated samples show an obvious increase of adsorbed nitrogen volume occurred in the first step (at $P/P_0 = \sim 0.4$). This phenomenon is also clearly revealed by the pore size distribution curves (Fig. 4f). The pore sizes for three samples hydrothermally treated at different pH have slight variations between 2.8 and 3.1 nm, similar to that of MMSNs-60 (3.1 nm). The BET surface area, the total and internal pore volume increase gradually from 199, 409 to 543 $m^2$/g, 0.63, 0.70 to 0.77 $cm^3$/g and 0.21, 0.39 to 0.50 $cm^3$/g, respectively, as pH value increases from 10.0, 11.5 to

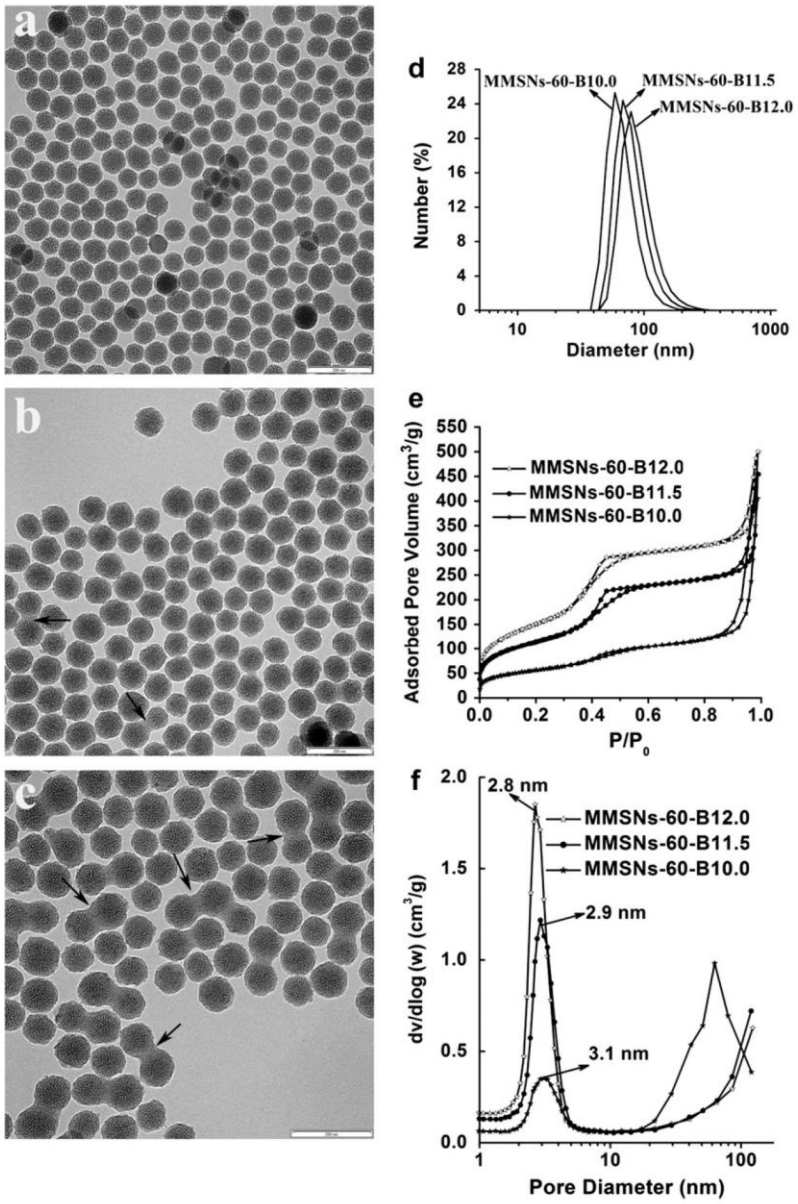


**Fig. 4.** TEM images of (a) MMSNs-60-B10.0, (b) MMSNs-60-B11.5, (c) MMSNs-60-B12.0; (d) DLS measurements of the samples; (e) nitrogen adsorption–desorption isotherms of the products and (f) corresponding pore size distributions. All scale bars for TEM image are 200 nm.

12.0 (summarized in Table 1), which reflects the same trend as that revealed in XRD observation.

The above results show that the mesoporous pore volume and total surface area can be increased by hydrothermal treatments under basic conditions in the pH value range of 10.0–12.0. However, the aggregation starts when the pH value is higher than 11.5. Therefore, in order to balance high mesopore volume and mono-dispersion of MMSNs, the optimized pH value for hydrothermal treatment at 130 °C of the mother solution of MMSNs-60 should be slightly below 11.5.

The post-synthesis hydrothermal treatment approach at elevated temperature has been widely studied for pore expansion of traditional MCM-41 type materials [40–42]. In previous reports, generally there are two types of aqueous mediums used for this aim. The first type is using the alkaline hydrothermal medium, where high pH condition leads to surfactant decomposition and pore increase [43,44]. In our experiments, the mesopore sizes of MMSNs have very slight variations during the post hydrothermal treatment under high pH, indicating that MMSNs prepared by our approach have different structures compared to typical MCM-41s. The other type is using acidic/neutral medium for the hydrothermal treatment [41,45]. For comparison, we further study the influence of acidic hydrothermal treatment on as-synthesized MMSNs-60 using a pH = 2 acidic medium [46], expecting to increase the mesopore volume and keep the spherical morphology from aggregation.

### 3.3. Hydrothermal treatment in acidic conditions

The influence of hydrothermal treatment under acidic solutions with pH = 2 on MMSNs has been investigated. MMSNs-60 was chosen in this study and treated at different hydrothermal temperatures of 100, 130 and 160 °C. From the XRD patterns of the hydrothermally treated samples (Fig. S2), a broad peak in the range of 0.7–2.5° can be observed in MMSNs-60-A100 and MMSNs-60-A130, similar to that of MMSNs-60 (Fig. 3B), and the peak intensity decreases as the hydrothermal treatment temperature increases. When the temperature further increases to 160 °C, even the broad peak disappears for MMSNs-60-A160. The ion exchange between the surfactant ions and protons together with the partial silica migration from the silica walls [47] may contribute to the mesostructure collapse. The solubility of silica increases with temperature increase, thus the diffraction peak cannot be observed (indicating fully structure collapse) at the highest temperature of 160 °C. From the DLS data (Fig. S3), it can be seen that all the samples show a narrow particle size distribution, indicating that all the samples keep mono-dispersed after hydrothermal treatment. The average particle size (Fig. S3 and Table 1) is 73.3, 69.3, 69.3 nm for MMSNs-60-A100, MMSNs-60-A130 and MMSNs-60-A160, respectively, similar to the untreated sample MMSNs-60 with a mean size of ~77 nm. TEM images shown in Fig. 5a–c further demonstrate three samples have uniform particle size with high dispersity, consistent with DLS data.

The $N_2$ adsorption–desorption isotherms and corresponding pore size distribution curves of the MMSNs-60-A100, MMSNs-60-A130 and MMSNs-60-A160 are shown in Fig. 5d–e. MMSNs-60-A100 shows a capillary condensation step occurring at a $P/P_0$ of ~0.3 (Fig. 5d), and its corresponding pore size distribution curve exhibits a peak centered at ~2.8 nm. The slightly decreased pore size compared to the untreated product (~3.1 nm) can be attributed to the shrinkage due to the ion exchange between the surfactant ions and protons as well as the high temperature hydrothermal treatment under acidic conditions. MMSNs-60-A130 has a capillary condensation step at a slightly higher $P/P_0$ of ~0.35. Accordingly, its average pore size seen from the pore size distribution plot is enlarged to 4.0 nm. However, for the sample obtained under acidic hydrothermal treatment at 160 °C, the pore size distribution curve is broadened in the range of 2–10 nm, which indicates that the mesopores are severely collapsed, consistent with the XRD observation (Fig. S2).

The BET surface areas and internal pore volumes of the above three samples are listed in Table 1. It can be seen that MMSNs-60-A100 shows an improved BET surface area of 539 $m^2/g$, which can be attributed to the migration of silica species during the acidic high temperature hydrothermal treatment process. As the hydrothermal treatment temperature increases, both BET surface area and pore volume decrease, MMSNs-60-A160 exhibits the lowest BET surface area of 126 $m^2/g$, which can be explained by the partially collapsed pore structure at this extremely high hydrothermal treatment temperature.

It is noted that MMSNs-60 prepared by our method before hydrothermal treatment has an exceptionally small surface area (136 $m^2/g$), much lower than typical MCM-41 materials [2]. Furthermore, all MMSNs have disordered pore structures, the only difference is the particle size. In order to understand the structure differences between MMSNs and MCM-41, the formation process of MMSNs has been studied.

### 3.4. MMSNs formation mechanism

To investigate the formation mechanism of MMSNs prepared by our method, the intermediate structures have been characterized by TEM and ATR-FTIR techniques. The reaction time ($t$) was recorded from the addition of TEOS into the solution. A quenching process was used to the reaction solution of MMSNs-60 at $t$ = 2 h by cooling it in a 4.5 °C fridge, to investigate the intermediate structures of MMSNs-60. As seen from Fig. 6a, the reaction solution contains two phases after cooling for 1 h, with white floccules on the top of transparent and stable colloidal solution. Even after centrifugation at 20,000 RMP for 10 min, the floccule layer is still on the top of solution. TEM was used to detect the structures in two different phases, namely the as-prepared MMSNs obtained from the colloidal solution after centrifugation (Fig. 6b) and the top

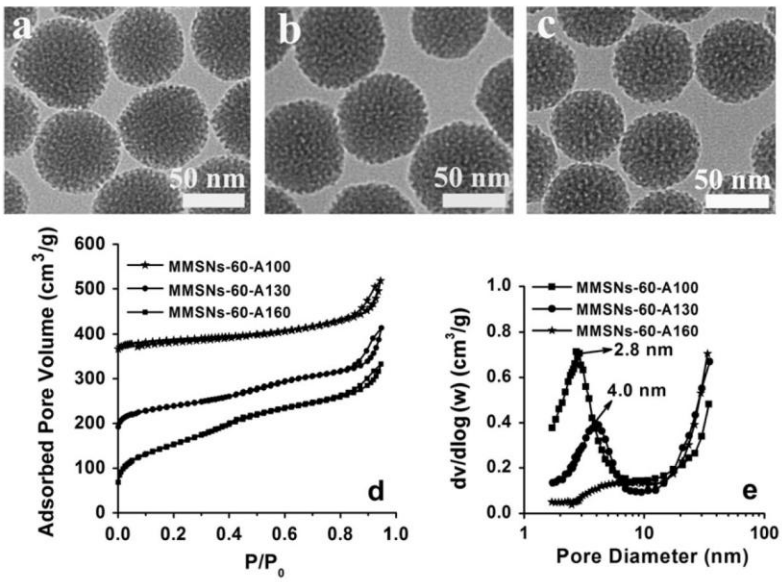


**Fig. 5.** TEM images of (a) MMSNs-60-A100; (b) MMSNs-60-A130; (c) MMSNs-60-A160; (d) Nitrogen adsorption–desorption isotherms of the products and (e) corresponding pore size distributions by the BJH method using adsorption branch. The *Y*-axis value of MMSNs-60-A130, MMSNs-60-A160 is raised by 150, 350 $cm^3/g$ respectively in (d).

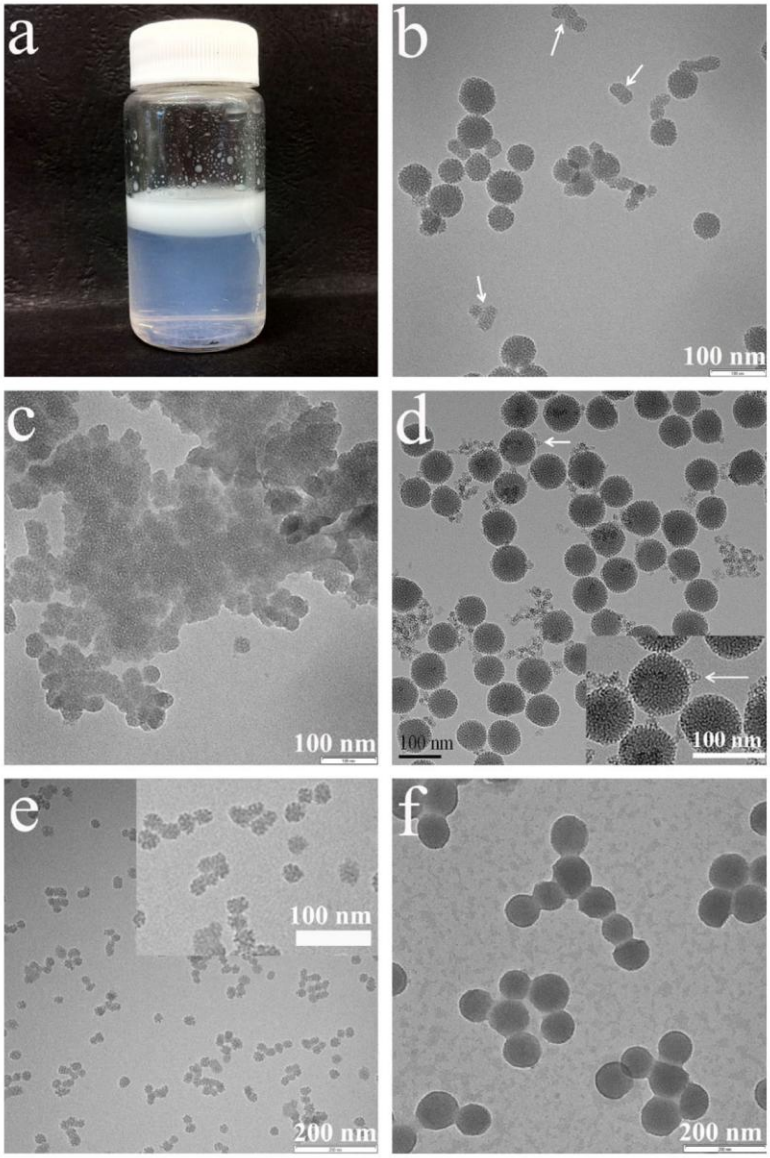


**Fig. 6.** (a) Digital image of the reaction solution at $t$ = 2 h at 60 °C after cooling in fridge at 4.5 °C for 1 h; TEM images of (b) as-synthesized MMSNs obtained from (a) after centrifugation; (c) the top layer of (a); (d) calcined MMSNs obtained from the reaction solution at 4 h after adding TEOS at 70 °C; as-synthesized samples obtained at 80 °C at a reaction time of 20 min (e) and 2 h (f).

floccule layer (Fig. 6c). From both Fig. 6b and c, large spherical particles (diameters of ~60 nm) can be seen aggregated together with smaller particles (diameters of 30 nm, indicated by arrows in Fig. 6b). Compared to Fig. 6b, the TEM image in Fig. 6c is opaque, which can be caused by unreacted silica species/surfactants. Nevertheless, for MMSN-60, we can draw a conclusion that the growth of particles is a time-dependent behavior. Initially there are particles with different sizes formed in reaction solution (~2 h), however MMSNs-60 with uniform sizes are obtained when the reaction time reaches 24 h (Fig. 1c).

As-synthesized MMSNs composed of organic surfactants and partially condensed silica are not very stable under electron beams, thus their TEM images typically show ambiguous contrast. Therefore, we prepare a calcined sample obtained from the preparation of MMSNs-70 when the reaction time is 4 h for TEM observation (Fig. 6d). In addition to the MMSNs nanospheres (diameters of ~84 nm), aggregated silica hollow spheres with mean particle diameters of ~6–7 nm and mesopores diameters of ~3 nm (indicated by arrows) are also observed. The above observation suggests that the as-synthesized MMSNs should be formed by silica-coated CTAC micelles and their further aggregation, thus silica hollow spheres are formed after calcination. We also studied the formation process of MMSNs-80 by directly dropping the reaction solutions on TEM grids. It can be seen that the particles obtained at $t$ = 20 min are clusters with diameters of ~20–40 nm (Fig. 6e), also formed by aggregation of silica coated spherical micelles with mean diameters of ~7 nm (inset of Fig. 6e). When the reaction time increases to 2 h (Fig. 6f), the clusters with smaller diameters of 20–40 nm cannot be found, instead only larger particles with diameters around 100 nm are obtained. Therefore, the reaction process

follows the same trend in our synthesis condition in reaction temperature range of 60–80 °C, that the MMSNs are gradually grown up from silica coated CTAC micelles as building blocks.

Based on above observations, we propose a spherical micelle templating mechanism to interpret the formation of monodisperse MMSNs in our system (Scheme 1). It has been reported that CTAC can form spherical micelles (diameters of 5 nm) in aqueous solutions at a concentration and pH value similar to our synthesis conditions [48]. After the addition of silica precursors, spherical silica coated composite micelles are formed. The composite micelles aggregate together to form nucleus, which further grow into monodispese particles. During the aggregation process, the voids between the composite spherical micelles are filled by the silica species, which is similar to densely packing pathway in FDU-12 [49], rather than that in hard-sphere packing (HSP) model proposed in our previous work [50] (see detailed justification in supporting information). The final size depends on the nucleation and further growth [51]. Compared to the reaction at 60 °C, a higher reaction temperature (such as 80 °C) favors a faster nucleation rate and the formation of nuclei with larger sizes, and eventually larger particle sizes. With increasing reaction time, the composite micelles will be consumed by preferential aggregation with nuclei to form bigger particles (e.g. Fig. 6e–f). In this regard, prolonging the reaction time, especially at relatively low reaction temperatures, favors the formation of MMSNs with uniform diameters (see contrast between Fig. 1c and Fig. 6b). It is also suggested at reaction temperatures lower than 60 °C, a reaction time >24 h may avoid the irregularly shaped particles (Fig. 1a–b). On the other hand, because the formation rate of large particles at 80 °C is faster compared to that at 60 °C (compare Fig. 6f with a–c), the silica is less condensed and thus the formed silica nanoparticles are not rigid, the collision between relatively flexible particles may be responsible for the formation of truncated spherical shape as shown in Fig. 1D.

In our synthesis system, the mesopore size and spherical morphology have little changes during the post hydrothermal treatment under high pH, but the internal pore volume has significant enhancement. As seen from Table 1, the internal pore volume of MMSNs-60-B12.0 (0.50 $cm^3/g$) is almost 4 times as large as that of MMSNs-60 (0.13 $cm^3/g$). It is suggested that under high pH and high temperature hydrothermal conditions, the silica migration occurs. Consequently, two or more adjacent mesopores are connected together to form wormlike channels with similar diameters. Evidence for this claim can be found in the TEM image of MMSNs-60-B12.0, where channel-like pores can be seen as indicated by the red arrows in the right image of Fig. S5. For comparison, such channel-like pores are difficult to be observed in MMSNs-60 (left image of Fig. S5). The silica migration and the resultant spherical pore to channel-like pore structure transition may explain for the internal pore volume increase after the hydrothermal treatment under basic conditions.

In order to further understand the formation of MMSNs prepared by our approach, the ATR-FTIR spectroscopy was used to monitor the siliceous species produced by the hydrolysis and condensation of TEOS as a function of reaction time in our MMSNs-60 reaction system The ATR-FTIR spectra (Fig. 7) obtained at reaction time from 10 min to 24 h show the same broad band at 965 $cm^{-1}$, which can be attributed to the Si–O stretching of Si–OH groups [52–54]. The intensity of this peak increases from $t$ = 10 min to $t$ = 1 h, and then decreases until finally disappears at $t$ = 24 h. The characteristic bands at 1083[$\nu$(C–O)/(C–O) + C–C)], 1105 [$\rho'(CH_3)$], 1169[$\rho(CH_3)$], 1296[$\tau(CH_2)$] and 1391 $cm^{-1}$ [$\delta s(CH_3)$] can be assigned to the –Si–$OCH_2CH_3$ group [52–54]. The presence of ethoxy groups is still observed when the reaction time is 4 h. The intensity of the other two bands at 877 and 1044 $cm^{-1}$, which are attributed to ethanol [54], increases with the reaction time from 3 to 24 h.

All the results indicate that the hydrolysis rate of TEOS is very slow in our system with a pH of 6.0. It is noted that the particles have already formed at $t$ = 2 h (see Fig. 6b), thus the hydrophobic group of Si–$OCH_2CH_3$ on the surface of silica nanoparticles during the reaction (<24 h) may favor the formation of silica coated spherical micelles and protect silica nanoparticle from further randomly aggregation, finally leading to monodisperse nanoparticles [18].

The above ATR-FTIR result can also explain the observation in Fig. 6a. When the reaction time is 2 h, there are still –Si–$OCH_2CH_3$ groups from the uncompletely hydrolyzed TEOS in the surfactant/silca composites. Once the stirring process stops, the hydrophobic clusters with ethoxy groups prefer to separate from the hydrophilic water solution and aggregate on the top of reaction solution. Therefore, a continuous stirring for 24 h is important to prepare MMSNs with high yield.

It is worth noting that our reaction system of MMSNs is similar to that of MCM-41 type materials (see details in Supporting information) [55], while the major difference is pH value. In our system, the synthesis pH is around 6, which gives rise to the spherical micelle templating pathway. In contrast, when the pH value is much higher (at 12.0) in the MCM-41 reaction system [55], TEOS can be fully hydrolyzed into hydrophilic silica species with silanol groups in <10 min (as indicated in Fig. S6 [54]), thus well ordered

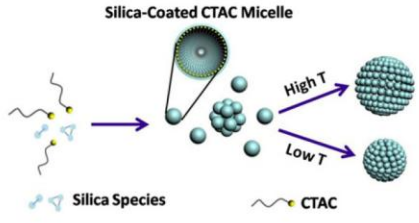


**Scheme 1.** The formation process of MMSNs through spherical micelle templating mechanism. (1) silica-coated CTAC micelles are formed through the co-organization of silica precursors and surfactant CTAC; (2) aggregation of a part of silica-surfactant composite micelles into disordered spherical nanospheres; (3) the primary-generated small particles grow homogeneously into bigger particles, and finally form monodisperse mesoporous silica nanospheres (MMSNs). The size of MMSNs increases as the reaction temperature increase.

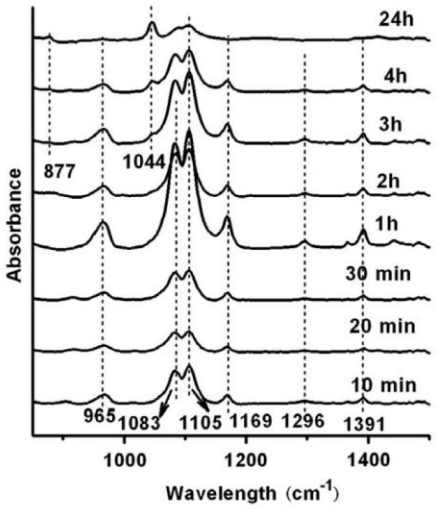


**Fig. 7.** ATR-FTIR spectra of the reaction mixtures as a function of time in MMSNs-60 reaction system.

hexagonal structure (data not provided here) is formed [1] [56]. The above observation is similar to the pH differentiating effect we observed before [54].

## 4. Conclusions

In summary, a simple spherical micelle templating approach has been successfully developed to synthesize a series of monodisperse mesoporous silica nanospheres with controlled particle sizes. The hydrothermal treatment under basic condition (pH = ~11.5, 130 °C) is an effective way to improve the mesoporous pore volume and surface area while maintaining the mono-dispersion characteristics. The pore size of nano-sized MMSNs obtained in our system can be adjusted from 2.8 to 4.0 nm by increasing hydrothermal treatment temperature from 100 to 130 °C under acidic conditions. The formation mechanism and the internal structures of MMSNs are different from that of traditional MCM-41 type materials. Given their uniform and adjustable particle size and pore properties, MMSNs are expected to have potential applications in drug delivery, cell imaging and composite bio-materials.

## Acknowledgment

We thank the Australian Research Council for support.

## Appendix A. Supplementary data

DLS data of the samples hydrothermally treated under acidic conditions at different temperatures, XRD patterns of the samples hydrothermally treated under basic and acidic conditions, the comparison between theoretical and measured mesopore volume of MMSNs-60, and ATR-FTIR spectra collection and results of the reaction mixtures as a function of time in MCM-41reaction system can be found in Supplementary material. Supplementary data associated with this article can be found, in the online version, at http://dx.doi.org/10.1016/j.jcis.2012.03.014.

## References

[1] C.T. Kresge, M.E. Leonowicz, W.J. Roth, J.C. Vartuli, J.S. Beck, Nature 359 (1992) 710–712.
[2] J.S. Beck, J.C. Vartuli, W.J. Roth, M.E. Leonowicz, C.T. Kresge, K.D. Schmitt, C.T.W. Chu, D.H. Olson, E.W. Sheppard, S.B. McCullen, J.B. Higgins, J.L. Schlenker, J. Am. Chem. Soc. 114 (1992) 10834–10843.
[3] A. Stein, Adv. Mater. 15 (2003) 763–775.
[4] Y. Wan, D.Y. Zhao, Chem. Rev. 107 (2007) 2821–2860.
[5] F. Hoffmann, M. Cornelius, J. Morell, M. Froba, J. Nanosci. Nanotechnol. 6 (2006) 265–288.
[6] C. Li, Catal. Rev. Sci. Eng. 46 (2004) 419–492.
[7] L.F. Giraldo, B.L. Lopez, L. Perez, S. Urrego, L. Sierra, M. Mesa, Macromol. Symp. 258 (2007) 129–141.
[8] A. Corma, Chem. Rev. 97 (1997) 2373–2419.
[9] B.G. Trewyn, S. Giri, Slowing II, V.S.Y. Lin, Chem. Commun. (2007) 3236–3245.
[10] Slowing II, B.G. Trewyn, S. Giri, V.S.Y. Lin, Adv. Funct. Mater. 17 (2007) 1225–1236.
[11] Y.S. Lin, S.H. Wu, Y. Hung, Y.H. Chou, C. Chang, M.L. Lin, C.P. Tsai, C.Y. Mou, Chem. Mater. 18 (2006) 5170–5172.
[12] C.P. Tsai, Y. Hung, Y.H. Chou, D.M. Huang, J.K. Hsiao, C. Chang, Y.C. Chen, C.Y. Mou, Small 4 (2008) 186–191.
[13] R.J. Tian, H. Zhang, M.L. Ye, X.G. Jiang, L.H. Hu, X. Li, X.H. Bao, H.F. Zou, Angew. Chem. Int. Ed. 46 (2007) 962–965.
[14] H.A. Meng, M. Liong, T.A. Xia, Z.X. Li, Z.X. Ji, J.I. Zink, A.E. Nel, ACS Nano 4 (2010) 4539–4550.
[15] A.M. Chen, M. Zhang, D.G. Wei, D. Stueber, O. Taratula, T. Minko, H.X. He, Small 5 (2009) 2673–2677.
[16] S. Giri, B.G. Trewyn, V.S.Y. Lin, Nanomedicine 2 (2007) 99–111.
[17] J. Lu, M. Liong, J.I. Zink, F. Tamanoi, Small 3 (2007) 1341–1346.
[18] J. Zhu, J.W. Tang, L.Z. Zhao, X.F. Zhou, Y.H. Wang, C.Z. Yu, Small 6 (2010) 276–282.
[19] F. Lu, S.H. Wu, Y. Hung, C.Y. Mou, Small 5 (2009) 1408–1413.
[20] B. Pauwels, G. Van Tendeloo, C. Thoelen, W. Van Rhijn, P.A. Jacobs, Adv. Mater. 13 (2001) 1317–1320.
[21] A. Walcarius, C. Delacote, Chem. Mater. 15 (2003) 4181–4192.
[22] K. Suzuki, K. Ikari, H. Imai, J. Am. Chem. Soc. 126 (2004) 462–463.
[23] N.J. Carroll, S.B. Rathod, E. Derbins, S. Mendez, D.A. Weitz, D.N. Petsev, Langmuir 24 (2008) 658–661.
[24] G. Derrien, C. Charnay, J. Zajac, D.J. Jones, J. Roziere, Chem. Commun. (2008) 3118–3120.
[25] Q. Cai, Z.S. Luo, W.Q. Pang, Y.W. Fan, X.H. Chen, F.Z. Cui, Chem. Mater. 13 (2001) 258–263.
[26] C.E. Fowler, D. Khushalani, B. Lebeau, S. Mann, Adv. Mater. 13 (2001) 649–652.
[27] R.I. Nooney, D. Thirunavukkarasu, Y.M. Chen, R. Josephs, A.E. Ostafin, Chem. Mater. 14 (2002) 4721–4728.
[28] J. Rathousky, M. Zukalova, P.J. Kooyman, A. Zukal, Colloid Surf. A Physicochem. Eng. Aspects 241 (2004) 81–86.
[29] K. Moller, J. Kobler, T. Bein, Adv. Funct. Mater. 17 (2007) 605–612.
[30] K. Moller, J. Kobler, T. Bein, J. Mater. Chem. 17 (2007) 624–631.
[31] J. Kobler, K. Moller, T. Bein, ACS Nano 2 (2008) 791–799.
[32] Z.A. Qiao, L. Zhang, M.Y. Guo, Y.L. Liu, Q.S. Huo, Chem. Mater. 21 (2009) 3823–3829.
[33] T. Yokoi, T. Karouji, S. Ohta, J.N. Kondo, T. Tatsumi, Chem. Mater. 22 (2010) 3900–3908.
[34] V. Polshettiwar, D. Cha, X.X. Zhang, J.M. Basset, Angew. Chem. Int. Ed. 49 (2010) 9652–9656.
[35] S. Sadasivan, C.E. Fowler, D. Khushalani, S. Mann, Angew. Chem. Int. Ed. 41 (2002) 2151–2153.
[36] J. Gu, W. Fan, A. Shimojima, T. Okubo, Small 3 (2007) 1740–1744.
[37] P.T. Tanev, T.J. Pinnavaia, Science 267 (1995) 865–867.
[38] C. Boissiere, A. Larbot, E. Prouzet, Chem. Mater. 12 (2000) 1937–1940.
[39] C.J. Brinker, G.W. Scherer, Sol–Gel Science: The Physics and Chemistry of Sol–Gel Processing, Academic Press, 1990.
[40] D. Khushalani, A. Kuperman, G.A. Ozin, K. Tanaka, J. Garces, M.M. Olken, N. Coombs, Adv. Mater. 7 (1995) 842.
[41] L.Y. Chen, T. Horiuchi, T. Mori, K. Maeda, J. Phys. Chem. B 103 (1999) 1216–1222.
[42] M. Kruk, M. Jaroniec, A. Sayari, Microporous Mesoporous Mater. 27 (1999) 217–229.
[43] C.F. Cheng, W.Z. Zhou, J. Klinowski, Chem. Phys. Lett. 263 (1996) 247–252.
[44] A. Sayari, Y. Yang, M. Kruk, M. Jaroniec, J. Phys. Chem. B 103 (1999) 3651–3658.
[45] M.V. Landau, S.P. Varkey, M. Herskowitz, O. Regev, S. Pevzner, T. Sen, Z. Luz, Microporous Mesoporous Mater. 33 (1999) 149–163.
[46] D.H. Pan, P. Yuan, L.Z. Zhao, N.A. Liu, L. Zhou, G.F. Wei, J. Zhang, Y.C. Ling, Y. Fan, B.Y. Wei, H.Y. Liu, C.Z. Yu, X.J. Bao, Chem. Mater. 21 (2009) 5413–5425.
[47] K. Zhang, H.L. Chen, B. Albela, J.G. Jiang, Y.M. Wang, M.Y. He, L. Bonneviot, Eur. J. Inorg. Chem. (2011) 59–67.
[48] T.M. Clausen, P.K. Vinson, J.R. Minter, H.T. Davis, Y. Talmon, W.G. Miller, J. Phys. Chem. 96 (1992) 474–484.
[49] J. Fan, C.Z. Yu, T. Gao, J. Lei, B.Z. Tian, L.M. Wang, Q. Luo, B. Tu, W.Z. Zhou, D.Y. Zhao, Angew. Chem. Int. Ed. 42 (2003) 3146–3150.
[50] J.W. Tang, X.F. Zhou, D.Y. Zhao, G.Q. Lu, J. Zou, C.Z. Yu, J. Am. Chem. Soc. 129 (2007) 9044–9048.
[51] K.T. Lee, A.N. Sathyagal, A.V. McCormick, Colloid Surf. A-Physicochem. Eng. Asp. 144 (1998) 115–125.
[52] M.I. Tejedor-Tejedor, L. Paredes, M.A. Anderson, Chem. Mater. 10 (1998) 3410–3421.
[53] B. Tan, S.E. Rankin, J. Phys. Chem. B 110 (2006) 22353–22364.
[54] J. Zhang, M.H. Yu, P. Yuan, H.N. Wang, K. Qian, L. Tan, Y.H. Wang, C.Z. Yu, J. Mater. Res. 25 (2010) 648–657.
[55] S. Yang, L.Z. Zhao, C.Z. Yu, X.F. Zhou, J.W. Tang, P. Yuan, D.Y. Chen, D.Y. Zhao, J. Am. Chem. Soc. 128 (2006) 10460–10466.
[56] A. Monnier, F. Schuth, Q. Huo, D. Kumar, D. Margolese, R.S. Maxwell, G.D. Stucky, M. Krishnamurty, P. Petroff, A. Firouzi, M. Janicke, B.F. Chmelka, Science 261 (1993) 1299–1303.

# Supplementary material

# A Simple Approach to Prepare Monodisperse Mesoporous Silica Nanospheres with Adjustable Sizes

Meihua Yu[a], Liang Zhou[a], Jun Zhang[a], Pei Yuan[a], Peter Thorn[b], Wenyi Gu[a], Chengzhong Yu[a]*

[a]ARC Centre of Excellence for Functional Nanomaterials and Australian Institute for Bioengineering and Nanotechnology, The University of Queensland, Brisbane, QLD 4072, Australia

[b]School of Biomedical Sciences, The University of Queensland, Brisbane, QLD 4072, Australia

*Corresponding author: Tel: +61-7-334 63283; Fax: +61-7-334 63973; E-mail address: c.yu@uq.edu.au

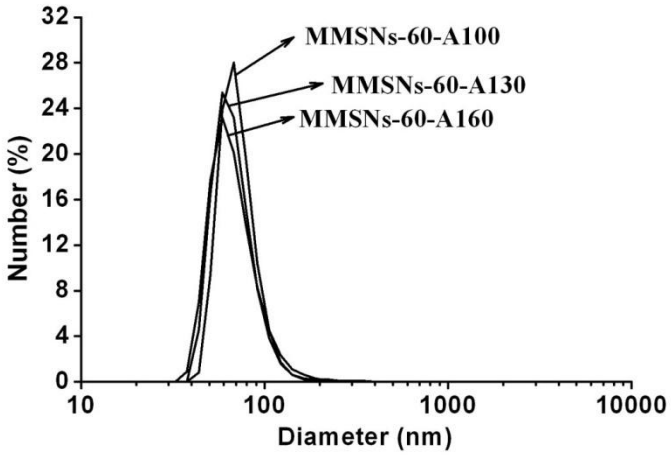


**Figure S1** DLS measurements of calcined MMSNs-60-A100, MMSNs-60-A130 and MMSNs-60-A160

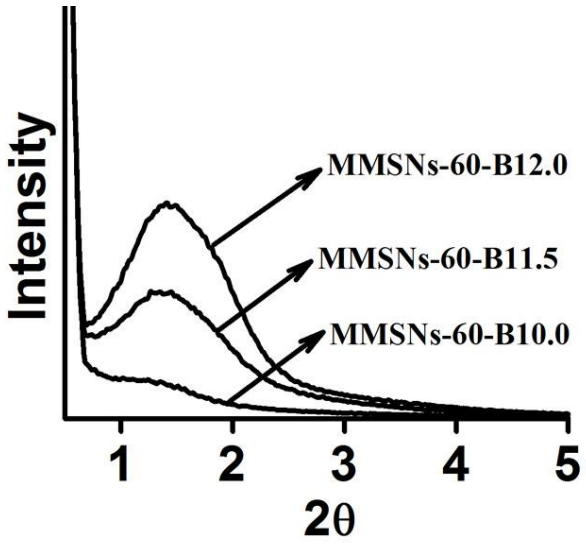

**Figure S2** XRD patterns of MMSNs-B10.0, MMSNs-60-B11.5 and MMSNs-60-B12.0

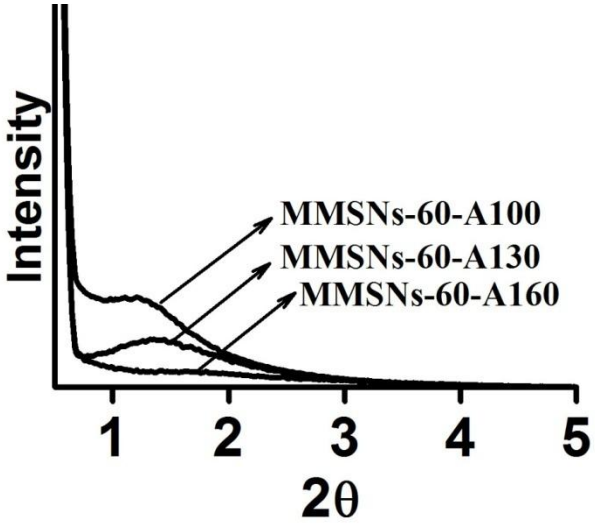


**Figure S3** XRD patterns of MMSNs-A100, MMSNs-60-A130 and MMSNs-60-A160

***Comparison between theoretical and measured mesopore volume***: In our proposed formation mechanism, the nano-sized composite micelles with a diameter of 6-7 nm are the basic building blocks, which randomly aggregate together to form the final mesostructured MMSNs. In order to calculate the structure parameters, we adopt a simple close-packing model, more specifically, a face-centered cubic (fcc) packing model. It is noted that for the fcc structure, there are two possible models. In the first model (left in Scheme S1), the fcc mesostructure is formed by a hard-sphere packing (HSP) model proposed in our previous work [1]. In this model, the hard spheres are silica coated composite spherical micelles. After removal of surfactants, it is indeed the packing of hollow spheres with both cage and cavity (the packing voids) as shown in Scheme S1, left.

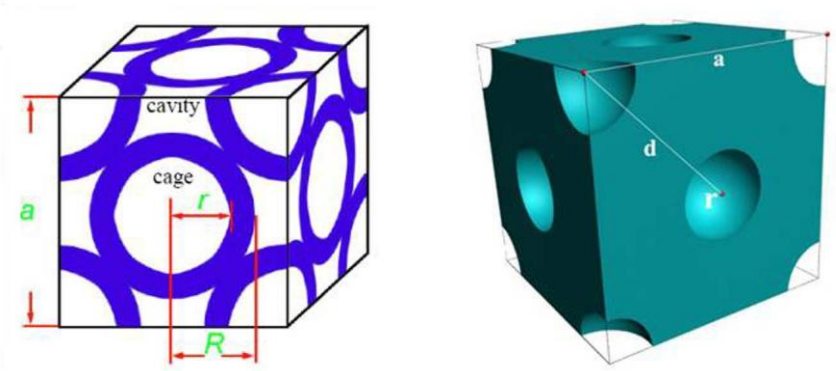


**Scheme S1** Face-centered cubic (fcc) packing models for the calculation of mesopore volume of MMSNs. (Left) A HSP packing model. (Right) A conventional fcc packing model.

In the HSP packing model, $R$ is the radius of a composite micelle or hollow sphere in a calcined material, $r$ represents the radius of cages and $a$ is the cell parameter of the fcc structure. In the case of MMSNs-60, $R = \frac{d}{2}$ =3.15 nm ($d$ stands for the closest pore-to-pore distance, calculated from the XRD peak in Figure 3B), $r$ =

$\frac{3.1\ \text{nm}}{2}$ = 1.55 nm (3.1 nm is the mesopore diameter of MMSNs-60, determined by $N_2$ sorption analysis in Figure 3C), $a = \sqrt{2}d = \sqrt{2} \times 6.3\ \text{nm} = 8.91\text{nm}$.

The number of spherical hollow nano-spheres belong to one fcc lattice is 4, so the internal pore volume ($V_p$) can be described as

$$Vp = \frac{4\times\frac{4\pi r^3}{3}+a^3-4\times\frac{4\pi R^3}{3}}{\left(4\times\frac{4\pi(R^3-r^3)}{3}\right)\times\rho_{SiO_2}} \quad \text{.....(1)}$$

where $R$ = 3.15 nm, $r$ = 1.55 nm, $a$ = 8.91nm, $\rho_{SiO2}$= 2.2 g/cm$^3$, then $V_p$= 0.24 cm$^3$/g.

The other model for an fcc mesostructure is similar to that of FDU-12 [2], where the spherical pores are the symmetrical points embedded in silica matrix (Scheme S1, right). Compared to the HSP model, the difference is that the cavities are filled by silica. The internal pore volume can be described as

$$Vp = \frac{4\times\frac{4\pi r^3}{3}}{\left(a^3-4\times\frac{4\pi r^3}{3}\right)\times\rho_{SiO_2}} \quad \text{.....(2),}$$

where $a$ = 8.91nm, $r$ = 1.55 nm, $a$ = 8.91nm, $\rho_{SiO2}$= 2.2 g/cm$^3$, thus $V_p$= 0.04 cm$^3$/g.

It should be pointed out that the internal pore volume calculated at $P/P_0$ = 0.90 is 0.13 cm$^3$/g (Table 1) in the $N_2$ sorption analysis, which includes the micropore volume, mesopore volume and a small amount of pore volume from textural porosity. In order to calculate the mesopore volume contributed specifically by the cages (and cavities), the pore size distribution of MMSNs-60 in the range of 0-20 nm is shown in the following Figure S4, from which it can be seen that the cage (and cavity) size should be in the range of 1.4 and 8.4 nm. The mesopore volume calculated from the difference between the cumulative pore volume values at 8.4 nm and 1.4 nm is 0.06 cm$^3$/g. This experimentally determined value is comparable to that theoretically calculated based on the second densely packing model, supporting our proposed mechanism.

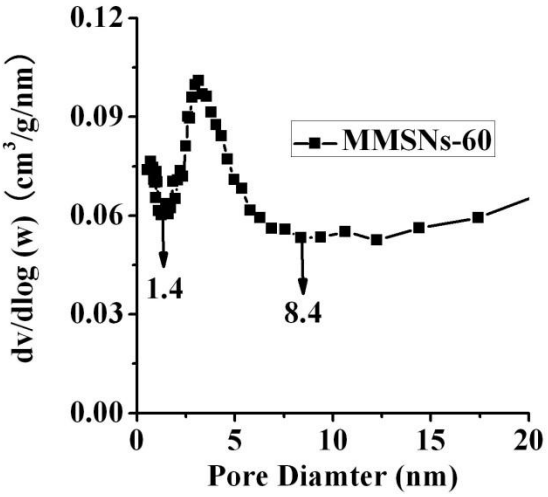


**Figure S4** Pore size distribution of MMSNs-60 in the range of 0-20 nm

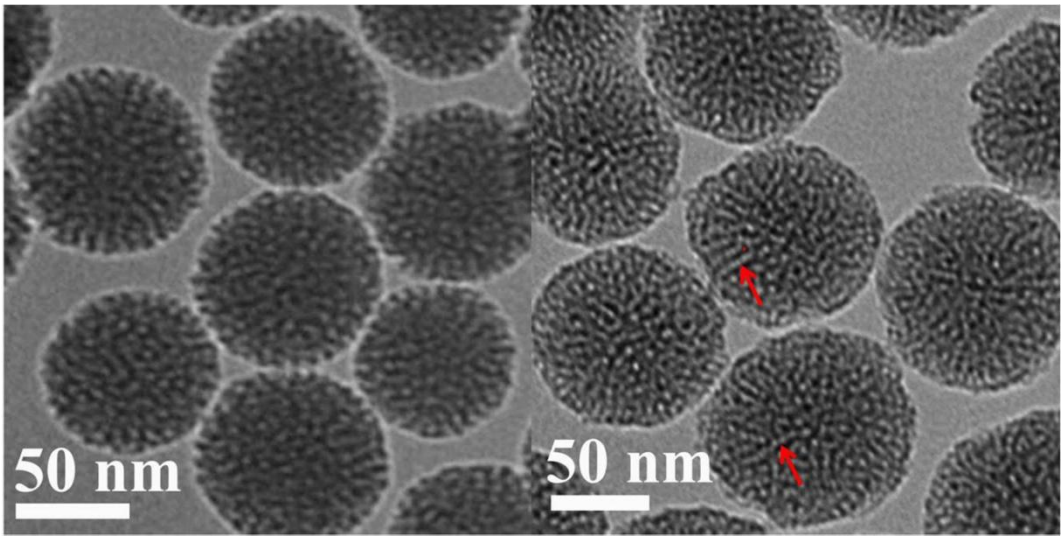


**Figure S5** High magnification TEM images of MMSNs-60 (left) and MMSNs-60-B12.0 (right).

***ATR-FTIR spectra collection of MCM-41 reaction solution:*** MCM-41 material was synthesized using the procedure reported in our previous work with slight modifications (using the same reaction temperature of MMSNs-60 instead of 80 ℃)[3]. In a typical synthesis, 0.2g of CTAB (Cetyl trimethylammonium bromide, Aldrich) was dissolved in 96 g of distilled water with stirring at room temperature followed by the addition of 0.7 mL of NaOH (2 M) into the solution. The temperature of the solution was raised and kept at 60 ℃. To this solution, 1.34 mL of TEOS was added. The mixture was continuously. A series of ATR-FTIR spectra were collected at different reaction times (10, 20, 30 min, 1, 2, 3h). The time was recorded from the addition of TEOS into the solution. Each spectrum was obtained against a background measured under diamond crystal.

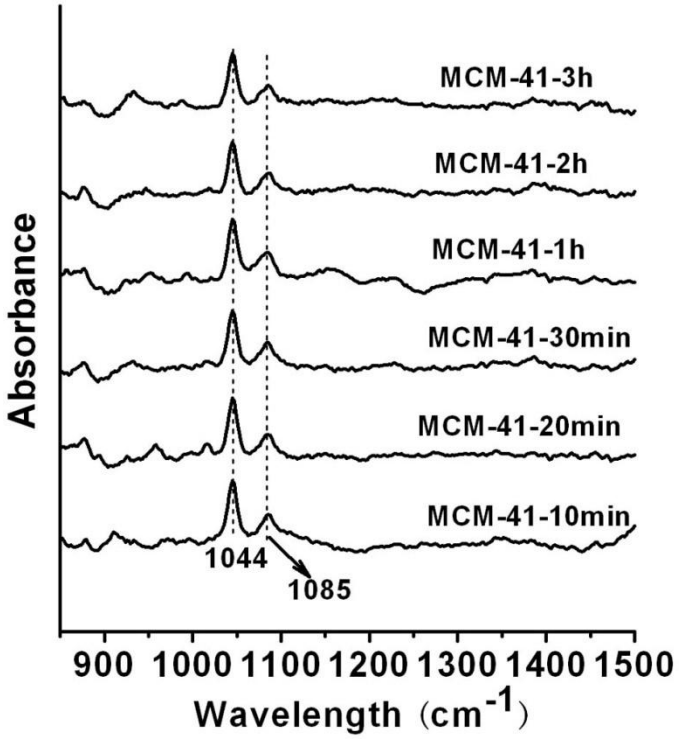


**Figure S6** ATR-FTIR spectra of the reaction mixtures as a function of time in MCM-41[3] reaction system

# References

[1] J. W. Tang; X. F. Zhou; D. Y. Zhao; G. Q. Lu; J. Zou; C. Z. Yu, J. Am. Chem. Soc. 129, (2007), 9044-9048.

[2] J. Fan; C. Z. Yu; T. Gao; J. Lei; B. Z. Tian; L. M. Wang; Q. Luo; B. Tu; W. Z. Zhou; D. Y. Zhao, Angew. Chem.-Int. Edit. 42, (2003), 3146-3150.

[3] S. Yang; L. Z. Zhao; C. Z. Yu; X. F. Zhou; J. W. Tang; P. Yuan; D. Y. Chen; D. Y. Zhao, J. Am. Chem. Soc. 128, (2006), 10460-10466.

# *Chapter 5*

# Facile synthesis of ultra-small hybrid silica spheres for enhanced penetration of 3D glioma spheroids

This chapter reported the synthesis of smaller mono-dispersed SiNPs (ultra-small hybrid silica spheres, UHSS) with a diameter of only ~ 10 nm by a new and facile strategy under phosphate-citrate buffer solution (pH = 4.6) at room temperature without addition of toxic additives. Compared to traditional MCM-41 nanomaterial, the designed novel UHSS showed enhanced penetration ability in three dimensional glioma spheroids. This work has been highlighted as back cover paper.

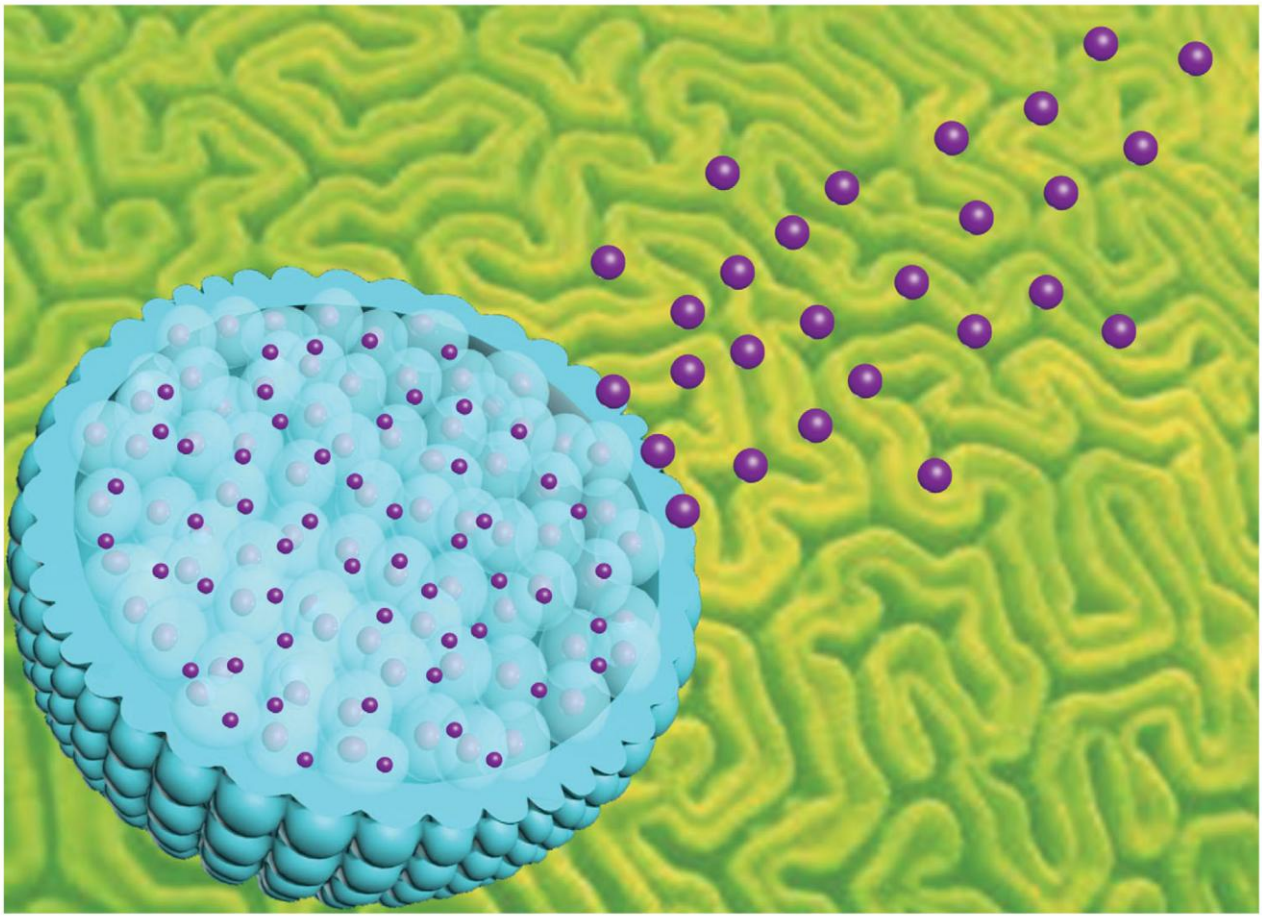

**Showcasing research from Prof. Chengzhong Yu's Laboratory/ Australian Institute for Bioengineering and Nanotechnology, The University of Queensland, Queensland, Australia**

Facile synthesis of ultra-small hybrid silica spheres for enhanced penetration in 3D glioma spheroids

A facile approach has been developed to prepare ultra-small hybrid silica spheres with a diameter of ~10 nm, which show highly enhanced penetration ability in 3D glioma spheroids.

**As featured in:**


See Chengzhong Yu, *Chem. Commun.*, 2014, **50**, 1527.

ChemComm

COMMUNICATION

# Facile synthesis of ultra-small hybrid silica spheres for enhanced penetration in 3D glioma spheroids†

Cite this: *Chem. Commun.*, 2014, 50, 1527

Received 3rd November 2013, Accepted 26th November 2013

DOI: 10.1039/c3cc48416e

www.rsc.org/chemcomm

Meihua Yu,‡[a] Surajit Karmakar,‡[a] Jie Yang,[a] Hongwei Zhang,[a] Yannan Yang,[a] Peter Thorn[b] and Chengzhong Yu*[a]

**A facile approach has been developed to prepare ultra-small hybrid silica spheres with a diameter of ~10 nm, which show highly enhanced penetration ability in 3D glioma spheroids compared to conventional mesoporous silica nanoparticles.**

Over the last two decades, nanomedicine research in disease diagnosis and treatment has been revolutionized due to the rapid developments in nanotechnology.[1] Various nano-materials have been extensively investigated as promising nanocarriers to deliver therapeutic or imaging agents into cells/tissues.[2] As emerging nanocarriers, monodisperse silica-based spheres, with diameters of several to a few tens of nanometres,[3] have attracted increasing attention in fluorescence and magnetic resonance imaging and diagnosis applications.[4] The small silica-based spheres with uniform nanometer-size and excellent monodispersity and stability in aqueous media have shown enhanced cellular uptake in their bio-applications.[3c] However, most of the studies were conducted using monolayer cell cultures, which are not representative of a multi-layer cellular environment in native tissues. Cells in three dimensional (3D) spheroid culture models are functionally more complex than monolayers and recapitulate much of the cellular orientation and organisation of solid tumours. Thus, 3D spheroid cultures bridge the gap between monolayer cell culture and live tissue.[5]

Several synthesis methods have been developed to generate monodisperse silica-based spheres with small sizes. For example, Huo *et al.* reported the use of FDA approved nonionic block copolymer (Pluronic F127) micelles as templates for silica deposition in the hydrophilic poly(ethylene oxide) (PEO) shell region, to form robust silica cross-linked micellar core–shell nanoparticles with an ultrafine and uniform size of ~12 nm.[3a] This approach involves strong acidic conditions. Additionally, to terminate the silicate condensation and prevent interparticle aggregation and growth, dimethyl-silane was introduced in the reaction solution after a certain time of adding tetraethoxysilane (TEOS). Tan *et al.* reported a facile synthesis of similar hybrid micelles with a diameter of ~14 nm, however, the harmful tetrahydrofuran (THF) is required in this approach.[3b] Yuan *et al.* reported the use of diblock copolymer micelles comprising cationic poly(2-(dimethyl-amino)ethyl methacrylate) (PDMA) coronas and hydrophobic poly-(2-(diisopropylamino)ethyl methacrylate) (PDPA) cores as nanosized templates for the deposition of silica in a neutral aqueous solution at 20 °C, to form silica hybrid spheres with a diameter of ~35 nm.[6] This method involves the complicated synthesis of commercially unavailable cationic polymers. In our previous work, ultra-small silica hollow spheres with a diameter of ~24.7 nm were synthesized after removing the surfactant where toxic trimethylbenzene (TMB) and strong acidic conditions are involved.[3c] Recently, Ma *et al.* reported one-pot synthesis of PEGylated mesoporous silica nanoparticles with controllable diameters from 6 to 9 nm wherein a toxic surfactant [cationic hexadecyltrimethyl ammonium bromide (CTAB)][7] was used as the template and its exaction removal process is complicated.[3d] It would be of great interest if the harsh conditions and toxic agents could be avoided to generate monodisperse small silica spheres.

Herein, we report a facile strategy for preparation of ultra-small hybrid silica spheres (UHSS) with a diameter of ~10 nm in a phosphate–citrate buffer solution (pH = 4.6) at room temperature, without addition of toxic additives. The biological buffer we used is essential to generate UHSS with a small diameter of 10 nm as it slows down the deposition of mixed silica sources of tetramethyl orthosilane (TMOS) and dimethoxydimethylsilane (DMDMS) on the shell of tri-block copolymer $EO_{106}PO_{70}EO_{106}$ [Pluronic F127, EO is poly(ethylene oxide), PO is poly(propylene oxide)] micelles. As shown in Scheme 1, the obtained UHSS consists of a PPO core and a methyl-silane terminated silica–PEO shell, demonstrating outstanding and uniform penetration ability in 3D glioma spheroids which mimic the solid tumour.

A representative transmission electron microscopy (TEM) image of UHSS is shown in Fig. 1a. A bright core and a dark silica shell can be observed in all ultra-small spherical particles with a very uniform

[a] *Australian Institute for Bioengineering and Nanotechnology, The University of Queensland, Brisbane, QLD 4072, Australia. E-mail: c.yu@uq.edu.au; Fax: +61-7-334-63973; Tel: +61-7-334-63283*

[b] *School of Biomedical Sciences, The University of Queensland, Brisbane, QLD 4072, Australia*

† Electronic supplementary information (ESI) available: Experimental details and results. See DOI: 10.1039/c3cc48416e

‡ These authors contributed equally to this paper.

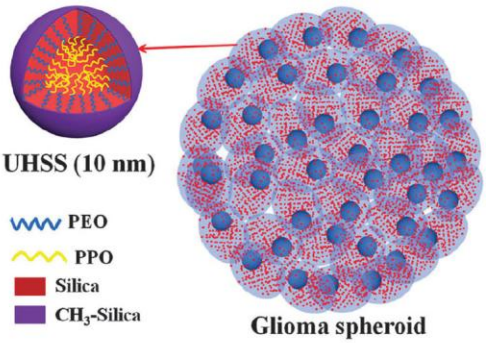


Scheme 1 Schematic representation of ultra-small hybrid silica spheres (UHSS) with a diameter of ~10 nm and their penetration in 3D glioma spheroids. The red dots in the glioma spheroid represent UHSS.

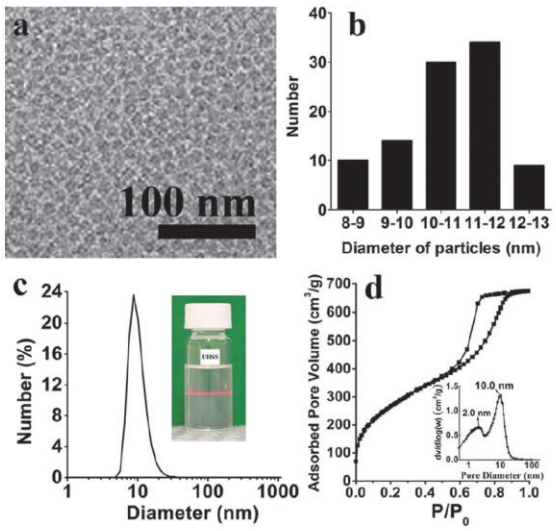


Fig. 1 (a) TEM image of UHSS, (b) diameter distribution of UHSS measured by TEM, (c) DLS measurement and digital image (inset) of UHSS and (d) $N_2$ adsorption–desorption isotherm and the corresponding pore size distribution curve (inset) of calcined UHSS.

size (Fig. 1a). The bright core is formed by the hydrophobic chains (PPO) of the surfactant F127 with a low contrast under TEM observation. The shell is formed by the deposition of silicate species in the hydrophilic PEO region with a high contrast. By measuring ~100 individual spheres directly from the TEM image (Fig. 1a), the average diameter of UHSS was found to be 10.9 nm (Fig. 1b). The UHSS solution is very clear and has an obvious Tyndall effect (inset of Fig. 1c), indicating the excellent stability and high dispersity of UHSS in aqueous solution.

The dynamic light scattering (DLS) measurements were further utilized to evaluate the size and dispersity of UHSS. In Fig. 1c, it can be seen that UHSS shows a narrow size distribution curve, indicating excellent dispersity of UHSS. The average diameter was found to be 10.1 nm (Table S1, ESI†), which is consistent with statistical results obtained from the TEM image. To further confirm the core–shell structure of UHSS, we evaporated the water and then calcined UHSS at 350 °C to remove the surfactant F127 while keeping the methyl groups on the walls, as evidenced by carbon nuclear magnetic resonance ($^{13}C$ NMR) results shown in Fig. S1 (ESI†). Fig. S2 (ESI†) shows hollow spheres of calcined UHSS with a diameter of ~10 nm and a pore size of ~2 nm, however, the aggregation of UHSS after calcination can be clearly observed due to the ultra-small size and thin silica walls of UHSS. The nitrogen sorption analysis was further utilized to determine the structure of UHSS calcined at 350 °C. In Fig. 1d, a type IV adsorption–desorption isotherm can be seen, which is typical of mesoporous materials. The corresponding pore size distribution curve (Fig. 1d, inset) displays two distinct peaks centred at 2.0 and 10.0 nm, which can be assigned to the core diameter of UHSS and the void size between the aggregated small particles of calcined UHSS, respectively. The pore volume and the Brunauer–Emmett–Teller (BET) surface area of calcined UHSS are 1.0 $cm^3\ g^{-1}$ and 968 $m^2\ g^{-1}$, respectively.

It should be noted that in previous reports, the termination agent (methyl-silane or PEG-silane) was added after a period of time (2–24 hours) after adding TEOS or TMOS.[3a,d] Here, the reactive TMOS and dimethyl-silane were simply added into the reaction solution at the same time. We investigated the influence of the molar ratio of the reactive silica source to the termination agent on the final structure and monodispersity of UHSS. It was found that the optimized TMOS molar percentage is 40–50% to obtain a high yield of UHSS (see details in the ESI,† *UHSS-1 to UHSS-6 synthesized at different TMOS molar percentages*, Fig. S3–S6, Scheme S1 and Table S1, ESI†). Furthermore, the mild phosphate–citrate buffer chosen in our approach was found to be essential to generate UHSS with a small diameter of 10 nm compared with UHSS prepared in HCl solution with the same pH of 4.6. (See details in the ESI,† *UHSS synthesized in HCl solution with a pH of 4.6*, Fig. S7, ESI†).

Rhodamine B isothiocyanate modified UHSS (RBTC-UHSS) were synthesized to evaluate their ability to enter into cells both in monolayer and in 3D spheroid models. As shown in Fig. S8 (ESI†), RBTC-UHSS retain the similar spherical structure with a diameter of ~10 nm (Fig. S8a, ESI†) and excellent dispersity in aqueous solution (Fig. S8b, ESI†) as UHSS. Confocal microscopy images (Fig. S9 and S10, ESI†) show concentration-dependent uptake into monolayer cell cultures. The red fluorescence coming from RBTC-UHSS was homogeneously distributed in the cytoplasm of mouse melanoma B16F0 cells (Fig. S9, ESI†), as observed in previous reports.[3a,b] Interestingly, the red signal permeates the whole cell both in the cytoplasm and in nuclei of human malignant brain tumour U87MG cells (Fig. S10, ESI†). The cell-dependent uptake behaviour could be explained by different cell-type specific mechanisms.

Glioblastoma is the most common primary brain tumour in humans. Poor penetration of the conventional drug into solid tumours in the brain is a major factor for failure of chemotherapy in malignant glioma.[8] In order to evaluate the ability of RBTC-UHSS to penetrate solid tumours, we cultured U87MG glioma 3D spheroids by a liquid overlay technique.[9] After 7 days of culture, the U87MG spheroids became compact and homogeneous (Fig. 2 and Fig. S11, ESI†). Confocal microscopy showed that red fluorescence was observed throughout the volume of the U87MG spheroids treated with RBTC-UHSS (Fig. 2). The apparent loading of RBTC-UHSS into the U87MG spheroids was concentration-dependent. In order to look

 

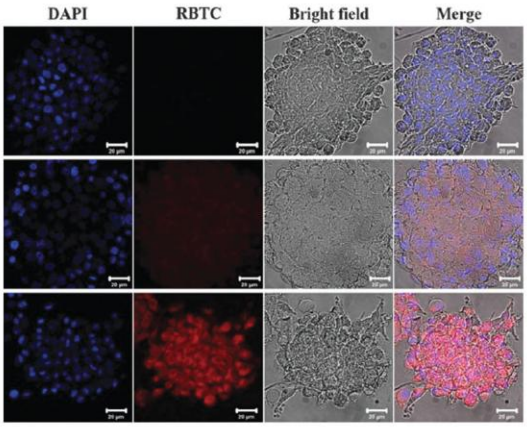


Fig. 2 Confocal microscopy images of U87MG spheroids treated with RBTC-UHSS at 0 μg ml$^{-1}$ (first row), 50 μg ml$^{-1}$ (second row) and 100 μg ml$^{-1}$ (third row).

into the RBTC-UHSS distribution in different layers of U87MG spheroids, confocal *Z*-stack images were collected at every 0.75 and 1.2 μm interval, as shown in Fig. S12 (ESI†) and Fig. 3, respectively. For the spheroids of U87MG without treatment with RBTC-UHSS (Fig. S12, ESI†), only blue fluorescence coming from nuclei stained by DAPI (4′,6-diamidino-2-phenylindole, dihydrochloride) could be detected in *Z*-stack images. When U87MG spheroids were treated with RBTC-UHSS, a strong red signal permeated homogeneously into every single cell in all the images collected at different depths (Fig. 3). For comparison, we employed the traditional MCM-41-type mesoporous silica nanoparticles modified with a fluorescent dye (FITC-MCM-41) (Fig. S13, ESI†), which were synthesized as previously described.[10] Their penetration ability was evaluated in U87MG spheroids. In contrast to RBTC-UHSS, we observed a heterogeneous distribution of green fluorescence with a strong signal in the central area while negligible signal in the periphery of spheroid cells (Fig. S14, ESI†). The big particle size and limited dispersity of FITC-MCM-41 in aqueous solution might have hindered its uniform penetration ability in the 3D model of U87MG cells. These results demonstrate that UHSS show enhanced penetration in 3D glioma spheroids, compared with traditional MCM-41 nanomaterials.

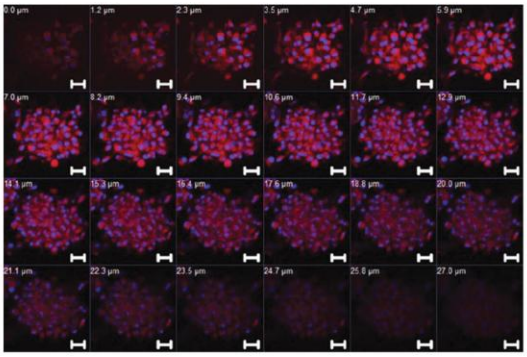

Fig. 3 *Z*-stack images of U87MG spheroids treated with RBTC-UHSS at 100 μg ml$^{-1}$. All scale bars are 20 μm.

Additionally, it was reported that cyclic RGD peptide modification was essential for uniform distribution of organic nanoparticles throughout the entire glioma spheroid, otherwise, the organic nanoparticles had limited ability to penetrate the core area of glioma spheroids.[8] Our UHSS without modification of any targeting moiety demonstrated a comparable glioma tissue penetration capability with organic nanoparticles with a specific ligand.

Nanoparticles should be biocompatible in bio-imaging applications, thus low cytotoxicity of UHSS is crucial at a certain range of dosages. In Fig. S15 (ESI†), it can be seen that UHSS are biocompatible in U87MG cells even at a high concentration of 100 μg ml$^{-1}$.

In conclusion, a facile approach has been successfully developed to synthesize ultra-small hybrid silica spheres (UHSS) with a diameter of ~10 nm in a phosphate–citrate buffer solution (pH = 4.6) at room temperature without addition of any toxic agents. We have demonstrated an enhanced penetration ability of UHSS in 3D glioma spheroids compared to conventional mesoporous silica nanoparticles. Our approach may be used to prepare new materials for bio-imaging and delivery applications.

The authors acknowledge the support from the Australian Research Council, the Australian National Fabrication Facility and the Australian Microscopy and Microanalysis Research Facility at the Centre for Microscopy and Microanalysis, the University of Queensland.

## Notes and references

1 B. Y. S. Kim, J. T. Rutka and W. C. W. Chan, *N. Engl. J. Med.*, 2010, **363**, 2434–2443.
2 (*a*) M. Liong, J. Lu, M. Kovochich, T. Xia, S. G. Ruehm, A. E. Nel, F. Tamanoi and J. I. Zink, *ACS Nano*, 2008, **2**, 889–896; (*b*) V. P. Torchilin, *Nat. Rev. Drug Discovery*, 2005, **4**, 145–160; (*c*) H.-C. Huang, S. Barua, G. Sharma, S. K. Dey and K. Rege, *J. Controlled Release*, 2011, **155**, 344–357; (*d*) I. Brigger, C. Dubernet and P. Couvreur, *Adv. Drug Delivery Rev.*, 2012, **64**, 24–36.
3 (*a*) Q. S. Huo, J. Liu, L. Q. Wang, Y. B. Jiang, T. N. Lambert and E. Fang, *J. Am. Chem. Soc.*, 2006, **128**, 6447–6453; (*b*) H. Tan, N. S. Liu, B. P. He, S. Y. Wong, Z. K. Chen, X. Li and J. Wang, *Chem. Commun.*, 2009, 6240–6242; (*c*) J. Zhu, J. W. Tang, L. Z. Zhao, X. F. Zhou, Y. H. Wang and C. Z. Yu, *Small*, 2010, **6**, 276–282; (*d*) K. Ma, H. Sai and U. Wiesner, *J. Am. Chem. Soc.*, 2012, **134**, 13180–13183.
4 (*a*) H. Tan, J. M. Xue, B. Shuter, X. Li and J. Wang, *Adv. Funct. Mater.*, 2010, **20**, 722–731; (*b*) E. Rampazzo, F. Boschi, S. Bonacchi, R. Juris, M. Montalti, N. Zaccheroni, L. Prodi, L. Calderan, B. Rossi, S. Becchi and A. Sbarbati, *Nanoscale*, 2012, **4**, 824–830; (*c*) H. Tan, Y. Zhang, M. Wang, Z. X. Zhang, X. H. Zhang, A. M. Yong, S. Y. Wong, A. Y. C. Chang, Z. K. Chen, X. Li, M. Choolani and J. Wang, *Biomaterials*, 2012, **33**, 237–246; (*d*) X. D. Wang, R. J. Meier and O. S. Wolfbeis, *Angew. Chem., Int. Ed.*, 2013, **52**, 406–409; (*e*) X. D. Wang, J. A. Stolwijk, T. Lang, M. Sperber, R. J. Meier, J. Wegener and O. S. Wolfbeis, *J. Am. Chem. Soc.*, 2012, **134**, 17011–17014.
5 F. Pampaloni, E. G. Reynaud and E. H. K. Stelzer, *Nat. Rev. Mol. Cell Biol.*, 2007, **8**, 839–845.
6 J. J. Yuan, O. O. Mykhaylyk, A. J. Ryan and S. P. Armes, *J. Am. Chem. Soc.*, 2007, **129**, 1717–1723.
7 (*a*) T. Niidome, M. Yamagata, Y. Okamoto, Y. Akiyama, H. Takahashi, T. Kawano, Y. Katayama and Y. Niidome, *J. Controlled Release*, 2006, **114**, 343–347; (*b*) Q. J. He, J. L. Shi, F. Chen, M. Zhu and L. X. Zhang, *Biomaterials*, 2010, **31**, 3335–3346.
8 X. Y. Jiang, X. Y. Sha, H. L. Xin, X. M. Xu, J. J. Gu, W. Y. Xia, S. Chen, Y. K. Xie, L. C. Chen, Y. Z. Chen and X. L. Fang, *Biomaterials*, 2013, **34**, 2969–2979.
9 J. Carlsson and J. M. Yuhas, *Recent Results Cancer Res.*, 1984, **95**, 1–23.
10 M. H. Yu, S. Jambhrunkar, P. Thorn, J. Z. Chen, W. Y. Gu and C. Z. Yu, *Nanoscale*, 2013, **5**, 178–183.

# Supporting information

## Facile synthesis of ultra-small hybrid silica spheres for enhanced penetration of 3D glioma spheroids

Meihua Yu, [a ‡] Surajit Karmakar, [a ‡] Jie Yang, [a] Hongwei Zhang, [a] Yannan Yang, [a] Peter Thorn [b] and Chengzhong Yu*[a]

[a]Australian Institute for Bioengineering and Nanotechnology, The University of Queensland, Brisbane, QLD 4072, Australia

[b]School of Biomedical Sciences, The University of Queensland, Brisbane, QLD 4072, Australia

∗Corresponding author: Tel: +61-7-334 63283; Fax: +61-7-334 63973; E-mail address: c.yu@uq.edu.au

‡ These authors contribute equally to this paper

### Experimental section

***Materials***: Tetramethyl orthosilane (TMOS, 98%), Dimethoxydimethylsilane (DMDMS, 95%), Pluronic F127, Rhodamine B isothiocyanate (RBTC), (3-aminopropyl)trimethoxysilane (APTMS), fluoroshield with DAPI (4',6-diamidino-2-phenylindole, dihydrochloride) and paraformaldehyde (PFA) were purchased from Sigma-Aldrich. Citric acid monohydrate (CA ·$H_2O$), dibasic sodium phosphate ($Na_2HPO_4$) were purchased from Ajax Finechem. Mouse melanoma B16F0 cell line was a kind gift of Dr. Barbara Rolfe from Australian Institute for Bioengineering and Nanotechnology, University of Queensland. Human malignant brain tumour U87MG cell was kindly provided by Prof. Marie-Odile Parat, School of Pharmacy, University of Queensland. Fetal calf serum (FCS) was purchased from Moregate Biotech, Australia. De-ionized (D.I.) water was generated using a Millipore Milli-Q system.

***Synthesis of UHSS***: For the synthesis of monodisperse ultra-small hybrid silica spheres (UHSS), 0.5g of F127 was dissolved in 30 ml of phosphate-citrate buffer solution (pH=4.6, 46.6μM $Na_2HPO_4$, 26.7μM HAc) under stirring at room temperature. Then mixed silica sources of TMOS and DMDMS at different molar ratios (see details in Table S1) was added into the surfactant homogeneous solution under stirring. The reaction was continued at room temperature for 3 days. Afterwards, the clear solution was transferred into a dialysis membrane tube (Sigma-Aldrich, molecular weight cut off 14,000) and dialyzed in 1L of D.I. water for 3 days, to completely remove the salts, methanol and ethanol (resulted from the hydrolysis of TMOS and DMDMS). The D.I. water was refreshed twice per day. Finally the UHSS particles were stored in D.I. water for further use.

**Table S1** Experimental conditions for the synthesis of monodisperse ultras-mall hybrid silica spheres.

| Sample | TMOS (mL) | DMDMS (mL) | TMOS molar percentage (%) | DLS Size (nm) |
|---|---|---|---|---|
| **UHSS-1** | 0.2 | 0.96 | 16.3 | 5.5 |
| **UHSS-2** | 0.4 | 0.77 | 32.5 | 7.0 |
| **UHSS-3** | 0.5 | 0.68 | 40.1 | 11.5 |
| **UHSS** | 0.6 | 0.59 | 48.8 | 10.1 |
| **UHSS-4** | 0.7 | 0.49 | 56.9 | 18.6 |
| **UHSS-5** | 0.8 | 0.40 | 65.0 | 557 |
| **UHSS-6** | 1.23 | 0 | 100 | 577 |

***Synthesis of RBTC-UHSS***: For the synthesis RBTC modified UHSS (RBTC-UHSS), 4 mg of RBTC and 44μl of APTMS was dissolved in 1ml of ethanol and stirred at room temperature overnight in dark. Afterwards, the mixture was added into 30 ml of phosphate-citrate buffer solution (pH=4.6, 46.6μM $Na_2HPO_4$, 26.7μM HAc) containing 0.5g of F127 under stirring at room temperature. After stirring for 2 minutes, the mixed silica sources of TMOS (0.6 ml) and DMDMS (0.59 ml) was added into above solution and stirred for 3 days. Afterwards, the clear red colour solution was transferred into a dialysis membrane tube and dialyzed in 50% (v/v) ethanol D.I. water solution for 2 days in dark, to completely remove the remaining RBTC, then dialyzed in D.I. water for another 3 days. The 50% ethanol solution or D.I. water was refreshed twice per day. Finally the RBTC-UHSS sample was stored in D.I. water for further use.

***Material Characterisation***: Transmission electron microscopy (TEM) images were obtained with a FEI Tecnai F30 operated at 300 or JEOL 1010 operated at 100 kV. For TEM measurement preparation, the carbon coated Cu TEM grids were treated by glow discharge using CRESSINGTON 208 to make the TEM grids hydrophilic. Afterwards, the samples diluted in

deionized were dropped on the treated TEM grids for 2 minutes, after which the drops were absorbed by filter paper, and the samples dried on TEM grids in air. Nitrogen adsorption/desorption isotherms were measured at 77 K by using a Micromeritics ASAP Tristar II 3020 system. The samples were degassed at 473 K overnight on a vacuum line. The pore size distribution curve was derived from the adsorption branch of the isotherm using the Barrett–Joyner–Halanda (BJH) method. The Brunauer–Emmett–Teller (BET) method was utilized to calculate the specific surface areas. The total pore volume was calculated from the amount adsorbed at a maximum relative pressure ($P/P_0$) of 0.99. Dynamic light scattering (DLS) studies were carried out on a Malvern NanoZS zetasizer at 25 °C in ethanol. $^{13}C$ CPMAS NMR spectra were measured by solid state Bruker Avance III spectrometer with 7T (300MHz for 1H) magnet, Zirconia rotor, 4mm, rotated at 7 kHz.

***Cellular uptake of RBTC-UHSS in B16F0***: B16F0 cells were maintained in Dulbecco's Modified Eagle Medium (DMEM) supplemented with FCS (10%), L-glutamine (2%), penicillin (1%), streptomycin (1%) in 5% $CO_2$ at 37 ℃. The medium was routinely changed every 2 days and the cells were separated by trypsinisation before reaching confluency. B16F0 cells were seeded in a 6-well plate ($1\times10^5$ cells per well) and incubated for 24 h prior to cell uptake assay. Before adding RBTC-UHSS stock solution into a well of 6-well plates, the medium was replaced by 2.0 ml of fresh serum-free DMEM medium. After incubation for 4 h at 37°C, the cells were washed twice with PBS to remove the remaining RBTC-UHSS, and dead cells. For fixed cell imaging, the cells were treated with 500 μl of 4% PFA PBS solution for 30 min at 4 °C, and their nuclei were stained with DAPI for 10 mins. Finally, the cells were observed under a confocal microscope (LSM Zeiss 710).

***Culturing of U87MG cells and spheroids***: U87MG cells grown in monolayer were maintained in DMEM supplemented with FCS (10%), L-glutamine (2%), penicillin (1%), streptomycin (1%) in 5% $CO_2$ at 37 ℃. The U87MG glioblastoma spheroids were developed using the modified liquid overlay technique.[1] In brief, exponentially growing monolayer cells were trypsinized and $3\times10^5$ cells were seeded in 1% agar-coated 6-well plates containing Dulbecco modified Eagle medium (GIBCO) supplemented with FCS (10%), L-glutamine (2%), nonessential amino acids (4%) and penicillin/streptomycin (2%). The plates were incubated in a tissue culture incubator at 37℃ (95% humidity, 95% air, and 5% $CO_2$) and cultured for 3-5 days, until spheroids were formed. Half of the culture medium was replaced with fresh medium twice a week. After round spheroids were formed and those with 200 μm diameter were collected, transferred and culture in agarose-coated (0.1%) glass cover slip in 6-well plates with same culture medium.

***Cellular uptake of RBTC-UHSS in U87MG monolayer cells and spheroids*:** The monolayer U87MG cells and spheroid grown on plain glass and agar-coated cover slips respectively in 6 well plates were treated with RBTC-UHSS (or FITC-MCM-41). After 4 hours, plates were washed with PBS for 2 times and cells or spheroids were fixed with 4% PFA, washed with PBS. Nuclei were stained with a DAPI mount solution on glass slides. The cellular uptake of RBTC-UHSS by U87MG monolayer cells and multilayer spheroid were assessed using a confocal microscopy (LSM Zeiss 710). The software was used for obtaining confocal z-stacks for spheroid. Images were taken every 20 μm down through multilayer, visualizing tumour cells in the individual layers.

***Hemotoxylin-Eosin (H&E) staining of U87MG spheroid sections***: U87MG spheroids were harvested (on 7th day) and fixed overnight in 4% PFA. Next day, spheroids were dehydrated with ethanol gradient started from 40% to 100% (1 hour each) followed by xylene (30 minutes) before impregnated in paraffin wax for 1 hour. The samples were then transferred and embedded into melted paraffin blocks (Thermo Scientific Embedding Centre). Solidified sample blocks were cut using a Hyrax M25 Rotary Microtome into 8 mm paraffin ribbons containing spheroid slices and collected on glass slides. During staining process, the U87MG spheroid sections were de-paraffinized and rehydrated in water and stained with hematoxylin (2 min) followed by eosin (2 min). The sections then went through an ethanol gradient for dehydration, clearing in xylene and coverslipped with DPX mounting medium. Morphology of the cells was observed by optical microscopy (Nikon Eclipse E200) and images were captured.

***Cell viability of UHSS in U87MG cells:*** The cytotoxicity of UHSS in U87MG monolayer cells was tested by MTT assay. U87MG cells were seeded in a 96-well cell culture plate with a density of $5\times10^3$ cells/well. After 24 hours, the cells were treated with different concentrations of UHSS solution for 4 hour. Afterwards, the cell viability was measured by adding MTT agent and reading the absorbance at 570 nm using a Synergy HT microplate reader. The cells incubated in the absence of particles were used as the control. All the experiments were performed in triplicates for each group. The statistical data were shown as mean±(SD).

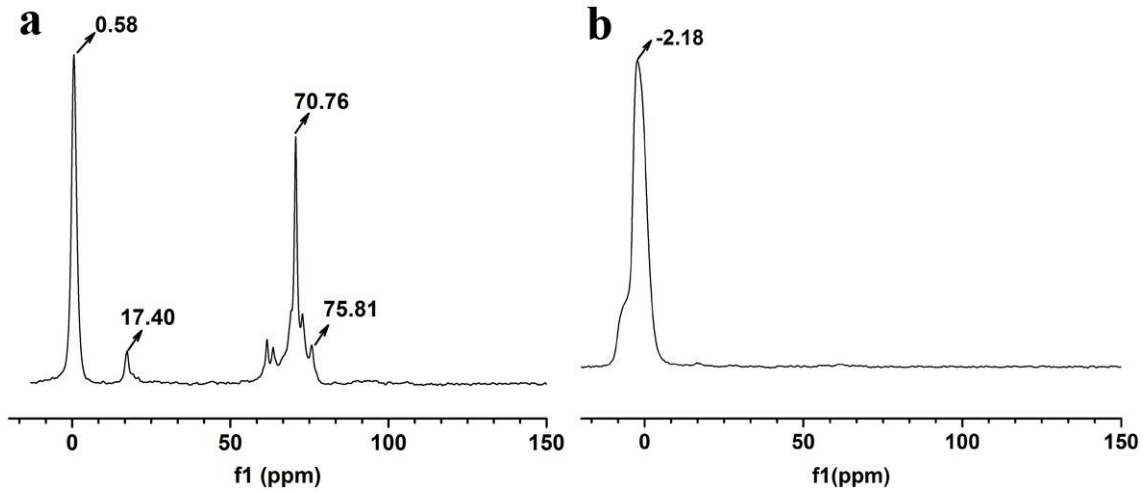


**Fig. S1** Solid state $^{13}$C NMR spectra of UHSS before (a) and after (b) calcination.

The solid state $^{13}$carbon cross-polarization magic angle spinning nuclear magnetic resonance ($^{13}$C CPMAS NMR) spectrum of as-synthesized UHSS (Fig. S1 a) shows a intense peak at 70.76 ppm, assigned to methylene carbons in EO units of F127, and a less defined peak at 75.81 ppm to the methylene carbons of PO units.[2] A weak peak at 17.4 ppm is attributed to methyl carbons of PO units, while the distinct peak at 0.58 ppm reveals the presence of methyl carbons connected to silicon atoms coming from the methyl-silane. In the spectrum of calcined UHSS at 350°C (Fig. S1 b), all the peaks attributed to surfactant F127 disappear. The only intense peak at -2.18pm can be detected, which can be assigned to methyl carbons to silicon atoms in the silica wall. This result indicates that the surfactant F127 in UHSS can be completely removed while retaining the methyl groups in the silica wall, as what observed in our previous report.[3]

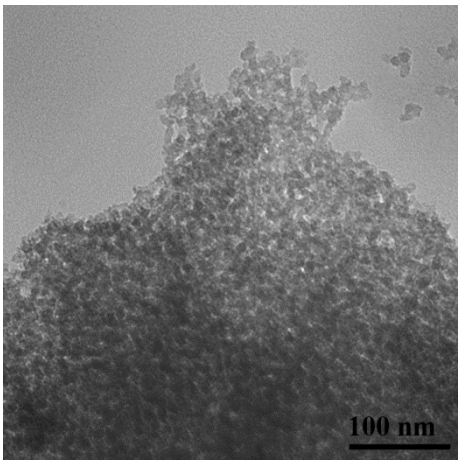


**Fig. S2** TEM image of calcined UHSS.

***UHSS-1 to UHSS-6 synthesized at different TMOS molar percentages***

To understand the influence of molar ratio of reactive silica source to termination agent on the final structure and monodispersity of UHSS, UHSS-1 to UHSS-6 were synthesized at different TMOS

molar percentages (from 16.3% to 100%) while keeping the total molar amount same (see details in Table S1). As shown in Fig. S3, a clear transparent solution and Tyndall effect can be observed for the samples with a TMOS molar percentage equal to or less than 56.9% (UHSS-1, UHSS-2, UHSS-3 and UHSS-4). In contrast, when the TMOS amount further increases to 65.0% (UHSS-5), a milky solution can be seen, suggesting that the aggregation between small particles occur. When TMOS only was used as the silica source without addition of DMDMS, the reaction solution turns to be white, indicating a severe aggregation among silica particles. To further confirm the structures of UHSS-1 to UHSS-6, TEM and DLS techniques were used. From the TEM images (Fig. S4 a-c), it can be seen that UHSS-1, UHSS-2 and UHSS-3 synthesized at lower TMOS molar percentage than that in UHSS, show monodisperse spherical hollow spheres with a diameter of about 5, 7, 11 nm respectively. Their narrow DLS size distribution curves in ethanol further confirm their monodispersity (Fig. S5), and the average diameter of UHSS-1, UHSS-2, and UHSS-4 measured by DLS is 5.5, 7.0, 11.5 respectively (Fig. S5 and Table S1), which is consistent with TEM observation. When TMOS molar percentage increases to 56.9% (higher than that in UHSS), slight aggregation can be observed between small particles from the TEM image shown in Fig. S4 d, even though UHSS-4 aqueous solution is very clear and transparent. The diameter of UHSS-4 determined by DLS measurement is ~ 18.6 nm, larger than a single small sphere size (10-11 nm), further confirms its slight aggregation. When the TMOS amount further increases to 65.0% and 100%, a bigger clusters aggregated by small particles can be detected in the TEM images (Fig. S4 e-f). Also the diameters determined by DLS measurements are in hundreds of nanometers.

The dried samples of UHSS-1 to UHSS-5 were further characterized by TEM. From Fig.S6, it can be seen that when TMOS molar percentage is lower that 40%, aggregated ultra-small hollow spheres and nonporous bulk amorphous silica co-exist in the dried samples UHSS-1 (Fig. S6 a) and UHSS-2 (Fig. S6 b). For the other samples (Fig. S6 c-e), only aggregated ultra-small hollow spheres can be observed. All the results indicate that the optimized TMOS molar percentage is 40% to 50% to obtain high yield of monodisperse UHSS.

The termination agent used here is a silane coupling agent $(CH_3)_2Si(OCH_3)_2$ having only two reactive methoxy groups. The hydrolysis and condensation of the organosilane coupling agent is slower than the other more reactive silica source $Si(O`CH_3)_4$ with four methoxy groups. As demonstrated in Scheme S1, during the formation of silica hybrid block copolymer micelles, silica oligomers derived from reactive $Si(OCH_3)_4$ first deposit between the PPO core and PEO shell, followed by the deposition of silica oligomers with methyl groups coming from the termination agent $(CH_3)_2Si(OCH_3)_2$ to inhibit the interaction between small silica hybrid particles. When

$Si(OCH_3)_4$ (TMOS) amount decreases, the silica deposition coming from TMOS was less and stopped earlier by methyl group modified silica deposition on the surface coming from increased $(CH_3)_2Si(OCH_3)_2$, leading to a smaller size of UHSS and extra silica oligomers. This deposition completion between two types of silica oligomers gives rise to different sizes of UHSS.

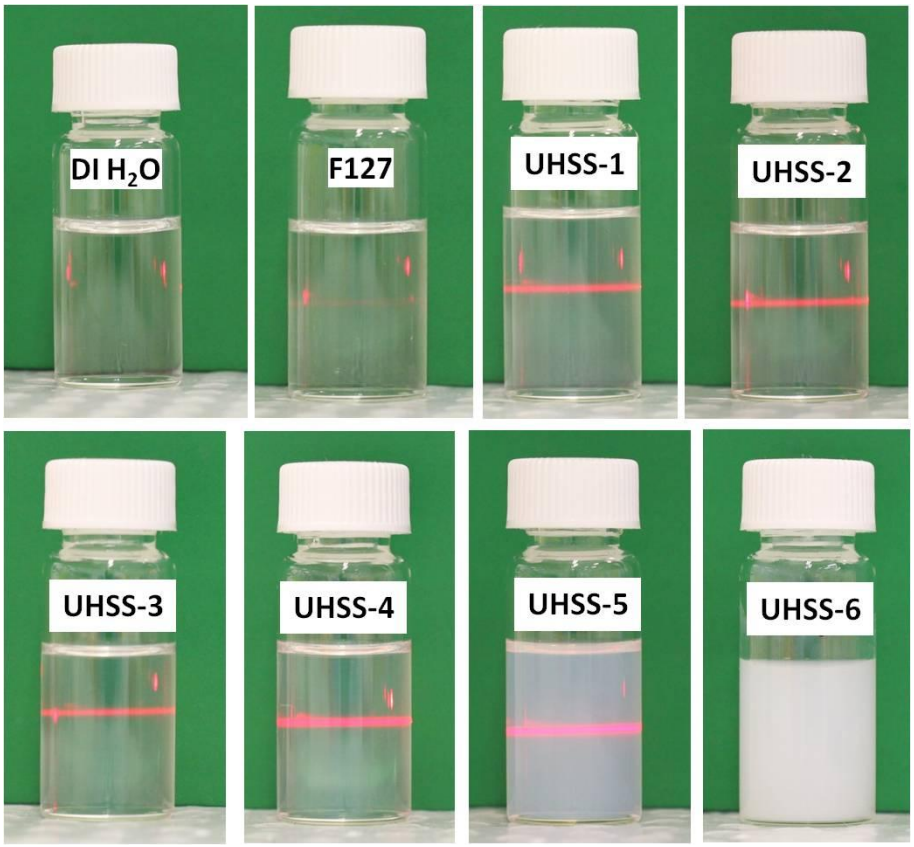


**Fig. S3** Digital images of samples of UHSS-1, UHSS-2, UHSS-3, UHSS-4, UHSS-5, and UHSS-6.

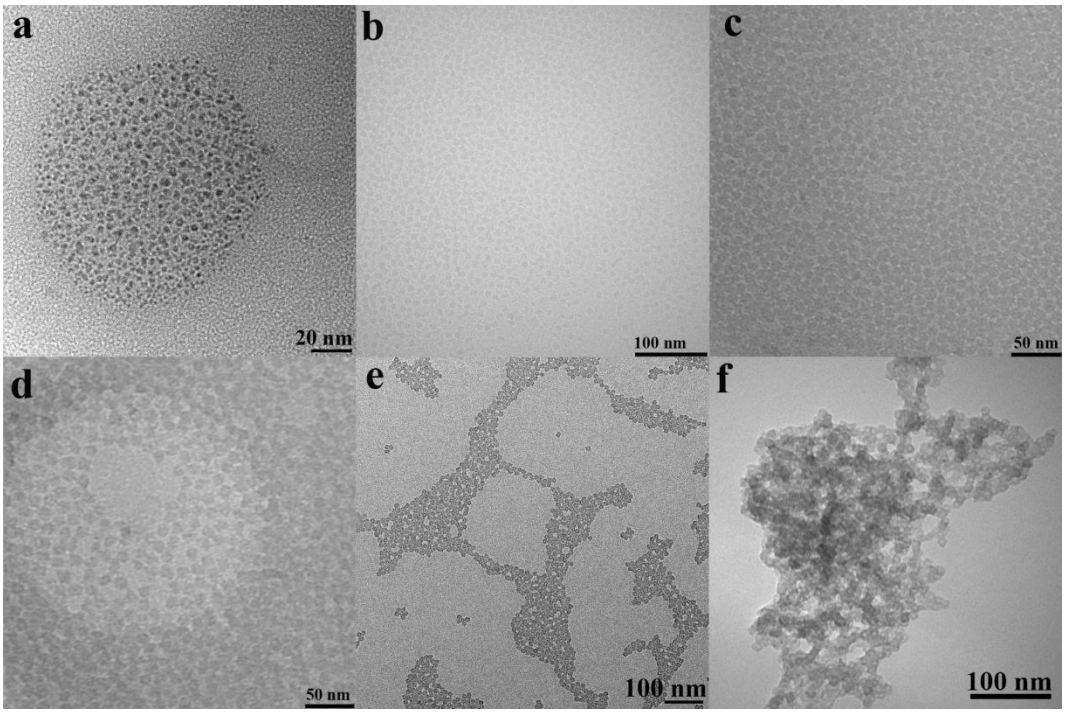

**Fig. S4** TEM images of (a) UHSS-1, (b) UHSS-2, (c) UHSS-3, (d) UHSS-4, (e) UHSS-5, and (f) UHSS-6.

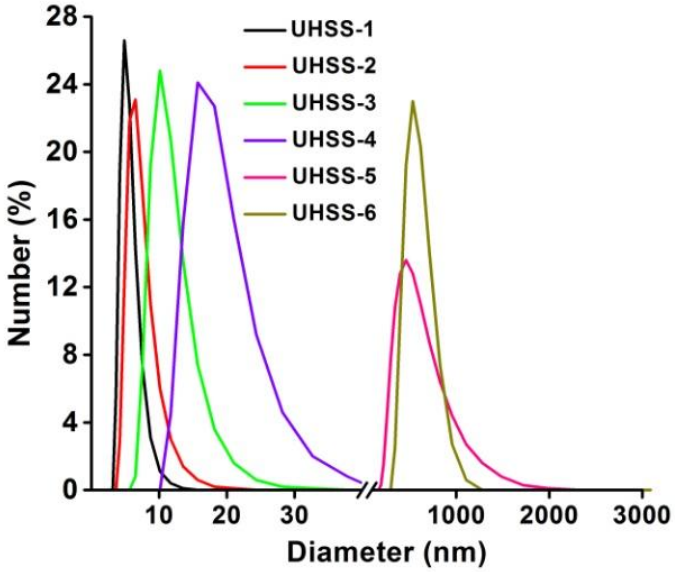


**Fig. S5** DLS measurements of UHSS-1, UHSS-2, UHSS-3, UHSS-4, UHSS-5, and UHSS-6.

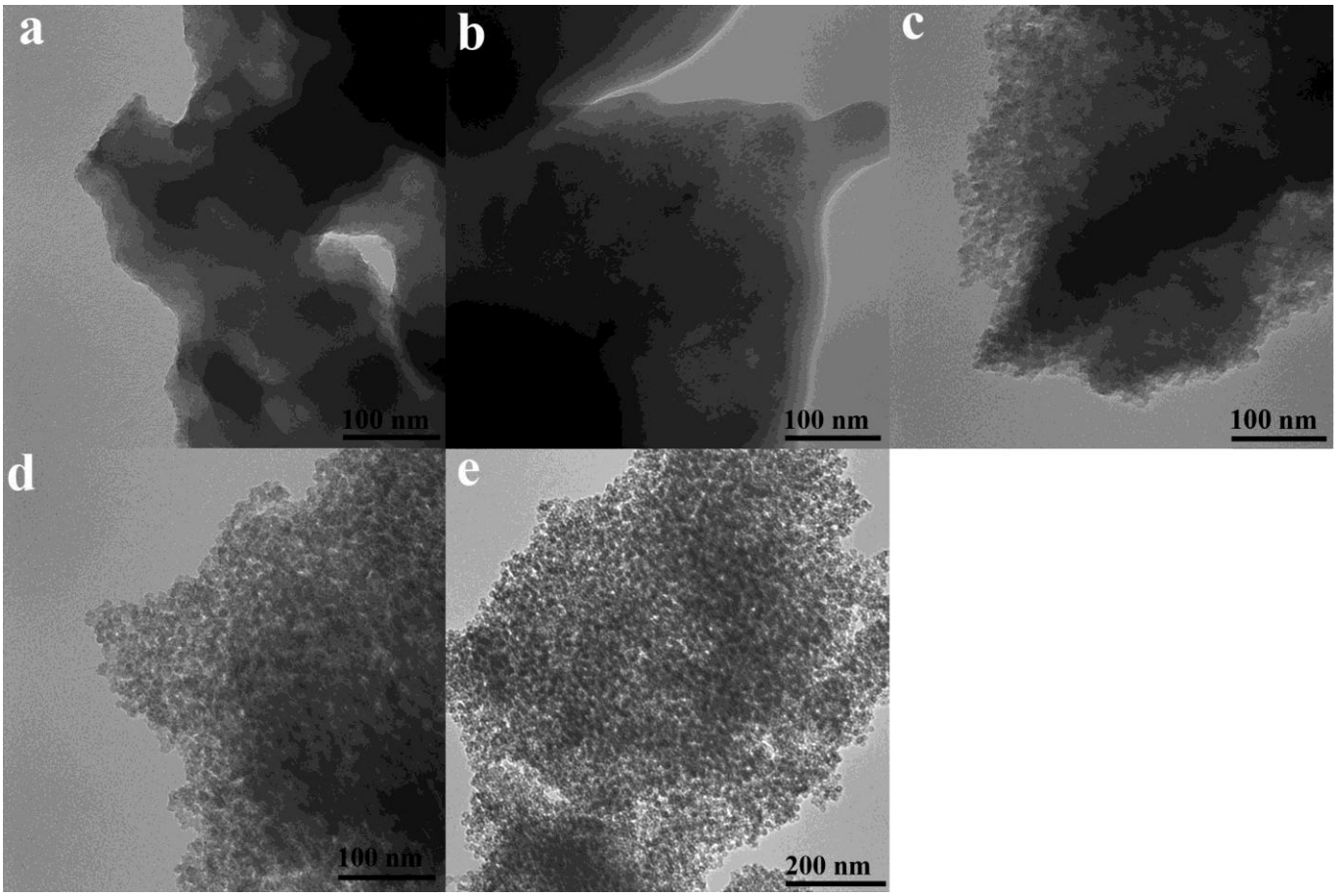


**Fig. S6** TEM images of calcined UHSS-1(a), UHSS-2(b), UHSS-3(c), UHSS-4(d), and UHSS-5(e).

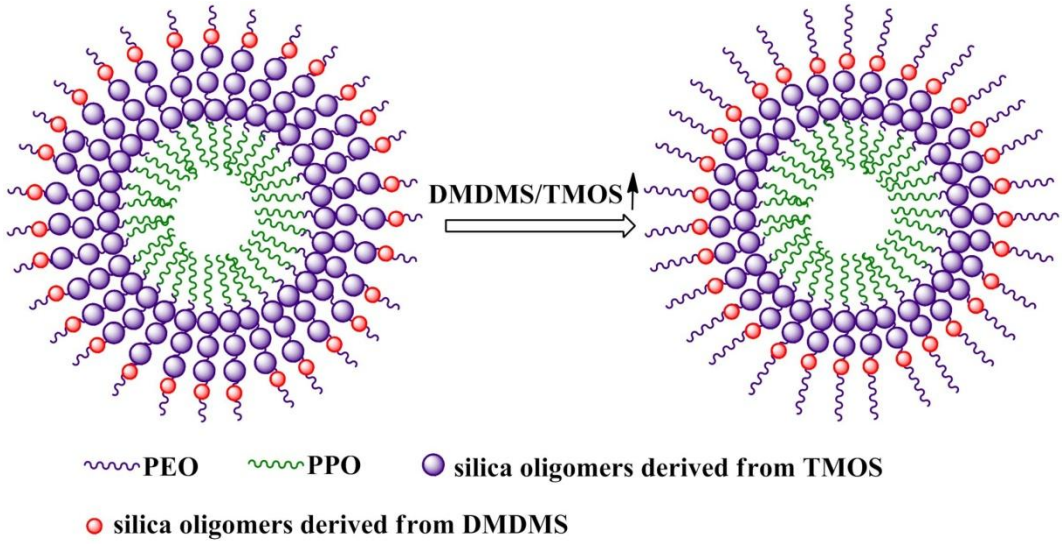


**Scheme S1** Illustration of the formation mechanism of UHSS with different diameters by adjusting the molar ratio of DMDMS/TMOS.

***UHSS synthesized in HCl solution with a pH4.6***

In order to understand the influence of phosphate-citrate buffer on the structure of UHSS, we synthesized UHSS in HCl solution with same pH of 4.6 while keep the other synthesis process same. The sample is denoted as UHSS-HCl. From Fig S7 (a), it can be seen that UHSS-HCl have a similar core-shell structure as UHSS but with a bigger size of ~ 14 nm, compared with UHSS in Fig.1. The average diameter measured by DLS measurement (Fig. S7 b) is 14.4 nm, which is consistent with the TEM observation.

The active silica source (TMOS) and citrate could form Si-citrate complex[4] during the formation process of UHSS. Complexation process may slow down the deposition of silica deposition coming from TMOS in PEO shell of surfactant, leading to a smaller size of UHSS compared with that obtained in HCl solution.

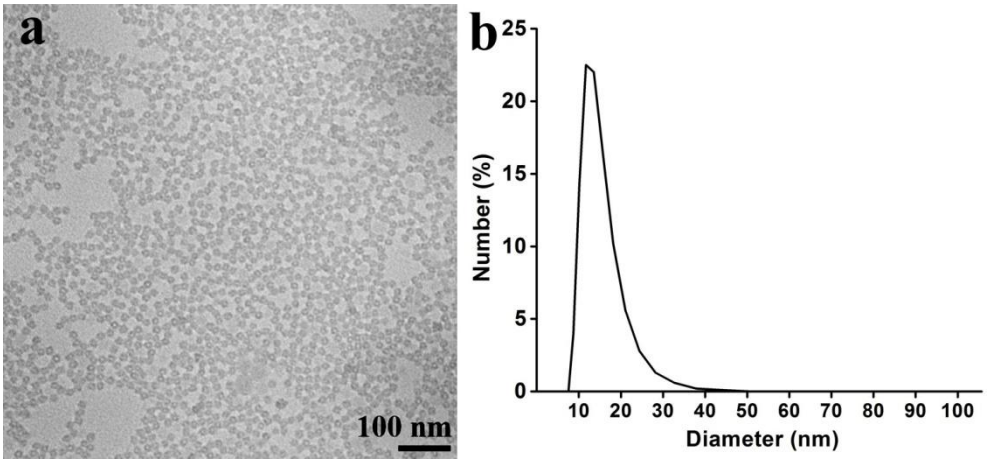


**Fig. S7** (a) TEM image and (b) DLS result of UHSS-HCl.

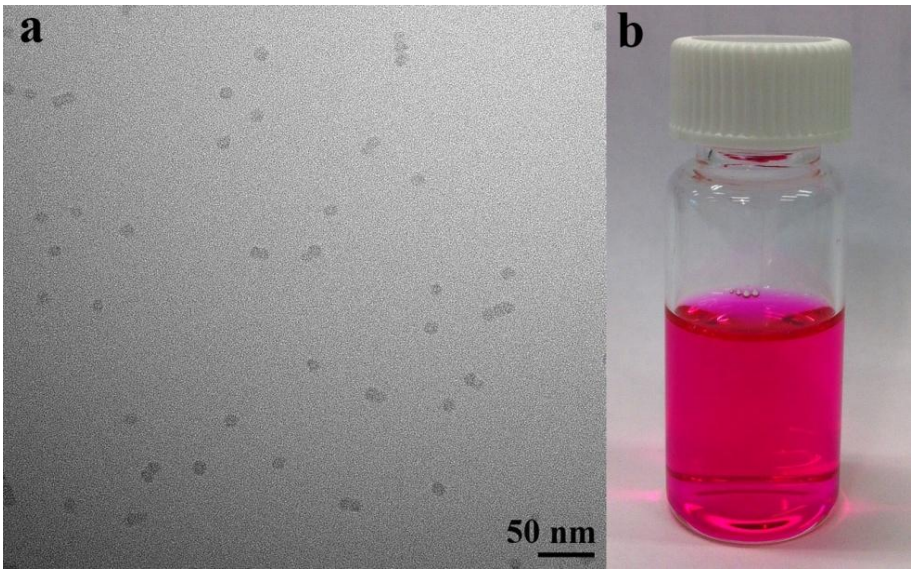


**Fig. S8** (a) TEM image, (b) digital image of RBTC-UHSS sample after dialysis.

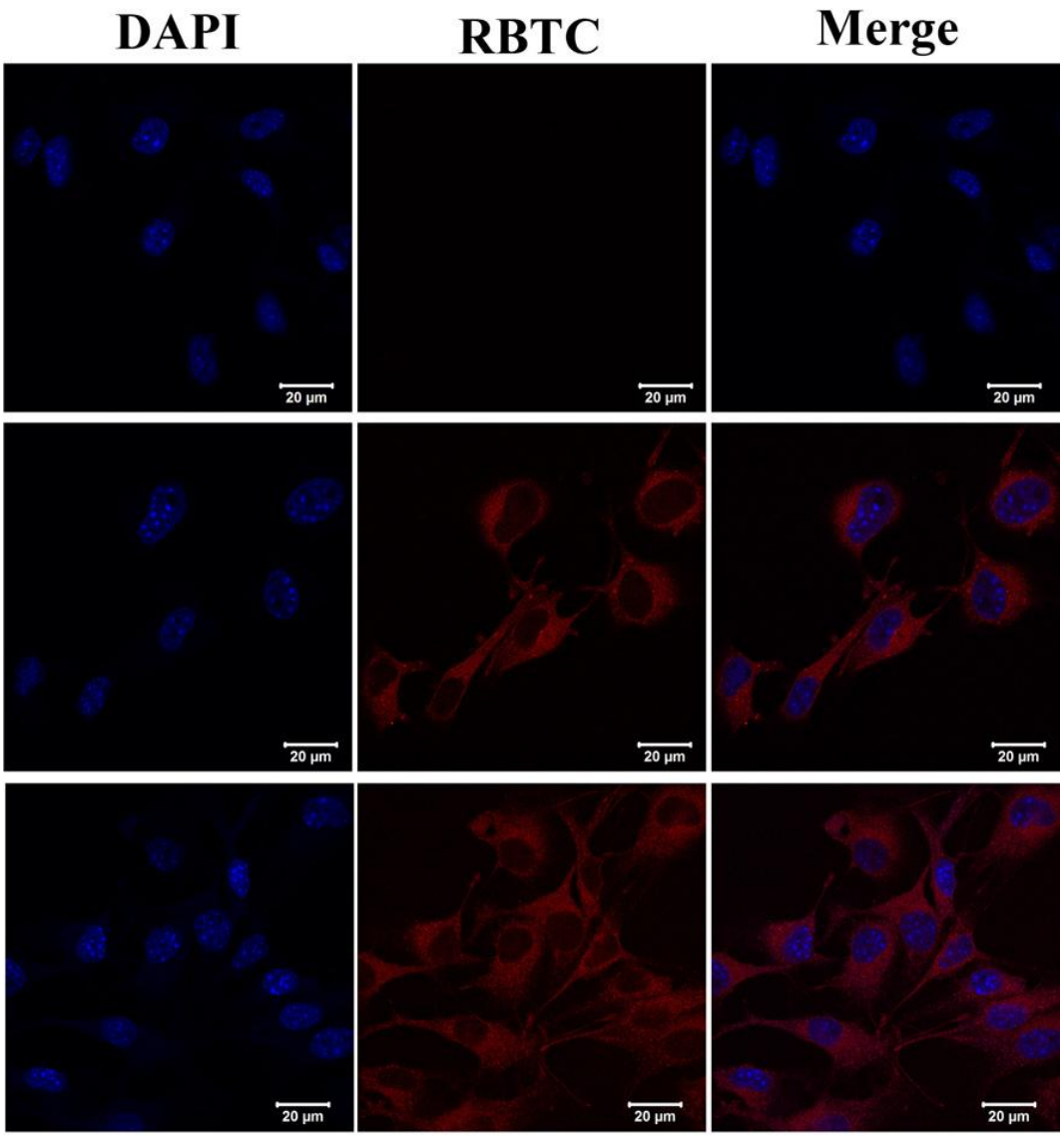


**Fig. S9** Confocal microscopy images of B16F0 cells treated with RBTC-UHSS at 0 μg/ml (first row), 50 μg/ml (second row) and 100 μg/ml (third row). Red fluorescence arises from RBTC dyes that are conjugated to UHSS and nuclei are stained with DAPI, showing blue fluorescence.

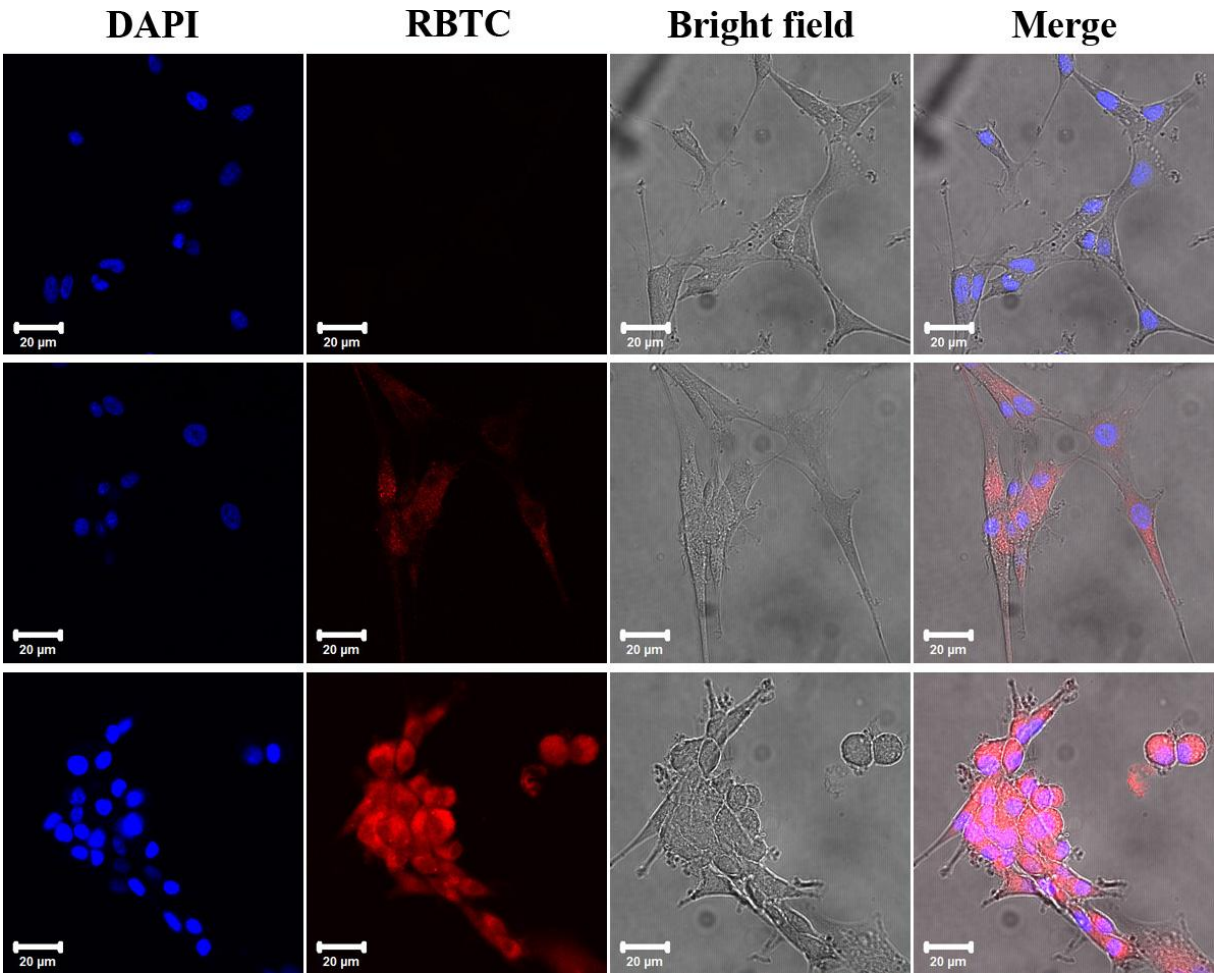


**Fig. S10** Confocal microscopy images of monolayer of U87MG cells treated with RBTC-UHSS at 0 μg/ml (first row), 50 μg/ml (second row) and 100 μg/ml (third row).

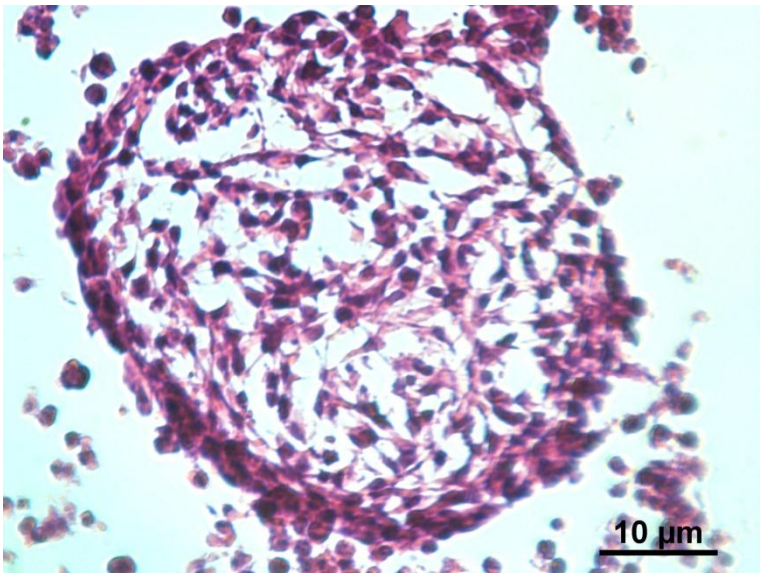


**Fig. S11** Hemotoxylin-Eosin (H&E) staining image of U87MG spheroid section from the middle.

Hematoxylin and eosin (H&E) staining of sectioned U87MG 3D spheroids was used for morphological and structural study. Fig. S11 showed a peripheral multi layers concentric rim of cells with inner cellular network connections throughout the centre of the spheroids. The spheroidal cells maintain their undifferentiated astrocytic phenotype and adjacent cellular connections. This spheroidal cell-cell and cell-extracellular matrix (ECM) interactions in multilayer mimic the characteristics of 3-D solid tumours, which is absent in conventional monolayer culture of tumour cells.

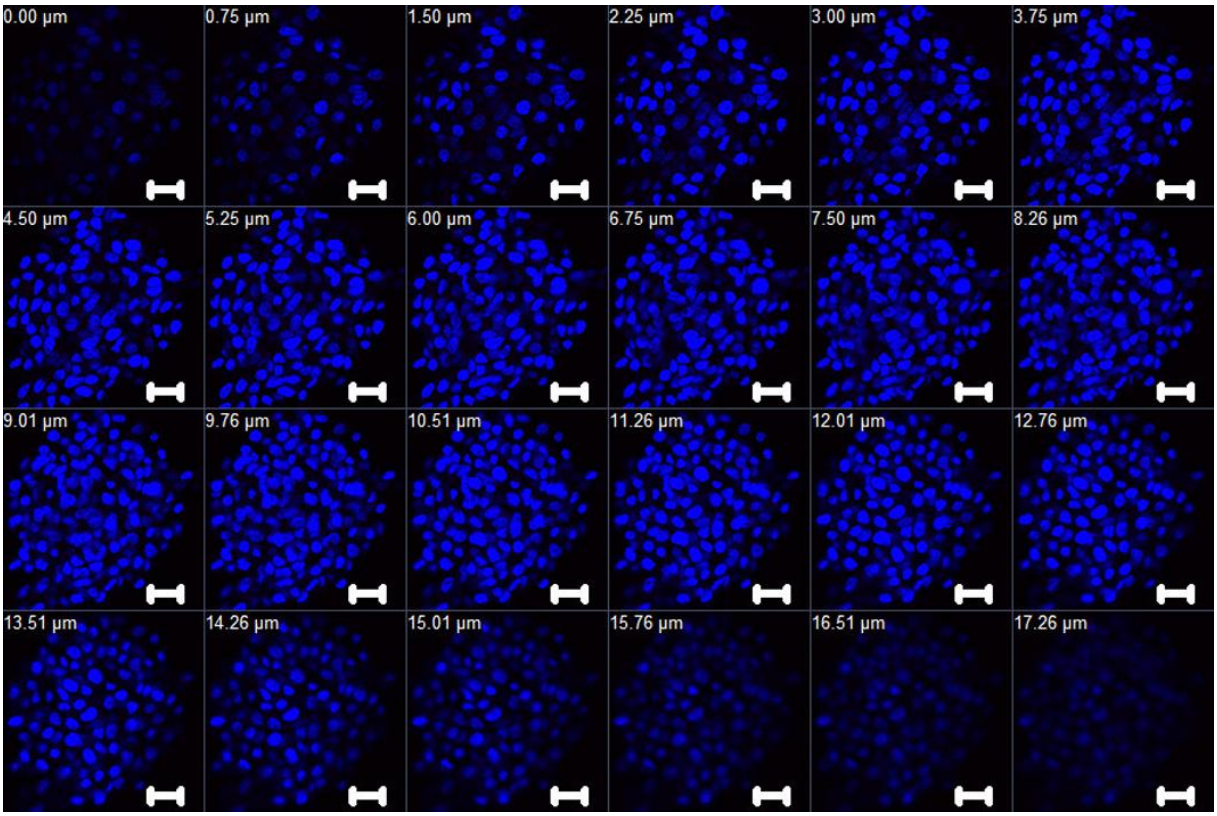


**Fig. S12** Z-stack images of spheroid of U87MG cells treated without RBTC-UHSS. All scale bars are 20 µm.

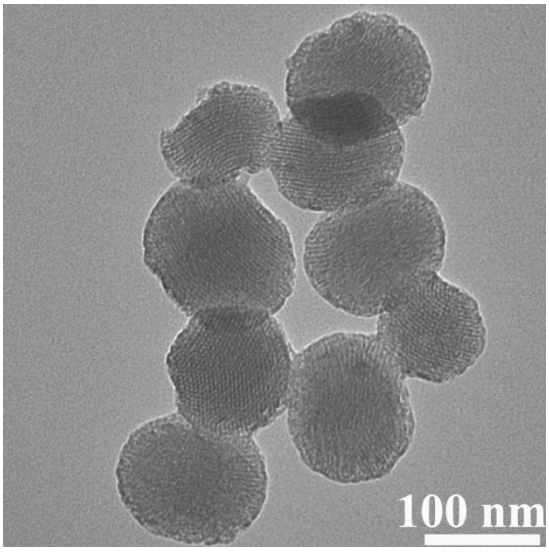


**Fig. S13** TEM image of FITC-MCM-41.

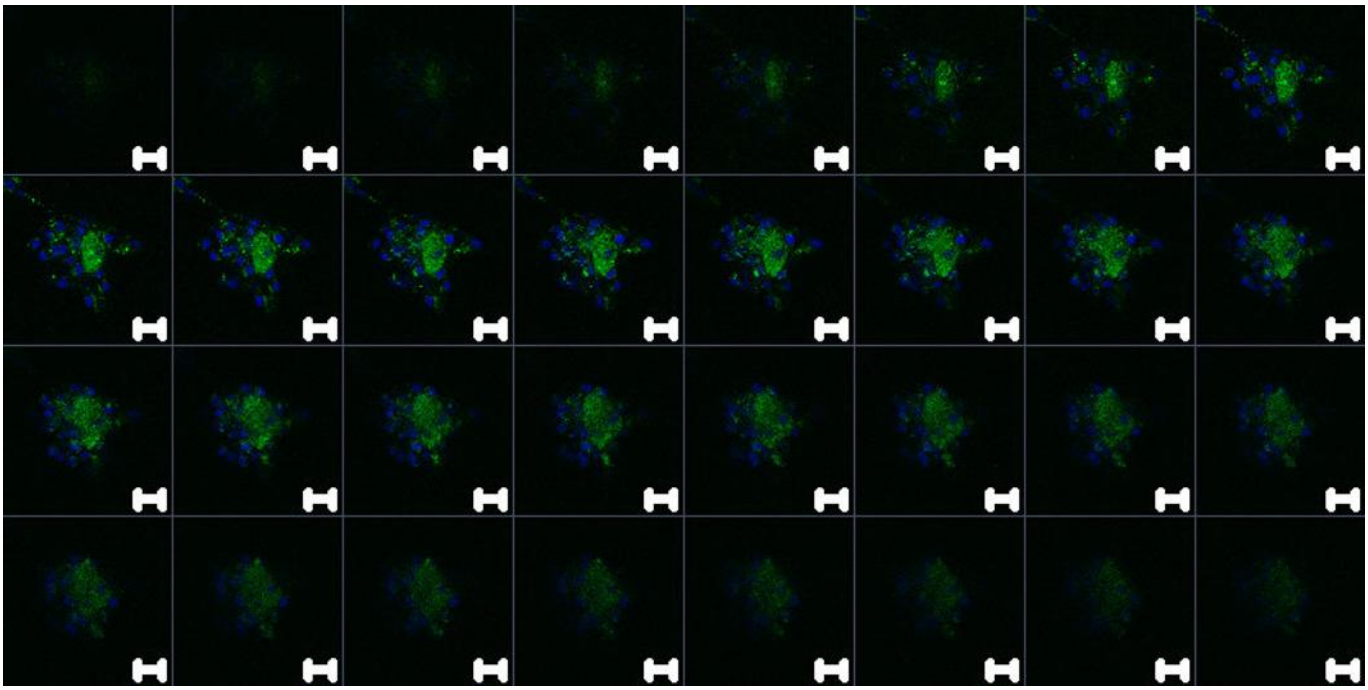

**Fig. S14** Z-stack images of spheroid of U87MG cells treated with FITC-MCM-41at 10 μg/ml. All scale bars are 20 μm.

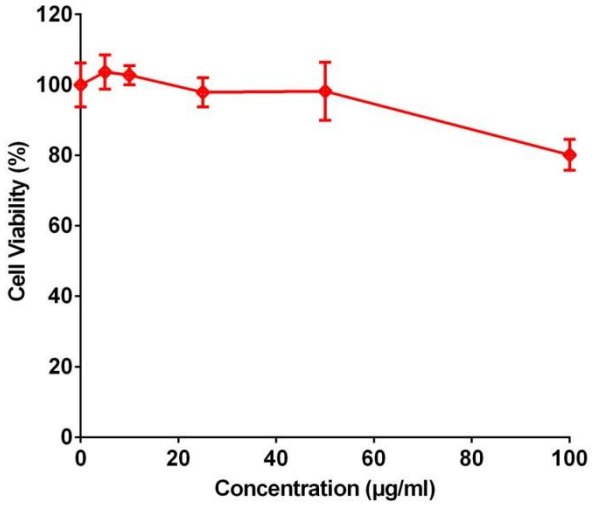


**Fig. S15** Cell viability of U87MG cells after treated with of UHSS at different Concentrations.

## References

1. J. Carlsson and J. M. Yuhas, *Rec. Res. Camcer Res.*, 1984, **95**, 1-23.
2. C. M. Yang, B. Zibrowius, W. Schmidt and F. Schuth, *Chem. Mat.*, 2004, **16**, 2918-2925.
3. J. Zhu, J. W. Tang, L. Z. Zhao, X. F. Zhou, Y. H. Wang and C. Z. Yu, *Small*, 2010, **6**, 276-282.
4. E. R. Leite, N. L. V. Carreno, E. Longo, F. M. Pontes, A. Barison, A. G. Ferreira, Y. Maniette and J. A. Varela, *Chem. Mat.*, 2002, **14**, 3722-3729.

# Chapter 6

# An approach to prepare polyethylenimine functionalized silica-based spheres with small size for siRNA delivery

This chapter reported the designed synthesis of epoxysilane functionalized UHSS (Epoxy-UHSS) with a diameter of ~ 10 nm under similar synthesis conditions as what descripted in Chapter 5, which can be easily covalently conjugated with cationic polyethylenimine (PEI) (PEI-UHSS). This designed positively charged PEI-UHSS demonstrated excellent delivery efficiency of functional siRNA against polo-like kinase 1 (PLK1-siRNA) in osteosarcoma cancer cells (KHOS) and survivin-siRNA in human colon cancer cells (HCT-116) by inducing a significant cell inhibition, which is comparable with commercial agents. These results indicated that suitable functionality of SiNPs is significant to achieve efficient gene delivery.

ACS APPLIED MATERIALS & INTERFACES

Letter

www.acsami.org

# An Approach to Prepare Polyethylenimine Functionalized Silica-Based Spheres with Small Size for siRNA Delivery

Meihua Yu,[†] Yuting Niu,[†] Yannan Yang,[†] Sandy Budi Hartono,[†] Jie Yang,[†] Xiaodan Huang,[†] Peter Thorn,[‡] and Chengzhong Yu*[,†]

[†]Australian Institute for Bioengineering and Nanotechnology and [‡]School of Biomedical Sciences, The University of Queensland, Brisbane, QLD 4072, Australia

Supporting Information

**ABSTRACT:** A novel approach has been developed to prepare polyethylenimine functionalized hybrid silica spheres with a diameter of ~10 nm, which show excellent delivery efficiency of siRNA into osteosarcoma cancer cells and human colon cancer cells with a significant cell inhibition comparable to commercial agents.

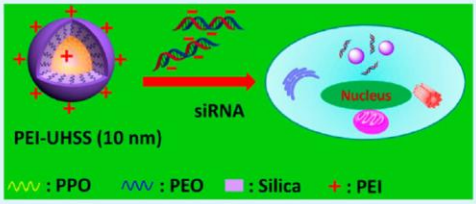


**KEYWORDS:** *silica nanoparticles, siRNA, surface modification, polyethylenimine, gene delivery*

Since the first report of long double-stranded ribonucleic acid (dsRNA) mediated gene silencing in worms in 1998,[1] RNA interference technology has already been regarded as a promising therapeutic approach to treat various diseases by inhibiting specific disease related gene expression.[2] The negative charge and big molecular size of small interfering RNA (siRNA) impair its accessibility to the cells. To achieve the gene silencing efficiency of siRNA, researchers have developed effective intracellular delivery systems including viral or nonviral vectors to exploit the therapeutic potential of siRNA.[3−5] Compared with viral vectors, synthetic nonviral siRNA delivery systems including organic[5] and inorganic nanoparticles[3] offer several advantages, such as easy fabrication and reduced immunogenicity. The development of new nonviral carriers is in great demand for gene silencing applications.

Silica-based nanoparticles (SiNPs) have attracted increasing attention for siRNA delivery because of their unique properties including tunable particle/pore size, stable and rigid framework, and feasibility of modification.[6−8] It has been well demonstrated that the cellular uptake performance of SiNPs is size-dependent; the smaller the particle, the higher endocytosis performance.[9] However, the conventional SiNPs tend to aggregate when the particle size is smaller than 50 nm. An emerging type of monodiperse SiNPs with small sizes from 6 to 30 nm has been developed by micelle templating approach.[10−12] Compared with conventional SiNPs, such small-sized SiNPs show enhanced cellular uptake performance and more uniform distribution in the cytoplasm of the cells both in monolayer and three-dimensional spheroid models.[13,14] Because of their unique advantages of excellent monodispersity and stability in aqueous media, small SiNPs have been utilized as bioimaging agents,[11] water-soluble electrochemiluminescence (ECL) materials[15] and dual nanosensors.[16] However, there is no report using small-sized SiNPs for siRNA delivery.

In previous studies, dimethyl-silane[10,13,14] or polyethylene glycol (PEG)-silane[12] was utilized to terminate the silicate condensation and prevent interparticle aggregation/growth to generate monodisperse small SiNPs. The protection groups are generally inert, making it difficult for the further modification of other functional groups. To facilitate the cellular uptake of the negatively charged siRNA, SiNPs need to be functionalized with positively charged amine groups,[17] poly-L-lysine (PLL),[18] or polyethylenimine (PEI).[19] Compared to other cationic groups, PEI has a higher endosomal escape capability, favoring a high gene silencing efficacy.[3,19] It remains a challenge to prepare PEI-modified monodisperse SiNPs with small sizes for siRNA delivery.

Herein, we report novel one-pot synthesis of epoxysilane functionalized ultrasmall hybrid silica spheres (Epoxy-UHSS) with a diameter of ~10 nm under phosphate-citrate buffer solution (pH 4.6) at room temperature. In this approach, a triblock copolymer $EO_{106}PO_{70}EO_{106}$ [Pluronic F127, EO is poly(ethylene oxide), PO is poly(propylene oxide)] is utilized as the template, and a mixture of tetramethyl orthosilane (TMOS) and diethoxy(3-glycidyloxypropyl)methylsilane (DGMS) are used as silica sources. As shown in Scheme 1, Epoxy-UHSS comprises a PPO core and epoxy-silane terminated silica/PEO shell, which can be easily covalently conjugated with PEI (PEI-UHSS) by nucleophilic addition to the epoxy groups. Different from previously reported methods,[10,12−14] our strategy, using a new precursor, leads to the grafting of both an inert alkyl group and a reactive group

Received: May 18, 2014
Accepted: September 3, 2014
Published: September 3, 2014

**Scheme 1. Illustration of the Polyethyleneimine Conjugation Process on the Surface of Epoxy-UHSS, Followed by the siRNA Delivery into Cells**

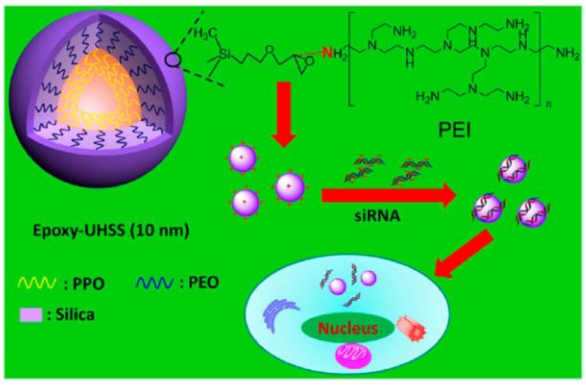


(epoxy), and eventually the successful preparation of PEI-modified monodisperse SiNPs with small sizes for siRNA delivery. This designed positively charged PEI-UHSS was proven to facilitate the cellular uptake of negatively charged siRNA by forming siRNA complexation via electrostatic interaction. PEI-UHSS demonstrated excellent delivery efficiency of a functional siRNA against polo-like kinase 1 (PLK1-siRNA) in osteosarcoma cancer cells (KHOS) and survivin-siRNA in human colon cancer cells (HCT-116) inducing a significant cell inhibition, which is comparable to a commercial product, Oligofectamine.

A representative transmission electron microscopy (TEM) image of Epoxy-UHSS is displayed in Figure 1a, which shows ultrasmall spherical core−shell particles with a uniform size. The core of Epoxy-UHSS is formed by the hydrophobic segment PPO of F127, showing low contrast under TEM observation. The shell is generated by the polymerization of silicate species in the hydrophilic PEO region, showing dark contrast. The average diameter was measured to be approximately 9.3 nm (see Figure S1a in the Supporting Information). The dynamic light scattering (DLS) measurement was further utilized to evaluate the size and dispersibility of Epoxy-UHSS. As shown in Figure S1b in the Supporting Information, Epoxy-UHSS shows a narrow size distribution curve with a small polydisperse index (PDI) value of 0.081 ± 0.006, suggesting that the Epoxy-UHSS are well-dispersed in aqueous solution. The hydrodynamic diameter of Epoxy-UHSS is 23.8 ± 0.7 nm, which is larger than that measured by TEM due to the surrounded water molecules.[20] Epoxy-UHSS solution is stable as a colloidal suspension over the period of this study (more than 10 months) (see Figure S1c in the Supporting Information).

It should be noted that the methyl group connected to silicon in DGMS (marked by red circle in its chemical structure in Figure S2 in the Supporting Information) is essential to obtain Epoxy-UHSS with excellent monodispersity. When DGMS was replaced by equal molar amount of (3-glycidyloxypropyl)trimethoxysilane (GPTMS, see Figure S2 in the Supporting Information) during the synthesis of Epoxy-UHSS, the small particles tend to aggregate to form big clusters (see Figure S3 in the Supporting Information).

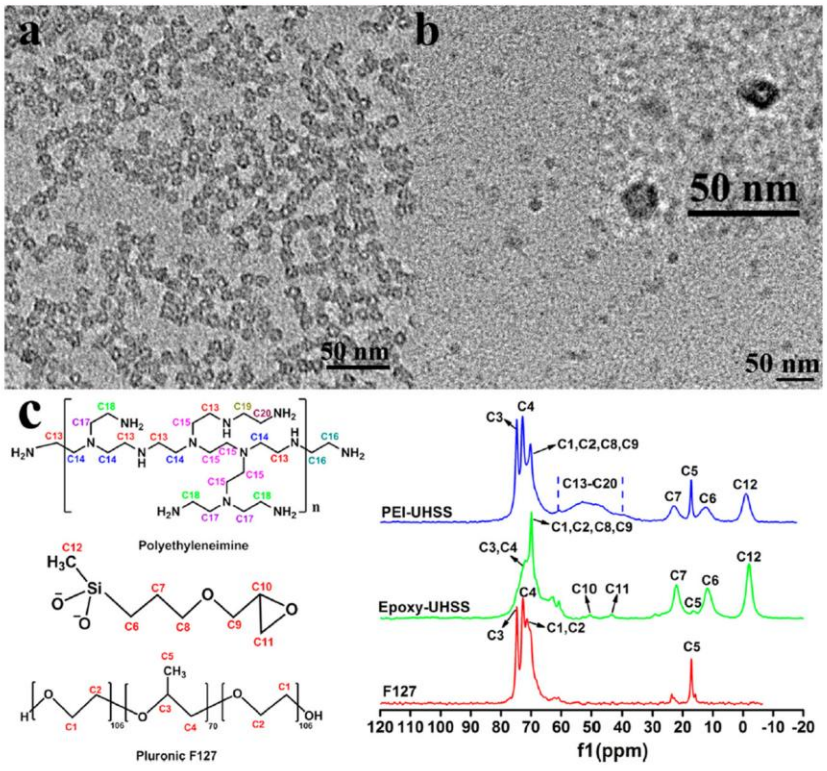


**Figure 1.** TEM images of (a) Epoxy-UHSS and (b) PEI-UHSS and (c) solid-state $^{13}C$ CPMAS NMR spectra of F127, Epoxy-UHSS, and PEI-UHSS.

In order to facilitate the cellular delivery of negatively charged siRNA, Epoxy-UHSS was modified with PEI (denoted as PEI-UHSS) via the nucleophilic reaction between epoxy groups and amino groups (see Scheme S1 in the Supporting Information).[18] From the TEM image (Figure 1b), it can be seen that PEI-UHSS have a spherical core−shell structure (inset of Figure 1b) with a uniform diameter of about 10 nm, similar to what observed in Epoxy-UHSS (Figure 1a). However, the shell structure of PEI-UHSS becomes vague, which may be caused by the coating of organic PEI polymer. A narrow size distribution (see Figure S4 in the Supporting Information) was observed in the DLS curve of PEI-UHSS, suggesting uniform particle size and high dispersity. The hydrodynamic diameter of PEI-UHSS is 13.3 ± 1.9 nm, close to that measured by TEM.

The chemical structures of organic species of the designed materials were investigated by solid state $^{13}C$ CPMAS NMR technique. As shown in Figure 1c, the well-resolved peaks in the spectrum of F127 are attributed to methane carbons C3 (74.7 ppm), methylene carbons C4 (72.7 ppm) and methyl carbons C5 (17.1 ppm) of PO chains, and methylene carbons C1 and C2 (71.4 ppm) of EO chains.[21] In the spectrum of Epoxy-UHSS, the intense peak at 70.0 ppm is assigned to methylene carbons in EO units, and the less defined broad peak centered at 72.0 ppm to the methylene carbons of PO units. A weak peak at 16.5 ppm is attributed to methyl carbons of PO units. Another two typical peaks at 50.5 and 43.7 ppm suggest the presence of the carbons C10 and C11 of the epoxide ring, respectively,[18] and the distinct peak at −2.0 ppm reveals the presence of methyl carbons C12 connected to silicon atoms. The characteristic peaks at 22.1 and 11.8 ppm are attributed to the methylene carbons C7, C6 close to silicon atoms, respectively. The other two methylene carbons C8 and C9 in epoxy-silane are overlapped by the carbons in EO chains. All the characteristic peaks confirm the chemical structure of epoxy/methyl-silane. According to different combinations of amine nearest neighbors (chemical structure of PEI, left top of Figure 1c), PEI has eight carbon peaks in the range of 38−60 ppm.[22] Besides the characteristic peaks coming from surfactant F127 and epoxy/methyl-silane, a very broad extra peak can be observed in the range of 38−60 ppm in the spectrum of PEI-UHSS, corresponding to the carbons in PEI.[23] On the basis of the reaction mechanism between the epoxy moiety of and primary amine groups, the epoxy ring will open to form $CH_2$−O−$CH_2$−CH(OH)−$CH_2$−NH-. The chemical shifts of C10 and C11 in epoxy-silane will be changed to ∼70 and 52 ppm, respectively,[24] which is overlapped by the typical carbons in the EO units and PEI, respectively.

The Zeta potential (see Figure S5 in the Supporting Information) and elemental analysis results (see Table S1 in the Supporting Information) further confirm the successful modification of PEI on Epoxy-UHSS. The grafted PEI weight percentage in PEI-UHSS is calculated to be ∼11.52% (see Table S1 in the Supporting Information).

To evaluate the cellular delivery performance of PEI-UHSS, e used the cyanine dye-labeled oligoDNA (Cy3-oligoDNA) was used as a model of nucleic acid entry into cells. As shown in Figure S6 in the Supporting Information, no Cy3 signals (red fluorescence) can be detected under confocal microsocpy when the cells are treated with Cy3-oligoDNA alone, indicating that nucleic acids themselves cannot enter into cells. In contrast, strong Cy3 signals can be observed within the cytoplasm of cells when PEI-UHSS are utilized to deliver Cy3-oligoDNA (Figure 2). These results demonstrate that the designed PEI-UHSS can efficiently deliver the negative charged genetic molecules into cells.

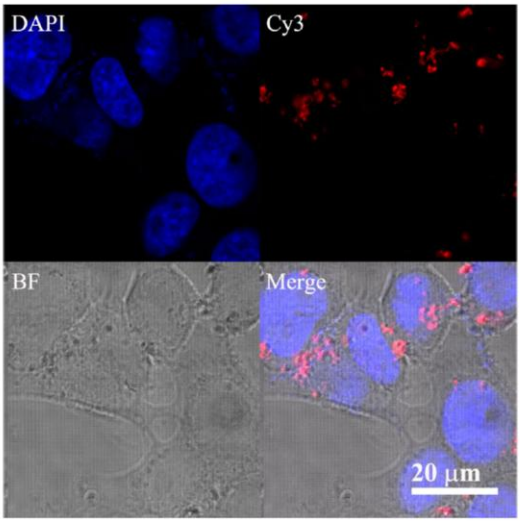


**Figure 2.** Confocal microscopy images of KHOS cells treated with Cy3-oligoDNA/PEI-UHSS.

The cytotoxicity of PEI-UHSS was evaluated in KHOS and human colon cancer cells (HCT-116). As shown in panels a and b in Figure 3, at the concentration of 10 μg/mL PEI-UHSS in two cell lines showed about 10% cell toxicity. This dosage was chosen for the following siRNA delivery studies.

A functional PLK1-siRNA was chosen to investigate the gene delivery efficiency of PEI-UHSS in KHOS cells. Before that, the protection of PLK1-siRNA against nuclease degradation was evaluated by measuring the percent increase in absorbance at 260 nm after RNase A treatment, as siRNA degradation results in a hyperchromic effect.[25,26] In our study, free PLK1-siRNA exhibited a 55% increase in absorbance at 260 nm (see Figure S7 in the Supporting Information), which is much higher than that of the complex of PEI-UHSS/PLK1-siRNA (28%). This result confirms that PEI-UHSS have the capacity to protect siRNA from rapid degradation by RNase A, which is important for successful gene delivery. It has been well reported that PLK1 gene is highly expressed in osteosarcoma cells and knockdown of PLK1 induces apoptosis of KHOS cells.[18,27] Another siRNA, S10-siRNA was chosen as a negative control, which silences human papillomavirus type 16 E6 gene expressed at only low levels in KHOS cells and therefore not expected to have large functional effects.[18] As displayed in Figure 3c, when PEI-UHSS is utilized to deliver PLK1-siRNA, the cell viability decreases in a dose-dependent manner (72, 55, and 43% at a dose of 25, 50, 100 nM, respectively). In contrast, only a small decrease in cell viability is seen when S10-siRNA is delivered into KHOS cells by PEI-UHSS. For comparison, a commercial transfection agent Oligofectamine, was chosen as a positive control. When Oligofectamine is used to deliver PLK1-siRNA, cell viability also shows a PLK1-siRNA dose-dependent behavior (51, 46, and 37% at a dose of 25, 50, 100 nM, respectively). Moreover, there is no significant difference ($p$ = 0.196) in cell viability between PEI-UHSS and Oligofectamine with a PLK1-siRNA dose of 100 nM. The negative control,

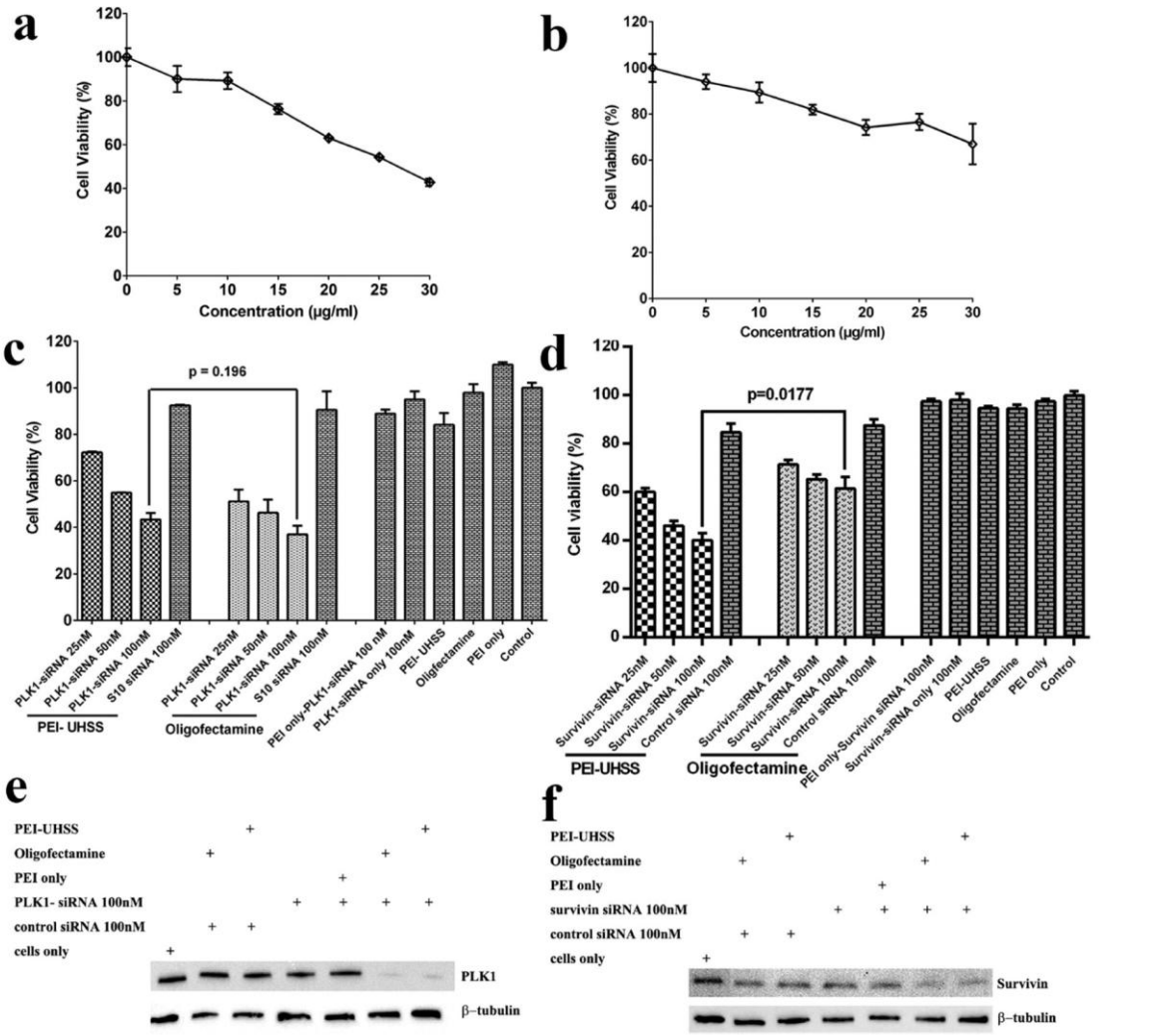


**Figure 3.** Cell viability of (a) KHOS and (b) HCT-116 cells after treated with PEI-UHSS at different concentrations; delivery efficiency of (c) PLK1-siRNA in KHOS cells and (d) survivin siRNA in HCT-116 cells; western-blot analysis of (e) PLK1 protein in KHOS cells and (f) survivin protein in HCT-116 cells.

delivering S10-siRNA by Oligofectamine, shows no effect on cell viability. To demonstrate the relative advantage of PEI-UHSS, we also investigated PLK1-siRNA delivery efficiency by PEI polymer only. The concentration of PEI used for PLK1-siRNA delivery was the same as that contained in PEI-UHSS, which was calculated from the dosage and PEI percentage of PEI-UHSS. PEI only shows only a slight cell inhibition, even at the highest PLK1-siRNA concentration (100 nM). In addition, all the tested carriers and PLK1-siRNA themselves do not show significant effects on cell viability. Compared to previously reported results where functionalized silica materials with larger sizes were utilized to deliver PLK1-siRNA,[18] the cell inhibition capacity in this study is relatively higher. These results demonstrate the excellent siRNA delivery efficiency of novel designed PEI-UHSS, which is comparable with the commercial agent.

The gene delivery efficiency of PEI-UHSS was further investigated in another functional siRNA, survivin-siRNA. Previous studies demonstrated that RNA interference of survivin led to a significant decrease in invasiveness and proliferation of HCT-116.[28] As displayed in Figure 3d, survivin-siRNA delivered by PEI-UHSS shows a dose-dependent behavior with a cell inhibition of 40%, 54% and 60% at the dose of 25, 50, 100 nM, respectively. When Oligofectamine is utilized to deliver survivin-siRNA, the cell proliferation is also inhibited in a survivin-siRNA dose-dependent behavior (29%, 35%, and 39% inhibition at the dose of 25, 50, 100 nM, respectively). However, there is a significant difference ($p$ = 0.0177) in cell inhibition between PEI-UHSS and Oligofectamine with a survivin-siRNA dose of 100 nM. In contrast, survivin-siRNA only or delivered by PEI only showed a negligible cell inhibition with a concentration of 100 nM. The negative control siRNA delivered by PEI-UHSS or Oligofectamine shows no effect on cell inhibition.

We further studied the knockdown efficiency of PLK1 protein in KHOS cells and survivin protein in HCT-116 cells by Western blot analysis. As shown in Figure 3e, upon incubation with PLK1-siRNA delivered by PEI-UHSS and

Oligofectamine, PLK1 protein expression was significantly suppressed in KHOS cells, compared to cells only group. Similarly, survivin protein expression in HCT-116 was obviously knocked down when survivin siRNA was delivered by PEI-UHSS and Oligofectamine (Figure 3f). In contrast, there is no significant PLK1 or survivin protein suppression in other groups (Figure 3e, f). The gene silencing at PLK1 and survivin protein is highly efficient with PEI-UHSS delivery system, which induces apoptosis and consequently cell death of KHOS and HCT-116, respectively.

In summary, a novel approach has been developed to generate polyethylenimine functionalized ultrasmall hybrid silica spheres (PEI-UHSS) with a diameter of ~10 nm. PEI-UHSS have been demonstrated to an excellent vector to efficiently deliver siRNA into cells, which is comparable with commercial agents. This approach could be helpful to design efficient siRNA delivery systems to improve gene therapy efficacy.

## ■ ASSOCIATED CONTENT

### Supporting Information

Experimental section, DLS, digital images, TEM figures, Zeta potential values, elemental analysi,s and confocal images. This material is available free of charge via the Internet at http://pubs.acs.org.

## ■ AUTHOR INFORMATION

### Corresponding Author

*E-mail: c.yu@uq.edu.au.

### Notes

The authors declare no competing financial interest.

## ■ ACKNOWLEDGMENTS

We acknowledge the support from the Australian Research Council, the Australian National Fabrication Facility and the Australian Microscopy and Microanalysis Research Facility at the Centre for Microscopy and Microanalysis, The University of Queensland. We thank Dr. Ekaterina Strounina for the $^{13}C$ NMR technical help from Centre for Advanced Imaging, The University of Queensland.

## ■ REFERENCES

(1) Fire, A.; Xu, S. Q.; Montgomery, M. K.; Kostas, S. A.; Driver, S. E.; Mello, C. C. Potent and Specific Genetic Interference by Double-Stranded RNA in Caenorhabditis Elegans. *Nature* **1998**, *391*, 806–811.

(2) Kurreck, J. RNA Interference: From Basic Research to Therapeutic Applications. *Angew. Chem., Int. Ed.* **2009**, *48*, 1378–1398.

(3) Sokolova, V.; Epple, M. Inorganic Nanoparticles as Carriers of Nucleic Acids into Cells. *Angew. Chem., Int. Ed.* **2008**, *47*, 1382–1395.

(4) Stewart, S. A.; Dykxhoorn, D. M.; Palliser, D.; Mizuno, H.; Yu, E. Y.; An, D. S.; Sabatini, D. M.; Chen, I. S. Y.; Hahn, W. C.; Sharp, P. A.; Weinberg, R. A.; Novina, C. D. Lentivirus-Delivered Stable Gene Silencing by RNAi in Primary Cells. *RNA-Publ. RNA Soc.* **2003**, *9*, 493–501.

(5) Urban-Klein, B.; Werth, S.; Abuharbeid, S.; Czubayko, F.; Aigner, A. RNAi-Mediated Gene-targeting Through Systemic Application of Polyethylenimine (PEI)-Complexed siRNA In Vivo. *Gene Ther.* **2005**, *12*, 461–466.

(6) Chen, A. M.; Zhang, M.; Wei, D. G.; Stueber, D.; Taratula, O.; Minko, T.; He, H. X. Co-delivery of Doxorubicin and Bcl-2 siRNA by Mesoporous Silica Nanoparticles Enhances the Efficacy of Chemotherapy in Multidrug-Resistant Cancer Cells. *Small* **2009**, *5*, 2673–2677.

(7) Xia, T. A.; Kovochich, M.; Liong, M.; Meng, H.; Kabehie, S.; George, S.; Zink, J. I.; Nel, A. E. Polyethyleneimine Coating Enhances the Cellular Uptake of Mesoporous Silica Nanoparticles and Allows Safe Delivery of siRNA and DNA Constructs. *ACS Nano* **2009**, *3*, 3273–3286.

(8) Meng, H. A.; Liong, M.; Xia, T. A.; Li, Z. X.; Ji, Z. X.; Zink, J. I.; Nel, A. E. Engineered Design of Mesoporous Silica Nanoparticles to Deliver Doxorubicin and P-Glycoprotein siRNA to Overcome Drug Resistance in a Cancer Cell Line. *ACS Nano* **2010**, *4*, 4539–4550.

(9) Lu, F.; Wu, S. H.; Hung, Y.; Mou, C. Y. Size Effect on Cell Uptake in Well-Suspended, Uniform Mesoporous Silica Nanoparticles. *Small* **2009**, *5*, 1408–1413.

(10) Huo, Q. S.; Liu, J.; Wang, L. Q.; Jiang, Y. B.; Lambert, T. N.; Fang, E. A New Class of Silica Cross-Linked Micellar Core-Shell Nanoparticles. *J. Am. Chem. Soc.* **2006**, *128*, 6447–6453.

(11) Tan, H.; Liu, N. S.; He, B. P.; Wong, S. Y.; Chen, Z. K.; Li, X.; Wang, J. Facile Synthesis of Hybrid Silica Nanocapsules by Interfacial Templating Condensation and Their Application in Fluorescence Imaging. *Chem. Commun.* **2009**, 6240–6242.

(12) Ma, K.; Sai, H.; Wiesner, U. Ultrasmall Sub-10 nm Near-Infrared Fluorescent Mesoporous Silica Nanoparticles. *J. Am. Chem. Soc.* **2012**, *134*, 13180–13183.

(13) Zhu, J.; Tang, J. W.; Zhao, L. Z.; Zhou, X. F.; Wang, Y. H.; Yu, C. Z. Ultrasmall, Well-Dispersed, Hollow Siliceous Spheres with Enhanced Endocytosis Properties. *Small* **2010**, *6*, 276–282.

(14) Yu, M. H.; Karmakar, S.; Yang, J.; Zhang, H. W.; Yang, Y. N.; Thorn, P.; Yu, C. Z. Facile Synthesis of Ultra-Small Hybrid Silica Spheres for Enhanced Penetration in 3D Glioma Spheroids. *Chem. Commun.* **2014**, *50*, 1527–1529.

(15) Zanarini, S.; Rampazzo, E.; Bonacchi, S.; Juris, R.; Marcaccio, M.; Montalti, M.; Paolucci, F.; Prodi, L. Iridium Doped Silica-PEG Nanoparticles: Enabling Electrochemiluminescence of Neutral Complexes in Aqueous Media. *J. Am. Chem. Soc.* **2009**, *131*, 14208–14209.

(16) Wang, X. D.; Stolwijk, J. A.; Lang, T.; Sperber, M.; Meier, R. J.; Wegener, J.; Wolfbeis, O. S. Ultra-Small, Highly Stable, and Sensitive Dual Nanosensors for Imaging Intracellular Oxygen and pH in Cytosol. *J. Am. Chem. Soc.* **2012**, *134*, 17011–17014.

(17) Na, H. K.; Kim, M. H.; Park, K.; Ryoo, S. R.; Lee, K. E.; Jeon, H.; Ryoo, R.; Hyeon, C.; Min, D. H. Efficient Functional Delivery of siRNA using Mesoporous Silica Nanoparticles with Ultralarge Pores. *Small* **2012**, *8*, 1752–1761.

(18) Hartono, S. B.; Gu, W. Y.; Kleitz, F.; Liu, J.; He, L. Z.; Middelberg, A. P. J.; Yu, C. Z.; Lu, G. Q.; Qiao, S. Z. Poly-L-lysine Functionalized Large Pore Cubic Mesostructured Silica Nanoparticles as Biocompatible Carriers for Gene Delivery. *ACS Nano* **2012**, *6*, 2104–2117.

(19) Niu, Y.; Yu, M.; Hartono, S. B.; Yang, J.; Xu, H.; Zhang, H.; Zhang, J.; Zou, J.; Dexter, A.; Gu, W.; Yu, C. Nanoparticles Mimicking Viral Surface Topography for Enhanced Cellular Delivery. *Adv. Mater.* **2013**, *25*, 6233–6237.

(20) Jung, H. S.; Moon, D. S.; Lee, J. K. Quantitative Analysis and Efficient Surface Modification of Silica Nanoparticles. *J. Nanomater.* **2012**, *2012*, 593471.

(21) Yang, C. M.; Zibrowius, B.; Schmidt, W.; Schuth, F. Stepwise Removal of the Copolymer Template from Mesopores and Micropores in SBA-15. *Chem. Mater.* **2004**, *16*, 2918–2925.

(22) Idris, S. A.; Mkhatresh, O. A.; Heatley, F. Assignment of H-1 NMR Spectrum and Investigation of Oxidative Degradation of Poly(ethylenimine) Using H-1 and C-13 1-D and 2-D NMR. *Polym. Int.* **2006**, *55*, 1040–1048.

(23) Lee, H.; Sung, D.; Veerapandian, M.; Yun, K.; Seo, S. W. PEGylated Polyethyleneimine Grafted Silica Nanoparticles: Enhanced Cellular Uptake and Efficient siRNA Delivery. *Anal. Bioanal. Chem.* **2011**, *400*, 535–545.

(24) Sales, J. A. A.; Prado, A. G. S.; Airoldi, C. The Incorporation of Propane-1,3-diamine into Silylant Epoxide Group Through Hornogeneous and Heterogeneous Routes. *Polyhedron* **2002**, *21*, 2647–2651.

(25) Yu, S. S.; Lau, C. M.; Barham, W. J.; Onishko, H. M.; Nelson, C. E.; Li, H. M.; Smith, C. A.; Yull, F. E.; Duvall, C. L.; Giorgio, T. D.

Macrophage-Specific RNA Interference Targeting via "Click", Mannosylated Polymeric Micelles. *Mol. Pharmaceutics* **2013**, *10*, 975−987.

(26) Kirkland-York, S.; Zhang, Y. L.; Smith, A. E.; York, A. W.; Huang, F. Q.; McCormick, C. L. Tailored Design of Au Nanoparticle-siRNA Carriers Utilizing Reversible Addition - Fragmentation Chain Transfer Polymers. *Biomacromolecules* **2010**, *11*, 1052−1059.

(27) Yamaguchi, U.; Honda, K.; Satow, R.; Kobayashi, E.; Nakayama, R.; Ichikawa, H.; Shoji, A.; Shitashige, M.; Masuda, M.; Kawai, A.; Chuman, H.; Iwamoto, Y.; Hirohashi, S.; Yamada, T. Functional Genome Screen for Therapeutic Targets of Osteosarcoma. *Cancer Sci.* **2009**, *100*, 2268−2274.

(28) Gao, F.; Zhang, Y. Q.; Yang, F.; Wang, P.; Wang, W. J.; Su, Y.; Luo, W. R. Survivin Promotes the Invasion of Human Colon Carcinoma Cells by Regulating the Expression of MMP-7. *Mol. Med. Rep.* **2014**, *9*, 825−830.

# Supporting information

## An approach to prepare polyethylenimine functionalized silica-based spheres with small size for siRNA delivery

Meihua Yu,[a] Yuting Niu,[a] Yannan Yang,[a] Sandy Budi Hartono,[a] Jie Yang,[a] Xiaodan Huang,[a] Peter Thorn[b] and Chengzhong Yu[a]*

[a]ARC Centre of Excellence for Functional Nanomaterials and Australian Institute for Bioengineering and Nanotechnology, The University of Queensland, Brisbane, QLD 4072, Australia

[b]School of Biomedical Sciences, The University of Queensland, Brisbane, QLD 4072, Australia

*Corresponding author: Tel: +61-7-334 63283; Fax: +61-7-334 63973; E-mail address: c.yu@uq.edu.au

### Experimental section

***Materials***: Tetramethyl orthosilane (TMOS, 98%), diethoxy(3-glycidyloxypropyl)methylsilane (DGMS, 97%), (3-Glycidyloxypropyl)trimethoxysilane (GPTMS, 97%), Pluronic F127, fluoroshield with DAPI (4',6-diamidino-2-phenylindole, dihydrochloride), dimethylsulfoxide (DMSO), paraformaldehyde (PFA), twenty-one-nucleotide (oligo) DNA conjugated with cyanine dye (Cy-3), antifade fluorescent mounting medium with 4'-6-diamidino-2-phenylindole (DAPI) and 3-[4,5-dimethylthiazol-2-yl]-2,5-diphenyl tetrazolium bromide (MTT) were purchased from Sigma-Aldrich. Citric acid monohydrate (CA $\cdot H_2O$), dibasic sodium phosphate ($Na_2HPO_4$) were purchased from Ajax Finechem. Polyethylneimine, (branched, M.W. 1800, 99%) was purchased from Alfa Aesar. A Cell-Titer-Glo cell viability assay kit was purchased from Promega. Osteosarcoma cell line KHOS/NP (CRL-1544) was purchased from ATCC (American Type Culture Collection). Fetal calf serum was purchased from Moregate Biotech, Australia. De-ionized (D.I.) water was generated using a Millipore Milli-Q system.

The sequences of human PLK1-siRNA (Sigma-Aldrich) are PLK1-S: 5'-CCAUUAACGAGCUGCUUAATT-3' and PLK1-AS: 5'-UUAAGCAGCUCGUUAAUGGTT-3'.

The sequences of synthetic S10-siRNA (Sigma-Aldrich) are as follows: S10-S, 5'-GCAACAGUUACUGCGACGUUU-3' and S10-AS, 5'-ACGUCGCAGUAACUGUUGCUU- 3'.

Survivin siRNA (h) (sc-29499) and negative control siRNA were purchased from Santa Cruz Biotechnology. The primary antibodies of Survivin (71G4B7) Rabbit mAb, β-Tubulin (9F3) Rabbit mAb and PLK1(208G4) Rabbit mAb and the secondary antibody Anti-rabbit IgG, HRP-linked Antibody were purchased from Cell Sigaling Technology.

***Synthesis of Epoxy-UHSS***: For the synthesis of monodisperse epoxy group modified ultrasmall hybrid silica spheres (Epoxy-UHSS), 0.5g of F127 was dissolved in 30 ml of phosphate-citrate buffer solution (pH=4.6, 46.6 μM $Na_2HPO_4$, 26.7 μM HAc) under stirring at room temperature. Then a mixed silica sources of 0.8ml TMOS and 0.75ml DGMS was added into the surfactant homogeneous solution under stirring. The reaction was continued at room temperature for 3 days. Afterwards, the clear solution was transferred into a dialysis membrane tube (Sigma-Aldrich, molecular weight cut off 14,000) and dialyzed in 1L of D.I. water for 3 days, to completely remove the salts, methanol and ethanol (resulted from the hydrolysis of TMOS and DGMS). The D.I. water was refreshed twice per day. Finally the Epoxy-UHSS particles were stored in deionized water for further use.

***Synthesis of PEI-UHSS***: The conjugation process of polyethyleneimine (PEI, M.W. 1800) on Epoxy-UHSS was performed using a modified approach reported in our previous study.[1] Typically, 4 ml of Epoxy-UHSS solution prepared in the last step was added in to 8 ml of 2.5mg/ml PEI solution in carbonate buffer ($NaHCO_3$-$Na_2CO_3$, $\boldsymbol{C}_t$ [$CO_3^{2-}$] = 50 mM, pH= 9.5) at room temperature, and the mixture stirred for 8 hours. After that, the final product was dialyzed in 1L of deionized water for 3 days using dialysis membrane tube, to complete remove the salts and free PEI molecules. The sample was denoted as PEI-UHSS.

***Material Characterisation***: Transmission electron microscopy (TEM) images were obtained with a FEI Tecnai F30 operated at 300. For TEM measurement preparation, the carbon coated Cu TEM grids were treated by glow discharge using CRESSINGTON 208 to make the TEM grids hydrophilic. Afterwards, the samples diluted in deionized were dropped on the treated TEM grids for 2 minutes, after which the drops were absorbed by filter paper, and the samples dried on TEM grids in air. Dynamic light scattering (DLS) studies and zeta potential measurements were carried out on a Malvern NanoZS zetasizer at 25 °C in deionized water solution. $^{13}C$ CPMAS NMR spectra were measured by solid state Bruker Avance III spectrometer with 7T (300MHz for 1H) magnet, Zirconia rotor, 4mm, rotated at 7 kHz. Elemental Analyses were determined by CHNS-O Analyzer (Flash EA1112 Series, Thermo Electron Corporation).

***Cell culture:*** KHOS and HCT-116 cells were maintained in Dulbecco's Modified Eagle Medium (DMEM) supplemented with fetal calf serum (10%), L-glutamine (2%), penicillin (1%), streptomycin (1%) in 5% $CO_2$ at 37 ℃. The medium was routinely changed every 2 days and the cells were separated by trypsinisation before reaching confluency.

***Cellular uptake of Cy3-oligoDNA/PEI-UHSS***: KHOS cells were seeded in a 6-well plate ($1\times10^5$ cells per well) and incubated for 24 h prior to cell uptake assay. 50 μg of PEI-UHSS and 2 μl of 100 μM Cy3-oligoDNA was mixed in 100 μl of phosphate buffered saline (PBS) solution and incubated at 4°C overnight. After incubation, the mixture was added to a well of 6-well plates containing 2.0 ml of serum-free DMEM medium, and the final concentration of PEI-UHSS and Cy3-oligoDNA

was 25 μg/ml and 100nM, respectively. After incubation for 4 h at 37°C, the cells were washed twice with PBS to remove the remaining nanoparticles, free Cy3-oligoDNA and dead cells. For fixed cell imaging, the cells were treated with 500 μl of 4% PFA PBS solution for 30 min at 4 °C, and their nuclei were stained with DAPI for 10 mins. Finally, the cells were observed under a confocal microscope (LSM Zeiss 710).

***RNase A protection assay***: 10μg of PEI-UHSS and 50pmol of PLK1-siRNA were mixed in RNase free water and incubated at room temperature for 30 minutes. Afterwards, 1μg of RNase A was added into the complex solution with a total volume of 10μl, then the absorbance at 260 nm ($Abs_{260}$) was measured by a Nanodrop 1000 with an incubation time of 0 and 30 minutes at room temperature. For the free PLK1-siRNA control, 50pmol of PLK1-siRNA and 1μg of RNase A were mixed in RNase free water with a total volume of 10μl, then the value of $Abs_{260}$ was measured by Nanodrop after incubation at room temperature for 0 and 30 minutes. The increase percentage of $Abs_{260}$ = [$Abs_{260}$ (30 minutes) - $Abs_{260}$ (0 minute)]/$Abs_{260}$ (0 minute).

***Cell viability test of PEI-UHSS***: The cytotoxicity of PEI-UHSS in KHOS and HCT-116 cells was tested by Cell-Titer Glo assay and MTT method, respectively. KHOS or HCT-116 cells were seeded in a 96-well cell culture plate with a density of $5\times10^3$ cells/well. After incubation for 24 h, the cells were treated with different concentrations of PEI-UHSS solution. After incubation at 37°C for 48h, the cell viability was measured according to the protocol provided by the manufacturer. The cells incubated in the absence of particles were used as the control. All the experiments were performed in triplicates for each group. The statistical data were shown as mean± (SD).

***Functional siRNA delivery***: To test siRNA delivery efficiency of PEI-UHSS particles, PLK1-siRNA was chosen as functional molecules to treat PLK1 over-expressing KHOS cells. S10-siRNA was used as a negative control, because it is effective against human papillomavirus (HPV) type 16 E6 gene, which is low-expressed in KHOS cells. The cells were seeded in a 96-well cell culture plate with a density of $5\times10^3$ cells/well in 100 μL of complete DMEM medium, and grew for 24h before treatment. The complexes of PLK1-siRNA/PEI-UHSS, and PLK1-siRNA/PEI were formed after mixing and incubating in PBS solution at 4°C overnight, then were added to cells. After further incubation at 37°C for 48h, the silencing effect or cell viability was determined by Cell-Titer Glo method. The cells incubated in the equal amount of PBS solution were used as the control. All the experiments were performed in triplicates for each group. The statistical data were shown as mean± (SD). The delivery of survivin siRNA and negative control siRNA into HCT-116 cells was performed as what describe above. Finally, the cell viability was measured by adding MTT agent and reading the absorbance at 570 nm using a Synergy HT microplate reader.

***Western-blot analysis*:** KHOS or HCT-116 cells were seeded in 6-well plates at a seeding density of $1\times10^5$ cells/well. After 24 h incubation, the complexes of survivin-siRNA/PEI-UHSS, control siRNA/PEI-UHSS, survivin siRNA/PEI, survivin siRNA/Oligofectamine, control siRNA/ Oligofectamine along with survivin siRNA only were added into the cells. After further incubation at 37°C for 48h, cells were washed with PBS, collected and lysed in cold RIPA buffer (50 mM Tris, pH 8.0, 150 mM NaCl, 1 mM EGTA, and 0.25% sodium deoxycholate). The lysates were incubated

for 15 min at 4°C and removed by centrifugation at 12,000 rpm for 15 min. Supernatants were analysed for protein concentrations using the Bradford assay (Bio-Rad, Hercules, USA). Equal amount (10 mg) of protein was subjected to electrophoresis on a polyacrylamide gel containing SDS and then transferred to nitrocellulose membranes. Afterwards, the membranes were blocked with tris-buffered saline (TBS) containing 5% (w/v) skimmed milk. After being washed with TBS, the membranes were incubated 4°C overnight at with the first antibody (PLK1 Rabbit mAb, survivin Rabbit mAb and β-Tubulin Rabbit mAb) diluted in TBS. After washing, the membranes were incubated at room temperature for 1 h with the second antibody (Anti-rabbit IgG, HRP-linked Antibody). Bands were detected by were visualized on a Bio-Rad reader.

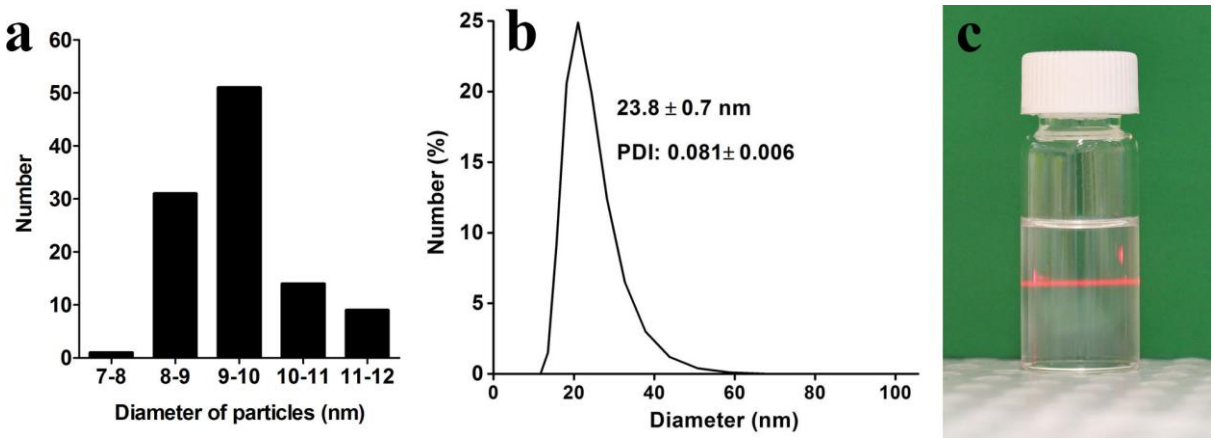


**Figure S1** (a) diameter distribution measured by TEM, (b)DLS measurement (left) and (c) digital image of Epoxy-UHSS.

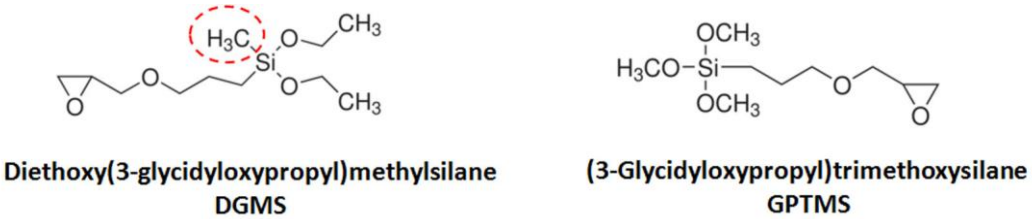


**Figure S2** Chemical structures of DGMS and GPTMS.

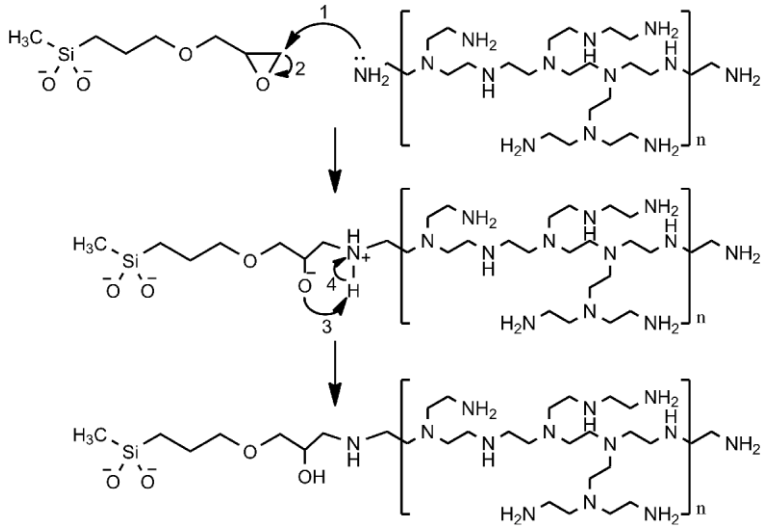

Scheme S1 The chemical reaction between the epoxy moiety of Epoxy-UHSS and PEI.

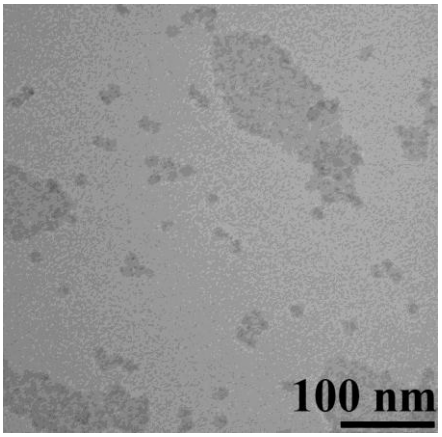


**Figure S3** TEM image of epoxysilane functionalized small particles synthesized by using (3-Glycidyloxypropyl)trimethoxysilane and TMOS as silica source.

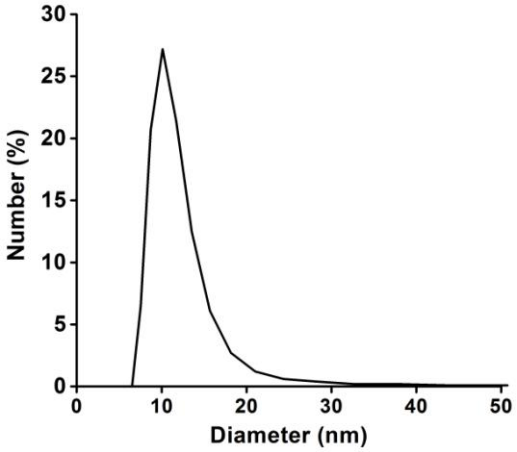


**Figure S4** DLS measurement of PEI-UHSS

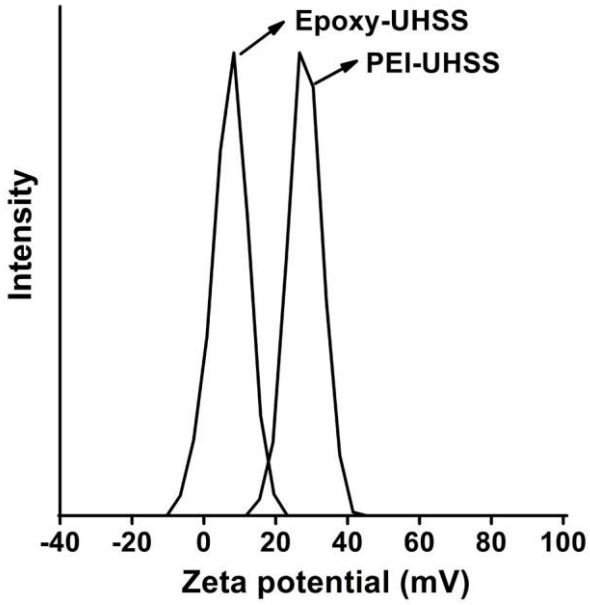


**Figure S5** Zeta potential distribution curves of Epoxy-UHSS and PEI-UHSS.

The surface features of Epoxy-UHSS and PEI-UHSS was studied using Zeta potential measurement. As shown in Figure S5, Epoxy-UHSS has a slightly positive charge of +7.1 mV, indicating the existence of protection groups of methyl and epoxy groups, because pure silica nanoparticles with a similar diameter show a negatively charged surface (~ -40 mV).[2] The introduction of cationic PEI leads to a high positive potential value of +28.0 mV for PEI-UHSS.

**Table S1** Percentages of carbon (C), hydrogen (H) and nitrogen (N) of F127, Epoxy-UHSS and PEI-UHSS.

| | N (%) | C (%) | H (%) |
|---|---|---|---|
| F127 | 0 | 55.25±0.10 | 9.20±0.16 |
| Epoxy-UHSS | 0 | 31.48±0.58 | 5.26±0.03 |
| PEI-UHSS | 3.75±0.17 | 50.78±0.42 | 8.68±0.04 |

The contents of carbon, nitrogen and hydrogen of pure F127, Epoxy-UHSS and PEI-UHSS are listed in Table S1. The carbon and hydrogen percentages of F127 measured by elemental analysis are in agreement with their theoretical values from the chemical structure of F127. Epoxy-UHSS sample does not contain any nitrogen, thus the nitrogen coming from PEI contributes the nitrogen in the sample PEI-UHSS. Based on the measured nitrogen percentage of PEI-UHSS (3.75%) and

theoretical nitrogen percentage of pure PEI (32.56%), it is easy to calculate the amount of PEI modified onto silica hybrid particles, about 11.52%.

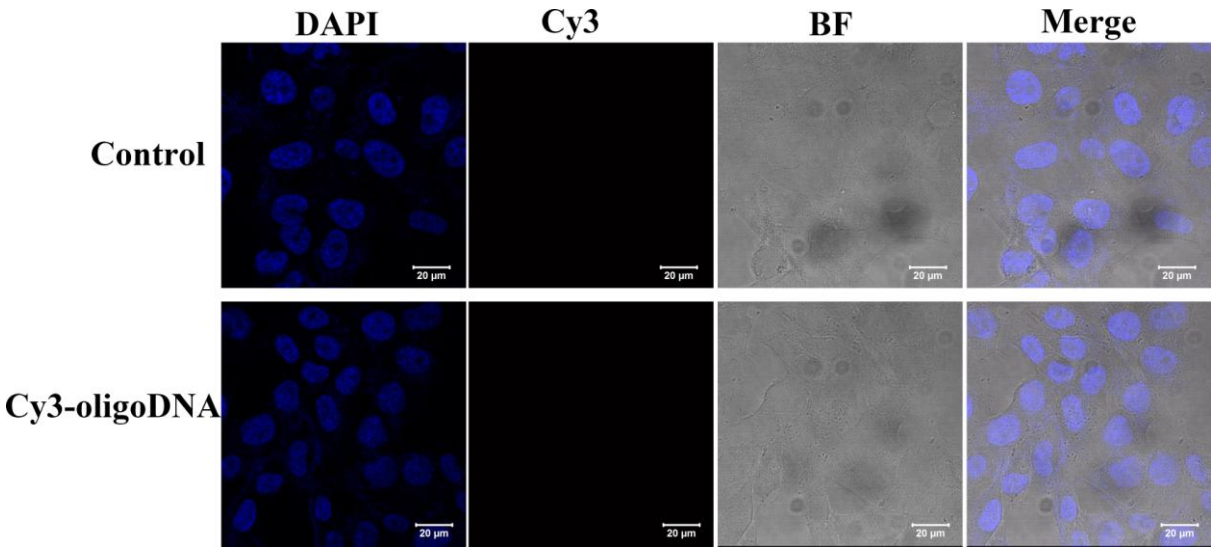


**Figure S6** Confocal microscopy images of KHOS cells with the treatment of free Cy3-oligoDNA. The cells without any treatment are as a control.

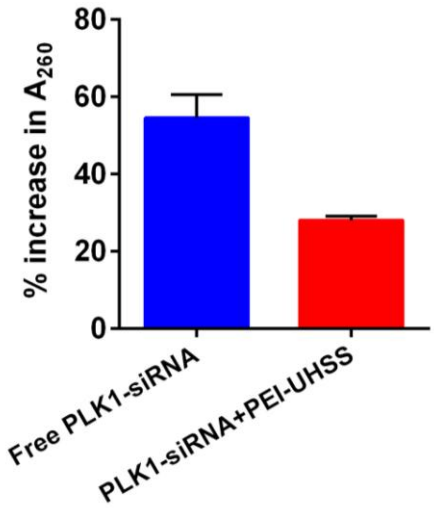


**Figure S7** Degradation of free PLK1-siRNA and its complex with PEI-UHSS after treated with RNase A monitored by the percent increase in absorbance at 260 nm.

**References**

1 Hartono, S. B.; Gu, W. Y.; Kleitz, F.; Liu, J.; He, L. Z.; Middelberg, A. P. J.; Yu, C. Z.; Lu, G. Q.; Qiao, S. Z., Poly-L-lysine Functionalized Large Pore Cubic Mesostructured Silica Nanoparticles as Biocompatible Carriers for Gene Delivery. *ACS Nano* **2012,** *6*, 2104-2117.

2 Niu, Y.; Yu, M.; Hartono, S. B.; Yang, J.; Xu, H.; Zhang, H.; Zhang, J.; Zou, J.; Dexter, A.; Gu, W.; Yu, C., Nanoparticles Mimicking Viral Surface Topography for Enhanced Cellular Delivery. *Adv. Mater.* **2013,** *25*, 6233-6237.

# Chapter 7

# Hyaluronic Acid Modified Mesoporous Silica Nanoparticles for Targeted Drug Delivery to CD44-overexpressing Cancer Cells

This chapter reported the designed synthesis of hyaluronic acid (HA) modified mesoporous silica nanoparticles (MSNs), which possess specific affinity to CD44 over expressed on the surface of a specific cancer cell line, HCT-116 (human colon cancer cells). Compared to bare MSNs, HA-MSNs exhibited a higher cellular uptake via HA receptor mediated endocytosis. An anticancer drug, doxorubicin hydrochloride (Dox), was loaded into MSNs and HA-MSNs. Dox loaded HA-MSNs showed greater cytotoxicity to HCT-116 cells than free Dox and Dox-MSNs due to the enhanced cell internalization behaviour of HA-MSNs. These results indicated that desired surface functionality is also crucial to improve drug delivery efficiency. This work has been highlighted as inside cover paper.

Nanoscale

www.rsc.org/nanoscale

Volume 5 | Number 1 | 7 January 2013 | Pages 1–444

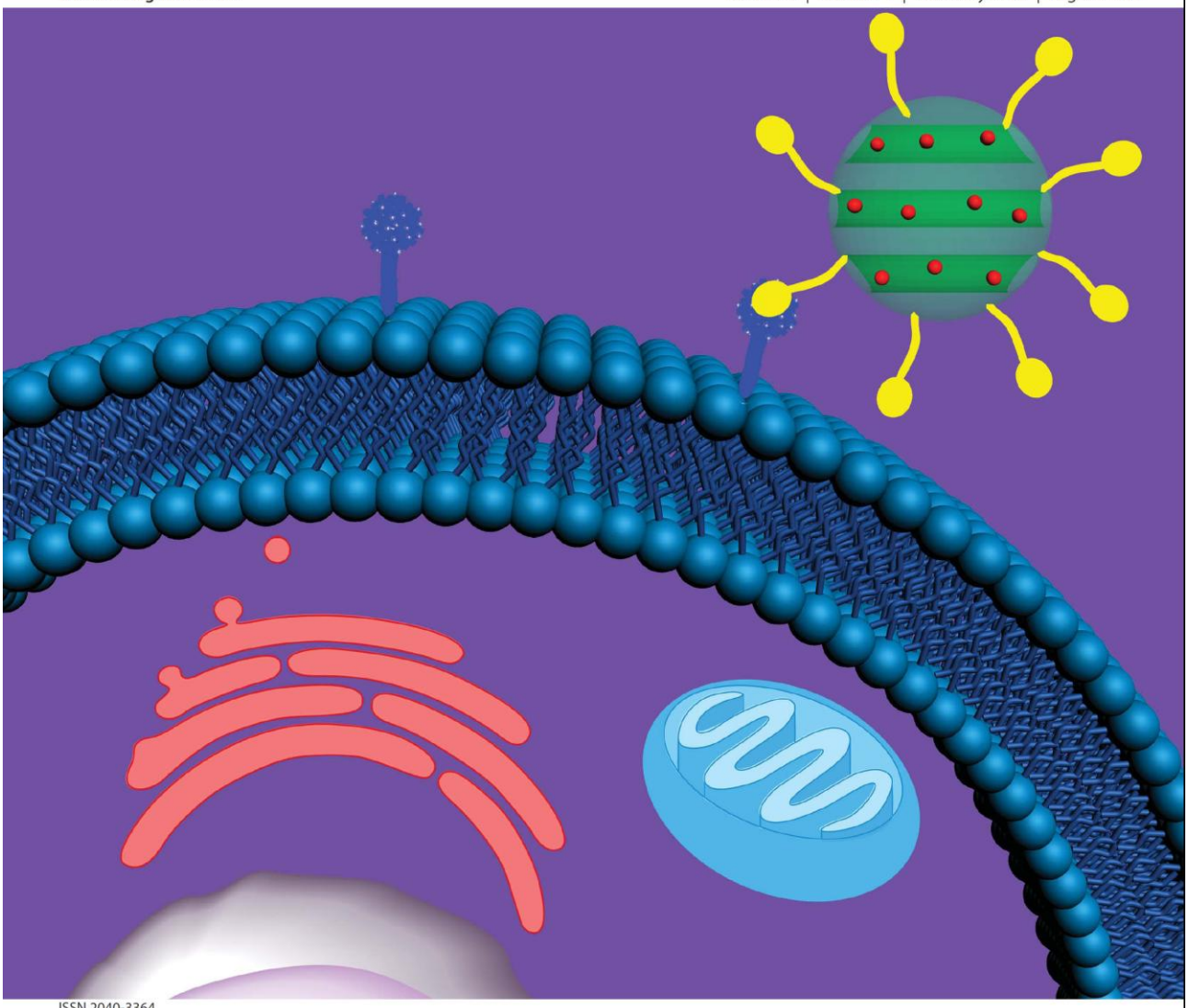

ISSN 2040-3364

RSC Publishing

**PAPER**

Yu *et al.*

Hyaluronic acid modified mesoporous silica nanoparticles for targeted drug delivery to CD44-overexpressing cancer cells

Nanoscale

RSC Publishing

PAPER

# Hyaluronic acid modified mesoporous silica nanoparticles for targeted drug delivery to CD44-overexpressing cancer cells

Cite this: *Nanoscale*, 2013, 5, 178

Meihua Yu,[a] Siddharth Jambhrunkar,[a] Peter Thorn,[b] Jiezhong Chen,[c] Wenyi Gu*[a] and Chengzhong Yu*[a]

In this paper, a targeted drug delivery system has been developed based on hyaluronic acid (HA) modified mesoporous silica nanoparticles (MSNs). HA-MSNs possess a specific affinity to CD44 over-expressed on the surface of a specific cancer cell line, HCT-116 (human colon cancer cells). The cellular uptake performance of fluorescently labelled MSNs with and without HA modification has been evaluated by confocal microscopy and fluorescence-activated cell sorter (FACS) analysis. Compared to bare MSNs, HA-MSNs exhibit a higher cellular uptake *via* HA receptor mediated endocytosis. An anticancer drug, doxorubicin hydrochloride (Dox), has been loaded into MSNs and HA-MSNs as drug delivery vehicles. Dox loaded HA-MSNs show greater cytotoxicity to HCT-116 cells than free Dox and Dox-MSNs due to the enhanced cell internalization behavior of HA-MSNs. It is expected that HA-MSNs have a great potential in targeted delivery of anticancer drugs to CD44 over-expressing tumors.

Received 4th August 2012
Accepted 25th September 2012

DOI: 10.1039/c2nr32145a

www.rsc.org/nanoscale

## 1 Introduction

In recent decades, the application of nanotechnology in medicine (so called nanomedicine) has attracted much attention.[1] Various nanomaterials have been widely used in nanomedicine as potential diagnostic and therapeutic agents for cancer imaging and treatment.[2] Compared to traditional organic lipids or polymer-based nanoparticles,[3–5] the inorganic counterparts exhibit unique properties such as inertness, stability, and ease of functionalisation.[2] Specifically, mesoporous silica nanoparticles (MSNs) with high surface areas, tunable pore structures as well as particle sizes, and controllable surface chemistry have attracted enormous research interest in various bio-applications, including cell imaging,[6] diagnosis and bioanalysis,[7] and drug/gene delivery.[8,9]

For efficient cancer treatments, it has been well documented that a targeted delivery is vital[10] because most anticancer drugs distribute throughout the body and can be harmful to healthy cells. To minimize the side effects, it would be desirable to specifically increase the anticancer drug concentration at the target sites. Nanoparticles with small sizes (1–200 nm) preferably accumulate at tumor sites caused by the enhanced permeability and retention (EPR) effect,[11] also called passive targeting. With the advantage of controllable sizes with diameters within 100 nm, MSNs as nanocarriers have the potential to improve cancer treatments. Moreover, there have been considerable efforts devoted to developing MSNs modified with active targeting moieties, including specific ligands (such as folic acid,[12–14] mannose[15] and arginine–glycine–aspartate (RGD)[16,17]), peptides,[18] and antibodies.[19,20] The abundant silanol groups (Si–OH) facilitate the modification of the above active moieties, thereby achieving active targeting of MSNs to specific cancer cells. The active targeting action together with the EPR effect will further enhance the cellular uptake of MSNs in defective cells, leading to a significant improvement in cancer therapy.

Hyaluronic acid (HA) is a biodegradable, biocompatible and non-immunogenic glycosaminoglycan. As a major component of the extracellular matrix, HA is essential for proper cell growth, organ structural stability and tissue organization,[21,22] and has been extensively investigated for biomedical and pharmaceutical applications. In particular, researchers focused on the use of HA as a targeting moiety for cancer therapy, because many types of tumor cells over-express HA receptors like CD44.[10] Since HA has multiple functional groups available for chemical conjugation with anticancer drugs[10,23] or nanocarriers of drugs/genes,[24,25] HA-attached drugs/nanocarriers have been developed to increase drug/cargo accumulation specifically in CD44 over-expressing cancer cells. In addition to the targeting function, HA modified delivery systems can enter cells more efficiently *via* the HA receptor medicated endocytosis pathway. Utilizing the CD44–HA specific affinity is therefore an attractive strategy for cancer targeting treatments. However, to the best of our knowledge, there are few reports on HA conjugated MSNs as the delivery system for targeting CD44 over-expressing cancer cells. Very recently, a HA-MSN conjugate was

[a]*ARC Centre of Excellence for Functional Nanomaterials and Australian Institute for Bioengineering and Nanotechnology, The University of Queensland, Brisbane, QLD 4072, Australia. E-mail: c.yu@uq.edu.au; w.gu@uq.edu.au; Fax: +61-7-334 63973; Tel: +61-7-334 63283*

[b]*School of Biomedical Sciences, The University of Queensland, Brisbane, QLD 4072, Australia*

[c]*Illawarra Health and Medical Research Institute, University of Wollongong, NSW 2522, Australia*

reported by Ma and co-workers.[26] After loading with the hydrophobic drug camptothecin (CPT), HA-MSNs showed enhanced cytotoxicity to HeLa cells. However, the improvement in cell toxicity was not significant compared to free CPT. Although it was claimed in this report that CD44 positive HeLa cells were used, there is no evidence or literature to support that the HeLa cells used in this work were CD-44 positive. Moreover, because HA coated at the outer surface of MSNs is very hydrophilic, the nature of the drug may also have an influence on the cytotoxicity. Therefore, it is hypothesized that in order to show the advantage of HA-MSN delivery systems, both the target cell lines and suitable drug molecules should be carefully designed in the study.

In the present work, MSNs with a mean particle size of 70–100 nm have been synthesized as drug nanocarriers, and their surface is further modified with HA as the targeting ligand. The specificity of HA-MSNs to CD44 over-expressing HCT-116 cells has been studied. HA modified MSNs show a higher endocytosis performance, compared to bare MSNs. Moreover, an anticancer drug doxorubicin (Dox) has been encapsulated into the MSNs with or without HA modification. Dox loaded HA-MSNs show a much more potent effect in HCT-116 cells than free Dox or Dox-MSNs. Our results have demonstrated that MSNs conjugated with HA are effective as a targeted drug delivery system and have a great potential in treating CD44 over-expressing tumors with improved efficiency.

## 2 Experimental section

### 2.1 Chemicals

Tetraethylorthosilicate (TEOS), cetyltrimethylammonium bromide (CTAB), (3-aminopropyl)triethoxysilane (APTES), fluorescein-5-isothiocyanate (FITC), *N*-hydroxysuccinimide (NHS), *N*-(3-dimethylaminopropyl)-*N*-ethylcarbodiimide hydrochloride (EDC), fluoroshield with DAPI (4′,6-diamidino-2-phenylindole, dihydrochloride), triethylamine (TEA), paraformaldehyde (PFA), and doxorubicin hydrochloride (Dox) were purchased from Sigma-Aldrich. Sodium hyaluronate (HA) ($M_w$ = 200 kDa) was purchased from Lifecore Biomedical (Chaska, MN). Reagent grade sodium hydroxide (NaOH) was received from Chem-Supply. CellTiter-Blue® Reagent and human CD44 FITC conjugate were ordered from Promega and Invitrogen, respectively.

### 2.2 Synthesis of MSNs

MSNs were synthesized according to an approach reported in our previous work[27] with slight modifications. In a typical synthesis, 1.0 g CTAB was dissolved in 480 g deionized water under stirring at room temperature followed by the addition of 3.5 mL NaOH (2 M). The temperature of the solution was raised and kept at 80 °C. To this solution, 6.7 mL TEOS was added. The mixture was continuously stirred for an additional 2 h. The resultant products were collected by filtration and dried at room temperature. The templates were removed by calcination at 550 °C for 5 h.

### 2.3 Synthesis of HA conjugated MSNs (HA-MSNs)

First, 1.5 g calcined MSNs was added to 60 mL toluene and stirred for 6 h before adding 1.0 mL APTES. After stirring at room temperature for 24 h, the particles were extensively washed with toluene and dried in a fume-hood at room temperature (denoted $NH_2$-MSNs). Next, in order to graft HA, the carboxyl group of HA was activated with NHS, using EDC as a coupling agent. The activated carboxyl group of HA then combined with the amine end of the $NH_2$-MSNs. Specifically, 1 g of the prepared $NH_2$-MSNs powder was dispersed in 100 mL deionized water. In another reaction vessel, 20 mL of an aqueous solution containing NHS (0.37 g) and EDC (0.2 g) was mixed with 60 mL HA (113 mg) deionized water solution. Finally the two solutions were mixed and the pH was adjusted to 9.0 using triethylamine as a catalyst. The mixture was stirred at 38 °C overnight. The HA modified MSNs (HA-MSNs) were obtained by centrifugation, washing three times with deionized water, and freeze-drying using Christ Alpha 2-4 LDplus (John Morris Scientific).

### 2.4 FITC modification of MSNs and HA-MSNs

Not all amino groups in $NH_2$-MSNs reacted with HA, thus the remaining free $NH_2$ moieties were utilized for labelling with FITC. The functional group of FITC, thiocyanate, is highly aminoreactive, therefore the prepared $NH_2$-MSNs and HA-MSNs can be conjugated with FITC. Specifically, 20 mg powdered HA-MSNs or $NH_2$-MSNs were dissolved in 3 mL deionized water, and mixed with 5 mL FITC ethanol solution (0.3 mg $mL^{-1}$). After stirring in the dark for 6 h, the nanoparticles were centrifuged and washed with ethanol three times until the supernatants were colorless. The FITC labelled nanoparticles were used for confocal microscopy observations and flow cytometry analysis after applying in HCT-116 cell uptake experiments.

### 2.5 Characterisation

Transmission electron microscopy (TEM) images were obtained with a JEOL 1010 operated at 100 kV. For TEM measurements, the samples were prepared by dispersing the powder samples in ethanol, after which they were dispersed and dried on carbon film on a Cu grid. An X-ray diffraction (XRD) pattern was recorded on a Rigaku Miniflex X-ray diffractometer with Fe-filtered Co radiation. Nitrogen adsorption–desorption isotherms were measured at 77 K using a Micromeritics ASAP Tristar II 3020 system. The samples were degassed at 473 K overnight on a vacuum line. The pore size distribution curve was derived from the adsorption branch of the isotherm using the Barrett–Joyner–Halanda (BJH) method. The Brunauer–Emmett–Teller (BET) method was utilized to calculate the specific surface areas. The total pore volume was calculated from the amount adsorbed at a maximum relative pressure ($P/P_0$) of 0.99. Zeta potential measurements were carried out on a Malvern NanoZS zetasizer at 25 °C in phosphate buffered saline (PBS) solution. Fourier transform infrared (FTIR) spectra were collected on a ThermoNicolet Nexus 6700 FTIR spectrometer equipped with a Diamond ATR (attenuated total reflection) Crystal. For each spectrum, 32 scans were collected at a resolution of 4 $cm^{-1}$ over the range 400–4000 $cm^{-1}$. Before FTIR measurements, all the samples were freeze dried.[13]C NMR spectra were measured by a solid state Bruker Avance III spectrometer with a 7T (300 MHz for 1 h) magnet and a zirconia rotor, 4 mm, rotated at 7 kHz.

### 2.6 Loading doxorubicin (Dox)

60 μL PBS solution containing 150 μg MSNs or HA-MSNs was mixed with 60 μL Dox–PBS solution (1 mg $mL^{-1}$). After shaking for 10 minutes, the mixtures were kept in a 4 °C fridge overnight under dark conditions. Then the Dox-HA-MSNs or Dox-MSNs were centrifuged and washed with 120 μL PBS. The Dox-HA-MSNs and Dox-MSNs samples were used for a subsequent cytotoxicity assay against HCT-116 cells. To evaluate the Dox-loading efficiency, the supernatant and washed solutions were collected and the residual Dox content was measured by using a UV-2450 (UV-Vis spectrophotometer, Shimadzu) at a wavelength of 233 nm. The loading amount of Dox can be calculated based on the original and residual Dox concentrations and volumes. Finally, the amount of loaded Dox was 1.81 and 40.25 μg for HA-MSNs and MSNs respectively. The weight percentage of loaded Dox to HA-MSNs and MSNs is 1.2% and 26.8% respectively.

### 2.7 Cell culture and uptake

HCT-116 cells were maintained in Dulbecco's Modified Eagle Medium (DMEM) supplemented with fetal calf serum (10%, Sigma, MO), L-glutamine (2%), penicillin (1%) and streptomycin (1%) in 5% $CO_2$ at 37 °C. The medium was routinely changed every 2 days and the cells were separated by trypsinisation before reaching confluency. HCT-116 cells were seeded in a 6-well plate ($5 \times 10^5$ cells per well) and incubated for 24 h. After washing twice with PBS, the cells were incubated with 25 μg $mL^{-1}$ FITC labeled MSNs or HA-MSNs in 2 mL of the serum-free DMEM medium for 4 h. Subsequently, the cells were washed twice with PBS to remove the remaining nanoparticles and dead cells. For fixed cell imaging, the cells were treated with 500 μL 4% PFA solution for 30 min at 4 °C, and their nuclei were stained with DAPI for 10 min. Finally, the cells were viewed under a confocal microscope (LSM Zeiss 710).

For competitive inhibition studies, the medium was replaced with 2 mL serum-free culture medium containing HA polymer (10 mg $mL^{-1}$) and then FITC labeled HA-MSNs (25 μg $mL^{-1}$) in HCT-116 cells, followed by the same treatment as described above.

### 2.8 Fluorescence-activated cell sorter (FACS) analysis

A quantitative determination of the cellular uptake of nanoparticles by FACS analysis was performed as follows. HCT-116 cells were seeded in a 6-well plate ($5 \times 10^5$ cells per well) and were cultured as described above. After removal of the free FITC–MSNs or FITC–HA-MSNs and dead cells, the cells were trypsinized, and then centrifuged and washed twice with PBS. After that, the cells were suspended in 1 mL 2% PFA–PBS solution. Then the intracellular delivery of the nanoparticles was analyzed using a FACSAria Cell Sorter (Becton Dickinson BD). All the data of the mean fluorescence were obtained from a population of 10 000 cells after the gating of single cells. Cells incubated in the absence of particles were used as the control.

### 2.9 Measurements of CD44 receptor levels in cultured cells

$5 \times 10^5$ HCT-116 cells were suspended in 2 mL 2% bovine serum albumin (BSA) in PBS solution and incubated at 37 °C for 30 min. After centrifugation, the cells were suspended in 0.5 mL 2% BSA solution, followed by the addition of 2.5 μL FITC labeled CD44-antibody. After incubation at 37 °C for 45 min, the cells were washed twice with 2% BSA solution, then resuspended in 1 mL 2% PFA solution and incubated for 30 min at 4 °C. The binding efficiency of the CD-44 antibody was tested by FACS analysis.

### 2.10 Cytotoxicity of Dox-HA-MSNs and Dox-MSNs against HCT-116 cells

HCT-116 cells were seeded in a 96-well plate at a density of $2 \times 10^4$ cells per well and cultured in 5% $CO_2$ at 37 °C for 24 h. Then, free Dox, Dox-HA-MSNs and Dox-MSNs were added to the cells in DMEM medium at different Dox concentrations of 0.25, 0.125, 0.05 μg $mL^{-1}$ respectively, and the cells were further incubated in 5% $CO_2$ at 37 °C for 24 h. Subsequently, 15 μL CellTiter-Blue Reagent was added to each well, shaken for 10 seconds and then incubated at 37 °C for 4 h. Then fluorescence readings were measured with an excitation wavelength of 560 nm and an emission wavelength of 590 nm using a microplate reader (SpectraMax M5, Bio-Strategy, Ltd). Cells incubated in the absence of particles were used as the control. All the experiments were performed in triplicate for each group. The statistical significance between the two groups was analyzed by an unpaired Student's *t*-test using the software in GraphPad Prism. The differences were considered to be significant if $p < 0.05$.

## 3 Results and discussion

### 3.1 Synthesis of MSNs and HA-MSNs

The XRD pattern (Fig. 1a) of the MSNs shows three typical well-resolved diffraction peaks that can be assigned to the 10, 11 and 20 reflections of a highly ordered two dimensional (2D) hexagonal mesostructure, similar to previous reports.[27,28] The nitrogen adsorption–desorption plot of the MSNs (Fig. 1b) exhibits a typical type IV isotherm and a steep capillary condensation step occurring at a relative pressure ($P/P_0$) of ~0.3, corresponding to a narrow pore size distribution centred at 2.13 nm (inset of Fig. 1b). The surface area and pore volume are calculated to be 918.5 $m^2 g^{-1}$ and 0.67 $cm^3 g^{-1}$ respectively. From the typical TEM image shown in Fig. 1c, it can be seen that the MSNs are nanoparticles with well-ordered mesopores. The mean particle sizes are estimated to be 70–100 nm. Fig. 1d shows the representative TEM image of HA-MSNs. A vague thin layer as indicated by a white arrow can be seen on the surface of the HA-MSNs, indicating the existence of the HA polymer grafted on the MSNs.

The surface modification of MSNs has been studied by zeta potential, FTIR and $^{13}C$ NMR analysis (Fig. 2a–c). From Fig. 2a, it can be seen that the zeta potential of MSNs, $NH_2$-MSNs and HA-MSNs is −23.3, +11.3, and −18.8 mV respectively, consistent with the modification of amine groups ($NH_2$-MSNs) on the negatively charged silica surface (MSNs) and subsequent conjugation of HA on the positively charged $NH_2$-MSNs. Because the carboxyl groups of HA are ionized at pH ~7.0 (ref. 29), HA-MSNs are negatively charged. As indicated in Fig. 2b, pure HA exhibits a broad O–H stretching bond at 3200–3650 $cm^{-1}$, a shoulder peak at around 2900 $cm^{-1}$ associated with –

 

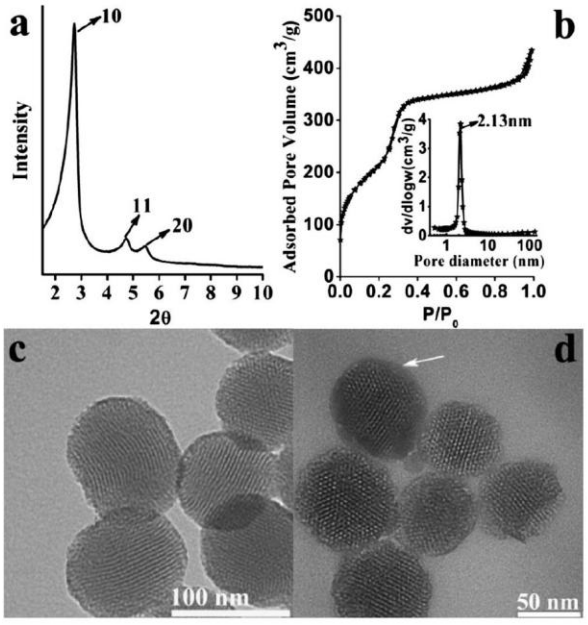


**Fig. 1** (a) XRD pattern; (b) $N_2$ adsorption–desorption isotherm and the corresponding pore size distribution (inset of (b)) of calcined MSNs; TEM images of (c) MSNs and (d) HA-MSNs.

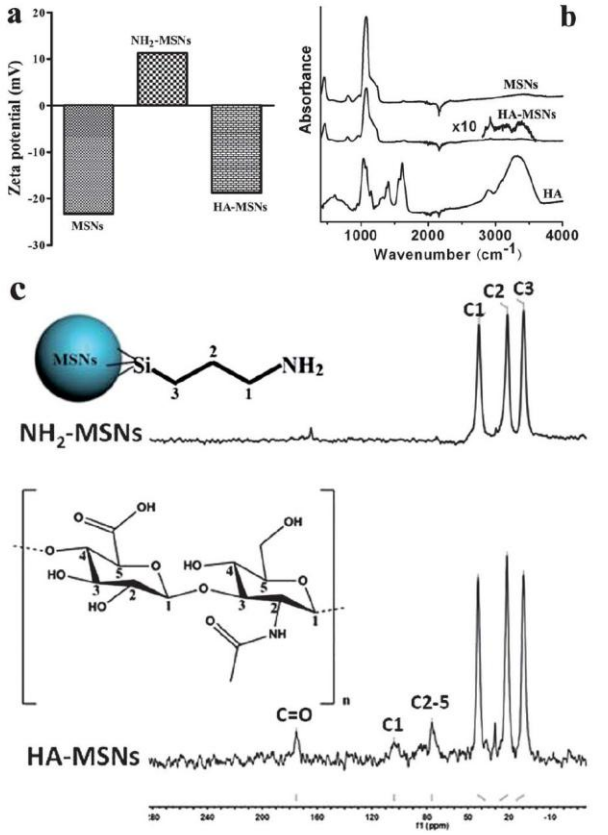


**Fig. 2** (a) Zeta potential analysis of MSNs, $NH_2$-MSNs and HA-MSNs in PBS solution; (b) FTIR spectra of freeze dried MSNs, HA-MSNs and HA polymer; (c) $^{13}C$ NMR spectra of $NH_2$-MSNs and HA-MSNs.

$CH_2$, a C═O stretching bond at 1100–1300 $cm^{-1}$, and a CO–NH (amide) bond at 1630–1680 $cm^{-1}$ (ref. 30). HA-MSNs exhibit typical bonds at 2920 $cm^{-1}$ (C–H stretching) and 3380 $cm^{-1}$ (O–H) from HA. The characteristic peaks at 810 and 1060 $cm^{-1}$ for HA-MSNs can be indexed to Si–O–Si stretching.[31] In addition, a shoulder peak at 960 $cm^{-1}$ can also be observed in HA-MSNs, which can be attributed to the stretching mode of Si–O in the Si–OH group. The band at 1630 $cm^{-1}$ with a very low intensity is observed in HA-MSNs and MSNs, which is assigned to the bending mode of physisorbed water.[31] The $^{13}C$ NMR solid-state spectra of $NH_2$-MSNs and HA-MSNs are presented in Fig. 2c. Three sharp peaks observed at about 43, 22 and 10 ppm in the spectrum of $NH_2$-MSNs can be assigned to three types of methylene carbons from the amino-silica source (see the inset chemical structure in Fig. 2c). The above three peaks are also observed in the spectrum of HA-MSNs. The extra peaks in the range 70–180 ppm can be attributed to C1 anomeric carbons, C2–C5 carbons and the carboxylate and/or carbonyl acetamide carbons of the HA polymer (103, 75, and 175 ppm, respectively, see the inset structure of HA and indexing).[32,33] The results have shown that HA has been successfully conjugated on HA-MSNs.

### 3.2 Cellular uptake of MSNs and HA-MSNs

To visualize the cellular uptake of silica nanoparticles, both MSNs and HA-MSNs were labelled with FITC and studied by confocal microscopy. As shown in Fig. 3, when no nanoparticles are used to treat the cells (control group), only the nuclei are observed in blue color after staining with DAPI. When the cells are incubated with FITC labelled HA-MSNs, strong green fluorescent signals originating from FITC are detected inside the cells, indicating that HA-MSNs are readily taken up by HCT-116 cancer cells (Fig. 3). In contrast, when FITC labelled MSNs without HA modification are incubated with HCT-116, a weaker signal is observed, suggesting a decreased amount of MSNs internalized by HCT-116 cells. Furthermore, when HCT-116 cells are pretreated with free HA (10 mg $mL^{-1}$) to block CD44 prior to FITC labelled HA-MSNs treatment, the green intracellular fluorescence is also weaker compared to the HA-MSN group.

To provide a quantitative comparison, the cellular uptake performance of MSNs and HA-MSNs in HCT-116 is further studied by FACS analysis. Before studying the specific affinity of HA-MSNs, the CD44 receptor level of HCT-116 cancer cells has been evaluated using the human FITC–CD44 antibody and FACS analysis. As can be seen from Fig. 4a, compared to the control cells without any treatment, the cells incubated with the FITC–CD44-antibody show a much higher intensity of FITC, indicating the existence of a high level of CD44 on the surface of HCT-116 cells, consistent with a previous description.[24]

After treating HCT-116 cells with FITC labelled HA-MSNs, the FITC signal emitted from the cells is very strong (Fig. 4b), indicating a high cellular uptake of HA-MSNs. In contrast, the mean intensity of FITC from the cells incubated with FITC labelled MSNs without HA modification is only 61% of that of the FITC labelled HA-MSNs group. To further confirm the

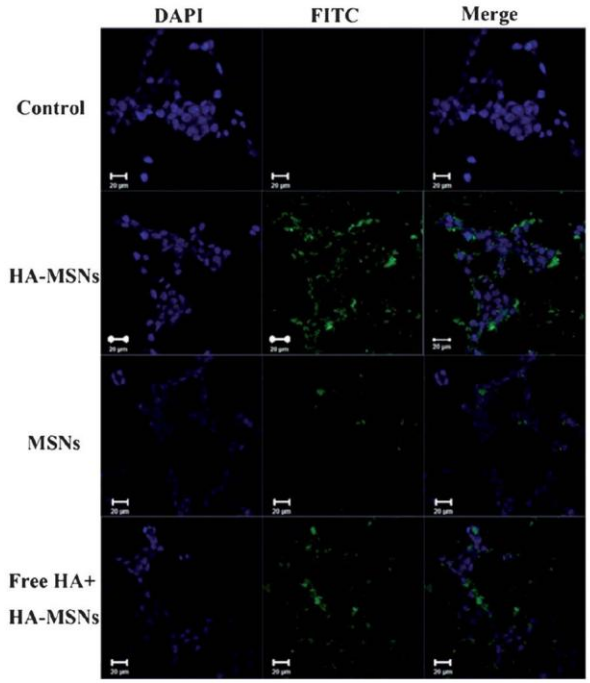


**Fig. 3** Confocal microscopy images of HCT-116 cells without any treatment as a control (first row), with the treatment FITC labelled HA-MSNs (second row), MSNs (third row) and free HA (10 mg $mL^{-1}$) together with FITC labelled HA-MSNs (last row). Green fluorescence arises from FITC dyes that are conjugated to silica nanoparticles and nuclei are stained with DAPI, showing blue fluorescence.

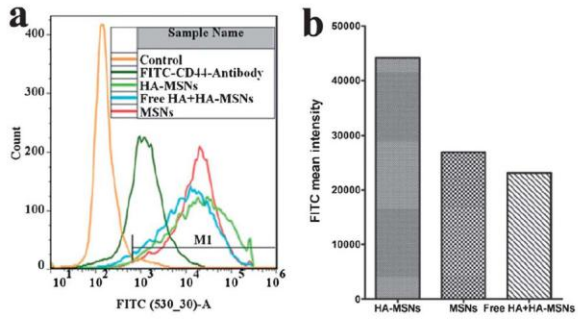


**Fig. 4** (a) Fluorescence activated cell sorter (FACS) analysis of the FITC intensity of the cells treated with an FITC labeled CD44 antibody, MSNs, and HA-MSNs in the absence or in the presence of free HA (10 mg $mL^{-1}$); (b) bar chart of FITC mean intensity of the gated positive cells (M1 indicated in Fig. 4a) treated with FITC modified silica particles.

specific interaction of HA-MSNs with HCT-16 cells, free HA (10 mg $mL^{-1}$) is added prior to the addition of FITC labelled HA-MSNs in the cell culture medium. The FITC signal intensity decreases by 48% compared to the FITC labelled HA-

**Table 1** Details of the concentrations of Dox-HA-MSNs, Dox-MSNs, HA-MSNs, MSNs and free Dox in Fig. 5

| | Dox-HA-MSNs | Dox-MSNs | HA-MSNs | MSNs | Free Dox |
|---|---|---|---|---|---|
| C1 (μg $mL^{-1}$) | 20.95 | 1.18 | 20.70 | 0.93 | 0.25 |
| C2 (μg $mL^{-1}$) | 10.48 | 0.59 | 10.35 | 0.47 | 0.125 |
| C3 (μg $mL^{-1}$) | 4.19 | 0.24 | 4.14 | 0.19 | 0.05 |

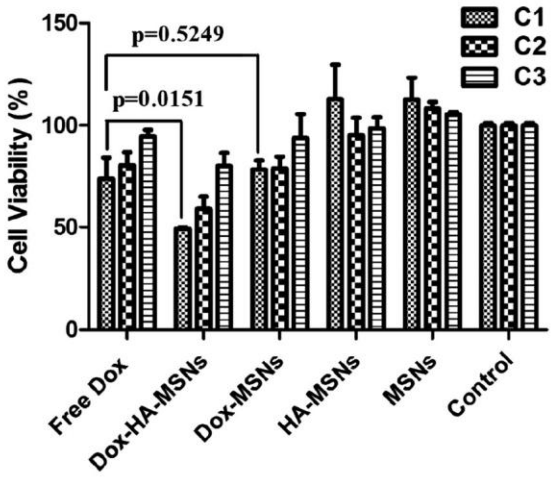


**Fig. 5** Cytotoxicity of free Dox, Dox-HA-MSNs, Dox-MSNs, HA-MSNs and MSNs against HCT-116 cells at different concentrations C1, C2 and C3 (for details, see Table 1).

MSNs group, suggesting that the interaction between CD44 and HA-MSNs and the subsequent HA receptor-mediated endocytosis has been weakened due to the competition of free HA. The above results have confirmed that HA-MSNs can target CD44 over-expressing HCT-16 cancer cells *via* the HA receptor-mediated endocytosis pathway and show an improved endocytosis performance compared to the unmodified MSNs. The FACS results provide a quantitative comparison, which is consistent with the confocal microscopy observations (Fig. 3).

### 3.3 *In vitro* cytotoxicity of Dox-loaded HA-MSNs and MSNs against HCT-116 cells

Finally, the anti-cancer effects of free Dox, Dox loaded HA-MSNs and MSNs were investigated. HCT-116 cells were treated with free Dox, Dox-HA-MSNs or Dox-MSNs with the same concentration of Dox (see details in Table 1). It should be noted that the Dox loading capacity of the MSNs (26.8%) is much higher than that of the HA-MSNs (1.2%). This is because Dox is a water-soluble molecule with a $pK_a$ of 8.2 and thus has a positive charge in PBS solution.[9] Consequently, the negatively charged HA on the surface of the HA-MSNs may inhibit the penetration of Dox into the pore channels of HA-MSNs and dramatically decrease the Dox loading percentage.

The results in Fig. 5 reveal that both HA-MSNs and MSNs show almost no toxicity to HCT-116 at three concentrations (C1–C3, 20.70, 10.35, 4.14 μg $mL^{-1}$ in HA-MSNs and 0.93, 0.47, 0.19 μg $mL^{-1}$ in MSNs respectively), indicating both MSNs and HA-MSNs are excellent biocompatible nano-carriers. HCT-116 cells treated with free Dox, Dox-HA-MSNs and Dox-MSNs show a Dox dosage dependent behavior. However, both free Dox and Dox-MSNs have very low cytotoxicity (~20% inhibition) to the cells even at the highest concentration (C1). There is no significant difference ($p = 0.5249$) in cell viability between the two groups. In contrast, the cell proliferation is significantly inhibited when treated with Dox-HA-MSNs (51% inhibition). The antiproliferative action between the two groups (Dox-HA-MSNs and free Dox) shows a significant difference with a $p$ value of 0.0151, as indicated in Fig. 5. This

 

enhanced cytotoxicity can be explained by the enhanced cellular uptake of HA-MSNs *via* HA receptor-mediated endocytosis.

As introduced before, when the hydrophobic drug CPT was loaded in HA-MSNs,[26] HA-MSNs (~55% inhibition) showed a slight enhancement in cytotoxicity to CD44 positive cells, compared to free CPT (~43%). It is possible that hydrophobic anticancer drugs are difficult to release from the mesopores due to the hydrophilic HA polymer layer coated at the outer surface of the MSNs. Thus, HA-MSNs are more feasible for the target delivery of hydrophilic anticancer drugs or some hydrophobic agents, like photosensitizers,[34] where drug release is not required. Nevertheless, new approaches should be found to increase the loading amount of such drugs inside HA-MSNs, which can further decrease the dosage needed for efficient cancer treatment.

## 4 Conclusions

In summary, an anticancer drug delivery system based on HA conjugated MSNs has been developed to specifically target CD44 over-expressing cancer cells. In this study we have demonstrated that HA modified MSNs show enhanced cellular uptake performance *via* HA receptor mediated endocytosis in CD44 positive HCT-116 cells, compared to that of MSNs without HA modification. Furthermore, HA-MSNs loaded with the hydrophilic anticancer drug Dox has a much better antiproliferative action on HCT-116 cells than free Dox or Dox encapsulated in bare MSNs. This targeted approach based on HA conjugated silica nanoparticles to target CD44 over-expressing cancer cells could have a great potential to improve cancer treatments.

## Acknowledgements

We thank the Australian Research Council for support, the facilities, and the scientific and technical assistance, of the Australian Microscopy & Microanalysis Research Facility at the Centre for Microscopy and Microanalysis, The University of Queensland, Dr Ekaterina Strounina for the $^{13}C$ NMR technical help from Centre for Advanced Imaging, the University of Queensland.

## Notes and references

1 B. Y. S. Kim, J. T. Rutka and W. C. W. Chan, *N. Engl. J. Med.*, 2010, **363**, 2434–2443.
2 H.-C. Huang, S. Barua, G. Sharma, S. K. Dey and K. Rege, *J. Controlled Release*, 2011, **155**, 344–357.
3 T. Wang, G. G. M. D'Souza, D. Bedi, O. A. Fagbohun, L. P. Potturi, B. Papahadjopoulos-Sternberg, V. A. Petrenko and V. P. Torchilin, *Nanomedicine*, 2010, **5**, 563–574.
4 V. P. Torchilin, *Nat. Rev. Drug Discovery*, 2005, **4**, 145–160.
5 W. C. Hartner, D. D. Verma, T. S. Levchenko, E. A. Bernstein and V. P. Torchilin, *Wiley Interdiscip. Rev.: Nanomed. Nanobiotechnol.*, 2009, **1**, 530–539.
6 J. K. Hsiao, C. P. Tsai, T. H. Chung, Y. Hung, M. Yao, H. M. Liu, C. Y. Mou, C. S. Yang, Y. C. Chen and D. M. Huang, *Small*, 2008, **4**, 1445–1452.
7 R. J. Tian, H. Zhang, M. L. Ye, X. G. Jiang, L. H. Hu, X. Li, X. H. Bao and H. F. Zou, *Angew. Chem., Int. Ed.*, 2007, **46**, 962–965.
8 J. Lu, M. Liong, J. I. Zink and F. Tamanoi, *Small*, 2007, **3**, 1341–1346.
9 H. A. Meng, M. Liong, T. A. Xia, Z. X. Li, Z. X. Ji, J. I. Zink and A. E. Nel, *ACS Nano*, 2010, **4**, 4539–4550.
10 V. M. Platt and F. C. Szoka, *Mol. Pharmaceutics*, 2008, **5**, 474–486.
11 A. S. Hoffman, *J. Controlled Release*, 2008, **132**, 153–163.
12 J. Lu, M. Liong, Z. X. Li, J. I. Zink and F. Tamanoi, *Small*, 2010, **6**, 1794–1805.
13 Y. F. Zhu, Y. Fang and S. Kaskel, *J. Phys. Chem. C*, 2010, **114**, 16382–16388.
14 L. Pasqua, F. Testa, R. Aiello, S. Cundari and J. B. Nagy, *Microporous Mesoporous Mater.*, 2007, **103**, 166–173.
15 D. Brevet, M. Gary-Bobo, L. Raehm, S. Richeter, O. Hocine, K. Amro, B. Loock, P. Couleaud, C. Frochot, A. Morere, P. Maillard, M. Garcia and J. O. Durand, *Chem. Commun.*, 2009, 1475–1477.
16 I. J. Fang, I. I. Slowing, C. W. Wu and V. S. Y. Lin, presented in part at The 238th ACS National Meeting, Washington, DC, August 17, 2009.
17 I. J. Fang, I. I. Slowing, K. C. W. Wu, V. S. Y. Lin and B. G. Trewyn, *Chem.–Eur. J.*, 2012, **18**, 7787–7792.
18 S. H. Cheng, C. H. Lee, M. C. Chen, J. S. Souris, F. G. Tseng, C. S. Yang, C. Y. Mou, C. T. Chen and L. W. Lo, *J. Mater. Chem.*, 2010, **20**, 6149–6157.
19 I. I. Slowing, P. A. Kapke, S. Goodison and V. S. Y. Lin, presented in part at The 235th ACS National Meeting, New Orleans, LA, April 8, 2008.
20 C. P. Tsai, C. Y. Chen, Y. Hung, F. H. Chang and C. Y. Mou, *J. Mater. Chem.*, 2009, **19**, 5737–5743.
21 Q. Hua, C. B. Knudson and W. Knudson, *J. Cell Sci.*, 1993, **106**, 365–375.
22 C. B. Knudson and W. Knudson, *FASEB J.*, 1993, **7**, 1233–1241.
23 I. Rivkin, K. Cohen, J. Koffler, D. Melikhov, D. Peer and R. Margalit, *Biomaterials*, 2010, **31**, 7106–7114.
24 H. Lee, C. H. Ahn and T. G. Park, *Macromol. Biosci.*, 2009, **9**, 336–342.
25 M. Y. Lee, S. J. Park, K. Park, K. S. Kim, H. Lee and S. K. Hahn, *ACS Nano*, 2011, **5**, 6138–6147.
26 M. Ma, H. R. Chen, Y. Chen, K. Zhang, X. Wang, X. Z. Cui and J. L. Shi, *J. Mater. Chem.*, 2012, **22**, 5615–5621.
27 S. Yang, L. Z. Zhao, C. Z. Yu, X. F. Zhou, J. W. Tang, P. Yuan, D. Y. Chen and D. Y. Zhao, *J. Am. Chem. Soc.*, 2006, **128**, 10460–10466.
28 J. S. Beck, J. C. Vartuli, W. J. Roth, M. E. Leonowicz, C. T. Kresge, K. D. Schmitt, C. T. W. Chu, D. H. Olson, E. W. Sheppard, S. B. McCullen, J. B. Higgins and J. L. Schlenker, *J. Am. Chem. Soc.*, 1992, **114**, 10834–10843.
29 K. Y. Choi, K. H. Min, J. H. Na, K. Choi, K. Kim, J. H. Park, I. C. Kwon and S. Y. Jeong, *J. Mater. Chem.*, 2009, **19**, 4102–4107.
30 E. K. Lim, H. O. Kim, E. Jang, J. Park, K. Lee, J. S. Suh, Y. M. Huh and S. Haam, *Biomaterials*, 2011, **32**, 7941–7950.
31 M. Muroya, *Colloids Surf., A*, 1999, **157**, 147–155.
32 W. Sicinska, B. Adams and L. Lerner, *Carbohydr. Res.*, 1993, **242**, 29–51.
33 S. Al-Qadi, A. Grenha and C. Remunan-Lopez, *Carbohydr. Polym.*, 2011, **86**, 25–34.
34 B. Z. Zhao, J. J. Yin, P. J. Bilski, C. F. Chignell, J. E. Roberts and Y. Y. He, *Toxicol. Appl. Pharmacol.*, 2009, **241**, 163–172.

# Chapter 8

# An unusual size-dependent gene delivery relationship of monodispersed silica nanoparticles

Apart from surface functionality, the particle size of SiNPs is expected to have significant effect on gene delivery efficiency. In this chapter, amine modified mono-dispersed Stöber spheres ($NH_2$-SS) with various diameters of 125, 230, 330, 440 and 570 nm were synthesized. The *in vitro* transfection efficiencies of $NH_2$-SS were studied in HEK293T cells by delivering plasmid DNA encoding green fluorescent protein (GFP) (pcDNA3-EGFP, abbreviated as pcDNA, 6.1kbp). It was found that an optimized particle size of 330 nm exhibited the highest expression of GFP. The mechanistic study showed that the binding affinity of pcDNA/$NH_2$-SS complexes decreased while the cellular uptake ability increased with $NH_2$-SS size increasing from 125 to 570 nm. The opposite effects lead to an optimal $NH_2$-SS size of 330 nm that provides the maximum gene delivery efficiency. A similar size-dependent gene delivery relationship was further demonstrated in another plasmid DNA with a bigger size of 8.9 kbp. This work for the first time demonstrates the significant role of particle size of cationic silica nano-carriers on gene delivery efficiency. The knowledge obtained from this work is crucial for the rational design of synthetic gene delivery systems with improved efficiency for gene therapy. This work has been resubmitted to *ACS Nano*.

ACS Nano



# An Unusual Size-Dependent Gene Delivery Relationship of Monodispersed Silica Nanoparticles

| | |
|---|---|
| Journal: | *ACS Nano* |
| Manuscript ID: | Draft |
| Manuscript Type: | Article |
| Date Submitted by the Author: | n/a |
| Complete List of Authors: | Yu, Meihua; University of Queensland, Australian Institute for Bioengineering and Nanotechnology (AIBN),<br>Niu, Yuting; University of Queensland, Australian Institute for Bioengineering and Nanotechnology (AIBN)<br>Zhang, Jun; University of Queensland, Australian Institute for Bioengineering and Nanotechnology (AIBN)<br>Zhang, Hongwei; University of Queensland, Australian Institute for Bioengineering and Nanotechnology (AIBN)<br>Yang, Yannan; University of Queensland, Institute for Bioengineering and Nanotechnology (AIBN)<br>Taran, Elena; University of Queensland, Chemical Engineering<br>Jambhrunkar, Siddharth; The University of Queensland, Australian Institute for Bioengineering and Nanotechnology<br>Gu, Wenyi; University of Queensland,<br>Thorn, Peter; University of Queensland, School of Biomedical Sciences<br>Yu, Chengzhong; University of Queensland, Australian Institute for Bioengineering and Nanotechnology (AIBN) |
| | |



ACS Paragon Plus Environment

# An Unusual Size-Dependent Gene Delivery Relationship of Monodispersed Silica Nanoparticles

*Meihua Yu*[a, ‡], *Yuting Niu*[a, ‡], *Jun Zhang*[a], *Hongwei Zhang*[a], *Yannan Yang*[a], *Elena Taran*[a,b], *Siddharth Jambhrunkar*[a], *Wenyi Gu*[a], *Peter Thorn*[c], *and Chengzhong Yu*[a]*

[a]Australian Institute for Bioengineering and Nanotechnology, The University of Queensland, Brisbane, QLD 4072, Australia

[b]Australian National Fabrication Facility – QLD Node

[c] School of Biomedical Sciences, The University of Queensland, Brisbane, QLD 4072, Australia

**KEYWORDS**: silica nanoparticles, gene delivery, plasmid DNA, particle size, cellular uptake

**ABSTRACT**: Silica based nanoparticles are promising carriers for gene delivery applications. In order to gain insight into the role of particle size on gene transfection efficiency, amine modified monodisperse Stöber spheres ($NH_2$-SS) with various diameters of 125, 230, 330, 440 and 570 nm were synthesized. The *in vitro* transfection efficiencies of $NH_2$-SS were studied in HEK293T cells by delivering plasmid DNA encoding green fluorescent protein (GFP) (pcDNA3-EGFP, abbreviated as pcDNA, 6.1 kbp). $NH_2$-SS with a diameter of 330 nm ($NH_2$-SS330) showed the highest GFP transfection level compared to $NH_2$-SS particles with other sizes. The transfection efficiency was found as a compromise between the binding capacity and cellular uptake performance of $NH_2$-SS330 and pcDNA conjugates. $NH_2$-SS330 also demonstrated the highest

transfection efficiency for another plasmid DNA with a bigger size of 8.9 kbp. This work demonstrates for the first time the significance of particle size on gene transfection efficiency in silica based gene delivery systems. Our findings are crucial to the rational design of synthetic vectors for gene therapy.

Gene therapy is a promising treatment where foreign genetic molecules (nucleic acids) are introduced into living cells to supplement or alter genes to treat various diseases.[1, 2] Naked nucleic acids themselves cannot enter into cells and are easily degraded by nucleases,[3] therefore efficient carriers including viral[4] or non-viral vectors[5] are needed to deliver nucleic acids (DNA or RNA) into cells. Initial studies mainly focused on viral carriers due to their high delivery efficiency; however, the inherent immunogenicity, inflammatory response and toxicity limit their wide applications.[6-8] Compared with viral vectors, synthetic gene delivery systems including polymeric[9] and liposomal[10] agents, peptides[11] and inorganic nanoparticles[12] offer many advantages such as ease of preparation and reduced risk of immunogenicity, but their gene delivery efficiency is moderate. It remains a challenge to prepare non-viral carriers with enhanced efficacy to deliver genetic molecules for various applications.

Silica based nanocarriers have attracted increasing attention for gene delivery because of their unique properties such as tunable particle/pore size, biocompatibility and low cost.[13-16] The first example of inorganic gene delivery systems was the aminosilane modified solid silica nanoparticles with diameters of 10-100 nm, which showed strong binding capacity toward negatively charged plasmid DNA (pDNA) and excellent *in vitro* gene transfection.[17, 18] Since then, various silica based nanocarriers have been extensively studied for both *in vitro* and *in vivo* pDNA delivery.[14, 19] So far there are a few reports investigating the impact of structure parameters of silica nanoparticles on pDNA delivery efficiency.[16, 20] Kim et al. demonstrated that compared to silica nanocarriers with smaller pores (~2 nm), aminated monodispersed mesoporous silica nanoparticles (MMSN) with large pores (~ 23 nm) showed a higher loading capacity for pDNA, significant protection from nuclease-mediated degradation and much higher transfection efficiency.[16] Cebrián et al. reported that high colloidal stability of silica

nanoparticles was beneficial for gene delivery.[20] However, the influence of particle size of silica nanoparticles on gene transfection efficiency has not been reported to the best of our knowledge.

In the present study, a series of amine modified monodisperse silica Stöber spheres ($NH_2$-SS) with various diameters (125, 230, 330, 440 and 570 nm) were synthesised to investigate the influence of particle size on gene transfection efficiency (Scheme 1). The solid structure was chosen to exclude the influence of internal porosity of nanoparticles. The *in vitro* transfection efficiencies of $NH_2$-SS were tested in HEK 293T cells by delivering plasmid DNA encoding green fluorescent protein (GFP) (pcDNA3-EGFP, abbreviated as pcDNA, 6.1 kbp). It was found that an optimized particle size of 330 nm exhibited the highest expression of GFP. As shown in Scheme 1, when the size of $NH_2$-SS increased from 125 to 570 nm, the binding affinity of pcDNA/$NH_2$-SS complexes decreased while the cellular uptake ability increased. The opposite effects lead to an optimal $NH_2$-SS size of 330 nm that provides the maximum gene delivery efficiency. A similar size-dependent gene delivery relationship was further demonstrated in another plasmid DNA with a bigger size of 8.9 kbp. This work for the first time demonstrates the significant role of particle size of cationic silica nanocarriers on gene delivery efficiency. The knowledge obtained from this work is crucial for the rational design of synthetic gene delivery systems with improved efficiency for gene therapy.

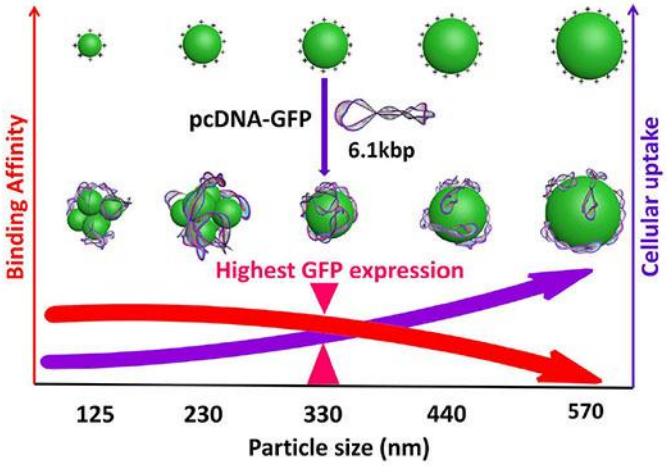


**Scheme 1** A schematic illustration of the bind affinity between $NH_2$-SS and pcDNA and cellular uptake performance of their complexes as a function of particle size. The GFP transfection efficiency is the highest when the binding affinity and cellular uptake of pcDNA/$NH_2$-SS complexes is balanced.

## RESULTS AND DISCUSSION

**Synthesis of amine modified monodisperse Stöber spheres ($NH_2$-SS) with various diameters.** Monodisperse Stöber spheres with different diameters were synthesized by adjusting the reaction parameters (see Table S1 and experimental section) followed by amine modification. Figures 1a-e illustrate representative transmission electron microscopy (TEM) images of amine modified Stöber spheres ($NH_2$-SS) with controllable diameters, showing that all the samples of $NH_2$-SS are very uniform in size. The average particle size of $NH_2$-SS by measuring ~100 silica spheres is 125, 230, 330, 440 and 570 nm for samples $NH_2$-SS125, $NH_2$-SS230, $NH_2$-SS330, $NH_2$-SS440 and $NH_2$-SS570, respectively (Figure 1a-e and Table 1).

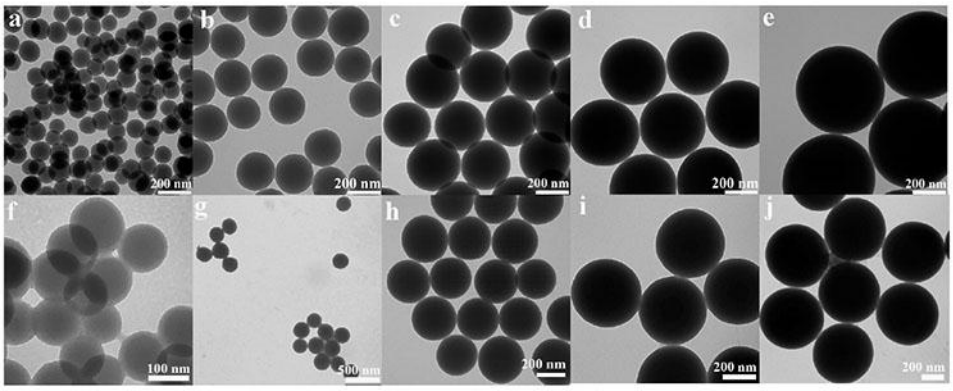


**Figure 1.** TEM images of $NH_2$-SS125 (a), $NH_2$-SS230 (b), $NH_2$-SS330 (c), $NH_2$-SS440 (d), $NH_2$-SS570 (e), $NH_2$-SS125/pcDNA (f), $NH_2$-SS230/pcDNA(g), $NH_2$-SS330/pcDNA(h), $NH_2$-SS440/pcDNA(i) and $NH_2$-SS570/pcDNA(j).

The dynamic light scattering (DLS) method was utilized to determine the size and dispersity of $NH_2$-SS samples with various diameters in PBS solution. As shown in Figure S1 and Table 1, the hydrodynamic diameter of $NH_2$-SS125, $NH_2$-SS230, $NH_2$-SS330, $NH_2$-SS440 and $NH_2$-SS570 is 211±16, 290±22, 436±25, 502±27 and 585±9 nm, respectively. The sizes of $NH_2$-SS measured from DLS are larger than those determined by TEM analysis (Table 1), due to the surrounded water molecules and/or swelling effect of surface molecules.[21] Additionally, the particles in all samples show a relatively narrow size distribution peak (see also polydisperse index from DLS measurements, PDI values listed in Table 1), indicating that $NH_2$-SS samples are monodisperse without significant aggregation after amine modification.

The amine functionalization on the negatively charged silica spheres was proved by Zeta potential measurement in PBS solution. As seen from Table 1, the Zeta potential value of $NH_2$-SS125, $NH_2$-SS230, $NH_2$-SS330, $NH_2$-SS440 and $NH_2$-SS570 is + 26.8±2.1, + 25.5±0.59, + 27.0±1.1, + 21.0±0.1 and +26.7±1.2 mV, respectively, indicating that all $NH_2$-SS have been

successfully grafted with amine groups[22] and possess a similar surface charge. From the above results, it can be seen that all $NH_2$-SS samples have similar structures while the major difference is the particle size, which is crucial to elucidate the particle size influence on transfection efficiency in the following study.

**Table 1.** Particle sizes and Zeta potential values of $NH_2$-SS samples and their complexes with pcDNA or H1 at w/w = 160.

| Sample | Particle size (nm) | | PDI | Zeta potential (mV) |
|---|---|---|---|---|
| | TEM | DLS | | |
| $NH_2$-SS125 | 125 | 211±16 | 0.191±0.034 | + 26.8±2.1 |
| $NH_2$-SS230 | 230 | 290±22 | 0.206±0.180 | + 25.5±0.59 |
| $NH_2$-SS330 | 330 | 436±25 | 0.413±0.069 | + 27.0±1.1 |
| $NH_2$-SS440 | 440 | 502±27 | 0.426±0.094 | + 21.0±0.1 |
| $NH_2$-SS570 | 570 | 585±9 | 0.213±0.019 | + 26.7±1.2 |
| pcDNA | - | 269±25 | 0.650±0.136 | -10.5±6.1 |
| $NH_2$-SS125/pcDNA | - | 488±29 | 0.925±0.129 | -29.6±4.0 |
| $NH_2$-SS230/pcDNA | - | 279/1156±38 | 0.694±0.268 | -25.0±2.5 |
| $NH_2$-SS330/pcDNA | - | 371±38 | 0.848±0.081 | -28.9±0.7 |
| $NH_2$-SS440/pcDNA | - | 492±31 | 0.979±0.037 | -34.8±1.5 |
| $NH_2$-SS570/pcDNA | - | 725±7 | 0.765±0.083 | -34.0±2.9 |
| H1 | - | 311±14 | 0.237±0.127 | -18.4±1.32 |
| $NH_2$-SS125/H1 | - | 705±30 | 0.770±0.032 | -33.9±2.5 |
| $NH_2$-SS230/H1 | - | 288/1693±28 | 0.789±0.016 | -35.9±1.9 |
| $NH_2$-SS330/H1 | - | 436±36 | 0.413±0.069 | -28.6±3.1 |
| $NH_2$-SS440/H1 | - | 679±61 | 0.679±0.004 | -36.1±4.1 |

| | | | | |
|---|---|---|---|---|
| $NH_2$-SS570/H1 | - | 752±59 | 0.622±0.095 | -41.1±1.9 |

**pcDNA transfection efficiency in HEK 293T cells.** To investigate the relationship of transfection efficiency of $NH_2$-SS and their particle sizes, $NH_2$-SS was mixed with pcDNA (6.1 kbp) encoding green fluorescent protein (GFP) in PBS solution, followed by the addition of the complexes to HEK 293T cells. The influence of weight ratio (w/w) of $NH_2$-SS to pcDNA on transfection efficiency was also studied by increasing amounts of $NH_2$-SS while keeping pcDNA amount constant (2.5 μg).

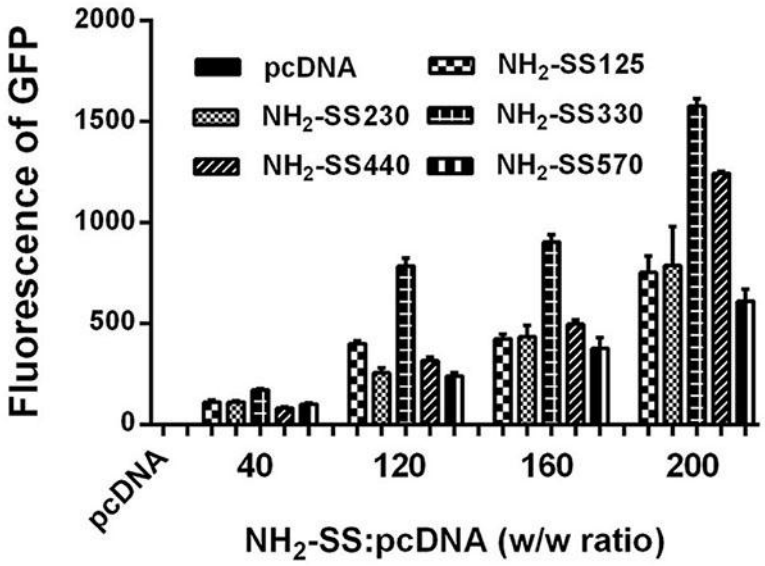


**Figure 2.** GFP expression levels in HEK 293T cells by flow cytometry, after treated with naked pcDNA, $NH_2$-SS125/pcDNA, $NH_2$-SS230/pcDNA, $NH_2$-SS330/pcDNA, $NH_2$-SS440/pcDNA and $NH_2$-SS570/pcDNA at different weight ratios of $NH_2$-SS to pcDNA. The Y value of

fluorescence intensity of GFP = GFP positive cell percentage × GFP mean intensity per GFP positive cell.

To provide a quantitative comparison, GFP fluorescence intensity of HEK 293T cells was studied by flow cytometry, which combined the results of GFP positive cell percentage and GFP mean intensity per GFP positive cell. As shown in Figure 2, naked pcDNA is not able to induce GFP protein expression at all. In contrast, GFP expression can be detected when using $NH_2$-SS as carriers, and its transfection efficiency increases with increasing w/w ratio of $NH_2$-SS to pcDNA from 40 to 200 for all $NH_2$-SS with different diameters. This finding agrees with what observed in previously reported silica based delivery systems.[16] At all w/w ratios, the GFP expression efficiency increases firstly as the diameter of $NH_2$-SS increases, reaching a maximum point at 330 nm, followed by decrement when the particle size of $NH_2$-SS further increases to 570 nm. This unusual trend is more distinguished at w/w ratios of 160 and 200, compared to that observed at w/w ratios of 40, 120, indicating that the nitrogen/phosphate (N/P) ratio is not the only factor that influences the gene transfection efficacy because $NH_2$-SS125 and $NH_2$-SS230/ have much higher N/P ratios compared to $NH_2$-SS-330 (Table S2). The gene expression level in the case of $NH_2$-SS330 is overwhelmingly higher compare to that of $NH_2$-SS570 at w/w = 200. Specifically, the GFP fluorescence intensity transfected by $NH_2$-SS330 (~ 1578) is ~ 1.6 times higher than that transfected by $NH_2$-SS570 (~ 613). For comparison, a standard-transfection agent, polyethylenimine (PEI) with a molecular weight of 25 kDa, was utilized to deliver pcDNA as shown Figure S2. The GFP expression transfected by $NH_2$-SS330/pcDNA at w/w = 200 can reach approximately 30% and 70% of that induced by PEI/pcDNA complex with an N/P ratio of 10 (highest expression level in PEI/pcDNA complexes) and 5 (similar N/P ratio with $NH_2$-SS330/pcDNA complex at w/w = 200, shown in Table S2), respectively. The transfection

efficiency of our optimized delivery system is comparable with previously reported silica based pDNA carriers[18] where the gene expression level of silica carriers (~ 30 nm in diameter) is about 30% of that transfected by PEI, however, chloroquine was required to enhance gene expression of such smaller silica particles (10-fold enhancement).

Confocal microscopy was further utilized to compare GFP expression levels of HEK 293T cells transfected by $NH_2$-SS/pcDNA complexes with a w/w ratio of 200. As shown in Figure S3, no GFP expression can be observed for the naked pcDNA. In contrast, GFP expression can be clearly detected when using $NH_2$-SS as carriers. GFP expression efficiency increases with increasing the particle size of $NH_2$-SS from 125 to 330 nm. However, GFP transfection efficiency decreases when the particle size of $NH_2$-SS further increases to 570 nm. It appears that there is both an increase (or decrease) in the numbers of cells that are expressing GFP and an increase (or decrease) in the amount of GFP that is expressed within a cell. The trend of size-dependent transfection efficiency from confocal microscopy results is consistent with that observed in flow cytometry (Figure 2).

These results suggest that the diameter of silica carriers has a significant role on transfection activity. It is also noted that in most of previously reported silica based pDNA delivery systems, the sizes of silica nanoparticles were smaller than the optimized size (330 nm) observed in our study.[14, 16, 18]

Luo et al. found that in a three-component transfection system (i.e., pDNA/ commercial transfection agent/ unmodified solid silica nanoparticles), the unmodified dense silica nanoparticles could enhance β-galactosidase protein expression by up to 750% over the commercial transfection reagents.[23] The increment was attributed to increased accumulation of pDNA-transfection agent complexes at the cell surface. Moreover, the enhancement of gene

transfection was dependent on the diameter of silica nanoparticles; the larger silica nanoparticles with a diameter of 225 nm increased the gene transfection more significantly than the smaller ones (25 and 50 nm in diameters), which was attributed to the faster sedimentation of larger silica particles on the cell surface.[24] Based on the sedimentation mechanism, one may expect that larger silica nanoparticles such as $NH_2$-SS570 should exhibit higher gene transfection compared to $NH_2$-SS330, in conflict with our observations. The observed size-dependent behavior is also different from the well-accepted understanding that small particle sizes (< 300 nm) are preferred for efficient cellular delivery.[25] Therefore the underlying reason for the unusual size dependent gene transfection relationship in our binary system (i.e. cationic silica nanoparticle-pDNA) should be studied in details.

**The configuration and size of pcDNA.** The structures of both $NH_2$-SS and pcDNA are important to understand their interactions. The conformation and size of pcDNA used in this study was investigated by atomic force microscope (AFM) and DLS. The pcDNA helix is under a torsional stress because the two helical strands are twisted around the axis. To minimise the torsional strain, an intertwined helix conformation called pcDNA supercoils is formed. Under AFM observation, pcDNA molecules attach homogeneously to the mica, most of which are in supercoiled structures (indicated by red arrows in Figure 3a) with a few in relaxed closed circular form (indicated by black arrow). The diameter of circular pcDNA (Figure 3b) is estimated to be 250-600 nm by measuring from different directions. The coiled pcDNA in aqueous solution has a hydrodynamic diameter of ~ 287 nm measured by DLS (Figure S2 and Table 1), in the range of which detected in AFM analysis.

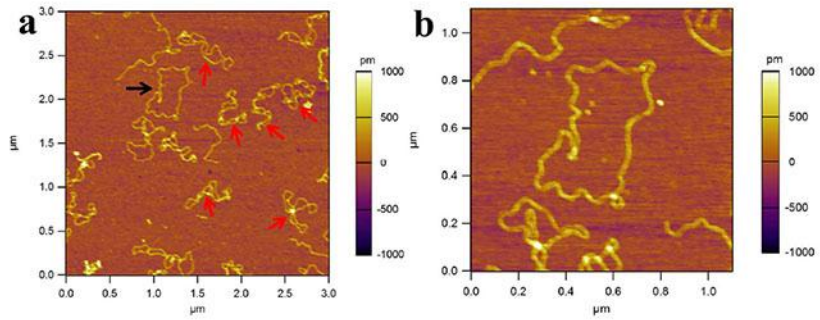


**Figure 3.** AFM images of pcDNA deposited onto mica.

**Interaction between $NH_2$-SS and pcDNA.** The interaction of gene carriers with genetic molecules and the subsequent cellular uptake are prerequisite to successful gene transfection.[12] We first investigated the interaction between pcDNA and $NH_2$-SS with various diameters by Zeta potential analysis, Nanodrop, agarose gel electrophoresis, DLS and TEM. As mentioned before, all $NH_2$-SS samples are positively charged with a value around +25 mV. After mixing with pcDNA, the Zeta potential of all pcDNA/$NH_2$-SS complexes with a weight ratio ($NH_2$-SS to pcDNA) of 160 turns to highly negatively charge in the range of -25 to -35 mV (Table 1), indicating that positively charged $NH_2$-SS bind with negatively charged pcDNA forming $NH_2$-SS/pcDNA complexes. Compared to the individual pcDNA, the absolute zeta potential values of pcDNA/$NH_2$-SS complexes are higher (more negative), suggesting that several pcDNA molecules are associated with one $NH_2$-SS.[16]

For the polycationic polymer, PEI, the complexes of PEI/DNA exhibit a net positive charge when the N/P ratio is $\geq 5$.[26] In contrast, $NH_2$-SS/pcDNA complexes at w/w = 160 is negatively charged irrespective of the N/P ratio (the N/P ratio is 14.4, 14.2, 3.7, 2.1 and 1.7 for $NH_2$-SS125/pcDNA, $NH_2$-SS230/pcDNA, $NH_2$-SS330/pcDNA, $NH_2$-SS440/pcDNA and $NH_2$-SS570/pcDNA, respectively, shown in Table S2). Different from polymers or much smaller

positive silica nanoparticles (~ 30 nm in diameter),[18] $NH_2$-SS have a rigid dense framework with a rather large diameter, thus the negatively charged pcDNA molecules can only adhere to the surface of $NH_2$-SS resulting in a net negative surface charge, which is consistent with previously reported results.[16] It is well-accepted that cationic complexes advantageously adhere to the negatively charged cell surface and translocate across the cell membrane.[27] However, the cellular uptake of negatively charged silica nanoparticles/DNA complexes is also efficient for gene transfection, although the mechanism of this cellular uptake is not yet fully understood.[16, 18, 28]

The binding capacity of $NH_2$-SS toward pcDNA was measured by Nanodrop. From Figure 4, it can be seen that $NH_2$-SS with the smallest diameter of 125 nm has the highest pcDNA binding capacity of ~ 27.7 ng /μg. $NH_2$-SS with the biggest diameter of 570 nm shows the lowest binding capacity of ~ 10.0 ng /μg, which is almost two times less than that of $NH_2$-SS125. The $NH_2$-SS with diameters of 230, 330 and 440 nm display a moderate binding capacity in the range of 12-15 ng/μg. The overall trend of binding capacity toward pcDNA decreases as the particle size of $NH_2$-SS increases, which could be attributed to the decreasing of surface area with the increasing particle size.[29]

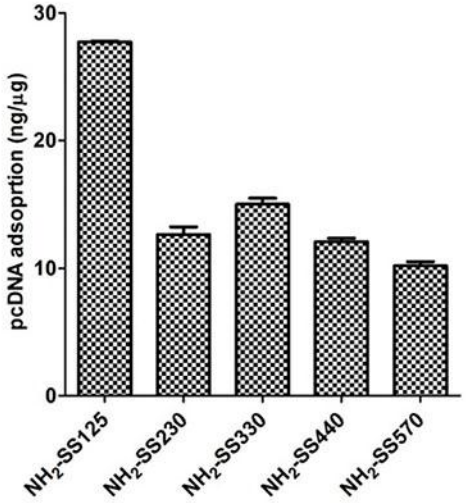


**Figure 4.** pcDNA binding capacities of $NH_2$-SS125, $NH_2$-SS230, $NH_2$-SS330, $NH_2$-SS440 and $NH_2$-SS570 measured by Nanodrop.

To study the binding affinity of $NH_2$-SS toward pcDNA, a gel retardation assay was performed. A constant amount of pcDNA (0.5 μg) was mixed with various amounts of $NH_2$-SS from 20 to 120 μg. As shown in Figure 5, a complete electrophoretic shift can be observed for naked pcDNA in both pieces of agarose gels. The more compact supercoiled form appears as the main band, while slower-running open circular form and the relaxed closed circular form appears as the minor faint bands.[30] In contrast, when only 20 μg of $NH_2$-SS125 is used, the band intensity of pcDNA retained in the well is very strong while the intensity of shifted pcDNA is relatively weak. As the amount of $NH_2$-SS125 increases to 40 μg or more, no shifted pcDNA can be detected at all, suggesting complete binding of pcDNA.

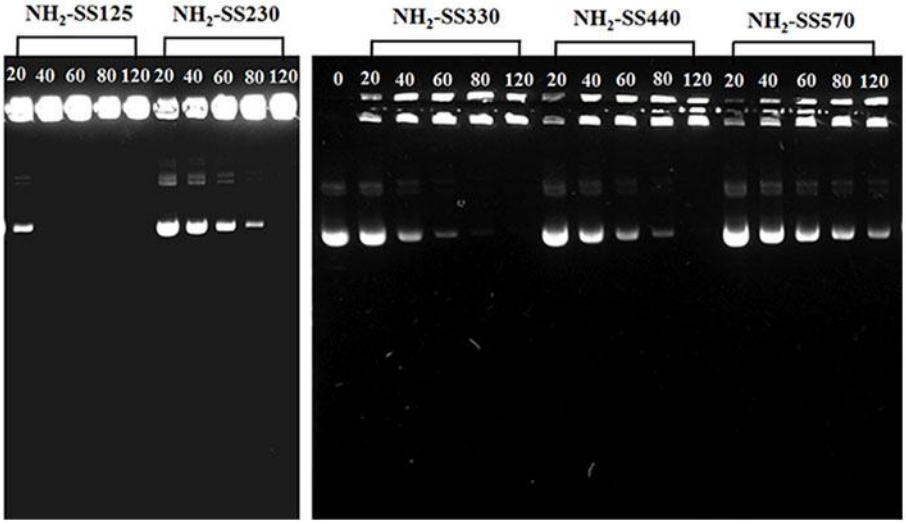


**Figure 5.** Agarose gel electrophoresis of $NH_2$-SS/pcDNA demonstrating plasmid DNA/nanoparticle complexation with increasing amounts of $NH_2$-SS (μg). The amount of pcDNA was constant (0.5 μg).

As summarized in Table S3, the calculated amount of $NH_2$-SS125 to completely bind 0.5 μg of pcDNA is about 18 μg based on the Nanodrop data (27.7 ng/μg), which is a little less than that value (40 μg) in gel retardation assay. These results suggest that a few amount of pcDNA detached from $NH_2$-SS125/pcDNA complex during the electrophoresis process. For $NH_2$-SS230, the band intensity of pcDNA retained in the well increases as the amount of $NH_2$-SS230 increases, and 120 μg of $NH_2$-SS230 is needed to completely retain pcDNA in the well. Similar observations can be found in the cases of $NH_2$-SS330 and $NH_2$-SS440. The estimated amount of $NH_2$-SS230, $NH_2$-SS330 and $NH_2$-SS440 from Nanodrop data (12.7, 15.0 and 12.1ng/μg, respectively) to completely bind 0.5 μg of pcDNA, is about 39.4, 33.3, 41.3 μg, respectively, which is much lower than the values (80-120 μg) estimated from electrophoresis. These results

suggest that pcDNA molecules after interacting with $NH_2$-SS230, $NH_2$-SS330 and $NH_2$-SS440 are more easily detached from their complexes than $NH_2$-SS125. For $NH_2$-SS570, free pcDNA can be seen at even the highest amount of 120 μg. The amount of $NH_2$-SS570 to completely bind pcDNA calculated from Nanodrop (10.0 ng/μg) is about 50 μg, which is much less than the value (> 120 μg) in electrophoresis. By comparing the results from Nanodrop and electrophoresis, it is concluded that $NH_2$-SS125 shows the highest binding capacity and strongest binding affinity. $NH_2$-SS230, $NH_2$-SS330 and $NH_2$-SS440 demonstrate moderate binding capacity as well as binding affinity. $NH_2$-SS570 not only displays lowest binding capacity but also weakest binding affinity toward pcDNA. The curvature of nanoparticle surface decrease as particle size increases, which causes the decrease of DNA packing ability.[31]

The hydrodynamic diameters of $NH_2$-SS/pcDNA complexes were measured by DLS in PBS solution. After forming complex with pcDNA, the diameter of $NH_2$-SS125 and $NH_2$-SS230 increases to 408±29 and 279/1156±38 nm, respectively (Figure S1 and Table 1), indicating the aggregation of $NH_2$-SS after interacting with pcDNA. Similar aggregation phenomenon was also observed in a previous report where the complex diameter of silica nanoparticles (~ 250 nm)/pDNA increased to 1223 nm.[16] However, there is no report on the size change of silica nanoparticles with a large diameter of 300-500 nm after forming complex with pDNA. Interestingly, we found that the diameters of $NH_2$-SS330/pcDNA, $NH_2$-SS440/pcDNA, and $NH_2$-SS570/pcDNA (371±38, 492±31, 725±7 nm respectively) are close to the size of $NH_2$-SS before incubation with pcDNA (Figure S1 and Table 1). The PDI values of the complexes are higher than those of pure $NH_2$-SS (Table 1), indicating the dispersity of complexes decreases in some degree.

The TEM observation shows that $NH_2$-SS125/pcDNA (Figure 1f) and $NH_2$-SS230/pcDNA (Figure 1g) have higher tendency to form big aggregated clusters than $NH_2$-SS330/pcDNA (Figure h), $NH_2$-SS440/pcDNA (Figure i) and $NH_2$-SS570/pcDNA (Figure j). However, single particle formed complexes are also found in the case of $NH_2$-SS230/pcDNA. These results are consistent with what observed in DLS measurements of $NH_2$-SS/pcDNA.

Based on the DLS, AFM and TEM results, we propose a possible interaction model between pcDNA and $NH_2$-SS with different diameters, as shown in Scheme 1. Specifically, pcDNA molecules in preferred supercoiled form adhere on the surfaces of several $NH_2$-SS125 particles and form big clusters, leading to particle size increase after forming complexes (Figure S1). In the case of $NH_2$-SS230, both big clusters and single particles are formed dependent on the compact status of pcDNA. However, one pcDNA coil is difficult to attach on the surface of more than one particle of $NH_2$-SS330, $NH_2$-SS440 or $NH_2$-SS570 to form big clusters. Instead, several pcDNA coils attach on one silica particle. Therefore, the diameters of $NH_2$-SS330, $NH_2$-SS440 and $NH_2$-SS570 after incubation with pcDNA are similar with those before incubation (Table 1 and Figure S1).

**Cellular uptake of $NH_2$-SS/pcDNA in HEK 293T cells.** The correlation between internalization efficiency and silica nanoparticle size has been well documented: smaller silica nanoparticles possess higher cellular uptake performance than larger ones.[32, 33] However, in gene delivery applications, the size of $NH_2$-SS/pcDNA complexes rather than $NH_2$-SS alone matters in the cell uptake process. To quantitatively compare the cellular uptake efficiency of pcDNA/$NH_2$-SS complexes with different sizes, Inductively Coupled Plasma Optical Emission Spectrometer (ICPOES) was used to determine the amount of silica nanoparticles internalized

into HEK 293T cells. Figure 6 shows that the cellular uptake performance of $NH_2$-SS330/pcDNA, $NH_2$-SS440/pcDNA and $NH_2$-SS570/pcDNA complexes is higher that of $NH_2$-SS125/pcDNA and $NH_2$-SS230/pcDNA. The silicon amount internalized into cells treated with $NH_2$-SS125/pcDNA (20.6 pg/cell) is much less than that of $NH_2$-SS230/pcDNA (93.2 g/cell). In the case of $NH_2$-SS125/pcDNA, almost all silica spheres form big clusters, based on the DLS measurement and TEM observation (Table 1 and Figure 1f), while for $NH_2$-SS230/pcDNA, there are still some single particles apart from big clusters (Table 1 and Figure 1g). Compared to $NH_2$-SS570/pcDNA, $NH_2$-SS330/pcDNA and $NH_2$-SS440/pcDNA with smaller sizes demonstrate relatively lower cell internalization performance, which may be caused by their larger PDI values. In addition, pcDNA molecules are easily detached from the $NH_2$-SS570/pcDNA complexes, as demonstrated by the binding affinity results in Figure 4, Figure 5 and Table S3. Thus $NH_2$-SS570/pcDNA complexes have a possibility to be less negative charge during the treatment, which is beneficial for crossing the cell membrane, leading to more efficient cellular uptake.

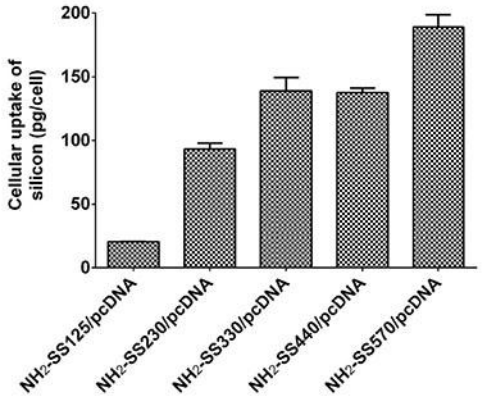

**Figure 6** Internalization performances of complexes $NH_2$-SS125/pcDNA, $NH_2$-SS230/pcDNA, $NH_2$-SS330/pcDNA, $NH_2$-SS440/pcDNA and $NH_2$-SS570/pcDNA at w/w = 160 into HEK 293T cells by measuring the silicon amount per cell.

As mentioned before, efficient binding affinity and subsequent cellular uptake performance are significant for successful nano-carrier medicated gene transfection. Although $NH_2$-SS125 has efficient binding affinity toward pcDNA, its deficiency in cellular uptake after forming complexes causes low GFP expression efficiency (w/w = 160, Figure 2). The cell uptake performance of $NH_2$-SS570/pcDNA is the highest among all of $NH_2$-SS/pcDNA, however, the binding affinity of $NH_2$-SS570 toward pcDNA is too weak, resulting in relatively low GFP expression. The other three $NH_2$-SS demonstrate similar sufficient binding affinity which is desired for successful gene transfection, however, the cell uptake performance of $NH_2$-SS330 and $NH_2$-SS440 is higher than that of $NH_2$-SS230. This accounts for higher GFP transfection efficiencies in $NH_2$-SS330 and $NH_2$-SS440, compared to that in $NH_2$-SS230.

**Cytotoxicity of $NH_2$-SS in HEK293T cells.** Gene carriers should be biocompatible in gene therapy, thus the low cytototoxicity of $NH_2$-SS is crucial. To evaluate the cytotoxicity of $NH_2$-SS, HEK 293T cells were treated with $NH_2$-SS at different concentrations, followed by cell viability test using MTT assay. From Figure S4, it can be seen that all the $NH_2$-SS nanoparticles are biocompatible even at the highest concentration (300 μg/ml). In the above GFP transfection experiments, the concentration was 60-300 μg/ml for all $NH_2$-SS nanoparticles with excellent biocompatibility.

**Transfection efficiency and binding capacity of $NH_2$-SS tested in H1.** The size-dependent GFP expression efficiency was also demonstrated in another pDNA (namely, H1) with a bigger size of 8.9 kbp. The quantification of expressed GFP in HEK 293T cells was determined by flow

cytometry. As shown in Figure 7, H1 alone shows no GFP expression. $NH_2$-SS/H1 complexes reveal GFP expression increment with weight ratio of $NH_2$-SS to H1 increasing for all $NH_2$-SS. There is also an optimum particle size of $NH_2$-SS, which is 230 nm (slightly higher than that in $NH_2$-SS330) at w/w = 40 and 330 nm at w/w = 120, 160 and 200, respectively. The influence of particle size on transfection activity is similar with what observed in the case of pcDNA (Figure 2). The optimized particle size to achieve the highest transfection efficiency is 330 nm in both pDNA under test (pcDNA and H1). It is noted that all $NH_2$-SS/H1 complexes (Figure 7) induced lower GFP expression compared to $NH_2$-SS/pcDNA complexes (Figure 2). Moreover, GFP expression transfected by $NH_2$-SS330 at w/w = 200 is only about 8% and 10% of that induced by PEI/H1complex with an N/P ratio of 10 and 5, respectively (Figure S5). This result is consistent with a previous report that the transfection efficiency of a pDNA with a larger size is lower than that of a smaller size.[34]

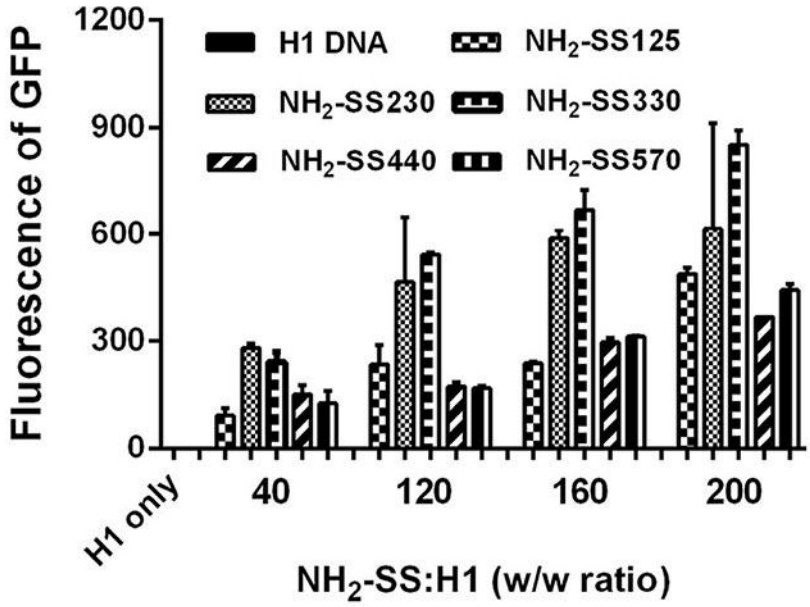


**Figure 7.** GFP expression levels in HEK 293T cells by flow cytometry after treated with naked H1, $NH_2$-SS125/H1, $NH_2$-SS230/H1, $NH_2$-SS330/H1, $NH_2$-SS440/H1 and $NH_2$-SS570/H1 at different weight ratios of $NH_2$-SS to H1. The Y value of fluorescence intensity of GFP = GFP positive cell percentage × GFP mean intensity per GFP positive cell.

Confocal microscopy was further used to study GFP expression levels transfected by $NH_2$-SS/H1 complexes with a weight ratio ($NH_2$-SS to H1) of 200. As shown in Figure S6, GFP expression cannot be detected when naked H1 is used, the same as what observed in pcDNA (Figure S3). When $NH_2$-SS125 is used to deliver H1, GFP expression is still hardly observed. The expressed GFP level increases with increasing the diameter of $NH_2$-SS from 230 to 330 nm, then turns to decrease when the particle size of $NH_2$-SS further increases to 440 and 570 nm. The influence of particle size on transfection activity detected by confocal microscopy is in

agreement with what observed in flow cytometry (Figure 7). These results further prove that the silica particle size has a significant influence on gene transfection efficiency.

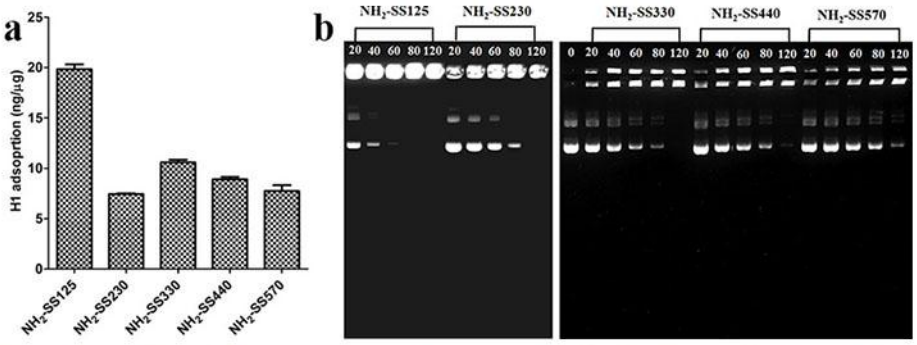


**Figure 8.** a) H1 adsorption capacities of $NH_2$-SS125, $NH_2$-SS230, $NH_2$-SS330, $NH_2$-SS440 and $NH_2$-SS570 measured by Nanodrop; b) agarose gel electrophoresis of $NH_2$-SS/H1demonstrating plasmid DNA/nanoparticle complexation with increasing amounts of $NH_2$-SS (μg). The amount of H1 was constant (0.5 μg).

The binding capacities of $NH_2$-SS with various particle sizes toward H1 were evaluated by Nanodrop and gel retardation assay. As shown in Figure 8a, the overall trend of binding capacity of $NH_2$-SS decreases with increasing particle size of $NH_2$-SS, which is similar as what observed in pcDNA (Figure 4). However, the binding capacity of H1 in all $NH_2$-SS is slightly less than those of pcDNA (Figure 4) due to the bigger size of H1 compared to pcDNA. In gel retardation analysis (Figure 8b), the amount of $NH_2$-SS required to completely retain H1 (0.5 μg) in the wells increases as increasing the particle size of $NH_2$-SS, further confirming the influence of particle size on H1 binding capacity. Compared with pcDNA (Figure 5), more $NH_2$-SS125 (about 80 μg) is required to completely bind the same amount of the bigger H1. $NH_2$-SS with diameters of 230 and 330 nm demonstrate similar binding ability as in pcDNA case, in which 80-120 μg of silica nanoparticles are needed to completely retain pcDNA or H1 in the wells.

However, more than 120 μg are needed to efficiently bind same give amount of H1 in both $NH_2$-SS440 and $NH_2$-SS570, similar as the binding affinity of $NH_2$-SS570 toward pcDNA. By analysing the data in Figures 8a-b, it can be found that $NH_2$-SS125 show the strongest binding affinity to H1 while $NH_2$-SS440 and $NH_2$-SS570 demonstrate the weakest binding capacity. $NH_2$-SS230 and $NH_2$-SS330 demonstrate a moderate binding affinity to H1.

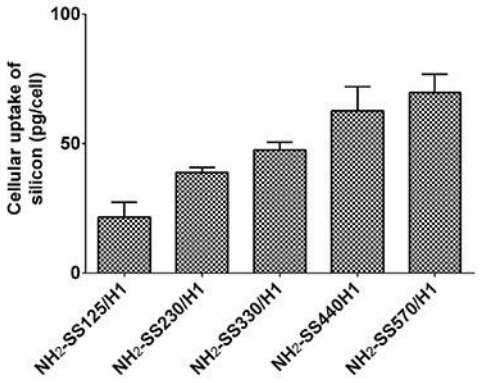


**Figure 9** Internalization performances of complexes $NH_2$-SS125/H1, $NH_2$-SS230/H1, $NH_2$-SS330/H1, $NH_2$-SS440/H1and $NH_2$-SS570/H1 at w/w = 160 into HEK 293T cells by measuring the silicon amount per cell.

The cellular uptake performance of $NH_2$-SS/H1 complexes was investigated by ICPOES method. As shown in Figure 9, the cellular uptake ability increases with particle size of $NH_2$-SS increases, which is similar to what detected in pcDNA (Figure 6). The silicon amount internalized into cells treated with $NH_2$-SS125/H1 and $NH_2$-SS230/H1 is less than those of $NH_2$-SS330/H1, $NH_2$-SS440/H1 $NH_2$-SS570/H1, due to big clusters formed in $NH_2$-SS125/H1 and $NH_2$-SS230/H1 (Table 1 and Figure S1). The difference of GFP transfection efficiency mediated by $NH_2$-SS with different sizes could be contributed by two aspects of binding affinity and

cellular uptake performance likewise in the pcDNA case. It should be noted that $NH_2$-SS230/H1 shows much higher transfection efficiency compared to that induced by $NH_2$-SS440/H1, which is different from the results in pcDNA. $NH_2$-SS440 have a much weaker binding affinity of H1 with a larger size compared to that of pcDNA, leading to a relatively lower transfection efficiency.

The size-dependent gene delivery relationship of monodispersed $NH_2$-SS in *in vitro* could be altered in *in vivo* gene transfection. When a foreign nanoparticle interacts with biological fluid, it is quickly covered by proteins in the medium, forming a complex layer defined as "protein corona". Such corona is composed by a core of strongly bound proteins and an outer layer of fast exchanging molecules.[35, 36] Therefore, when the complexes of $NH_2$-SS/DNA are applied in the biological fluid, proteins and DNA molecules compete for the adsorption sites of $NH_2$-SS. For example, DNA with a relatively low affinity would be replaced by the proteins with a higher mobility in the case of $NH_2$-SS570, leading even lower gene transfection efficiency. More efforts are needed to investigate the formation of a protein corona around $NH_2$-SS and subsequent influences on cellular uptake and gene transfection efficiency in *in vivo* transfection.

## CONCLUSIONS

In summary, a series of amine modified monodisperse Stöber spheres ($NH_2$-SS) were synthesised with different diameters from 125 to 570 nm, and the influence of particle size on gene transfection efficiency was investigated in a plasmid DNA ( namely pcDNA, 6.1kbp), encoding GFP. $NH_2$-SS with a diameter of 330 nm was demonstrated to be the most efficient gene delivery carrier compared to other $NH_2$-SS with diameters of 125, 230, 440, 570 nm. By studying the binding affinity between $NH_2$-SS and pcDNA and cellular uptake performance of

the complexes $NH_2$-SS/pcDNA, we found that $NH_2$-SS330 has sufficient binding affinity toward pcDNA and high cellular uptake performance after forming complexes with pcDNA, beneficial for its high GFP expression level. Furthermore, $NH_2$-SS330 was also shown to be the most efficient gene carrier using another plasmid DNA with a bigger size of 8.9kbp. This work demonstrates the significance of carrier size on gene transfection efficiency in silica based gene delivery systems, providing a new understanding for the improvement of gene transfection efficiency of synthetic gene delivery systems.

## EXPERIMENTAL SECTION

**Chemicals:** Tetraethoxysilane (TEOS, 98%), (3-aminopropyl)triethoxysilane (APTES), dimethylsulfoxide (DMSO), ammonia ($NH_3$, 28wt% aqueous solution), paraformaldehyde (PFA) and 3-(4,5-dimethylthiazol-2-yl)-2,5-diphenyltetrazolium bromide (MTT) were purchased from Sigma-Aldrich. UltraPure™ 10×TAE (Tris-acetate-EDTA) buffer, and SYBR® Safe DNA gel stain (10000× in DMSO) were purchased from Invitrogen Australia. Cell lysis buffer (10×) was purchased from Cell Signaling Technology. Polyethylenimine (branched, M.W. 25k) was purchased from Alfa Aesar.

**Synthesis of $NH_2$-SS125, $NH_2$-SS230, $NH_2$-SS330, $NH_2$-SS440 and $NH_2$-SS570:** Monodisperse silica spheres were prepared by the modified Stöber method.[37] In a typical experiment, two solutions were rapidly mixed together. The first solution was the mixture of TEOS and ethanol (EtOH), and the second solution was the mixture of 28 wt% ammonia, deionized water, and EtOH. The first solution was added to the second solution under stirring. The resulting mixture was further stirred for certain time. Finally, silica spheres were separated from the suspension by centrifugation and washed with ethanol twice, and further washed with water twice. The detailed chemical amount and synthesis condition are listed in Table S1. After

drying in a 50°C oven overnight, 0.1g of silica spheres were suspended in 40 ml of toluene. Then the mixture was refluxed in a three-neck flask under stirring at 110 °C for 2h, followed by adding 93.6µl of APTES. After stirring for further 20h, the suspension was centrifuged and washed with ethanol and water. The final products were collected by drying process at 50°C overnight, and denoted as $NH_2$-SSx, where 'x' stands for the particle diameters of amine modified Stöber spheres ($NH_2$-SS) estimated by TEM analysis. For example, $NH_2$-SS125 represents amine modified Stöber spheres with a diameter of 125 nm.

**Characterisation**: Transmission electron microscopy (TEM) images were obtained with a JEOL 1010 operated at 100 kV. For TEM measurements, the samples were prepared by dispersing the powder samples in ethanol, after which they were dispersed and dried on carbon film on a Cu grid. Dynamic light scattering (DLS) studies and zeta potential measurements were carried out on a Malvern NanoZS zetasizer at 25 °C in phosphate buffered saline (PBS) solution. The measurements were repeated three times for each sample and the statistical data were shown as mean ±(SD). Elemental Analyses were determined by CHNS-O Analyzer (Flash EA1112 Series, Thermo Electron Corporation).

**Cell Culture:** HEK 293T (human embryonic kidney cell line) cells were maintained in Dulbecco's Modified Eagle Medium (DMEM) supplemented with fetal bovine serum (10%, Moregate Biotech Australia), L-glutamine (2%), penicillin (1%), and streptomycin (1%) in a 5% $CO_2$ incubator at 37 °C. The medium was routinely changed every 2 days and the cells were separated by trypsinisation before reaching confluency.

**Amplification and purification of plasmid DNA:** pcDNA3-EGFP (abbreviated as pcDNA) and psiHIV-InH1™ (abbreviated as H1) are 6.1 and 8.9 kbp plasmid DNA, respectively, encoding green fluorescent protein (GFP) driven by cytomegalovirus (CMV) promoter. Both

plasmid DNA (pDNA) were amplified in *E. coli* strain DH5α and purified by a GenElute™ HP Endotoxin-Free Plasmid Maxiprep Kit (Sigma-Aldrich Australia) according to the manufacturer's protocol. Both purified pDNA were dissolved in endotoxin-free water and their concentrations were determined by UV absorbance at 260nm by Nanodrop 1000 spectrophotometer.

**GFP plasmid transfection of cultured cells:** HEK 293T cells were seeded in a 6-well cell culture plate at a density of $1\times10^5$ cells per well and incubated for 36 h. After washing the cells with PBS, 1.9 ml of serum-free DMEM medium was added to each well. Prior to transfection, GFP plasmid DNA/$NH_2$-SS complexes were prepared as follows: 2.5 μg of plasmid DNA was incubated with 500 μg of $NH_2$-SS with various sizes, in 100 μl of PBS at 4°C overnight. Each mixture was then added into each well with serum-free medium. After incubation at 37°C for 4 h, the medium in each well was replaced by 2 ml of fresh serum-containing media, and then the cells were incubated for additional 48 h. Subsequently, the cells were washed with PBS for 2 times. For fixed cell imaging, the cells were treated with 500 μL of 4% PFA solution for 30 minutes at 4 °C. Finally, the cells were viewed under a confocal microscope (LSM Zeiss 710).

A quantitative determination of GFP transfected cells by flow cytometry analysis. Prior to transfection, GFP plasmid DNA/$NH_2$-SS complexes were prepared as follows: 2.5 μg of plasmid DNA was incubated with 100, 300, 400 and 500 μg of $NH_2$-SS in 100 μl of PBS solutions at 4°C overnight, to obtain the complexes with weight ratio ($NH_2$-SS to plasmid DNA) of 40, 120, 160 and 200, respectively. HEK 293T cells were seeded in a 6-well plate ($1\times10^5$ cells per well) and incubated for 36 h. After washing the cells with PBS, 1.9 ml of serum-free DMEM medium was added to each well. The complexes was then added into each well with serum-free medium. After incubation at 37°C for 4 h, the medium was replaced by 2 ml of fresh serum-containing

media, and then the cells were incubated for additional 48 h. The cells were trypsinized, and then centrifuged and washed two times with PBS. After that, the cells were suspended in 0.5 ml of 2% PFA-PBS solution, and put in a 4°C fridge for 30 min. Afterwards, the fluorescence intensity of positive cells was analyzed by using a BD LSR II Analyser (Becton Dickinson BD). All the data of positive cell distribution were obtained from a population of 20,000 cells after gating of single cells. All the experiments were performed in triplicates for each group. The statistical data were shown as mean± (SEM).

The GFP transfection efficiency of PEI/DNA complexes was performed as described by Lehr, et al. with slight modification.[38] PEI (25k) dissolved in D.I. water with a concentration of 1mg/ml at -4°C for further use. Then 1.6, 2.4, 2.9 and 3.3μl of PEI solution and plasmid DNA (2.5μg) was added into D.I. water (final volume 100μl) to obtain PEI/DNA complexes with an N/P ratio of 5, 7.5, 9, 10 respectively. Then the solution was immediately mixed for 10 seconds, followed by incubation for 30 minutes at room temperature. Afterwards, the prepared mixture was added into plate well with 1ml Hank's Balanced Salt Solution (HBSS buffer) pH 7.4 and incubated for 4h. After incubation, the buffer was replaced by 2 ml of fresh serum-containing media, and then the cells were incubated for additional 48. The following steps for confocal microscopy and flow cytometry analysis were same as what described in $NH_2$-SS/DNA systems.

**Atomic force microscopy:** The pcDNA sample was prepared as described by Révet et al. with some modifications.[39] The stock pcDNA solution was diluted in 10 mM Tris, pH 7.4, 5mM $MgCl_2$ with a final concentration of 0.5ng/μl. 5 μl of pcDNA sample was deposited onto a freshly cleaved mica substrate. After 1 min, the sample was rinsed with 2-3 drops of 0.2% (w/v) aqueous uranyl acetate and dried. The measurements were performed with a Cypher S AFM (Oxford Instruments Company). All the images were obtained by employing the Tapping Mode

of the AFM in air. The cantilevers used were HA_NC (Etalon) from NT-MDT, having a nominal resonance frequency of 135 kHz.

**pDNA binding analysis by Nanodrop:** 1 μg of pDNA (pcDNA or H1) was mixed well with 20 μg of $NH_2$-SS with different diameters in 20 μl PBS solution and then incubated at 4°C fridge overnight. The complexes of $NH_2$-SS/pDNA were centrifuged at 13,000 rpm for 10 minutes. The supernatant was collected and analysed at 260 nm using a Nanodrop 1000 spectrophotometer to obtain the pDNA concentration. The pDNA adsorption capacity was calculated based on the original and residual concentrations as following equation. All the experiments were repeated three times.

Binding Capacity (ng/μg) = [*C* (original pDNA, ng/μl) - *C* (residual pDNA, ng/μl)]×Volume of mixture (μl )/*w* ($NH_2$-SS, μg)

**Agarose gel electrophoresis**: The $NH_2$-SS/pDNA complex was prepared by the following process. Briefly, 0.5 μg of pDNA was incubated with varying amounts of $NH_2$-SS at 4 °C in 10 μl of PBS overnight. 2 μl of 6×DNA loading buffer was added into each mixture, and then the mixtures were loaded on a 1% agarose gel containing 1× SYBR Safe. The electrophoresis was carried out at 80V for 1h in TAE buffer, and the bands were visualized on a UV trans-illuminator (Bio-Rad reader).

**Cell viability test of $NH_2$-SS**: The cytotoxicity of $NH_2$-SS with different sizes was tested in HEK 293T cells by MTT assay. HEK 293T cells were seeded in a 96-well cell culture plate with a density of $5\times10^3$ cells/well. After incubation for 24 h, the cells were added with different concentrations of $NH_2$-SS PBS solution. After 48 h, the media was removed, and 100 μl of fresh DMEM medium was added each well, followed by addition of 10 μL of MTT solution (5mg/ml). Plate was then incubated in the culture oven for 4 h before adding 100 μl of DMSO to each well.

Then absorbance readings were measured at wavelength of 540 nm using a Synergy HT microplate reader, and background absorbance of media was subtracted. The cells incubated in the absence of particles were used as the control. All the experiments were performed in triplicates for each group. The statistical data were shown as mean± (SD).

**Cellular uptake of $NH_2$-SS/pcDNA**: To quantitatively determine the cellular uptake of the complexes of $NH_2$-SS/pcDNA (H1), HEK 293T cells were seeded in a 6-well cell culture plate at a density of $1\times10^5$ cells per well and incubated for 36 h. Afterwards, the complexes of $NH_2$-SS/pcDNA was added to each well, as described above in the GFP transfection experiment. After further incubation for another 24 h, the cells were washed with PBS three times and harvested with trypsin. After washing with PBS twice and centrifugation, 120 µl of 1× cell lysis buffer was added to each tube to allow dissolution of cells under sonication process. The supernatants (containing cell components) were discarded after centrifugation at 13,000 rpm for 10 minutes, and the precipitates were washed with PBS twice, followed by drying at 50°C overnight. 150 µl of aqueous NaOH solution (1 M) was then added to dissolve the silica nanoparticles. The silicon concentrations in the final solutions were measured by Inductively Coupled Plasma Optical Emission Spectrometer (ICPOES) with a Vista-PRO instrument (Varian Inc, Australia). The mass of silicon in per cell was calculated based on the ICPOES results and cell numbers by counting.

**Supporting Information**.

The supporting information contains the table of $NH_2$-SS synthesis conditions, DLS, confocal images of GFP expression, Nanodrop and flow cytometry analysis of PEI/DNA complexes. This information is available free of charge *via* the Internet at http://pubs.acs.org

**Corresponding Author**

*Address correspondence to: c.yu@uq.edu.au

**Author Contributions**

‡These authors contributed equally.

**ACKNOWLEDGMENT**

We thank the support from Australian Research Council, the Australian Microscopy & Microanalysis Research Facility at the Centre for Microscopy and Microanalysis, The University of Queensland, and the Queensland node of the Australian National Fabrication Facility (ANFF).

**REFERENCES**

1 Roy, K.; Mao, H. Q.; Huang, S. K.; Leong, K. W., Oral Gene Delivery with Chitosan-DNA Nanoparticles Generates Immunologic Protection in a Murine Model of Peanut Allergy. *Nat. Med.* **1999,** *5*, 387-391.

2 Luo, D.; Saltzman, W. M., Synthetic DNA Delivery Systems. *Nat. Biotechnol.* **2000,** *18*, 33-37.

3 Lew, D.; Parker, S. E.; Latimer, T.; Abai, A. M.; Kuwahararundell, A.; Doh, S. G.; Yang, Z. Y.; Laface, D.; Gromkowski, S. H.; Nabel, G. J., et al., Cancer Gene-Therapy Using Plasmid DNA - Pharmacokinetic Study of DNA Following Injection in Mice. *Hum. Gene Ther.* **1995,** *6*, 553-564.

4 Giacca, M.; Zacchigna, S., Virus-Mediated Gene Delivery for Human Gene Therapy. *J. Control. Release* **2012,** *161*, 377-388.

5 Mintzer, M. A.; Simanek, E. E., Nonviral Vectors for Gene Delivery. *Chem. Rev.* **2009,** *109*, 259-302.

6 Crystal, R. G., Transfer of Genes to Humans - Early Lessons and Obstacles to Success. *Science* **1995,** *270*, 404-410.

7 Tripathy, S. K.; Black, H. B.; Goldwasser, E.; Leiden, J. M., Immune Responses to Transgene-Encoded Proteins Limit the Stability of Gene Expression after Injection of Replication-Defective Adenovirus Vectors. *Nat. Med.* **1996,** *2*, 545-550.

8 Bessis, N.; GarciaCozar, F. J.; Boissier, M. C., Immune Responses to Gene Therapy Vectors: Influence on Vector Function and Effector Mechanisms. *Gene Ther.* **2004,** *11*, S10-S17.

9 Boussif, O.; Lezoualch, F.; Zanta, M. A.; Mergny, M. D.; Scherman, D.; Demeneix, B.; Behr, J. P., A Versatile Vector for Gene and Oligonucleotide Transfer into Cells in Culture and in-Vivo - Polyethylenimine. *Proc. Natl. Acad. Sci. U. S. A.* **1995,** *92*, 7297-7301.

10 Zhang, S. B.; Zhi, D. F.; Huang, L., Lipid-Based Vectors for Sirna Delivery. *J. Drug Target.* **2012,** *20*, 724-735.

11 Hoyer, J.; Neundorf, I., Peptide Vectors for the Nonviral Delivery of Nucleic Acids. *Accounts Chem. Res.* **2012,** *45*, 1048-1056.

12 Sokolova, V.; Epple, M., Inorganic Nanoparticles as Carriers of Nucleic Acids into Cells. *Angew. Chem.-Int. Edit.* **2008,** *47*, 1382-1395.

13 Niu, Y.; Popat, A.; Yu, M.; Karmakar, S.; Gu, W.; Yu, C., Recent Advances in the Rational Design of Silica-Based Nanoparticles for Gene Therapy. *Ther. Deliv.* **2012,** *3*, 1217-1237.

14 Radu, D. R.; Lai, C. Y.; Jeftinija, K.; Rowe, E. W.; Jeftinija, S.; Lin, V. S. Y., A Polyamidoamine Dendrimer-Capped Mesoporous Silica Nanosphere-Based Gene Transfection Reagent. *J. Am. Chem. Soc.* **2004,** *126*, 13216-13217.

15 Chen, A. M.; Zhang, M.; Wei, D. G.; Stueber, D.; Taratula, O.; Minko, T.; He, H. X., Co-Delivery of Doxorubicin and Bcl-2 Sirna by Mesoporous Silica Nanoparticles Enhances the Efficacy of Chemotherapy in Multidrug-Resistant Cancer Cells. *Small* **2009,** *5*, 2673-2677.

16 Kim, M. H.; Na, H. K.; Kim, Y. K.; Ryoo, S. R.; Cho, H. S.; Lee, K. E.; Jeon, H.; Ryoo, R.; Min, D. H., Facile Synthesis of Monodispersed Mesoporous Silica Nanoparticles with Ultralarge Pores and Their Application in Gene Delivery. *ACS Nano* **2011,** *5*, 3568-3576.

17 Kneuer, C.; Sameti, M.; Haltner, E. G.; Schiestel, T.; Schirra, H.; Schmidt, H.; Lehr, C. M., Silica Nanoparticles Modified with Aminosilanes as Carriers for Plasmid DNA. *Int. J. Pharm.* **2000,** *196*, 257-261.

18 Kneuer, C.; Sameti, M.; Bakowsky, U.; Schiestel, T.; Schirra, H.; Schmidt, H.; Lehr, C. M., A Nonviral DNA Delivery System Based on Surface Modified Silica-Nanoparticles Can Efficiently Transfect Cells in Vitro. *Bioconjugate Chem.* **2000,** *11*, 926-932.

19 Bharali, D. J.; Klejbor, I.; Stachowiak, E. K.; Dutta, P.; Roy, I.; Kaur, N.; Bergey, E. J.; Prasad, P. N.; Stachowiak, M. K., Organically Modified Silica Nanoparticles: A Nonviral Vector for in Vivo Gene Delivery and Expression in the Brain. *Proc. Natl. Acad. Sci. U. S. A.* **2005,** *102*, 11539-11544.

20 Cebrian, V.; Yague, C.; Arruebo, M.; Martin-Saavedra, F. M.; Santamaria, J.; Vilaboa, N., On the Role of the Colloidal Stability of Mesoporous Silica Nanoparticles as Gene Delivery Vectors. *J. Nanopart. Res.* **2011,** *13*, 4097-4108.

21 Jung, H. S.; Moon, D. S.; Lee, J. K., Quantitative Analysis and Efficient Surface Modification of Silica Nanoparticles. *J. Nanomater.* **2012**.

22 Yu, M. H.; Jambhrunkar, S.; Thorn, P.; Chen, J. Z.; Gu, W. Y.; Yu, C. Z., Hyaluronic Acid Modified Mesoporous Silica Nanoparticles for Targeted Drug Delivery to Cd44-Overexpressing Cancer Cells. *Nanoscale* **2013,** *5*, 178-183.

23 Luo, D.; Saltzman, W. M., Enhancement of Transfection by Physical Concentration of DNA at the Cell Surface. *Nat. Biotechnol.* **2000,** *18*, 893-895.

24 Luo, D.; Han, E.; Belcheva, N.; Saltzman, W. M., A Self-Assembled, Modular DNA Delivery System Mediated by Silica Nanoparticles. *J. Control. Release* **2004,** *95*, 333-341.

25 Slowing, II; Vivero-Escoto, J. L.; Wu, C. W.; Lin, V. S. Y., Mesoporous Silica Nanoparticles as Controlled Release Drug Delivery and Gene Transfection Carriers. *Adv. Drug Deliv. Rev.* **2008,** *60*, 1278-1288.

26 Zou, S. M.; Erbacher, P.; Remy, J. S.; Behr, J. P., Systemic Linear Polyethylenimine (L-Pei)-Mediated Gene Delivery in the Mouse. *Journal of Gene Medicine* **2000,** *2*, 128-134.

27 Ahn, S.; Seo, E.; Kim, K.; Lee, S. J., Controlled Cellular Uptake and Drug Efficacy of Nanotherapeutics. *Scientific Reports* **2013,** *3*.

28 Roy, I.; Ohulchanskyy, T. Y.; Bharali, D. J.; Pudavar, H. E.; Mistretta, R. A.; Kaur, N.; Prasad, P. N., Optical Tracking of Organically Modified Silica Nanoparticles as DNA

Carriers: A Nonviral, Nanomedicine Approach for Gene Delivery. *Proc. Natl. Acad. Sci. U. S. A.* **2005,** *102*, 279-284.

29 Cebrian, V.; Martin-Saavedra, F.; Yague, C.; Arruebo, M.; Santamaria, J.; Vilaboa, N., Size-Dependent Transfection Efficiency of Pei-Coated Gold Nanoparticles. *Acta Biomater.* **2011,** *7*, 3645-3655.

30 Aaij, C.; Borst, P., The Gel Electrophoresis of DNA. **1972,** *239*, 192-200.

31 Cederquist, K. B.; Keating, C. D., Curvature Effects in DNA:Au Nanoparticle Conjugates. *ACS Nano* **2009,** *3*, 256-260.

32 Lu, F.; Wu, S. H.; Hung, Y.; Mou, C. Y., Size Effect on Cell Uptake in Well-Suspended, Uniform Mesoporous Silica Nanoparticles. *Small* **2009,** *5*, 1408-1413.

33 Zhu, J.; Tang, J. W.; Zhao, L. Z.; Zhou, X. F.; Wang, Y. H.; Yu, C. Z., Ultrasmall, Well-Dispersed, Hollow Siliceous Spheres with Enhanced Endocytosis Properties. *Small* **2010,** *6*, 276-282.

34 Yin, W. X.; Xiang, P.; Li, Q. L., Investigations of the Effect of DNA Size in Transient Transfection Assay Using Dual Luciferase System. *Anal. Biochem.* **2005,** *346*, 289-294.

35 Walczyk, D.; Bombelli, F. B.; Monopoli, M. P.; Lynch, I.; Dawson, K. A., What the Cell "Sees" in Bionanoscience. *J. Am. Chem. Soc.* **2010,** *132*, 5761-5768.

36 Lynch, I.; Cedervall, T.; Lundqvist, M.; Cabaleiro-Lago, C.; Linse, S.; Dawson, K. A., The Nanoparticle - Protein Complex as a Biological Entity; a Complex Fluids and Surface Science Challenge for the 21st Century. *Advances in Colloid and Interface Science* **2007,** *134-35*, 167-174.

37 Stober, W.; Fink, A.; Bohn, E., Controlled Growth of Monodisperse Silica Spheres in Micron Size Range. *J. Colloid Interface Sci.* **1968,** *26*, 62-69.

38 Yamada, H.; Loretz, B.; Lehr, C. M., Design of Starch-Graft-Pei Polymers: An Effective and Biodegradable Gene Delivery Platform. *Biomacromolecules* **2014,** *15*, 1753-1761.

39 Revet, B.; Fourcade, A., Short Unligated Sticky Ends Enable the Observation of Circularised DNA by Atomic Force and Electron Microscopies. *Nucleic Acids Res.* **1998,** *26*, 2092-2097.

TOC

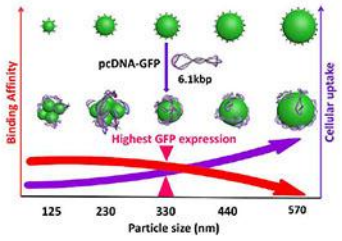

# Supporting information

## An Unusual Size-Dependent Gene Delivery Relationship of Monodispersed Silica Nanoparticles

Meihua Yu[a, ‡], Yuting Niu[a, ‡], Jun Zhang[a], Hongwei Zhang[a], Yannan Yang[a], Elena Taran [a,b], Siddharth Jambhrunkar[a], Wenyi Gu[a], Peter Thorn[c], and Chengzhong Yu[a]*

[a]Australian Institute for Bioengineering and Nanotechnology, The University of Queensland, Brisbane, QLD 4072, Australia

[b]Australian National Fabrication Facility – QLD Node

[c]School of Biomedical Sciences, The University of Queensland, Brisbane, QLD 4072, Australia

*Corresponding author: Tel: +61-7-334 63283; Fax: +61-7-334 63973; E-mail address: c.yu@uq.edu.au

‡ these authors contributed equally.

**Table S1**: Experimental conditions for the synthesis of silica Stöber spheres with different diameters.

| Sample | The first solution | | | The second solution | | T(°C) | *t*(h) |
|---|---|---|---|---|---|---|---|
| | EtOH(ml) | TEOS(ml) | $H_2O$(ml) | EtOH(ml) | $NH_4OH$(ml) | | |
| $NH_2$-SS125 | 22.2 | 2.8 | 6.8 | 17.6 | 0.7 | 25 | 13 |
| $NH_2$-SS230 | 22.2 | 4.5 | 6.8 | 17.6 | 0.7 | 25 | 4.5 |
| $NH_2$-SS330 | 45.5 | 5.0 | 16.25 | 24.75 | 9.0 | 25 | 2 |
| $NH_2$-SS440 | 45.5 | 5.0 | 16.25 | 24.75 | 9.0 | 22 | 2 |
| $NH_2$-SS570 | 45.5 | 5.0 | 16.25 | 24.75 | 9.0 | 15 | 2 |

*T*: reaction temperature; *t*: reaction time

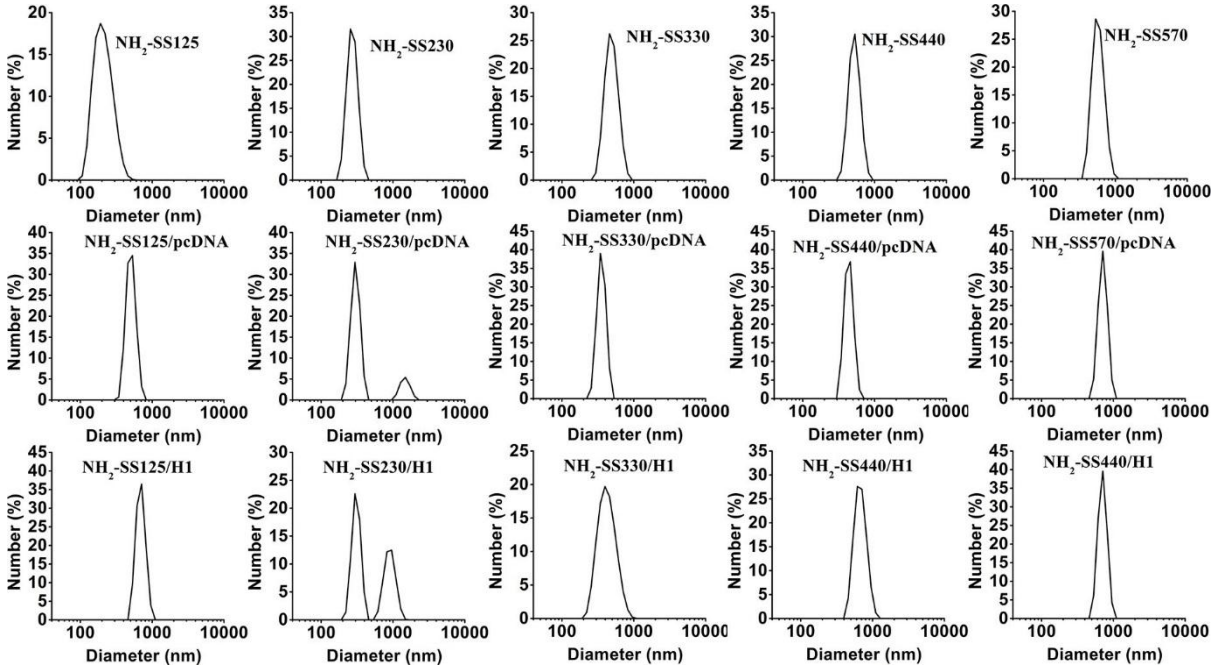


**Figure S1.** Particle size distribution curves measured by DLS method of $NH_2$-SS125, $NH_2$-SS230, $NH_2$-SS330, $NH_2$-SS440, $NH_2$-SS570 and their complexes with pcDNA or H1.

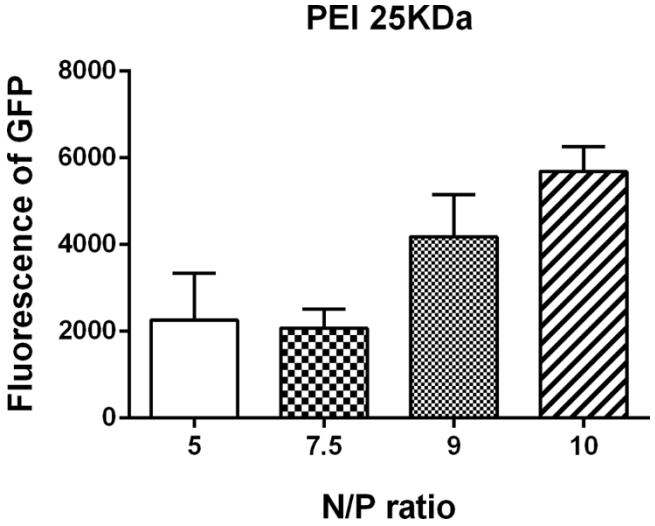


**Figure S2.** GFP expression levels in HEK 293T cells by flow cytometry, after treated with PEI/pcDNA complexes with different N/P ratios. The Y value of fluorescence intensity of GFP = GFP positive cell percentage × GFP mean intensity per GFP positive cell.

**Table S2**: Elemental analysis results of $NH_2$-SS and the calculated N/P ratios of $NH_2$-SS/DNA complexes with different w/w ratios.

| Sample | N (%) | N/P ratio* | | | |
|---|---|---|---|---|---|
| | | w/w = 40 | w/w = 120 | w/w = 160 | w/w = 200 |
| $NH_2$-SS125 | 0.846 | 3.6 | 10.8 | 14.4 | 17.8 |
| $NH_2$-SS230 | 0.834 | 3.6 | 10.7 | 14.2 | 17.7 |
| $NH_2$-SS330 | 0.218 | 0.9 | 2.8 | 3.7 | 4.6 |
| $NH_2$-SS440 | 0.121 | 0.5 | 1.6 | 2.1 | 2.6 |
| $NH_2$-SS570 | 0.099 | 0.4 | 1.3 | 1.7 | 2.1 |

*: N/P ratio = 330/31× w/w × N %, assuming an average molecular weight of 330g/mol of nucleotide.

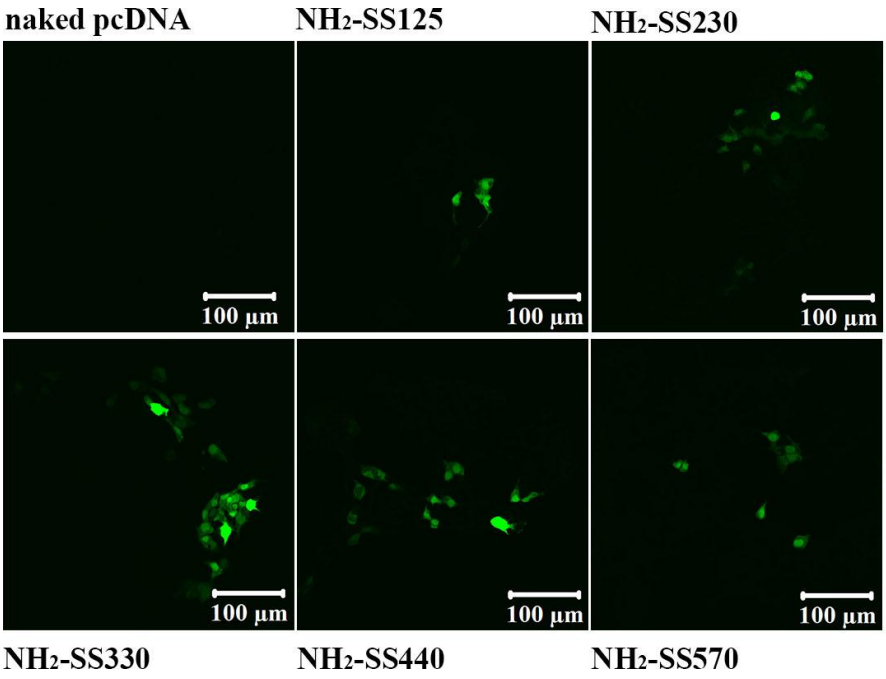


**Figure S3.** Confocal images indicating expressed GFP in HEK 293T cells, after treated with naked pcDNA, $NH_2$-SS125/pcDNA, $NH_2$-SS230/pcDNA, $NH_2$-SS330/pcDNA, $NH_2$-SS440/pcDNA and $NH_2$-SS570/pcDNA.

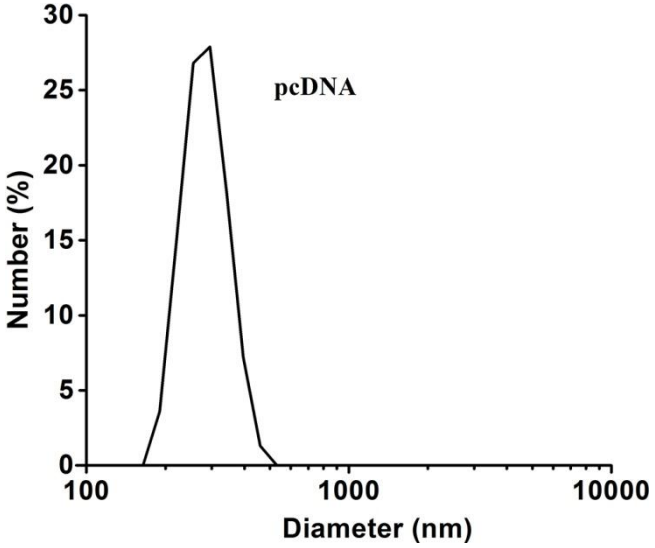


**Figure S4**. Particle size distribution curve of pcDNA measured by DLS method.

**Table S3**: The comparison of $NH_2$-SS binding affinity toward pcDNA measured by Nanodrop and gel retardation assay.

| Sample | Binding capacity measured by Nanodrop (ng/μg) | $W_N$ (μg) | $W_R$(μg) | $W_{R-N}$ (μg) |
|---|---|---|---|---|
| $NH_2$-SS125 | 27.7 | 18.0 | 40 | 22.0 |
| $NH_2$-SS230 | 12.7 | 39.4 | 80-120 | 40.6-80.6 |
| $NH_2$-SS330 | 15.0 | 33.3 | 80-120 | 40.6-80.6 |
| $NH_2$-SS440 | 12.1 | 41.3 | 80-120 | 40.6-80.6 |
| $NH_2$-SS570 | 10.0 | 50.0 | > 120 | > 70.0 |

$W_N$: $NH_2$-SS amount needed to completely bind 0.5μg pcDNA determined by Nanodrop; $W_R$: $NH_2$-SS amount needed to completely bind 0.5μg pcDNA determined by gel retardation assay; $W_{R-N} = W_R - W_N$.

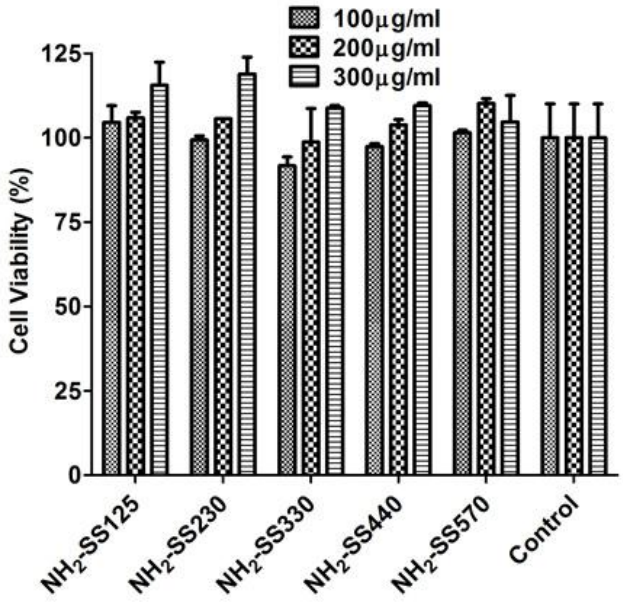


**Figure S5.** Cell viability of HEK 293T after treated with $NH_2$-SS particles at different concentrations (100, 200, 300μg/ml).

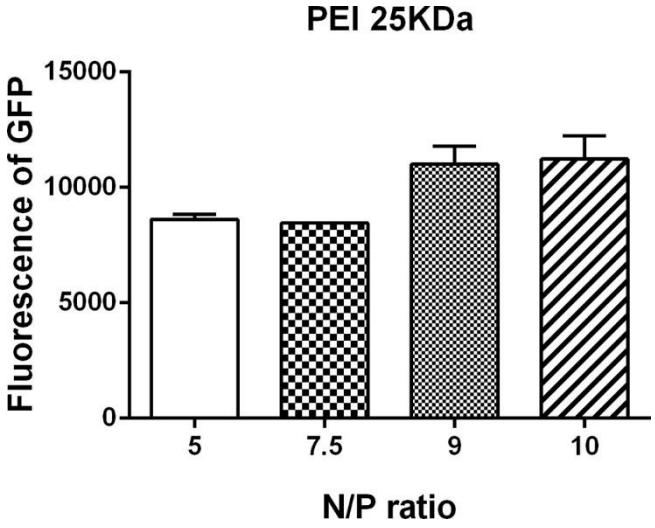


**Figure S6.** GFP expression levels in HEK 293T cells by flow cytometry, after treated with PEI/H1 complexes with different N/P ratios. The Y value of fluorescence intensity of GFP = GFP positive cell percentage ×GFP mean intensity per GFP positive cell.

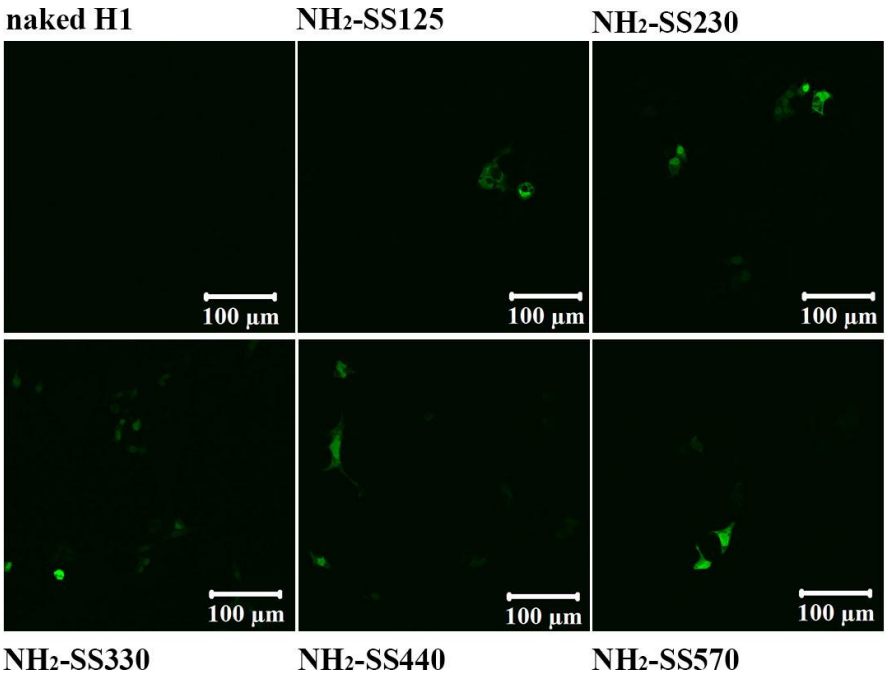


**Figure S7.** Confocal images indicating expressed GFP in HEK 293T cells, after treated with naked H1, $NH_2$-SS125/H1, $NH_2$-SS230/H1, $NH_2$-SS330/H1, $NH_2$-SS440/H1 and $NH_2$-SS570/H1.

# Chapter 9

# General discussion and outlook

## 9.1 General discussion

Silica based nanoparticles (SiNPs) with excellent biocompatibility, tunable pore/ particle size and controllable surface chemistry have attracted enormous research interest in various bio-applications, including cell imaging, diagnosis and bioanalysis, and drug/gene delivery into various cells or animal models.[1-3] SiNPs with a small size (< 100 nm) and high monodispersity possess advantages in cell endocytosis process, which is vital to achieve high efficiency in biomedical applications.[4,5] There have been tremendous efforts in the synthesis of mono-dispersed nanometer-sized SiNPs,[6-9] but still more efforts are highly desired to develop facile, economic and environmentally friendly synthesis approaches for fabricating novel mono-dispersed SiNPs with desired particle size and nano-structure. Thus the first aim of this thesis was to develop facile approaches to synthesize various types of highly mono-dispersed SiNPs with finely controlled pore structure and particle size (10-100 nm). Chapter 4 described a new and facile approach to prepare monodisperse mesoporous silica nanospheres (MMSNs) with controlled particle sizes (50-100 nm) and pore diameters (2.8-4.0 nm) where NaAc was utilized as a catalyst to initiate the hydrolysis and condensation of silicon alkoxides without any harsh conditions in previous reports (e.g. strong acids or alkali). As we hypothesized, the salt of NaAc of a weak acid and a strong base could slow down the hydrolysis and condensation of silica sources of tetraethoxysilane (TEOS). The derived hydrophobic group of $Si–OCH_2CH_3$ on the surface of silica nanoparticles during the reaction protects silica nanoparticle from further random aggregation, finally leading to mono-dispersed nanoparticles. However, it is hard to synthesize highly mono-dispersed MMSNs with smaller than 50 nm. In chapter 5, even smaller mono-dispersed SiNPs (ultra-small hybrid silica spheres, UHSS) with a diameter of only ~ 10 nm were developed by a new and facile strategy under phosphate-citrate buffer solution (pH = 4.6) at room temperature without addition of toxic additives. As expected, this biological buffer with a near neutral pH slows down the deposition of mixed silica sources of tetramethyl orthosilane (TMOS) and dimethoxydimethylsilane (DMDMS) on the shell of tri-block copolymer

$EO_{106}PO_{70}EO_{106}$ [Pluronic F127, EO refers to poly(ethylene oxide), PO refers to poly(propylene oxide)] micelles.

Most reported biological studies of SiNPs are based on two-dimensional (2D) cell models (monolayers). However, such simplified conditions in monolayer cell cultures are not representative of multi-layer cellular environment in the real tissues, limiting the potential of 2D cell culture model to predict the cellular responses of real organisms. In contrast, three-dimensional (3D) culture models more closely mimic the cell-to-cell and cell-to-extracellular matrix (ECM) interactions as well as the topography found in an *in vivo* tumor environment.[10] Therefore, the second aim of this thesis is to evaluate the influence of particle size and mono-dispersity of SiNPs on cell penetration ability in both monolayer and three dimensional spheroid models of various types of cells. In Chapter 5, the penetration ability of novel designed UHSS was evaluated in 3D glioma spheroids. It was found UHSS show enhanced cellular uptake performance and more uniform distribution in the cytoplasm of the cells both in monolayer and three dimensional spheroid models, compared to conventional SiNPs (MCM-41). The relatively large particle size (100 nm in diameter) and limited dispersity of MCM-41 in aqueous solution hindered its uniform penetration ability in 3D glioma spheroids. Additionally, it was reported that cyclic RGD peptide modification was essential for uniform distribution of organic nanoparticles throughout the entire glioma spheroid, otherwise, the organic nanoparticles had limited ability to penetrate the core area of glioma spheroids.[11] UHSS without modification of any targeting moiety demonstrated a comparable glioma tissue penetration capability with organic nanoparticles with a specific ligand.

Apart from particle sizes and monodispersity, surface property is another key factor affecting the efficacy of SiNPs in bio-applications. SiNPs modified with desired functional groups have demonstrated improved adsorption capacities to bioactive molecules/drugs, increased targeting ability to desired sites, enhanced biocompatibility, demanded release of cargos, etc.[1] For example, to facilitate the cellular uptake of the negatively charged siRNA, SiNPs need to be functionalized with positively charged amine groups,[12] poly-L-lysine (PLL),[13] or polyethylenimine (PEI).[14] Compared to other cationic groups, PEI has a higher endosomal escape capability, favoring a high gene silencing efficacy.[14,15]

Chapter 6 extended the synthesis approach developed in Chapter 5, where epoxysilane functionalized UHSS (Epoxy-UHSS) with a same diameter of ~10 nm were designed under similar synthesis condition, but a new precursor diethoxy(3-glycidyloxypropyl)methylsilane was utilized instead of dimethyl-silane in Chapter 5, leading to the grafting of both an inert alkyl group and a reactive group (epoxy). Eventually the obtained Epoxy-UHSS can be easily covalently conjugated

with cationic PEI by nucleophilic addition to the epoxy groups. As hypothesized, this designed positively charged PEI-UHSS demonstrated excellent delivery efficiency of functional siRNA, by taking advantages of ultra-small particle size, excellent monodispersity and desired surface functionality of PEI. The delivery results are comparable to commercial agents. This work is the first report on utilizing mono-dispersef SiNPs with ultra-small sizes for siRNA delivery.

Another beneficial surface functionality of SiNPs is targeting delivery, which is vital for efficient cancer therapy because most anticancer drugs distribute throughout the body and can be harmful to healthy cells.[16] To minimize side effects, it would be highly desirable to specifically increase therapeutic agents' concentration at the target sites. Many efforts have been devoted to develop SiNPs modified with targeting moieties, including specific ligands (such as folic acid,[17,18] mannose[19] and arginine-glycine-aspartate (RGD)[20]), peptides,[21] and antibodies.[22] The abundant silanol groups (Si–OH) facilitate the modification of the above targeting moieties, thereby achieving targeting of SiNPs to specific cancer cells. Targeting delivery will enhance the cellular uptake of SiNPs in defective cells, leading to significant improvement in cancer therapy. Hyaluronic acid (HA) is a biodegradable, biocompatible and non-immunogenic glycosaminoglycan.[23,24] HA has been widely utilized as a targeting moiety for cancer therapy, because many types of tumor cells over-express HA receptors like CD44.[16] Utilizing CD44-HA specific affinity is therefore an attractive strategy for cancer targeting treatment. Ma *et al.* firstly reported the designed synthesis of MSNs-HA conjugate.[25] After loading with CPT, HA-MSNs showed enhanced cytotoxicity to HeLa cells. However, the improvement in cell toxicity is not significant compared to free CPT. Because HA coated on the outer surface of MSNs is very hydrophilic; the nature of drug may also have influence on the cytotoxicity. Therefore, more efforts are still needed to rationally design targeting moieties modified SiNPs to improve drug deliveries at targeted cells.

In Chapter 7, HA modified SiNPs were designed, which possess specific affinity to CD44 over expressed on the surface of a specific cancer cell line, HCT-116 (human colon cancer cells). A hydrophilic anticancer drug, doxorubicin hydrochloride (Dox), loaded HA-SiNPs showed greater cytotoxicity to HCT-116 cells than free Dox and Dox-SiNPs due to the enhanced cell internalization behavior of HA-SiNPs. As expected, the desired surface functionality is also crucial to improve drug delivery efficiency by modification of biodegradable and biocompatible targeting ligand of HA on the surface of SiNPs.

The results presented in Chapters 6 and 7 confirm that surface functionality of SiNPs play an important role in delivery efficiency of both siRNA and anticancer drugs. Different from such small

cargoes, plasmid DNA (pDNA) is much larger and the length of pDNA could be in micrometre scale. The influences of structure parameters of SiNPs on pDNA delivery efficiency are expected to be significantly different from those on small cargoes. For example, it has been well documented that small SiNPs less than 100 nm are beneficial for cellular delivery of small molecules. However it is not clear how the particle size of SiNPs would affect pDNA delivery. Therefore, the fourth aim of this thesis is to gain insight of the role of particle size of highly mono-dispersed SiNPs on large pDNA transfection efficiency by deeply investigating the interaction between SiNPs and pDNA and the cellular uptake performance. The results presented in Chapter 8 suggest that an optimized particle size of SiNPs is 330 nm for the highest expression of GFP by delivering the large pDNA (6.1 and 8.9 kbp). As hypothesized, it was found that pDNA would affect the sizes of SiNPs and subsequent cellular uptake after forming complexes due to its large size. The transfection efficiency was found as a compromise between the binding capacity and cellular uptake performance of SiNPs and pDNA conjugates. This work demonstrates for the first time the significance of particle size on gene transfection efficiency in silica based gene delivery systems. These findings are crucial to the rational design of synthetic vectors for gene therapy.

In summary, the development of SiNPs has profoundly affected their applications in drug/gene delivery. The desired structure parameters of SiNPs are of great significance to enhance their biological efficacy, including monodispersity, particle sizes and surface functionality. This thesis provides novel facile synthesis approaches to fabricate highly mono-dispersed SiNPs with tunable particle sizes and new nanostructures, avoiding any harsh conditions (e.g. strong acids, alkali or organic solvents). These designed SiNPs with desired particle size, monodispersity and surface functionality have shown their enhanced capacity in penetration in three dimensional spheroid models, improved cellular drug/gene delivery efficiency.

## 9.2 Outlook

There are more space to exploit the capacity of highly mono-dispersed SiNPs developed in this thesis using the novel and facile approaches in other biomedical applications, as exampled below.

1) Combination therapy using MMSNs to deliver both photosensitizers (PSs) and siRNA.

As introduced in Chapter 2, photodynamic therapy (PDT) is one of the promising approaches for cancer treatments; it utilizes photosensitizers (PSs) and visible light together with oxygen to produce cytotoxic reactive oxygen species (ROS) to kill cancer cells. However, most PSs are hydrophobic; this can cause aggregation in the physiological environment, limiting their clinical applications. Therefore, enhancing the cellular bioavailability of PSs is a big challenge in PDT. In

live cancer cells, excess ROS are normally degraded by anti-oxidizing agents triggered by the cellular defense system. Thus, suppression of antioxidant activity is an alternative way to increase the cytotoxicity of ROS and subsequently enhance PDT efficiency. These issues represent the hurdles of developing effective PDT treatments.

An integrated approach based on MMSNs with high pore volume could be utilized to address the above issues, enhancing PDT efficiency. The key strategies include: 1) using MMSNs (<100 nm) as nano-carriers to deliver hydrophobic PSs to enhance their bioavailability; 2) modification of MMSNs with PEI to deliver specific siRNA to knock down antioxidant enzymes for further enhancing ROS production. The combination therapy provides great promising for improving PDT efficiency by co-delivering PSs and siRNA using MMSNs as nano-carriers. The outcomes of this design would lead to new more effective therapeutic tools.

2) Multi-functional UHSS for effective *in vivo* imaging.

It has been well documented that the bared SiNPs with negatively charged surface would easily interact with serum, and then be rapidly cleared from circulation by macrophages in reticuloendothelial system (RES) during the *in vivo* studies. The most efficient approach to address this issue is PEGylation modification on the surface of SiNPs. The hydrophilic PEG layers could greatly enhance the circulation time of SiNPs. Therefore, novel PEG-UHSS could be designed by utilizing PEG-silane as silica sources instead of dimethyl-siliane used in Chapter 5. At the same time the fluorescent dye can be incorporated into the PEG-UHSS utilizing the protocol in Chapter 5. Taking their unique advantages of excellent monodispersity and stability in aqueous media, this designed multi-functional UHSS are expected to be a promising probe in *in vivo* imaging.

3) Fluorescent UHSS for cell sensing

As introduced in Chapter 2, the real-time quantification of the intercellular analyte concentration using fluorescent probes is very important to provide insights into chemical microenvironment of sub-cellular compartments. UHSS developed in Chapter 5 are expected to be utilized as efficient nano-carriers to incorporate sensing dyes and a reference dye for intracellular detections of oxygen, pH, or ionic species. Not limited in drug/gene delivery and sensing/imaging, more applications of the developed highly mono-dispersed silica nanostructures in this thesis could be exploited in other fields of nanomedicine.

## 9.3 References

1. Tang, F.Q., L.L. Li, and D. Chen, Mesoporous Silica Nanoparticles: Synthesis, Biocompatibility and Drug Delivery. *Advanced Materials*, 2012, **24**(12), 1504-1534.
2. Chen, Y., H.-R. Chen, and J.-L. Shi, Construction of Homogenous/Heterogeneous Hollow Mesoporous Silica Nanostructures by Silica-Etching Chemistry: Principles, Synthesis, and Applications. *Accounts of Chemical Research*, 2013, DOI: 10.1021/ar400091e.
3. Mamaeva, V., C. Sahlgren, and M. Linden, Mesoporous silica nanoparticles in medicine-Recent advances. *Advanced Drug Delivery Reviews*, 2013, **65**(5), 689-702.
4. Lu, F., et al., Size Effect on Cell Uptake in Well-Suspended, Uniform Mesoporous Silica Nanoparticles. *Small*, 2009, **5**(12), 1408-1413.
5. Zhu, J., et al., Small Mesoporous Silica Nanoparticles as Carriers for Enhanced Photodynamic Therapy. *Chemistry-an Asian Journal*, 2011, **6**(9), 2332-2338.
6. Moller, K., J. Kobler, and T. Bein, Colloidal suspensions of mercapto-functionalized nanosized mesoporous silica. *Journal of Materials Chemistry*, 2007, **17**(7), 624-631.
7. Moller, K., J. Kobler, and T. Bein, Colloidal suspensions of nanometer-sized mesoporous silica. *Advanced Functional Materials*, 2007, **17**(4), 605-612.
8. Kobler, J., K. Moller, and T. Bein, Colloidal suspensions of functionalized mesoporous silica nanoparticles. *Acs Nano*, 2008, **2**(4), 791-799.
9. Qiao, Z.A., et al., Synthesis of Mesoporous Silica Nanoparticles via Controlled Hydrolysis and Condensation of Silicon Alkoxide. *Chemistry of Materials*, 2009, **21**(16), 3823-3829.
10. Pampaloni, F., E.G. Reynaud, and E.H.K. Stelzer, The third dimension bridges the gap between cell culture and live tissue. *Nature Reviews Molecular Cell Biology*, 2007, **8**(10), 839-845.
11. Jiang, X.Y., et al., Integrin-facilitated transcytosis for enhanced penetration of advanced gliomas by poly(trimethylene carbonate)-based nanoparticles encapsulating paclitaxel. *Biomaterials*, 2013, **34**(12), 2969-2979.
12. Na, H.K., et al., Efficient Functional Delivery of siRNA using Mesoporous Silica Nanoparticles with Ultralarge Pores. *Small*, 2012, **8**(11), 1752-1761.
13. Hartono, S.B., et al., Poly-L-lysine Functionalized Large Pore Cubic Mesostructured Silica Nanoparticles as Biocompatible Carriers for Gene Delivery. *Acs Nano*, 2012, **6**(3), 2104-2117.
14. Niu, Y., et al., Nanoparticles Mimicking Viral Surface Topography for Enhanced Cellular Delivery. *Advanced Materials*, 2013, **25**(43), 6233-6237.
15. Sokolova, V. and M. Epple, Inorganic nanoparticles as carriers of nucleic acids into cells. *Angewandte Chemie-International Edition*, 2008, **47**(8), 1382-1395.
16. Platt, V.M. and F.C. Szoka, Anticancer therapeutics: Targeting macromolecules and nanocarriers to hyaluronan or CD44, a hyaluronan receptor. *Molecular Pharmaceutics*, 2008, **5**(4), 474-486.

17. Zhu, Y.F., Y. Fang, and S. Kaskel, Folate-Conjugated Fe(3)O(4)@SiO(2) Hollow Mesoporous Spheres for Targeted Anticancer Drug Delivery. *Journal of Physical Chemistry C*, 2010, **114**(39), 16382-16388.
18. Lu, J., et al., Biocompatibility, Biodistribution, and Drug-Delivery Efficiency of Mesoporous Silica Nanoparticles for Cancer Therapy in Animals. *Small*, 2010, **6**(16), 1794-1805.
19. Brevet, D., et al., Mannose-targeted mesoporous silica nanoparticles for photodynamic therapy. *Chemical Communications*, 2009, (12), 1475-1477.
20. Fang, I.J., et al., Ligand Conformation Dictates Membrane and Endosomal Trafficking of Arginine-Glycine-Aspartate (RGD)-Functionalized Mesoporous Silica Nanoparticles. *Chemistry-a European Journal*, 2012, **18**(25), 7787-7792.
21. Cheng, S.H., et al., Tri-functionalization of mesoporous silica nanoparticles for comprehensive cancer theranostics-the trio of imaging, targeting and therapy. *Journal of Materials Chemistry*, 2010, **20**(29), 6149-6157.
22. Tsai, C.P., et al., Monoclonal antibody-functionalized mesoporous silica nanoparticles (MSN) for selective targeting breast cancer cells. *Journal of Materials Chemistry*, 2009, **19**(32), 5737-5743.
23. Knudson, C.B. and W. Knudson, HYALURONAN-BINDING PROTEINS IN DEVELOPMENT, TISSUE HOMEOSTASIS, AND DISEASE. *Faseb Journal*, 1993, **7**(13), 1233-1241.
24. Hua, Q., C.B. Knudson, and W. Knudson, INTERNALIZATION OF HYALURONAN BY CHONDROCYTES OCCURS VIA RECEPTOR-MEDIATED ENDOCYTOSIS. *Journal of Cell Science*, 1993, **106**, 365-375.
25. Ma, M., et al., Hyaluronic acid-conjugated mesoporous silica nanoparticles: excellent colloidal dispersity in physiological fluids and targeting efficacy. *Journal of Materials Chemistry*, 2012, **22**(12), 5615-5621.